DISSERTATION

Submitted to the
Combined Faculty of Mathematics,
Engineering and Natural Sciences
Heidelberg University, Germany
for the degree of
Doctor of Natural Sciences (Dr. rer. nat.)

presented by

Zhiyong Zhao

Oral examination: 09.02.2024

Design and fabrication of functional films and free-standing nanosheets on the basis of poly(ethylene glycols) and self-assembled monolayers

Referee: Prof. (apl.) Dr. Michael Zharnikov

Referee: Prof. Dr. Christine Selhuber-Unkel

Zusammenfassung

Diese Dissertation konzentriert sich auf die Eigenschaften und Anwendungen von ultradünnen Poly(ethylenglykol)-(PEG-)Filmen und freistehenden Nanoblättern, welche durch thermisch induzierte Quervernetzung von Amin/Epoxid-dekorierten STAR-PEG-Vorläufern hergestellt wurden. In dieser Arbeit wurde auch eine weitere Art von molekularen Filmen untersucht, sogenannte selbstorganisierte Monoschichten (engl. *self-assembled monolayers*, SAMs), für die die Leistung einer Modell-aromatisch-aliphatischen dreibeinigen SAM auf Au(111) im Zusammenhang mit der Elektronenstrahllithographie (engl. *electron beam lithography*, EBL) und der Herstellung von Kohlenstoffnanomembranen (engl. *carbon nanomembranes*, CNMs) – eine andere Art von Nanoblättern – getestet wurde.

Im ersten Teil dieser Arbeit wurde der Einfluss von Ultraviolett-(UV-)Strahlung (254 nm) auf die PEG-Filme untersucht. Es konnte gezeigt werden, dass unter Bestrahlung ein progressiver Abbau des PEG-Materials erfolgt, mit anschließender Desorption freigesetzter Fragmente, wobei die ursprüngliche chemische Zusammensetzung und die Eigenschaften der Filme erhalten bleiben. Dies bietet Potential für die 3D-Strukturierung von PEG-Materialien unter Beibehaltung der bioinerten und hydrogelen Eigenschaften. Neben der UV-Bestrahlung wurde im zweiten Teil dieser Arbeit auch der Einfluss des Molekulargewichts (engl. *molecular weight,* MW) der eingesetzten Vorläufer (2000–20000 g/mol) auf die Eigenschaften der PEG-Filme und Nanoblätter untersucht. Diese Systeme zeigten ausgeprägte biorepulsive, hydrogele und elastische Eigenschaften, die sich mit dem MW veränderten. Das MW beeinflusste insbesondere das Quellverhalten und die Permeabilität der PEG-Filme sowie die elastischen Eigenschaften der PEG-Nanoblätter. Als nächstes Teilprojekt wurde der Einfluss weiterer relevanter Parameter, wie eine Abweichung von der Gleichgewichtszusammensetzung 1:1 der Vorläufer sowie Elektronen- und UV-Behandlung (zusätzliche Studien) untersucht. Im Gegensatz zur UV-Bestrahlung (254 nm), konnte unter Elektronenbestrahlung eine starke Beeinträchtigung der Elastizität und Stabilität der PEG-Nanoblätter festgestellt werden. In den weiteren Teilprojekten wurden PEG-Filme als poröse und bioinerte Matrix für die DNA-Erkennung verwendet, die auf der Immobilisierung und Hybridisierung von einsträngiger DNA (engl. *single-stranded DNA*, ssDNA) in der PEG-Matrix beruhte. Die Immobilisierung der ssDNA-Sonde basierte entweder auf einer NHS-Ester-Amin-Verknüpfung oder einer Thiol-Epoxid-Verknüpfung mit den freien Amin- oder Epoxidgruppen der entsprechenden PEG-Matrix. In beiden Fällen konnte eine effiziente Immobilisierung der ssDNA-Sonde festgestellt werden und eine hohe Selektivität und Hybridisierungseffizienz der resultierenden 3D-ssDNA-

Arrays gegenüber den Zielsträngen nachgewiesen werden. Als geeignete Transduktionstechnik für die DNA-Erkennung, die keine Markierung der ssDNA erfordert, wurde hierfür die elektrochemische Impedanzspektroskopie eingesetzt.

In einem weiteren Teilprojekt wurde eine Serie dünner (80–100 nm) PEG-Fulleren (C60)-Verbundfilme durch Eintauch-, Ein-Topf- und Rückflussverfahren hergestellt. In diesen Filmen wurden die optischen und elektrochemischen Eigenschaften von C60 mit den vorteilhaften Merkmalen der PEG-Matrix kombiniert, was insbesondere zu einer guten elektrochemischen Leitfähigkeit und hoher Elastizität führte. Es konnte zudem gezeigt werden, dass diese Filme von ihrem Primärsubstrat abgelöst werden können, um freistehende Verbundnanoblätter zu bilden, die Potential für verschiedene Anwendungen wie flexible Elektronik, Fotodetektoren und elektrochemische Biosensoren haben.

Im letzten Abschnitt dieser Arbeit wurde die Elektronenstrahl induzierte Behandlung einer Triptycen basierten SAM (Trip-T1) untersucht. Nach Elektronenbestrahlung zeigte diese Monoschicht ein Verhalten, das denen von monopodalen aromatischen Monoschichten ähnelt und eine klare Dominanz der intermolekularen Vernetzung zeigte. Es wurde gezeigt, dass die Trip-T1 SAM als Negativlack in der EBL dienen kann, ähnlich zum monopodalen Benzylthiol (PT1) SAM, welches als Referenz diente. Schließlich konnten robuste und fehlerfreie CNMs erfolgreich aus der Trip-T1 SAM hergestellt werden, welche jedoch eine etwas höhere Dosis (80 mC/cm^2) erforderten als die Referenz PT1 Monoschicht (40 mC/cm^2). Diese CNMs entsprechen der unteren Materialdichte für solche Objekte.

Abstract

This thesis focuses on the properties and applications of ultrathin poly(ethylene glycol) (PEG) films and freestanding nanosheets, fabricated by thermally-induced crosslinking of amine/epoxy decorated STAR-PEG precursors. In addition, my research was also extended to another kind of molecular films – self-assembled monolayers (SAMs), for which the performance of a model aromatic-aliphatic tripodal SAM on Au(111) in the context of electron beam lithography (EBL) and fabrication of carbon nanomembranes (CNMs) – another kind of nanosheets – was tested.

As the first subproject, the effect of ultraviolet (UV) light (254 nm) on the PEG films was explored. UV irradiation was shown to result in progressive decomposition of the PEG material followed by desorption of released fragments, while preserving the original chemical composition and properties of the films, which offers potential for 3D patterning of PEG materials with retaining bioinert and hydrogel properties. As the second subproject, the effect of molecular weight (MW) of the precursors (2000–20000 g/mol) on the properties of the PEG films and nanosheets was studied. These systems exhibited pronounced biorepulsive, hydrogel, and elastic properties which varied with the MW. The MW affected in particular the swelling behavior and permeability of the PEG films as well as elastic properties of the PEG nanosheets. As the following subproject, the effect of other relevant parameters, such as a deviation from the equilibrium 1:1 composition of the precursors and electron and UV (additional studies) treatment were studied. In particular, the elasticity and stability of the PEG nanosheets were found to be strongly deteriorated by electron irradiation. In contrast, UV irradiation (254 nm) did not affect their elastic properties, in agreement with my previous results on this subject. Within the further subprojects, PEG films were used as a porous and bioinert matrix for DNA sensing, relying on immobilization and hybridization of single-stranded DNA (ssDNA) in the PEG matrix. The immobilization of the probe ssDNA was based on either NHS-ester-amine or thiol-epoxy linkage to the free amine or epoxy groups in the specifically prepared PEG matrix, respectively. In both cases, efficient immobilization of the probe ssDNA and high selectivity and hybridization efficiency of the resulting 3D ssDNA arrays with respect to the target strands were demonstrated. As a suitable transduction technique for the DNA sensing, requiring no ssDNA labeling, electrochemical impedance spectroscopy was employed.

Within a further subproject, a series of thin (80–100 nm) PEG-fullerene (C60) composite films were prepared by immersion, one-pot, and reflux methods. These films exhibited distinct

optical and electrochemical properties of C60, merged with some favorable characteristics of the PEG matrix, resulting, in particular, in good electrochemical conductivity and high elasticity. It was demonstrated that these films can be detached from the primary substrate to form free-standing composite nanosheets, having potential for various applications such as flexible electronics, photodetectors, and electrochemical biosensors.

The final subproject was the electron-beam-induced treatment of a triptycene-based SAM (Trip-T1). Upon electron irradiation, this monolayer was found to exhibit behavior similar to that of monopodal aromatic monolayers, showing a clear dominance of intermolecular crosslinking. It was demonstrated that the Trip-T1 SAM can serve as a negative resist in EBL, similar to the reference, monopodal benzylthiol (PT1) SAM. Finally, robust and defect-free CNMs could be successfully fabricated from the Trip-T1 SAM, which, however, required a somewhat higher dose (80 mC/cm^2) than for the reference PT1 monolayer (40 mC/cm^2). These CNMs correspond to the low limit of material density for such objects.

Table of Contents

Zusammenfassung i

Abstract iii

1. Introduction 1

2. Basics and Background 5

2.1. Poly(ethylene glycol) 5

2.2. Star poly(ethylene glycol) 5

2.3. Self-assembled monolayers 6

2.4. X-ray photoelectron spectroscopy 7

2.5. Near edge X-ray adsorption fine structure spectroscopy 10

2.6. Ellipsometry 12

2.7. Bulge test 14

2.8. Scanning electron microscopy 15

2.9. Atomic force microscopy 16

2.10. Ultraviolet and visible spectroscopy 16

2.11. Electrochemical characterization 17

2.12. E-beam lithography 20

3. Experimental 21

3.1. Materials and substrates 21

3.1.1. Chemicals 21

3.1.2. Substrates 22

3.2. General preparation procedures 22

3.2.1. PEG films preparation 22

3.2.2. Nanosheets fabrication 23

3.2.3. SAMs preparation 23

3.3. Characterization 23

4. Results and Discussion 26

4.1. The effect of ultraviolet light on the properties of PEG films 26

4.1.1. Motivation 26

4.1.2. Specific experiments and procedures 26

4.1.3. Film thickness 27

4.1.4. XPS 30

4.1.5. Swelling properties 31

4.1.6. Biorepulsive properties 33
4.1.7. General considerations 35
4.1.8. Patterning of the PEG films 38
4.2. Tuning the properties of PEG films and nanosheets by the molecular weight of the precursors 40
4.2.1. Motivation 40
4.2.2. Specific experiments and procedures 40
4.2.3. Film thickness 40
4.2.4. Film composition 41
4.2.5. Swelling properties 44
4.2.6. Biorepulsive properties 46
4.2.7. Nanoparticles loading 48
4.2.8. Free-standing PEG nanosheets 51
4.2.9. Mechanical properties of the nanosheets 52
4.2.10. Discussion 54
4.3. Elastic properties of free-standing PEG nanosheets and respective implications 57
4.3.1. Motivation 57
4.3.2. Specific experiments and procedures 57
4.3.3. Parameters of the bulge test 57
4.3.4. Effect of nanosheet thickness 60
4.3.5. Effect of nanosheet composition 61
4.3.6. Effect of electron irradiation 63
4.3.7. Effect of UV light 65
4.4. Rational design of amine-rich PEG films as matrixes for ssDNA immobilization and hybridization 69
4.4.1. Motivation 69
4.4.2. Specific experiments and procedures 69
4.4.3. XPS 71
4.4.4. Electrochemical studies 80
4.5. Exploiting epoxy-rich PEG films for highly selective ssDNA sensing via electrochemical impedance spectroscopy 85
4.5.1. Motivation 85
4.5.2. Specific experiments and procedures 85
4.5.3. General procedure and effect of concentration 86

4.5.4. Validity of the thiol-epoxy linkage 89
4.5.5. Hybridization ability of the ssDNA-loaded PEG film 91
4.5.6. Comparison to the reference Au/ssDNA system 92
4.5.7. XPS 95
4.5.8. Sensitivity of the ssDNA-loaded PEG films 97
4.6. PEG-C60 composite films and free-standing nanosheets for flexible electronic devices and sensors 99
4.6.1. Motivation 99
4.6.2. Specific experiments and procedures 99
4.6.3. Morphology of the PEG-C60 films 100
4.6.4. Composition of the PEG-C60 films 103
4.6.5. Optical properties 105
4.6.6. Electrochemical properties 106
4.6.7. Stability of the composite films 110
4.6.8. Free-standing and transferred nanosheets 112
4.7. Electron-induced modification of triptycene SAM in context of lithography and nanofabrication 115
4.7.1. Motivation 115
4.7.2. Specific experiments and procedures 116
4.7.3. XPS 117
4.7.4. NEXAFS spectroscopy 121
4.7.5. EBL studies 123
4.7.6. CNM fabrication 125
4.7.7. Discussion 127
5. Conclusions and Outlook 130
Lists 135
List of Figures 135
List of Tables 141
List of Abbreviations 142
List of Publications 144
Included in this thesis 144
Besides this thesis 144
References 146
Acknowledgements 166

1. Introduction

Functional nanoscale organic films, distinguished by their thickness, specific physicochemical properties, and function-adjustable character, have become one of the cornerstones of modern material design.[1–4] Meanwhile, in a variety of cases, free-standing nanosheets can be derived from the parent films, which normally not only preserve the original properties of these films but also possess superior flexibility.[5–7] Both functional films and free-standing nanosheets offer remarkable potential in diverse applications, ranging from organic electronics,[8] to sensors[9] and energy storage,[10] and beyond.[11–13] Among different types of these systems, functional films and free-standing nanosheets on the basis of poly(ethylene glycols) (PEGs) and self-assembled monolayers (SAMs) can be mentioned, which have been within the focal research fields of our group in the past.

Based on the previous research conducted by our group, this thesis embarks on an extending exploration into the design and fabrication of functional films and free-standing nanosheets on the basis of PEGs and SAMs. Through the integration of sophisticated molecular design and purpose-specific fabrication strategies, this thesis aims to unravel the intricate relations between material structures and the resultant properties, while also delving into specific applications. For the sake of clarity, I will first introduce the PEG-related subprojects, which represent the major part of this thesis, followed by the introduction of the SAM-related research.

PEG is a hydrophilic, synthetic polymer that has, despite the simple chemical structure, remarkable properties which make it interesting and suitable for both scientific research and commercial applications.[14,15] The most important feature of PEG is its biocompatibility (or, in other words, bioinertness) – this material resists non-specific adsorption of proteins,[16,17] oligonucleotides,[18] bacteria,[19] and other bioorganisms,[20] as well as cell adhesion.[21] The bioinert properties of PEG can be transferred to specific substrates through a suitable PEG coatings.[22–25] As a particular approach, weakly bound PEG films can be prepared with a sufficient adhesion to the primary substrate but still capable to be separated from it and transferred to a secondary substrate or even exist as a free-standing nanosheet.[26]

A representative and compelling example in this context is provided by thin PEG films formed from so-called STAR-PEG compounds (Figure 3.1)[27] which have been investigated by our group in the past within several research projects. These compounds, featuring four PEG ´arms´, decorated with mutually reactive terminal chemical groups, amine (STAR-NH_2) and epoxide

(STAR-EPX), can be mixed, deposited onto a suitable substrate, and crosslinked to form a porous 3D network by the formation of ethanol-amine bridges (Figure 3.1). The previous work by our group demonstrated a variety of excellent properties and applications of these PEG films. In particular, it was demonstrated that the thickness of these films can be precisely tuned across a broad range by adjusting the concentration of the precursors.[27] In addition, these films were found to possess pronounced bioinert and hydrogel properties and also exist as ultrathin free-standing nanosheets with exceptional elasticity.[27,28] Such free-standing nanosheets can be potentially used as highly transparent, bioinert supports for transmission electron microscopy (TEM) and as high-sensitivity pressure sensors.[28] Moreover, the parent PEG films can serve as matrices for nanoparticle adsorption, controlled protein attachment (biosensors), and humidity sensing.[27,29,30] Additional possibilities were provided by modification of these films by electron irradiation, also in the context of e-beam lithography (EBL).[31,32] Electron irradiation was shown to result in progressive desorption of the PEG material and chemical modification of the residual film.[31] The residual material loses both hydrogel and bioinert properties of the original PEG matrix, which can be in particular used for the fabrication of nanoparticle, dye, and protein patterns.[31,32] Considering the above properties and potential applications of the PEG films and nanosheets, it became highly meaningful and pertinent to extend the scope of investigations on these systems, which occurred within my PhD project.

I started the PEG-related research by exploring the effect of ultraviolet (UV) light on the properties of the PEG films, complementary to the previously studied effect of electron irradiation.[31] By intentionally avoiding functional, photoresponsive groups, I aimed to discern the impact of UV irradiation on the PEG matrix itself, for which the reaction to UV irradiation is of fundamental importance. The results of this research were indeed quite interesting and provided implications for 3D UV lithography on the PEG film basis.

As the next subproject, I varied the molecular weight (MW) of the STAR-PEG precursors, which was an important option considering that all experiments so far have been performed with an only one MW of 2000 g/mol (2k). In my experiments, MW was varied from 2000 to 20000 g/mol. To this end, I studied the effect of the MW variation on the basic parameters of the PEG films and related, free-standing nanosheets, viz. their thickness, permeability, and hydrogel, bioinert, and mechanical (elastic) properties. In order to investigate the mechanical properties of the PEG nanosheets in more detail, I took the nanosheets formed from 2k STAR-PEG precursors as a representative system and studied the effect of different parameters on their elastic properties, including the size of the window for the elasticity test, film thickness,

and film composition. I also explored the possibility to tune the elastic properties of the PEG nanosheets by the modification of the parent films by electron irradiation and UV light. The latter experiments, in combination with additional measurements, shed also some light on the effect of UV irradiation on the PEG films, complementary to the results of my previous research on this subject (see above).

Within further subprojects, I devoted my attention to expanding the bio-related applications of the PEG films. In this context, I explored the feasibility of utilizing these films as a matrix for the immobilization and hybridization of single-stranded DNA (ssDNA), aiming for DNA sensing, which is widely applied in biological detection, microarray technology, and related fields.[33–35] The DNA sensing usually relies on the immobilization of ssDNA on solid supports, serving as a probe for hybridization with target ssDNA sequences. To ensure a highly selective and effective hybridization process, it is essential to anchor probe ssDNA onto a bioinert substrate to prevent non-specific adsorption of mismatching strands and other biomolecules.[36–38] The PEG films represent an ideal "substrate" in this regard, featuring not only distinct bioinert properties, but also 3D character and high porosity, favorable for the accessibility of the entire matrix by both probe and target ssDNA. Consequently, I tried the immobilization of the probe ssDNA in the primary PEG matrix and monitored the hybridization performance of the resulting ssDNA array. The immobilization of the probe ssDNA was based on either NHS-ester-amine or thiol-epoxy linkage to the free amine or epoxy groups of the specifically prepared PEG matrix, respectively. The results are highly promising, opening a new path for highly-selective and effective ssDNA sensing.

I also dedicated my research to the PEG-fullerene (C60) composite films, exploring different synthetic routes. This innovative approach gave an addition option for shaping such films as mechanically robust, free-standing nanosheets – a challenge that has not been explored before. Specifically, I employed three different preparation procedures to fabricate PEG-C60 composite films. The properties of these films were monitored by various techniques. Notably, the stability, elasticity, and preservation of the original properties with respect to the parent films were meticulously examined for the free-standing PEG-C60 nanosheets. Such composite films and free-standing nanosheets, combining the biocompatible properties of PEG film and the unique properties of C60,[39,40] might have great potential in organic electronics,[41] photovoltaics,[42] and sensors.[43]

Finally, along with the PEG-related subprojects, a part of my research effort was devoted to the study of carbon nanomembranes (CNMs) derived from SAMs. CNMs are ultrathin (1–2 nm)

free-standing nanosheets, composed of interconnected saturated and unsaturated hydrocarbons.[44,45] They have gained significant attention in the context of both fundamental science[45] and various applications.[46–50] The approach for preparing such CNMs is through electron irradiation of thiolate-anchored, aromatic and aromatic-aliphatic SAMs prepared on a coinage metal substrate.[45,51] Unlike aliphatic SAMs, which predominantly disintegrate and lose coupling to the substrate in the course of electron irradiation,[52] aromatic monolayers feature extensive crosslinking upon irradiation, following the cleavage of C−H and C−C bonds in the SAM matrix.[52–56] This process prevents the desorption of molecular fragments and extensive damage of the SAM-substrate interface, so that robust, homogeneous, and strongly crosslinked 2D films are formed. These films can then be separated from the primary substrate and transferred to a secondary substrate as well-defined CNMs.[45,51] Alternatively, aromatic SAMs can be used as negative resists for EBL, transferring a pattern written by electron beam into the underlying substrate at the successive etching.[52,53,57]

While monopodal aromatic SAMs have been extensively studied in the above fields, the potential of multipodal SAMs, including tripodal SAMs in particular, remained mostly unexplored due to the challenges in obtaining high-quality monolayers.[58–60] However, our group, in collaboration with several partners, has recently reported the fabrication of well-ordered and densely packed tripodal triptycene-based SAMs, with the basic building block represented by 1,8,13-trimercaptomethyl-triptycene (Trip-T1).[61] The latter system provided thus a promising candidate for the EBL and CNM fabrication. Consequently, I explored the potential of using Trip-T1 SAM on Au(111) for these purposes. Additionally, a reference monopodal system, a SAM of benzylthiol, was studied. A variety of complementary spectroscopic and microscopic techniques was applied.

The thesis is organized in 5 chapters. Chapter 1 is the introduction of the thesis. Chapter 2 provides basic information regarding PEGs, SAMs, and the relevant characterization techniques. Chapter 3 is the general experimental. Chapter 4 presents the results and discussion of my PhD project as introduced above. Accordingly, this chapter is divided into 7 subchapters, corresponding to each subproject. Chapter 5 presents the final conclusions and outlook.

All the results presented in this thesis have already been published in peer-reviewed journals. I was the first author in all these publications.

2. Basics and Background

2.1. Poly(ethylene glycol)

Poly(ethylene glycol) (PEG) is a synthetic, nontoxic, hydrophilic polymer, which is composed of repeating units of ethylene oxide (CH_2CH_2O), resulting in a linear, flexible chain structure.[14] The molecular weight of PEG can vary significantly, ranging from a few hundred Daltons to several hundred thousand Daltons, depending on the desired application.

PEG is well-known for its resistance to non-specific protein adsorption, which is mainly attributed to its hydrophilicity, electric neutrality, and steric hindrance.[62] PEG is highly hydrophilic, which prevents the hydrophobic interaction of proteins, thus reducing non-specific adsorption. Additionally, PEG is electrically neutral, making it less prone to electrostatic interactions with proteins, which often carry charged residues on their surface, and when exposed to a charged surface, electrostatic attractions can drive non-specific binding. Moreover, as a long-chine polymer, PEG can provide large steric hindrance, preventing proteins from coming into direct contact and binding to the surface.

In addition to non-specific protein resisting, the other properties of PEG make it suitable for more applications. For example, PEG finds extensive use in pharmaceutical and biological fields due to its biocompatibility and low toxicity. It can serve various purposes, such as enhancing drug solubility, improving stability, controlling drug release, and increasing bioavailability.[63,64] PEG is also widely used in cosmetic and personal care products due to its emulsifying, moisturizing, and solubilizing properties.[65] PEG is also employed in various industrial processes, such as lubricants and coatings, where it can enhance product performance and modify material properties.[20]

2.2. Star poly(ethylene glycol)

Star poly(ethylene glycol) (STAR-PEG) contains at least three linear arms connected to a central core, in which the arms are all equivalent in length and structure (Figure 2.1). The great advantage of STAR-PEG is that it has more modifiable end groups for the improvement of functional selectivity. Compared with traditionally linear PEG, STAR-PEG is more favorable, especially in drug delivery and controlled release. For example, the tumor targeting and environmental responsive functions are easily integrated in the case that chemotherapeutic drugs are modified with STAR-PEGs, and the drug loading capacity could be dramatically enhanced.[66] Moreover, intermolecular crosslinking between STAR-PEGs with specifically-

modified terminal groups will be triggered easily, forming biocompatible network, with hydrogels as a representative,[67] which have received extensive attention in biomedical applications.[68,69]

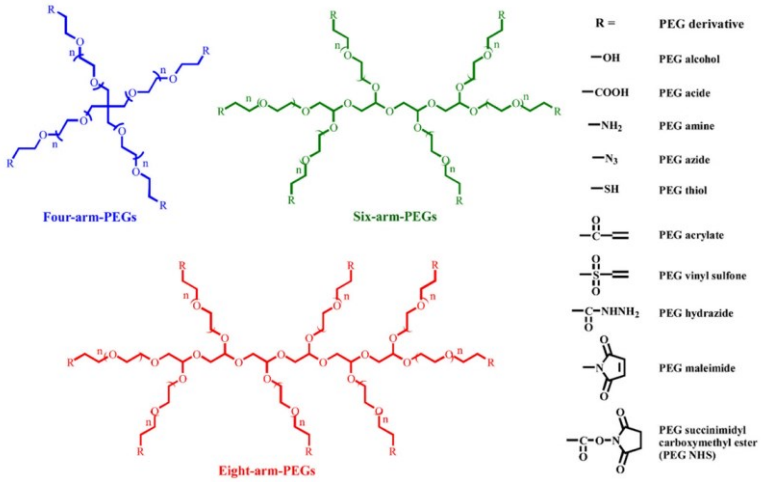

Figure 2.1. Structures of STAR-PEGs with various functional end groups.[66]

2.3. Self-assembled monolayers

Self-assembled monolayers (SAMs) refer to monomolecular films, which are formed by spontaneous organization of organic molecules onto a suitable substrate surface, due to the intermolecular forces between the molecules and the interactions between the molecules and the substrate.[70] Various substrates have been used for SAMs formation, including gold,[51,71,72] copper,[73] silver,[74] aluminum oxide,[75] and indium tin oxide.[76] Among them, gold is highly favorable, owing to its chemical stability, well-defined surface, and strong thiol binding.

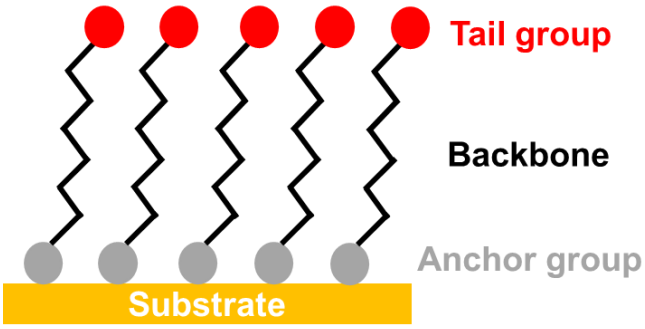

Figure 2.2. Illustration of an ideally ordered SAM. The components of the SAM are described on the right side.

As shown in Figure 2.2, SAMs are usually consisted of three parts: the anchor group, the backbone, and the tail group. Thiol moiety is one of the most typical anchor group, which can form chemical bonding with metals, such as gold or silver.[52,71,72] The backbone consists mostly of linked carbon atoms. The length and flexibility of the backbone can influence the ordering and packing of the molecules in the monolayer, which, in turn, affects the properties of the SAM. The tail group is the portion of the molecule that extends away from backbone and provides the desired functionality or properties to the SAM and ambient interface.[77,78]

The unique ability of SAMs to form highly ordered and well-defined molecular architectures on solid surfaces has enabled a wide range of applications, including surface modification,[79] nanotechnology,[80] molecular electronics,[78] sensors and biosensors,[81] and so on.[82,83] The vast array of applications continues to expand as researchers explore new molecules, surface chemistries, and techniques to harness the potential of SAMs.

2.4. X-ray photoelectron spectroscopy

Basic information. X-ray photoelectron spectroscopy (XPS), also known as electron spectroscopy for chemical analysis (ESCA), is a widely used surface analysis technique that provides information about the elemental composition and chemical states of materials. The basic physic involved in XPS is photoelectric effect. XPS utilizes low-energy X-rays as the excitation source to irradiate samples. When an X-ray photon with enough energy impinges upon an atom, the photon interacts with an atomic orbital electron with transfer of the photon energy to the electron, leading to electron emission from the atom. The photoemission process can be described by the Einstein equation, simply stated as:[84]

$$\mathrm{BE} = h\nu - \mathrm{KE} \qquad (2.1)$$

Where BE represents the binding energy of the electron in the atom, $h\nu$ is the energy of the X-ray source (a known value), and KE is the kinetic energy of the emitted electron which is measured by the XPS spectrometer. Thus, the BE which provides us with valuable information regarding the photoemitting atom is obtained from the known $h\nu$ and the KE.

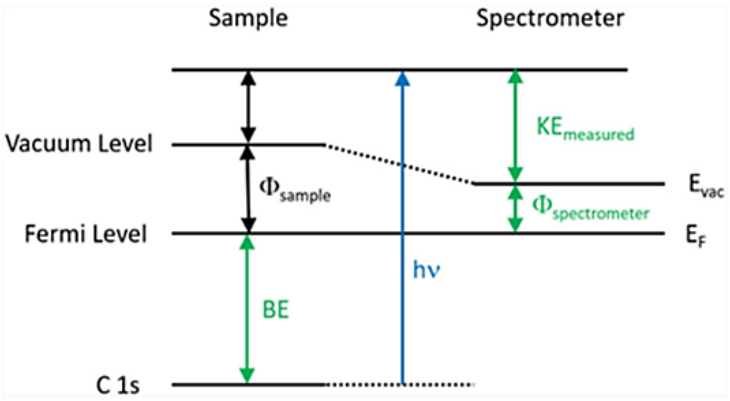

Figure 2.3. Energy level diagram in XPS measurements, including the *hν*, BE, KE, as well as the work function of the spectrometer ($\Phi_{spectrometer}$) and the sample (Φ_{sample}). Taken from ref [85].

In the XPS measurements, photoelectron energy is measured by referring to Fermi energy (E_f). In this way, the sum of the KE and BE does not exactly equal the *hν*, as shown in Figure 2.3. The difference is the $\Phi_{spectrometer}$. Thus, the Einsteein equation becomes:[84]

$$BE = h\nu - KE - \Phi_{spectrometer} \qquad (2.2)$$

Therefore, both KE and $\Phi_{spectrometer}$ have to be measured to determine BE. For conducting samples, the $\Phi_{spectrometer}$ can be calibrated by placing a clean Au substrate in the spectrometer and adjusting the instrumental settings so that the know BE values for Au are obtained (eg., E_f = 0 eV, $4f_{7/2}$ = 84.0 eV).

Spectrometer. The basic components of an XPS system are shown in Figure 2.4, which consists of three major parts: (i) the X-ray source, (ii) the energy analyzer, and (iii) the detector. The standard X-ray source for an XPS instrument uses an electron gun to excite X-ray emission from a metal anode, typically aluminum (*hν* = 1486.2 eV) or magnesium (*hν* = 1253.6 eV). Only a moderate vacuum (ca. 10^{-4} mbar) is required for the transmission of X-rays and photoelectrons through the system, but XPS instruments usually operate in the ultra-high vacuum (UHV) regime, ca. 10^{-7}–10^{-9} mbar, to keep the instrument and the sample surface clean during analysis. The energy analyzer determines the kinetic energy of photoelectrons using a hemispherical analyzer. Here, the photoelectrons must pass between two charged co-hemispherical plates. Only electrons within a narrow range of energies (the "pass energy") arrive at the detector. The role of the detector is to count the electrons according to their energy and intensity (in counts per second).[86]

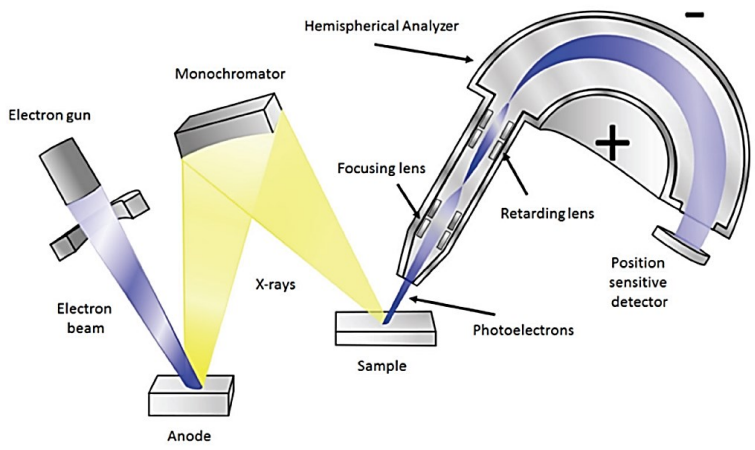

Figure 2.4. Schematic representation of an XPS system.[86]

Photoelectron spectra. The number of detected electrons is represented in an XPS spectrum as intensity, measured in counts per second, plotted against the corresponding BE. In Figure 2.5, we can observe an overview spectrum of a PEG film (~50 nm) deposited on an Au substrate. This spectrum exhibits distinct signals corresponding to the Au 4f, C 1s, and O 1s orbitals. As a reference, the Au $4f_{7/2}$ peak is shifted to 84 eV. In XPS spectra, the s-orbitals appear as singlets, while the p, d, and f orbitals manifest as doublets, with their respective energy and splitting.

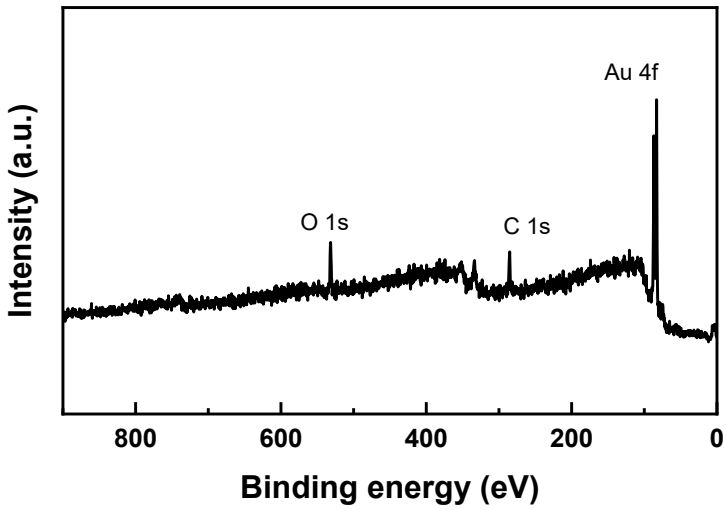

Figure 2.5. XPS overview spectrum of a PEG (50 nm) film on Au substrate, recorded with the MAX 200 instrument using MgKα X-ray source.

Chemical Shift. Chemical shift in XPS refers to the phenomenon where the binding energy of a specific element's peak in the spectrum shifts relative to a reference peak. This shift is influenced by various factors, including the chemical environment, oxidation state, and

electronic structure of the element. The chemical shift provides valuable information about the chemical bonding and electronic properties of the sample, allowing us to analyze the composition and identify different chemical species present on the surface. By measuring and analyzing these shifts, XPS enables precise characterization of materials at the atomic level.

Quantitative Analysis. Quantitative analysis in XPS usually includes determining the stoichiometric composition and calculating the thickness of thin films or surface layers. In both cases, the intensities of the respective XPS signals (the area of the peaks) are required, which can be obtained by XPS peak fitting and background subtraction. In addition, the attenuation length λ, which is defined as the average distance of an electron travel between two inelastic collisions, is also need.[84,87] This thesis only involves the calculation of the thickness of specific SAMs on Au substrates, which is described in detail as follows:

To calculate the thickness of a SAM on an Au substrate, one needs to use the Au 4f intensities of the SAM-covered and blank substrates, denoted as $I_{\text{Au-SAM}}$ and $I_{\text{Au-0}}$, respectively. The intensity of Au 4f is weakened due to the presence of the SAM, the effective thickness of the SAM (d_{SAM}) can be determined by equation 2.3:[84,88]

$$I_{\text{Au-SAM}} / I_{\text{Au-0}} = \exp\left(- d_{\text{SAM}} / \lambda \cos\alpha \right) \qquad (2.3)$$

where α is the angle between the analyzer and the surface.

Another method for thickness calculation is using a reference SAM with well-known thickness. For example, a 1-Hexadecanethiol (C16) SAM on Au substrate has a thickness of 1.89 nm.[89] One can get the thickness of the SAM on the basis of the following equation:

$$d_{\text{SAM}} = d_{\text{ref}} - \lambda \cos\alpha \ln\left(I_{\text{Au-SAM}} / I_{\text{Au-ref}}\right) \qquad (2.4)$$

where d_{ref} and $I_{\text{Au-ref}}$ are the thickness of the reference sample and the intensity of the Au 4f signal for the sample, respectively.

2.5. Near edge X-ray adsorption fine structure spectroscopy

Near edge X-ray adsorption fine structure spectroscopy (NEXAFS) is also often used for surface analysis, which is a highly sensitive technique to resolve the electronic structure and orientation of adsorbates (e.g. SAMs) on metal substrates.[91] In the NEXAFS case, the X-ray adsorption edge describes the point, at which the energy of the X-ray photons is just enough to excite core electrons (mostly K shell) to unoccupied molecular orbitals that are lowers or at vacuum level.[92] A NEXAFS spectrum shows the dependence of the photoabsorption cross section on the photon energy with values from just below the core level ionization threshold

up to around 50 eV. For the oversimplified case of an electron in a single bound state (core level) without any other empty electron state, the photoabsorption cross section changes like a step function as the photon energy is scanned across the ionization energy (thick dashed line in Figure 2.6). No absorption will occur if photon energies are below the core electron binding energy, whereas in the case that photon energies are above the ionization potential (IP), an excitation of the core electron into the continuum of final states enables an absorption of photons.

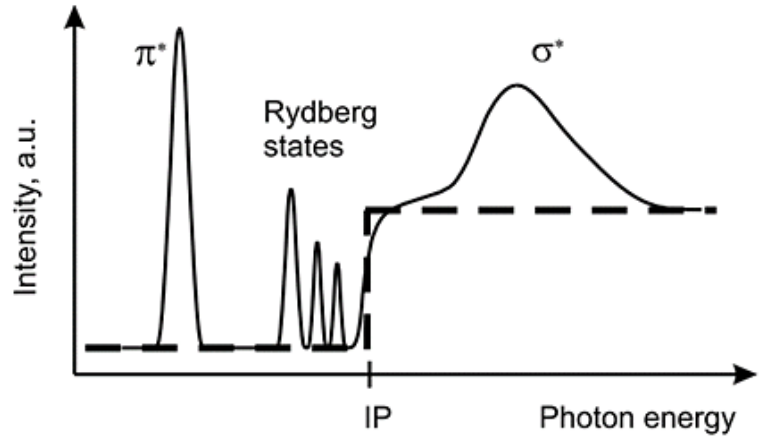

Figure 2.6. A NEXAFS spectrum (solid line) taken from ref [90]. The thick dashed line corresponds to the photoabsorption cross section of an electron located in a single bound state (core level).

However, even in the case of a single free atom (Figure 2.7a), the measured cross section appears significantly more intricate. This complexity arises from the existence of a larger number of final states compared to the oversimplified model mentioned earlier. The electrostatic potential of the atom's positively charged nucleus leads to multiple vacant electronic states, either below (bound states) or above (unbound states) the ionization threshold. The bound states can be broadly categorized into valence states localized near the core and Rydberg states with binding energies approaching the ionization threshold. On the other hand, the unbound states (molecular antibonding) are situated well above the ionization threshold. Notably, NEXAFS resonances resulting from excitations into these states exhibit a characteristic feature – a substantial energetic half-width.

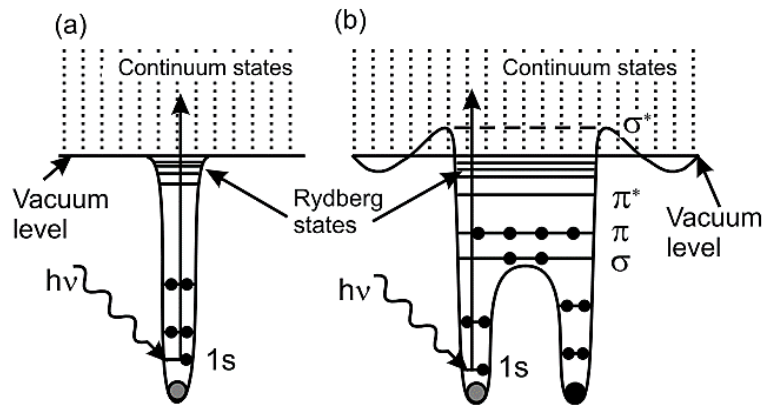

Figure 2.7. (a) Schematic potential for an isolated atom; (b) Schematic potential of a diatomic molecule. In addition to Rydberg states and a continuum of empty states similar to those expected for atoms, unfilled molecular orbitals are present (σ* and π*).[90]

Figure 2.7b shows an energy scheme for a diatomic molecule with the corresponding NEXAFS spectrum shown in Figure 2.6. The empty molecular orbitals are denoted as σ∗ and π∗ orbitals based on their symmetry. Generally, the lowest unoccupied molecular orbital (LUMO) of a π-bonded diatomic subunit of a molecule is a π∗ orbital, whereas σ∗ orbitals are found at higher energies (see Figure 2.7). The latter are typically found above the vacuum level for the neutral molecule. Note that a 1s→π∗ transition or π∗ resonance can only be observed for molecules with π bonding, i.e. double and triple bonds or aromatic systems, but not for single bonds.

Another advantage of NEXAFS is its capability of determining the molecule orientation, relative to the substrate. Bonds and the corresponding molecular orbitals are highly directional, Therefore the transition intensity (core level to unoccupied orbital) depends on the orientation of the electric field vector, which is related to the molecule's orientation. By utilizing the polarization characteristics of synchrotron radiation (assuming linear polarization for simplicity), the orientation of a molecular orbital can be determined by analyzing the intensity of the resonance at different angles of photon incidence (θ).

2.6. Ellipsometry

Ellipsometry is a powerful optical technique used to analyze the properties of thin films and surfaces. The key physics of ellipsometry is that it measures a change in polarized light as light reflects or transmits from a material structure.[93] The polarization change is represented as an amplitude ratio (Ψ) and the phase difference (Δ) between light waves known as p- and s-polarized light waves. (Figure 2.8) The measured response depends on optical properties and

thickness of individual materials. Thus, ellipsometry is primarily used to determine film thickness and optical constants. Moreover, it is also used to characterize crystallinity, roughness, doping concentration, and other material properties associated with a change in optical response.[94]

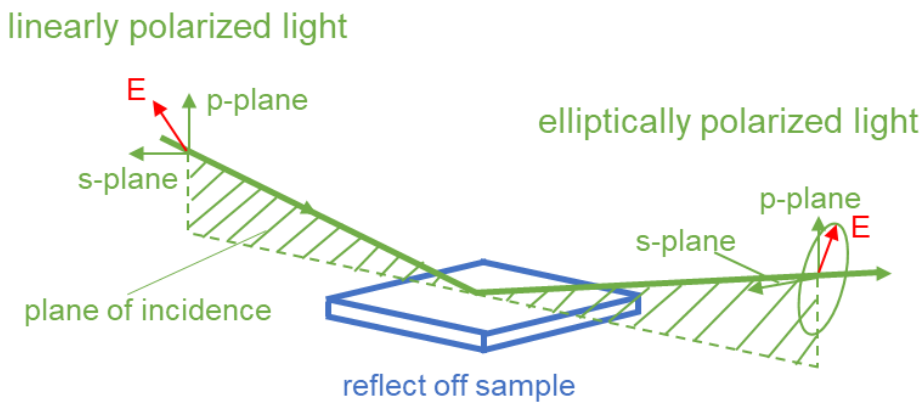

Figure 2.8. Schematic illustration of an ellipsometry experiment.

In any ellipsometry experiments, the object is to measure the complex ratio of Fresnel reflection coefficients,[93] which is given by

$$\rho = R_p / R_s = \tan\Psi \, e^{i\Delta} \qquad (2.5)$$

where R_p and R_s is the complex Fresnel reflection coefficient for light polarized parallel, and perpendicular to the plane of incidence, respectively.

Ellipsometry data collection relies on several key components: a light source, polarization generator, sample, polarization analyzer, and detector. The light source emits unpolarized light which is then sent through a polarizer. The polarizer allows light of a preferred electric field orientation to pass. The polarizer axis is oriented between the p- and s- planes, ensuring both arrive at the sample surface. Upon reflection (or transmission) from the sample surface, the linearly polarized light becomes elliptically polarized and passes through a continuously rotating polarizer known as the analyzer. The amount of light allowed to pass will depend on the polarizer orientation relative to the electric field "ellipse" coming from the sample. The detector converts light to electronic signal to determine the reflected polarization. This information is compared to the known input polarization to determine the polarization change caused by the sample reflection.

2.7. Bulge test

The bulge test is a well-established method to determine the mechanical properties of thin films or coatings. It is particularly useful for characterizing the elastic properties of thin films.[95,96] In the bulge test, a free-standing thin film is suspended over a window, usually a solid substrate with circular or square opening, and uniform pressure is applied to one side of the window, causing the film to deflect outwards (Figure 2.9). It is possible to obtain the stress (σ) and strain (ε) behavior and mechanical properties of the thin film from the measurements of the pressure difference on both sides of the film (Δp) and the film's deflection (h). Take a circular window for example, the relation between the pressure difference and the deflection of the suspended film is given by[97]

$$\Delta p = 4\,\frac{t}{a^2}\,\sigma_0 \cdot h + \frac{8}{3}\,\frac{t}{a^4} \cdot \frac{1}{1-\nu}\,E\,h^3 \qquad (2.6)$$

where t and a is the thickness of the film and the radius of the circular opening, respectively. The other parameters are related to the intrinsic properties of the membrane, viz. the residual stress (σ_0), the Poisson's ratio (ν), and the Young's modulus (E). Consequently, according to eq 2.6, a $\Delta p/h$ versus h^2 plot should represent a straight line with the slope defined by the parameters a, ν and E. Using the known value of a and making a reasonable assumption for ν (e.g. 0.25 for bulky gel-like material),[28] Young's moduli could be calculated.

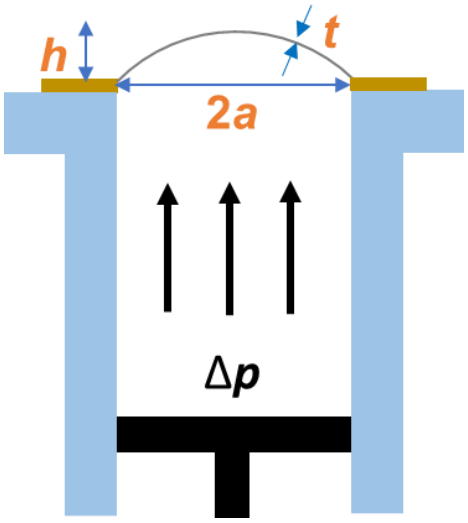

Figure 2.9. Schematic illustration of a bulge test setup along with the relevant parameters (see text for description).

In addition to the above evaluation, there is another method to calculate the Young's modulus of thin films ($t << a$). The deflected film can be considered as part of a virtual sphere (R, radius), and the σ of the film is expressed as: $\sigma = p\ R\ /\ 2\ t$. According to the geometry of the bulge test setup, when the deflection is small ($h << a$), the σ can be expressed as $\sigma = p\ a^2\ /\ 4\ t\ h$ and the ε can be expressed as $\varepsilon = 2\ h^2\ /\ 3\ a^2$, which gives the following equation for the calculation of the Young's modulus:

$$E = \sigma\ /\ \varepsilon = 3\ p\ a^4\ /8\ t\ h^3 \qquad (2.7)$$

2.8. Scanning electron microscopy

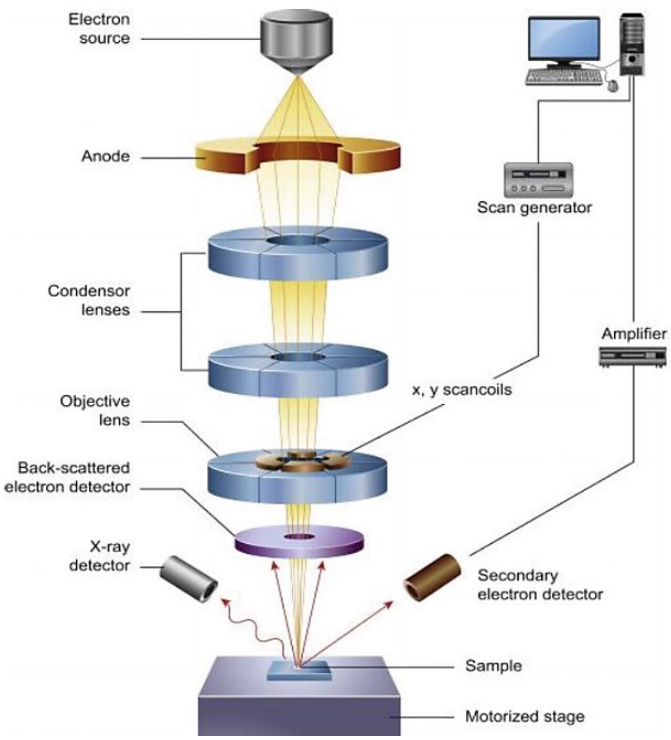

Figure 2.10. Schematic illustration of SEM, adapted from ref [98].

Scanning electron microscopy (SEM) is a powerful technique to observe the surface morphology and structure of samples at high resolutions. Unlike optical microscopes, which relies on visible lights, SEM utilizes a beam of high-energy electrons to generate images. The scheme of SEM is shown in Figure 2.10. In an SEM, electrons are emitted from an electron gun, which is typically a heated tungsten filament or a field emission gun. The emitted electrons are accelerated towards the sample by an electric field. As the high-energy electrons strike the

sample's surface, various signals are generated, including backscattered electrons, secondary electrons, Auger electrons and characteristic X-rays.[99] Among them, backscattered electrons, and secondary electrons are detected to create SEM images, with the former one providing topographic information, and the latter one showing compositional contrast. Furthermore, the detection of characteristic X-rays enables elemental analysis and mapping of the sample.

2.9. Atomic force microscopy

Atomic Force Microscopy (AFM) is a high-resolution imaging technique used in the field of nanotechnology to study the surface properties of a wide range of materials at the atomic scale. It provides detailed information about the topography, roughness, and mechanical properties of a sample. The basic principle behind AFM relies on the interaction forces between the tip of the probe (cantilever) and the sample surface,[100] which is explained in detail as follows:

In AFM measurements, the cantilever is brought from afar away from the sample surface into close proximity or contact with the sample surface. Then a scanning process is conducted, in which the tip moves across the surface in a systematic manner. As the tip interacts with the atoms on the surface, forces between the atoms on the tip and the atoms on the sample surface will cause the cantilever to bend. This deflection is measured using a laser beam reflected off the back of the cantilever onto a position-sensitive detector. The detector generates a signal that can maintain a constant force between the probe and the sample by adjusting the position of the probe. The deflection data is collected during the scanning process and a topographic image of the sample is obtained based on the vertical movements (z-axis) of the cantilever. The AFM images can be displayed in 2D or 3D fashions, revealing the surface features, such as bumps, pits, or variations in height.

2.10. Ultraviolet and visible spectroscopy

Ultraviolet and visible (UV-vis) spectroscopy is a technique used to analyze the absorption, transmission, and reflection of UV and visible light by substances. The basic principle of UV-vis spectroscopy is that substances absorb light in the UV and visible regions of the spectrum (ca.190–900 nm).[101] When a sample (e.g. an organic molecule) is exposed to light in this range, it will absorb energy, causing electronic transitions within the molecular orbitals, typically $\pi \rightarrow \pi^*$ and $n \rightarrow \pi^*$ transition. The transition energies correspond to specific wavelengths of light. By measuring the intensity of the light absorbed by the sample at different wavelengths, valuable information about the sample's electronic structure and properties can be obtained. Unlike molecular systems where electronic transitions between energy levels are responsible

for absorbance, the local phenomenon of surface plasmon resonance (LSPR) predominantly governs the UV-vis absorbance of noble metal nanoparticles, which is induced by collective oscillation of conduction electrons at the surface of metal nanoparticles when they are excited by UV-visible light. The position and intensity of the peaks in this case depend on the factors like nanoparticle size, shape, composition, and surrounding environment.[102,103]

2.11. Electrochemical characterization

Electrochemical characterization is performed to investigate the electrochemical properties of the materials under various electrochemical conditions. As illustrated in Figure 2.11,[104] electrochemical measurements are typically conduced within a conventional three-electrode cell, which is controlled by a potentiostat that applies a precise and adjustable voltage to the system, enabling a desired potential and accurately control of electrochemical conditions during an experiment. The working electrode is the electrode where the electrochemical reactions of interest take place, and it is usually composed specific materials that need to be studied. The reference electrode, providing a stable and known potential, is used as a reference point for measuring the potential of the working electrode. The counter electrode, also known as the auxiliary electrode, completes the electrical circuit in the electrochemical cell. It balances the current flow between the working electrode and the reference electrode. The counter electrode is usually an inert electrode made of materials like platinum or graphite, which do not participate in the electrochemical reactions under investigation.

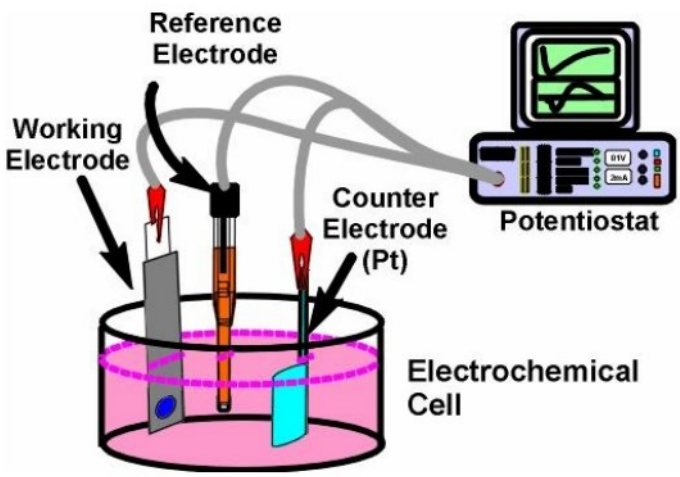

Figure 2.11. Illustration of an electrochemistry system with potentiostat and conventional three-electrode cell.[104]

There are lots of electrochemical characterization techniques, such as cyclic voltammetry (CV), chronoamperometry (CA), square-wave voltammetry (SWV), differential pulse voltammetry (DPV), chronopotentiometry (CP), galvanostatic charge discharge (GCD), and electrochemical impedance spectroscopy (EIS). I will introduce three of them that are related to this dissertation, viz. CV, SWV, and EIS.

CV. CV is a basic electrochemical technique for materials. In CV measurements, the current is recorded as a function of potential by sweeping the potential back and forth between the selected potential range. The information obtained from CV provides valuable insights into the electrochemical behavior of the material. Figure 2.12 illustrates a typical CV measurement, including input and output response where reduction and oxidation peaks are shown. The CV measurement involves providing a ramp signal as an input. During the forward scan, a positive ramp signal with a positive slope is applied, and after completing the first half-cycle, the voltage is reversed, leading to a negative ramp signal that reverses the cyclic voltammogram's nature for the subsequent half cycle. As the system undergoes redox reactions and aims to reach an equilibrium state, it cyclically repeats the pattern, providing information about the changes it has undergone. By thoroughly analyzing the CV curve, one can draw significant conclusions regarding the material properties (e.g., capacitive nature) and system behavior (reversible, irreversible, or quasi-reversible).

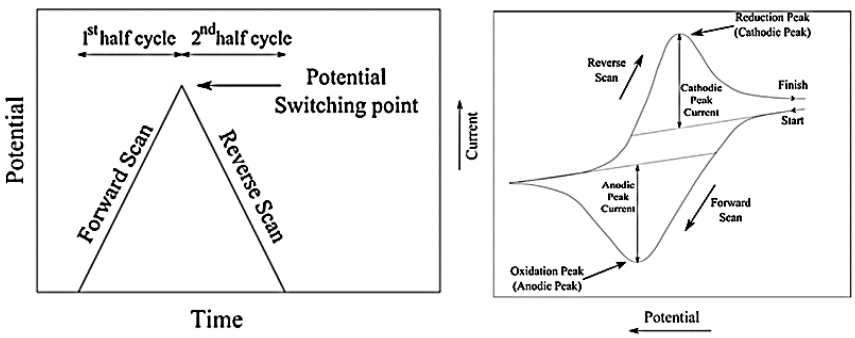

Figure 2.12. CV technique along with its input and output response.[105]

SWV. SWV is an electrochemical technique that involves the application of a linearly increasing input signal in the form of a square wave square wave for voltammetric analysis. As shown in the Figure 2.13a, the potential is swept linearly in SWV, but at each potential step, a constant amplitude square wave voltage pulse is applied. The square wave pulse consists of a rapid potential increase followed by an equal and opposite potential decrease. Because of the

large amplitude of the square wave, the reverse pulse will cause a reverse reaction of the reduction/oxidation product obtained by the previous pulse. The current passing through the working electrode is measured both at the end of forward (point "A") and reverse (point "B") half-cycles, and the difference between the two current provides the output current waveform as a function of the applied potential (Figure 2.13b). SWV is a highly sensitive technique that can easily detect the adsorption of specific reactants, as evidenced by a significant enhancement in their peak current.[106]

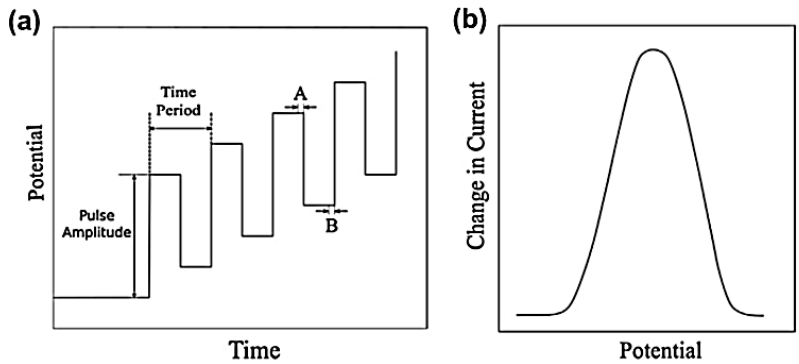

Figure 2.13. (a) General input nature of the linear sweep square-wave voltammogram. (b) Output of a linear sweep square-wave voltammogram.[105]

EIS. EIS is a powerful technique that can be utilized to determine the impedance of the electrochemical cell. In EIS experiments, a sinusoidal voltage (AC signal) with small amplitude is applied to the working electrode, and the amplitude and phase angle of the generated current are measured with respect to the applied sinusoidal voltage. The impedance is then determined using Ohm's law. Because the impedance is a function of frequency, different ranges of frequencies have to be examined to obtain an impedance spectrum.

The impedance is a complex quantity consisting of a real part (resistance) and an imaginary part (reactance). The real part represents the resistance to the flow of current, while the imaginary part represents the capacitive or inductive behavior of the system. By plotting the impedance under different frequencies, a Nyquist plot can be obtained, which displays the imaginary part of impedance against the real part.[107] By fitting the Nyquist plot, one can get an equivalent circuit of the cell. A typical Nyquist plot and its corresponding equivalent circuit are shown in Figure 2.14. They provide valuable information about various electrochemical processes, including solution (electrolyte) resistance (R_s), charge transfer resistance (R_{ct}), double-layer capacitance (C_{dl}), Warburg impedance (Z_w, related to diffusion processes).

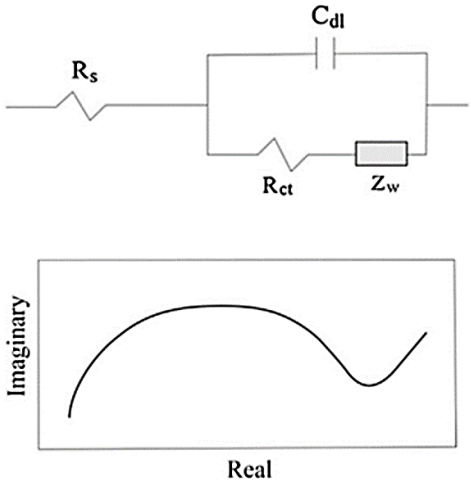

Figure 2.14. A basic equivalent circuit model along with its corresponding Nyquist plot.[105]

2.12. E-beam lithography

Electron beam lithography (EBL) is one of the key nanofabrication techniques used to create patterns on a substrate at the nanoscale. The development of EBL tools started in the late 1960s, by modifying the design of SEM.[108] The working principle of EBL is based on the scanning of a focused electron beam across a substrate coated with an electron-sensitive material, known as resist. The resist undergoes changes in its solubility properties upon exposure to the electron beam. Before the EBL process, a pattern is designed using computer-aided design software, which defines the desired structure to be created. After exposure, the resist undergoes a development process. In the case of positive resist, the exposed regions become soluble and are removed during development, leaving behind the unexposed regions as the desired pattern. As for negative resist, the exposed regions become crosslinked and remain after development. Since the discovery of polymethylmethacrylate (PMMA) as a positive electron resist by Hatzakis in 1969,[109] EBL has found extensive applications in various fields. It has been utilized for fabricating integrated circuits, photonic crystals, semiconductor devices, nanoelectronics, as well as in biological and life sciences research.[110–112]

3. Experimental

3.1. Materials and substrates

3.1.1. Chemicals

The 4-arm STAR-NH_2 and STAR-EPX compounds (Figure 3.1) were purchased from Creative PEG Works (USA) and used as received. Four MWs of these compounds were used, viz. 2000 (2k), 5000 (10k), 10000 (10k), and 20000 (20k) g/mol. The STAR-PEG precursors are characterized by low polydispersity and high purity, viz. 99% for STAR-NH_2 and 98% for STAR-EPX in terms of amine and epoxy substitution, respectively. The MWs of 2000, 5000, 10000, and 20000 g/mol correspond coarsely to the lengths of the PEG arms of 3.5–3.9 nm, 8.7–9.8 nm 17.5–19.5 nm, and 35–39 nm, respectively, comprising 9–11, 25–27, 53–55, and 100–112 monomers.

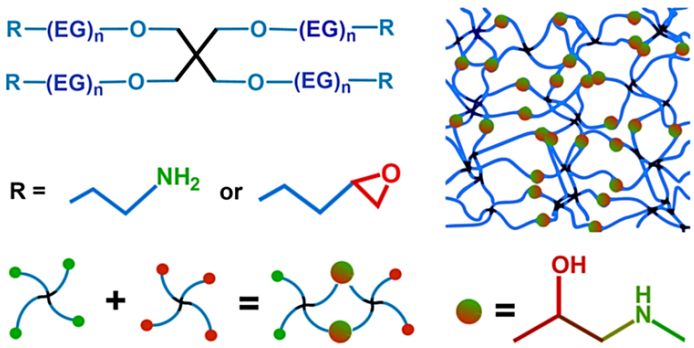

Figure 3.1. The chemical structures of STAR-NH_2 and STAR-EPX (EG = −O−CH_2−CH2−) and a schematic drawing of the reaction between the terminal epoxy and amine groups of the precursors resulting in the appearance of ethanol-amine-like crosslinking bonds. This reaction mediates the formation of porous PEG film, which can then be separated from the substrate as a free-standing nanosheet.

Desalted ssDNA sequences were purchased from Metabion International AG (Germany). The first group of these sequences included unmodified thymine (T) and adenine (A) homo-oligonucleotides, viz. 5'−TTTTT−3' (T5), 5'−TTTTTTTTTT−3' (T10), 5'−AAAAA−3' (A5), and 5'−AAAAAAAAAA−3' (A10). The second group included substituted homo-oligonucleotides, viz. N-hydroxy succinimide ester–$(CH_2)_{10}$−5'−TTTTT−3' (NHS-T5), N-

hydroxy succinimide ester–$(CH_2)_{10}$–5'–TTTTTTTTTT–3' (NHS-T10), and thiol–C6–5'–TTTTTTTTTT–3' (T10-SH).

Fullerene (purity > 99.5%) was acquired from Ossila (UK). The SAM precursors employed were Trip-T1, PT1, C16, and nitrile-substituted naphthalenethiolates. Their structure can be seen in Figure 4.66 in Chapter 4. Trip-T1 was synthesized by our partners in Japan. PT1 and C16 were purchased from Merck and used without further modification. Nitrile-substituted naphthalenethiolates was provided by our partners in Germany. All remaining chemicals and solvents in this thesis were obtained from Sigma-Aldrich and utilized as received.

3.1.2. Substrates

Glass substrates (Menzel-Gläser, Germany), SiO_2 passivated Si(100) substrates (Siegert Wafer GmbH, Germany), and evaporated Au(111) substrates (Georg-Albert PVD-Beschichtungen, Germany) were used for the preparation of the particular samples to meet specific requirements of different characterization techniques. Three types of Au substrates were used, including: (1) 30 nm of evaporated Au on polished Si(100) wafers precoated with a 5 nm Ti adhesion layer, (2) 100 nm of evaporated Au on Si(100) wafers precoated with a 5 nm Ti adhesion layer, and (3) 100 nm of evaporated Au on polished Si(100) wafers without a Ti interlayer.

As secondary substrates for bulge test, custom-fabricated metal frames with a circular window were used. The diameter of the window was 1 mm for most of the experiments but varied for some specific experiments (0.3 and 0.5 mm).

3.2. General preparation procedures

3.2.1. PEG films preparation

The standard PEG films were fabricated on 30 nm evaporated Au(111) substrates (5 nm Ti interlayer) following the established procedure,[27] as schematically illustrated by Figure 3.1. These films were primarily utilized for protein adsorption test, XPS study, UV modification, and ellipsometry measurements. In short, the PEG compounds (with the same MWs) were separately dissolved in chloroform with a concentration varied from 5 to 30 mg/ml, mixed together in the 1:1 ratio (wt./wt.), spin-coated onto the substrate, crosslinked by thermal annealing (6 h, 80 °C), followed by extensive rinsing with ethanol to remove weakly bound material. The variation of the concentration allowed us to control the thickness of the PEG films,[27] Note that the bonding of the PEG films to the supporting gold layer is quite robust

since the films cannot be separated from the support by ultrasonication[27] but only by dissolving of the gold film.[28] The bonding is presumably mediated by amino and epoxy groups.

In addition, other PEG films were prepared on various substrates. They included PEG film with different ratio of STAR-NH_2 and STAR-EPX, PEG films produced using toluene (TL) as the solvent and PEG/C60 composite films. Specific experiments about these PEG films are introduced in chapter 4.

3.2.2. Nanosheets fabrication

The PEG and PEG/C60 free-standing nanosheets were prepared from the originally films fabricated on SiO_2 passivated Si wafers. These films were first exposed to HF to diminish their bonding to the substrate by removal of the SiO_2 overlayer, and then separated from the substrate by an oblique immersion into water. The floating nanosheets were fished up from the surface of the solution or water and transferred onto the secondary substrate to monitor their thickness (SiO_2/Si substrate) and quality as well as to study their stability and elastic properties (bulge test substrate).

3.2.3. SAMs preparation

The SAMs were prepared by immersion of the fresh substrates into 1 mM of Trip-T1 in degassed tetrahydrofuran or into 1 mM of PT1 in absolute ethanol for 24 h at room temperature and under dark conditions. After immersion, the SAMs were rinsed with tetrahydrofuran or ethanol and dried in a stream of argon. In addition, reference SAMs of C16 and nitrile-substituted naphthalenethiolates were prepared on the same substrate using the analogous immersion procedure. The SAMs for spectroscopy studies were prepared on Au substrate 1. SAMs for EBL studies were prepared on Au substrate 2, to have a better lithographic contrast. For the CNM fabrication, Au substrate 3 was used to minimize adhesion to Si(100).

3.3. Characterization

XPS. The measurements were conducted with a MAX 200 (Leybold-Heraeus) spectrometer equipped with an Mg Kα X-ray source (260 W; ca. 1.5 cm distance to the samples) and a hemispherical analyzer (EA 200; Leybold-Heraeus). The spectra were collected in normal emission geometry with an energy resolution of ~0.9 eV. The BE scale of the spectra was referenced to the Au $4f_{7/2}$ emission at 84.0 eV.[113]

Ellipsometry. The measurements were performed with a spectroscopic ellipsometer (M-44, J.A. Woollam) at a fixed angle of 75°. The goals of these experiments were to monitor the

thickness of PEG and PEG/C60 films and to investigate the swelling ability of the PEG films. The thicknesses of the films on Au substrates were calculated by adapting the experimental data to a bilayer model consisting of the gold substrate and the PEG film. Another bilayer model on the basis of the SiO_2 layer and the PEG film was used to calculate the thickness of the films on SiO_2/Si substrates. The optical constants for the substrate were determined using a clean gold surface and SiO_2/Si substrate, respectively, whereas those of the polymer films were obtained by using a Cauchy layer dispersion relation including the first two terms and adapting both coefficients to the ellipsometric measurements.

In some experiments, the temperature of the films was varied from room temperature to nearly 0 °C by placing the samples on a Peltier plate (TES1-127030; Conrad Electronics SE), allowing to control relative humidity experienced by the sample. The temperature decrease increased the relative humidity and, consequently, the water uptake by the hydrogel film, allowing to monitor its swelling properties. The parameters of the experiments were kept unchanging for all films studied, allowing direct comparison of the results. Note that the swelling of the PEG films at the temperature variation is similar to that performed at the controlled relative humidity conditions.[29]

Protein adhesion experiments. The biorepulsive properties of the PEG films were monitored by protein adsorption experiments following the approach of ref [27]. The films were initially immersed into a phosphate-buffered saline (PBS) solution for 30 min. Subsequently, a filtered, PBS solution of the test protein, viz. bovine serum albumin (BSA), was added getting a total protein concentration of 0.25 mg/ml. After 60 min incubation time under ambient conditions, the PEG films were rinsing extensively with copious amounts of Milli-Q water. The amount of the adsorbed proteins was quantified by XPS, using the characteristic N 1s emission of the proteins and a protein-adhesive sample (evaporated Au film) as a reference. This approach is sufficiently sensitive and well suitable to the given purpose.[27,135]

Electrochemistry. Electrochemical measurements, which included CV, SWV, and EIS, were performed using a Zahner potentiostat (model IM6E). All measurements were performed in a customized three-electrode electrochemical cell in which a KCl saturated Ag/AgCl electrode and a platinum electrode (Osilla, UK) were used as the reference and counter electrodes, respectively. The working electrodes various according to different purpose. The exposed area of the working electrodes was ~0.5 cm^2.

For electrochemical sensing of the PEG/ssDNA films, blank Au substrates (30 nm Au with 5 nm Ti), PEG films prepared on Au substrates, and PEG/ssDNA films on Au substrates were used as working electrodes. The cyclic voltammograms (CVs) and EIS data were recorded in a 10 mM $[Fe(CN)_6]^{3-/4-}$electrolyte containing 0.1 M KCl. A scan rate of 300 mV/s or 200 mV/s in the range from −0.8 V to +0.7 V or −0.7 V to +0.7 V (vs. Ag/AgCl) was applied in CV measurements. The sensing capabilities of the specific electrodes toward target ssDNA were examined using EIS measurements, which were carried out by applying an alternating voltage with an amplitude of 5 mV over a frequency range from 10^{-1} to 10^{5} Hz.

For the PEG/C60 related experiments, clean and C60-covered glassy carbon electrodes (GCE), C60 deposited on Au substrate (30 nm Au with 5 nm Ti), the PEG-C60 composites films prepared on Au substrates, and the reflux PEG-C60 nanosheet transferred onto Au substrate were used as the working electrodes. A deoxygenated acetonitrile (MeCN) containing 0.1 M tetrabutylammonium tetrafluoroborate ($TBABF_4$) was used as the electrolyte in the CV and SWV measurements. For the CV measurements, a scan rate of 100 mV/s in the range from 0 V to –2 V (vs. Ag/AgCl) was applied. The SWV measurement were conducted from 0 V to –1 V (vs. Ag/AgCl) with an amplitude of 100 mV and a frequency of 25 Hz. The conditions of EIS measurements were same as the case for PEG/ssDNA film.

Other techniques The SEM measurements were performed with a LEO 1530 scanning electron microscope (Zeiss). The energy of the primary electron beam was set to 3 keV. The UV-vis measurements were carried out with the with a Jasco V-650 spectrophotometer (JASCO Deutschland GmbH). AFM measurements were conducted with a Solver Next device (NT-MDT), in tapping mode under ambient conditions.

4. Results and Discussion

4.1. The effect of UV light on the properties of PEG films

4.1.1. Motivation

Based on the previous work of our group with regard to the PEG films fabricated from the STAR-PEG precursors, it is of interest to study the effect of UV light on these PEG films, which was the subject of this specific subproject.

The UV treatment and respective lithographic approaches have certain advantages as compared to electron irradiation and EBL, since they require neither an expensive equipment nor any vacuum environment but can be in principle realized with a simple UV lamp, under ambient or even liquid cell conditions.[114–118] Apart from the most simple proximity printing geometry,[114,119–121] more sophisticated setups, providing additional options in terms of parallel patterning and lateral resolution, are available as well, relying, e.g., on interferometric lithographic process,[122] scanning near-field photolithography,[123–125] or commercial digital micro-mirror devices.[126–128] Finally, in contrast to EBL, UV lithography does not require conductive substrates.

In contrast to the OEG-terminated SAMs, combining the OEG moieties with alkyl or oligophenyl chain and specific docking group, the PEG films represent a nearly all-PEG material, for which the reaction to UV irradiation is of fundamental importance. Note that I intentionally avoided introduction of functional, photoresponsive groups into the PEG matrix, as performed in a variety of dedicated studies on biocompatible and biodegradable hydrogels (see e.g. refs [129–132]), including STAR-PEG based systems as well,[133] but rather intended to study the effect of UV irradiation on the matrix itself.

4.1.2. Specific experiments and procedures

UV light treatment. The PEG films (EPX:NH_2 = 1:1, wt./wt.)with different thicknesses, prepared on Au substrates, were exposed to UV light with a wavelength of 254 nm provided by a short wave (UV-C) Hg vapor lamp (Benda Konrad Laborgeräte). UV light with this wavelength is known to be very efficient for modification of ultrathin organic films, including the OEG-substituted SAMs in particular.[71,114,119,120] The UV treatment was performed at ambient conditions and room temperature, with a temperature increase by just few degrees during the irradiation. The distance between the UV source and samples was ~2.5 cm. The intensity of the UV light was monitored by UVX radiometer sensors (Ultra-Violet Products

Ltd.). It was kept at 2 mW/cm^2 for most of the experiments, but varied to some extent as well, to monitor the effect of UV flux. After the irradiation, the samples were washed with the solvent to remove weakly-bound species. The effect of washing was monitored in dedicated experiments.

UV lithography. Along with the homogeneous irradiation of the PEG films, their patterning in proximity printing geometry was performed. The same UV light source (2 mW/cm^2) was used. As a mask, a 1500 Cu mesh (Plano GmbH) with a ~7.5 μm opening was used. The fabricated patterns were imaged by AFM in the tapping mode.

4.1.3. Film thickness

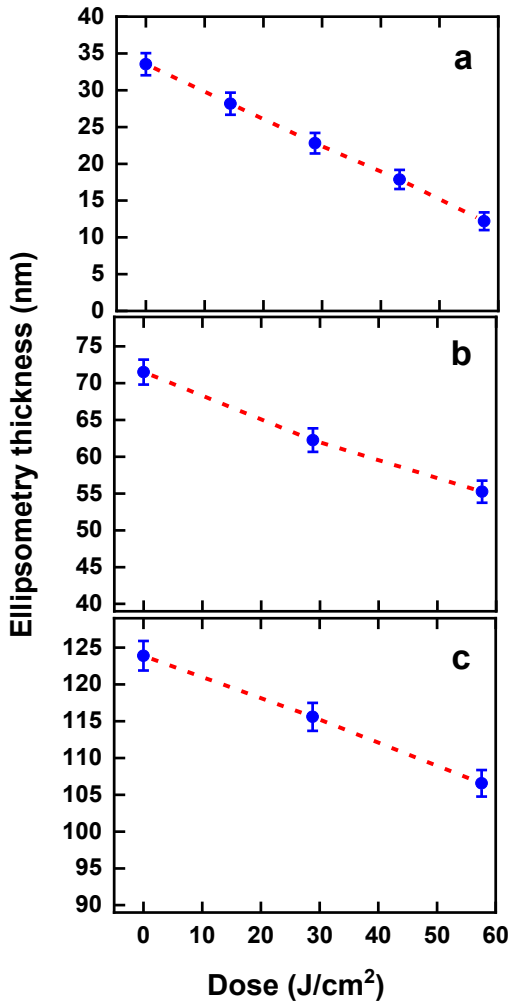

Figure 4.1. Thickness of the PEG films determined by ellipsometry as a function of the UV dose. The thickness of the pristine films was ~34 nm (a), ~71 nm (b), and ~124 nm (c). The behavior of the thickness is traced by the red dashed lines. The same scaling of the Y-axis is used in all panels.

The thickness of the PEG films during the UV irradiation was monitored by ellipsometry. The results for three representative PEG films with the different thicknesses are presented in Figure 4.1. All three films exhibit similar behavior: the thickness decreases in nearly linear fashion in the course of UV irradiation. This suggests a progressive removal of the PEG material, similar to electron irradiation[31,134] and UV treatment of the OEG-terminated SAMs.[114,119] However, in contrast to both these cases, in which the thickness decrease follows an exponential function (first-order kinetics), a nearly linear behavior is observed in the present case, corresponding to the zero-order kinetics in relation to the UV dose. Interestingly, the thickness decrease in Figure 4.1 is nearly independent of the thickness of the pristine PEG film, occurring with nearly similar rates for the ~34 nm, ~71 nm, and ~124 nm films. This rate represents a material property. An average rate constant, k_0, was calculated at 0.32±0.05 nm/(J/cm^2).

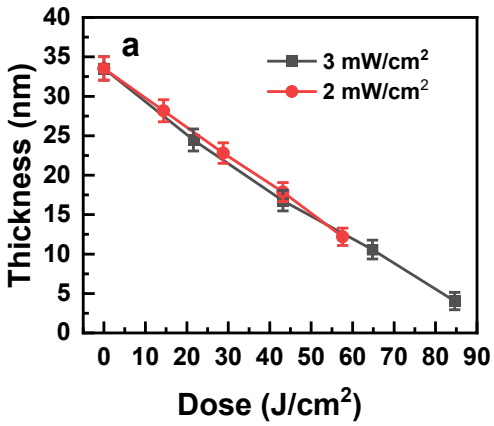

Figure 4.2. Thickness of the PEG films determined by ellipsometry as a function of the UV dose. The data for the generally used (2 mW/cm^2) and somewhat higher (3 mW/cm^2) flux are compared. The legend is given in the figure.

The rate does not change significantly with a higher UV flux as shown in Figure 4.2 for a representative data set. In addition, the decrease of the film thickness, observed by ellipsometry, could also be verified by XPS, using a comparably thin PEG film, for which the signal from the substrate (Au) could still be recorded. The respective data are presented in Figures 4.3 and 4.4. Figure 4.3 shows the Au 4f spectra of the substrate, with the intensity of the signal increasing progressively in the course of UV exposure. On the basis of this intensity, thicknesses of the PEG films could be calculated using the standard expression for the attenuation of photoemission signal[84] and the attenuation length determined experimentally for this type of material.[27] The XPS-derived values in Figure 4.4 agree satisfactory with the ellipsometry-derived ones, even though the correlation is not absolutely exact.

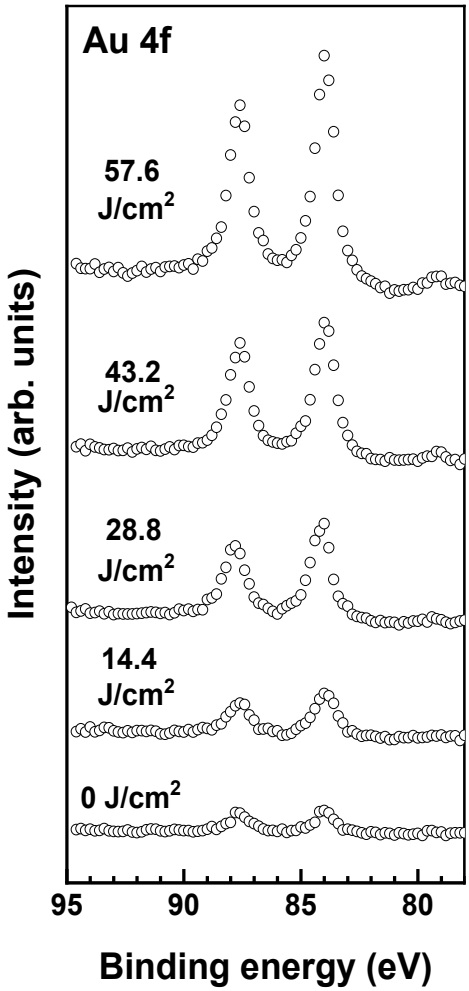

Figure 4.3. Au 4f XPS spectra of the pristine (~32 nm) and irradiated PEG films on Au substrate. The doses are marked at the respective curves.

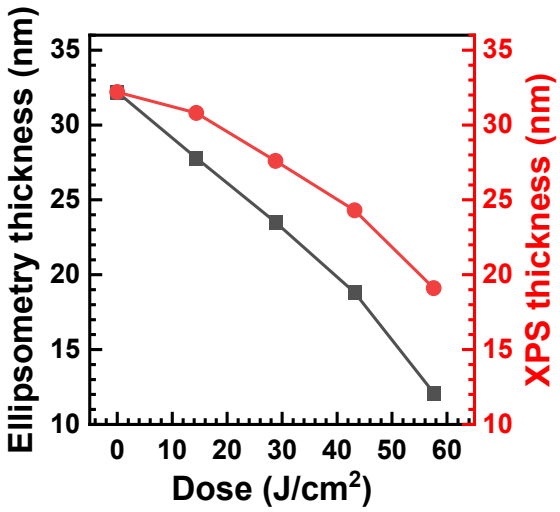

Figure 4.4. Thickness of a PEG film measured by ellipsometry (black squares and black line) and XPS (red circles and red line) as a function of the UV dose. The thickness values were

derived from the spectra in Figure 4.3. The XPS thickness of the pristine film was set according to the ellipsometry value (~32 nm).

4.1.4. XPS

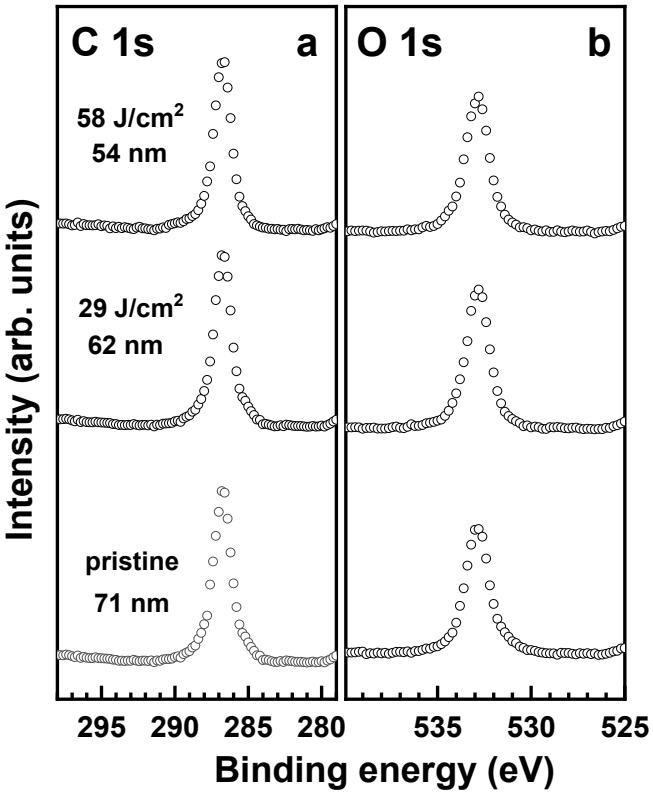

Figure 4.5. C 1s (a) and O 1s (b) XPS spectra of the pristine (~71 nm) and irradiated PEG films. The doses are marked at the respective curves.

The irradiation-induced removal of organic material, including PEG/OEG in particular, is usually accompanied by chemical modification of the residual film. This was monitored by XPS. Representative XPS spectra of the moderately thick (~71 nm) PEG film, in the pristine state and exposed to UV light, are shown in Figure 4.5. The C 1s and O 1s spectra of the pristine film in Figures 4.5a and 4.5b, respectively, exhibit the characteristic peaks of PEG/OEG at 286.7 eV (C 1s) and 532.8 eV (O 1s),[72,136] which are the only perceptible features. The chemical identity of the PEG films and the lack of any contamination are thus verified. Surprisingly and absolutely unexpected, the spectra of the irradiated films do not exhibit any difference from those of the pristine film: there are the same peaks at the same binding energies, with no other features being perceptible. Also, the relations of the peak intensities, reflecting the chemical composition of the films, do not change noticeably. This can only mean that the residual film is not subjected to any chemical modification at the exposure to UV light,

which is distinctly different from the case of electron irradiation of the PEG films[31,134] and the case of UV treatment of the OEG-terminated SAMs.[114,119] In the first case the residual film represents carbon-enriched and oxygen-depleted aliphatic compound and, in the second case, it represents a residual of the SAM-forming molecules. Note that the UV-induced desorption of a part of the PEG film cannot be reflected in the spectra in Figure 4.5 since the probing depth of XPS at the given kinetic energies of the photoelectrons, viz. ~7.5 nm for C 1s and ~6 nm for O 1s,[84] is noticeably smaller than the thickness of the films (71–54 nm).

4.1.5. Swelling properties

The finding that the chemical composition of the PEG films does not change noticeably in the course of the UV treatment could be additionally verified by testing the basic properties of these films depending on their composition, such as their hydrogel character. For this purpose, swelling of the PEG films at the variation of the relative humidity was monitored. This variation was achieved by the decrease of the film temperature following the approach of refs [27,31]. Representative data for the ~34 nm, ~71 nm, and 124 nm films are presented in Figures 4.6a, 4.6b, and 4.6c, respectively. As seen in these figures, the swelling ability of the PEG films, intrinsically linked to their chemical composition is still preserved after the UV treatment.

To quantify the swelling ability, we calculated the ratio (R) of the thickness at the lowest temperature (2 °C), corresponding to the maximal swelling in our experiments, to the thickness at room temperature, corresponding to the least swelled film. According to reference measurements, the PEG films are already slightly swelled at the ambient conditions in our lab, featuring usually a relative humidity of 40–50%.[29] Nevertheless, the selected swelling ratio, measured at the same conditions for all PEG films studied, represents a suitable fingerprint parameter to compare their hydrogel properties. The dependence of the swelling ratio on the UV doses for the films with the original thicknesses of ~34 nm, ~71 nm, and ~124 nm are presented in Figures 4.7a, 4.7b, and 4.7c, respectively. The observed values for the pristine films correlate well with the previous data (a swelling ratio of ~2 in the 40–100 nm range and somewhat higher values at the lower thicknesses) [27], showing similar values for the ~71 nm and ~124 nm films (1.82–1.84) and slightly higher value for the ~34 nm layer (~2.1), associated with a lower degree of crosslinking in the thinner PEG films[10]. Of the major importance in the context of the present study is, however, the invariable character of the swelling ratio in the course of the UV treatment, which suggests that the hydrogel properties of the PEG films are not affected by this procedure. This behavior is in the striking contrast to the effect of electron irradiation, which results in the loss of these properties in the residual film.[31] The observed

increase of the swelling ratio observed for the UV-treated ~34 nm film (Figure 4.7a) is presumably related to the progressive decrease of the thickness (Figure 4.1a) to the values which correspond to an increase of this ratio.[27]

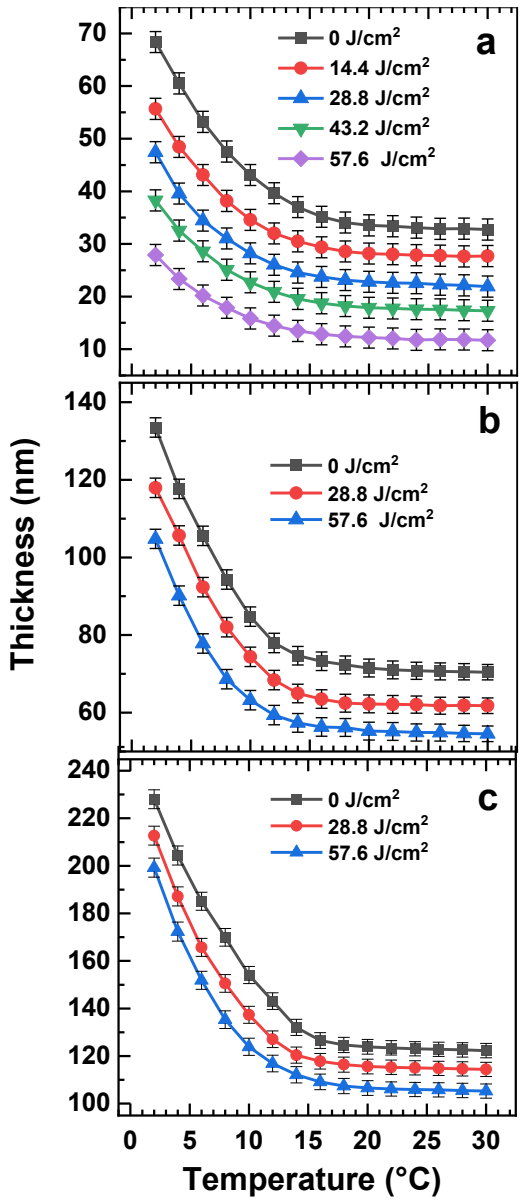

Figure 4.6. Thickness of the pristine and irradiated PEG films as a function of temperature. The thickness was determined by ellipsometry. The thicknesses of the pristine films were ~34 nm (a), ~71 nm (b), and ~124 nm (c). The legends are given in the panels.

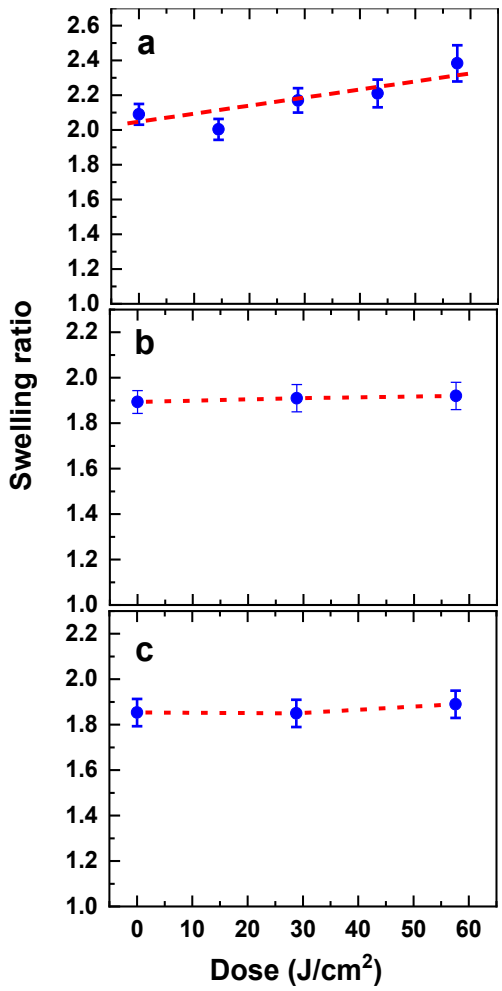

Figure 4.7. Swelling ratio for the PEG films as a function of the UV dose. The thickness of the pristine films was ~34 nm (a), ~71 nm (b), and ~124 nm (c). The behavior of the swelling ratio is traced by the gray dashed lines. The same scaling of the Y-axis is used for all panels. The observed increase of the swelling ratio, most pronounced for the 34 nm film, can be tentatively explained by a stronger decrease in the degree of crosslinking as compared to the thicker films.

4.1.6. Biorepulsive properties

Another important intrinsic ability of the pristine PEG films is their biorepulsive properties.[27,30,32] Possible effect of the UV-treatment on these properties was monitored using BSA as a test protein and the XPS in the N 1s range as a fingerprint tool to evaluate the adsorption of proteins The respective data are presented in Figure 4.8 by the example of the ~71 nm and the ~124 nm film. In Figure 4.8, the N 1s XPS spectra of the pristine and irradiated PEG films exposed to BSA are shown, along with the spectrum of the pristine PEG film before the BSA exposure and the spectrum of a reference protein-adhesive substrate (Au) after the BSA exposure.

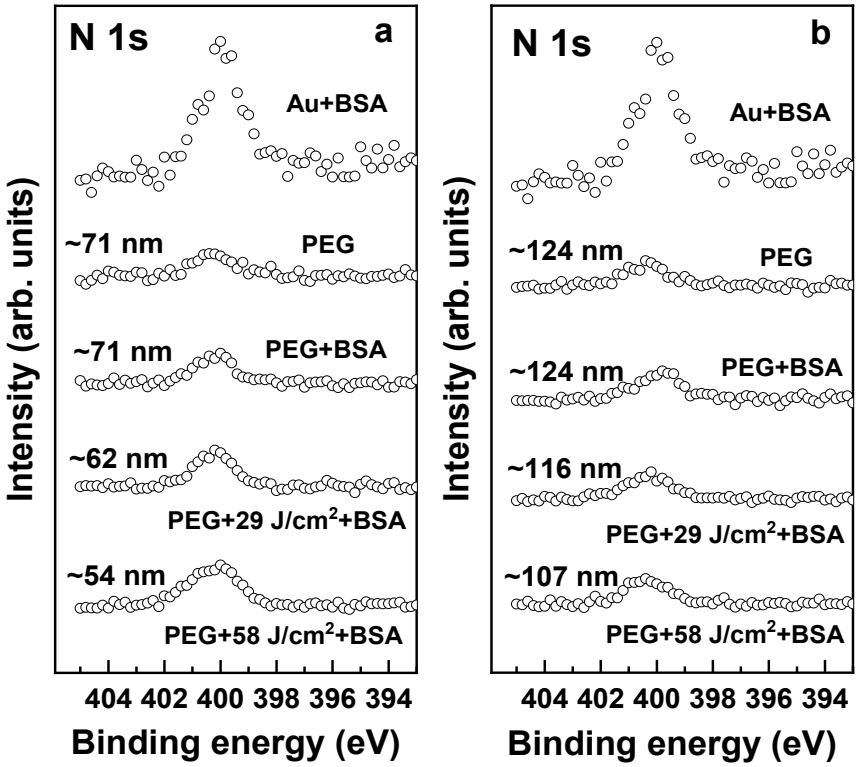

Figure 4.8. N 1s XPS spectra of the pristine (panel a: ~71 nm, panel b: ~124 nm) and irradiated PEG films exposed to BSA along with the spectrum of the pristine PEG film before the BSA exposure and spectrum of a protein-adhesive substrate (Au) after the BSA exposure. The last two spectra are given for comparison. The film thicknesses are marked at the respective curves.

The spectrum of the pristine PEG film exhibits a N 1s peak at ~400 eV associated with the nitrogen atoms in the crosslinking bridges of the PEG network (Figure 3.1) This signal does not change noticeably after the exposure of the film to BSA, verifying its biorepulsive properties. Significantly, nearly the same behavior is observed for the UV-treated films, which, after the exposure to BSA, exhibit only slightly higher intensities of the N 1s signal than before the exposure. Correcting the intensities of the N 1s signal for that of the PEG films before the exposure to BSA and referencing the result to the analogous intensity for the protein-adhesive substrate (Au in the present case; see Figure 4.8), one gets the relative extent of the protein adsorption for a particular PEG film. These values are presented in Figure 4.9 as a function of the film thickness. There are two sets of data, related to the pristine ~71 nm and ~124 nm films. The protein adsorption for the first set of data increases slightly with the UV dose, which, however, can be related to the thickness decrease, enabling, to some extent, the penetration of BSA to the protein-adhesive substrate (Au) through the porous PEG network (see Figure

3.1).[27,30] This effect should be absent for the thicker films and, indeed, the data set for the ~124 nm film corresponds to a nearly complete suppression of the protein adsorption, both for the pristine and UV-treated films. This is a direct evidence that the biorepulsive character of the PEG films does not change at their exposure to UV light.

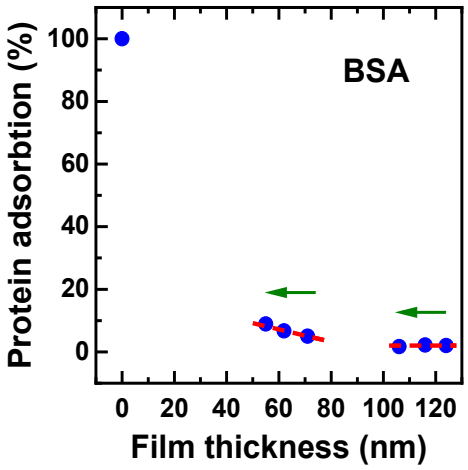

Figure 4.9. Relative extent of the protein adsorption as a function of the film thickness. The reference value for the protein-adhesive substrate (100%) and two series of data, corresponding to the UV treatment of the films with the ~71 nm and ~124 nm thicknesses are shown (see Figure 4.8 for the respective spectra). The directions of the thickness variation at the UV treatment for a particular series are shown by the gray arrows.

4.1.7. General considerations

The above results lead to the conclusion that the only effect of the UV treatment on the PEG films is progressive defragmentation and removal of the PEG material. This removal occurs in a linear fashion with respect to the UV dose (see Figure 4.1) and is mediated by the desorption of the PEG fragments taking place predominantly during the treatment. Such a behavior differs drastically from the case of electron irradiation of the PEG film, as shown schematically in Figure 4.10. As already mentioned above, the removal of the PEG material in that case is accompanied by substantial chemical modification of the residual film, which, as a consequence, loses completely its hydrogel and biorepelling properties.[31,32] In contrast, these properties are nearly fully preserved in the case of UV treatment, relying on the invariable chemical composition of the residual PEG film.

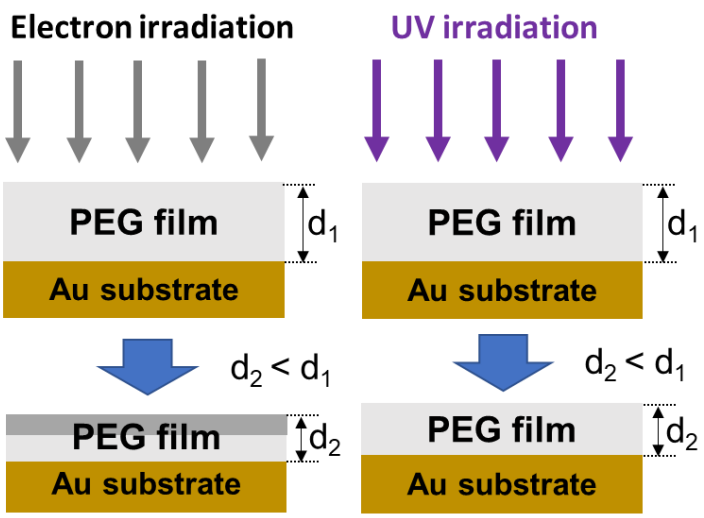

Figure 4.10. Schematic of the modification of the PEG films in the case of electron (at the left) and UV (at the right) irradiation. The chemically modified PEG material is shown by dark gray.

The substantial defragmentation and chemical modification of the PEG films in the case of electron irradiation is related to the extensive breaking of chemical bonds within the films, triggered, e.g., by dissociative attachment of electrons, electron impact ionization, etc.[138–142] The particular involvement of a specific mechanism depends on the excitation energy, which however can be selected in a quite broad range, from several ten electronvolts to several kiloelectronvolts[31] or, presumably, even at several electronvolts.[142] Whereas nearly all bonds can be cleaved, the bonds within the PEG chains, such as C–O ones, are predominantly affected, as shows the experiments on both PEG films[31] and OEG-substituted SAMs.[134,143]

The role of electrons in the considered case of UV light irradiation of the PEG films can however be nearly excluded. At the given wavelength, the kinetic energies of the photoelectrons and secondary electrons (≥ 4.88 eV) originating from the substrate are lower than its work function (5.3 eV)[144] and thus insufficient to reach molecular adsorbates. The so-called "hot" electrons, tunneling into empty states at the substrate-adsorbate interface over the barrier,[116,145–148] should not penetrate far into the PEG films and are probably of importance for the near vicinity of the substrate only (see below). The yield of photoelectrons from the film itself is presumably very low, in view of the limited amount of the material and comparably low photoionization cross-sections for the light elements constituting the PEG films.[149,150]

Thus, one is only left with a direct effect of UV irradiation on these films promoting the fragmentation of the PEG chains in contrast to their chemical modification, such as loss of

oxygen and chemical transformation. This behavior can be related to a higher and different selectivity of this effect with respect to the available chemical bonds, viz. C–C, C–O, and C–N, as compared to electrons and, most likely, involve a specific excitation of a specific bond kind, leading to its breaking. An involvement of ozone, playing frequently a role in photoinduced reactions, is rather unlikely since its formation is only efficient for UV light with wavelengths shorter than 242 nm with the peak at 185 nm.[151]

Whereas it is not clear what particular bonds are predominantly broken, these can be either PEG-core bonds, bonds within the PEG arms, or the crosslinking bonds. On the basis of the XPS spectra (Figure 4.5), one can conclude that these are most likely large fragments (oligomers) which are cleaved and released; otherwise changes in the chemical structure of the residual film would be expected. Significantly, to release such a fragment, not one but two bonds within the same network branch or even more bonds around a particular core should be broken, which explains the comparably low efficiency of the fragmentation process. This requirement is however less strict at the surface of the PEG films, which should contain loose branches and not fully crosslinked STAR-PEG molecules. Consequently, the release of material from this region of the film, directly exposed to the UV light, should be noticeably more extensive as compared to the bulk of the films. The released oligomers are presumably highly volatile, so that they desorb on spot instead of transforming to another species or making new chemical bonds to the PEG matrix.

The near zero-order kinetics of the fragmentation process (see Figure 4.1) is most likely related to the "unlimited" amount of the PEG material, which does not change its character during the UV treatment and is again and again available for the fragmentation process, which is presumably most effective at the film surface and its very vicinity. This situation corresponds to a high excess of reactant with respect to the rate-determining step of a chemical reaction, as described by the general kinetic theory.

Interestingly, the effect of UV irradiation on the PEG films differs drastically from that for the OEG-substituted SAMs. For the latter systems, the effect of UV irradiation does not differ noticeably from that of electrons, resulting in progressive desorption of the OEG fragments and chemical transformation of the residual, which loses the biorepulsive properties (hydrogel properties were not monitored).[114,123,134,137,143] Since the direct impact of UV light on the OEG matrix is entirely different, as shown in the present work, the only rational explanation for the effect of UV light on the OEG-substituted SAMs, which are noticeably thinner than the PEG films (2–3 nm vs. 30–100 nm), is an involvement of electrons from the substrate. Because of

the work function barrier (see above), these can only be "hot" electrons, as suggested by some models.[116,145–148] Even though the penetration depth of these electrons into an organic film is limited, it is most likely sufficient to affect the entire SAM. Thus, the results of the present study provide a strong support in favor of the "hot" electron model for the description of the effect of UV light on OEG-substituted SAMs and, consequently, on all other SAMs in general, since the generation of "hot" electrons is not related to the character of SAM (apart from the availability of suitable empty states for the tunneling) but to the substrate.

As to the OEG-substituted SAMs, it is important that the modification of the OEG part occurs with a much higher rate than all other UV-induced processes, such as the oxidation of the anchoring group and defragmentation of the alkyl linker. This suggests that the effect of "hot" electrons is not limited to the SAM/substrate interface but is still noticeable in its close vicinity, within several nm range, typical of the SAM thickness.[114] A dose of 8−10 J/cm^2 at a wavelength of 254 nm is sufficient to fully decompose and modify the OEG part of a SAM (ca. 10−11 nm).[114] In the case of PEG films, the respective thickness reduction is just 3−4 nm (see Figure 4.1), suggesting much lower efficiency of the defragmentation process, apart from the lack of chemical modification.

Finally, the behavior of the PEG films under UV irradiation can be compared with the effect of ion beam on the PEG films prepared from PEG powders.[152] Depending on the energy of the ions such a treatment results in either remarkable chemical modification of the PEG films, similar to the case of electron treatment,[31] or in smothering of the film surface, accompanied by noticeably lesser extent of the chemical modification. The latter case has a certain similarity with the effect of UV light reported in the present manuscript, even though the underlying mechanisms are presumably distinctly different.

4.1.8. Patterning of the PEG films

Along with homogeneous exposure of the PEG films to UV light, such an exposure can be performed in a lithographic fashion, resulting in the fabrication of 3D PEG patterns. An example of such a pattern, fabricated in proximity printing geometry (see section 4.1.2 for the technical details), is shown in Figure 4.11. Figure 4.11a illustrates the procedure, Figure 11b shows a representative pattern, and Figure 4.11c exhibits a height profile across the pattern. Accordingly, the contrast seen in the AFM image reflects the height differences between the shadowed and irradiated areas. An important feature of this 3D pattern is it all-hydrogel and all-biorepulsive character, which probably can be useful for some specific applications. Such

a pattern differs principally from an analogous pattern "written" by electron irradiation of the PEG films and combining non-hydrogel/non-biorepelling and hydrogel/biorepelling areas.[18,31]

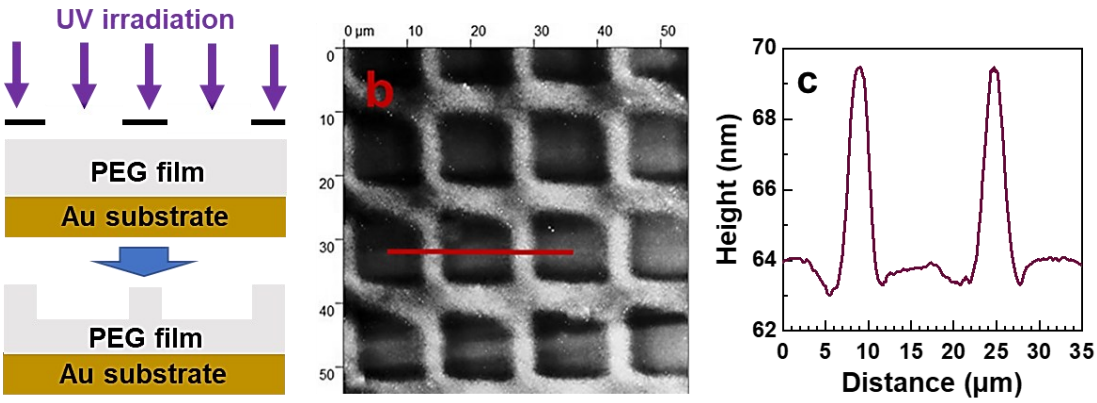

Figure 4.11. (a) Schematic of the patterning of the PEG films in proximity printing geometry; (b) AFM image of a representative pattern fabricated with a dose of 28.8 J/cm^2; and (c) height profile along the red line in the AFM image.

4.2. Tuning the properties of PEG films and nanosheets by the molecular weight of the precursors

4.2.1. Motivation

As I mentioned in the introduction part, the PEG films and free-standing nanosheets fabricated from STAR-PEG precursors are suitable for various applications. Noteworthy, the diversity of useful properties and applications has only been demonstrated so far for the STAR-PEG precursors with a comparably low MW of 2000 g/mol. It is however possible to vary this parameter significantly, relying on the commercial compounds, which should allow to tune the properties of the STAR-PEG-derived films and nanosheets in a controlled fashion. This was the goal of this particular subproject, in which I varied the MW of the STAR-NH_2 and STAR-EPX precursors from 2000 to 20000 g/mol in few steps and monitored the effect of this parameter onto the thickness, hydrogel, and biorepulsive properties of the PEG films as well as onto the stability and elastic properties of the free-standing PEG nanosheets.

4.2.2. Specific experiments and procedures

NP loading experiments. The ability of the PEG films to absorb objects dissolved in water was tested by their immersion into a freshly prepared solution of citrate-stabilized gold NPs (AuNPs). The immersion time was 6 h, with the subsequent rinsing with water and drying in a nitrogen stream. The AuNPs had an average size of ~13 nm; they were synthesized by reduction of $AuCl_3$ following the established procedure.[27]

4.2.3. Film thickness

The thickness of the PEG films with the different MWs of the precursors, determined by ellipsometry, is shown in Figure 4.12 as function of the concentration of the precursors in the primary solutions. First, the precursors with higher MW build a thicker PEG film at the same amount (in terms of weight) of the starting materials (Figure 4.12a). This effect is less apparent at the low concentrations, such as 15 mg/mL, but well pronounced at the higher concentrations. Second, whereas the thickness increases progressively with increasing concentration for all PEG films studied, this tendency becomes more significant with increasing MW. Whereas the increase of the concentration from 15 to 30 mg/mL results in increase of the film thickness by a factor of ~1.4 for a MW of 2k, it is a factor of ~4 for a MW of 20k (Figure 4.12a). The relation between the thicknesses of the films prepared from the different (MW) precursors varies, thus,

with the concentration, showing however no correlation with the MW values. Such a behavior indicates that the molecular network structure of the PEG films varies with the MW.

The dependence of the film thickness on the precursor concentrations given in the units of mM exhibits even a large difference between the different MWs (Figure 4.12b). Whereas in all cases a gradual increase of the film thickness with the concentration is observed, the curves become progressively steeper and non-linear with the increasing MW. A most likely explanation of such a behavior is the effect of the substrate on the exact network structure of the PEG films, such as a preferable in-plain orientation of the molecular chains imposed by the substrate, especially significant for the thin films and high MWs (long chains). The templating effect of the substrate diminishes with the increasing film thickness, resulting in progressively more stochastic orientation of the PEG chains and, consequently, in more rapid increase of the film thickness, with a stronger effect for the higher MWs.

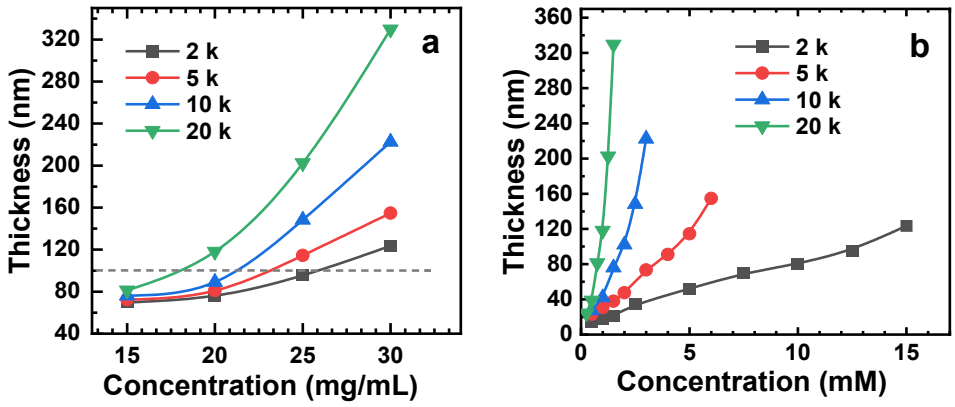

Figure 4.12. Thickness of the PEG films with the different MWs determined by ellipsometry as function of the concentration of the precursors in the primary solutions given either in mg/mL (a) or mM (b). The legends are given in the panels. The gray horizontal dashed line in (a) corresponds to the thickness of 100 nm, used for a variety of the experiments in the present study (see below). The entire range of the thickness variation was from 10 to 330 nm.

4.2.4. Film composition

The composition of the PEG films was monitored by XPS. Representative C 1s and O 1s and N 1s spectra of the films prepared at the concentration of the precursors in the primary solutions of 10 mg/mL are shown in Figure 4.13; the analogous data for 20 and 30 mg/mL can be found in Figures 4.14 and 4.15. The C 1s and O 1s spectra in Figures 4.13a and 4.13b, respectively, exhibit exclusively the characteristic peaks of PEG at 286.7 eV (C 1s) and 532.8 eV (O 1s),[72,136]

which are the only perceptible features. The chemical identity of the PEG films and the lack of any contamination are thus verified.

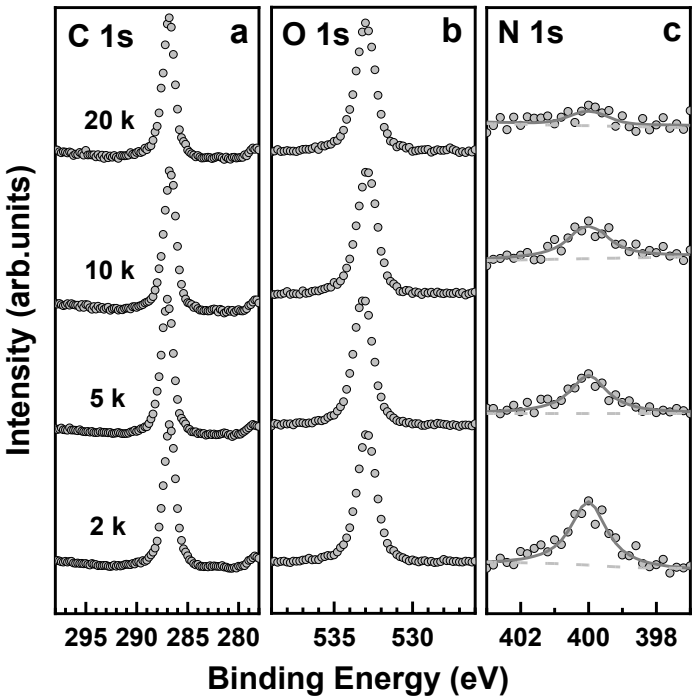

Figure 4.13. C 1s (a) and O 1s (b), and N 1s XPS spectra of the PEG films prepared from the precursors with the different MWs, as marked in panel a. The concentration of the precursors in the primary solutions was set to 10 mg/mL.

The intensity of the C 1s and O 1s peaks shows nearly no dependence on the MW, which is predictable since the major building blocks of these films – PEG arms – are chemically identical and the signals are saturated in view of the fact that the sampling depth of XPS (6–8 nm)[84] is in all cases noticeably smaller than the thicknesses of the films (70–120 nm, see Figure 4.12a). In contrast, the intensity of the N 1s peak in Figure 13c decreases with the increasing MW, reflecting the chemical composition of the STAR-NH_2 precursors. The PEG arms of these precursors, terminated with a sole NH_2 group, becomes progressively longer with the increasing MW, so that the N/C and N/O ratios become progressively smaller as well. These relationships are mimicked by the films, since the transformation of the NH_2 groups into NH ones does not change noticeably the elementary film composition.

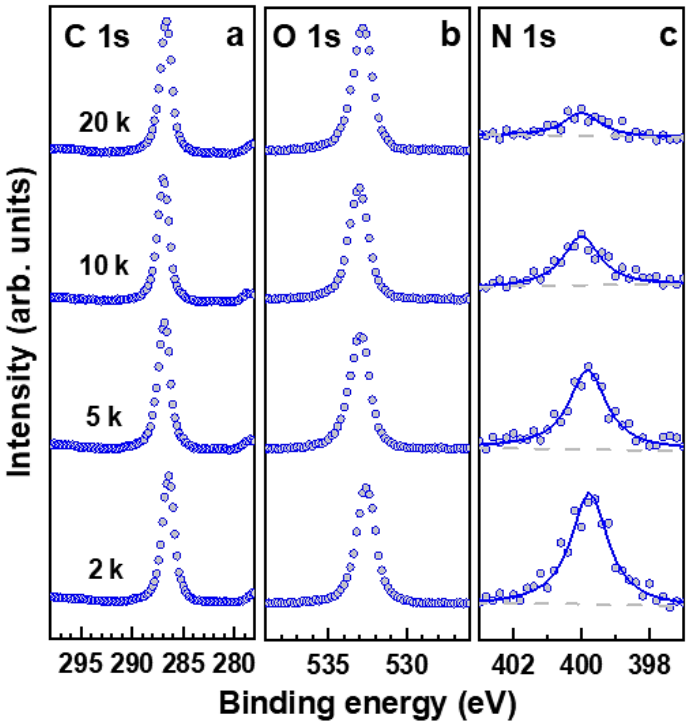

Figure 4.14. C 1s (a) and O 1s (b), and N 1s XPS spectra of the PEG films prepared from the precursors with the different MWs, as marked in panel a. The concentration of the precursors in the primary solutions was set to 20 mg/mL.

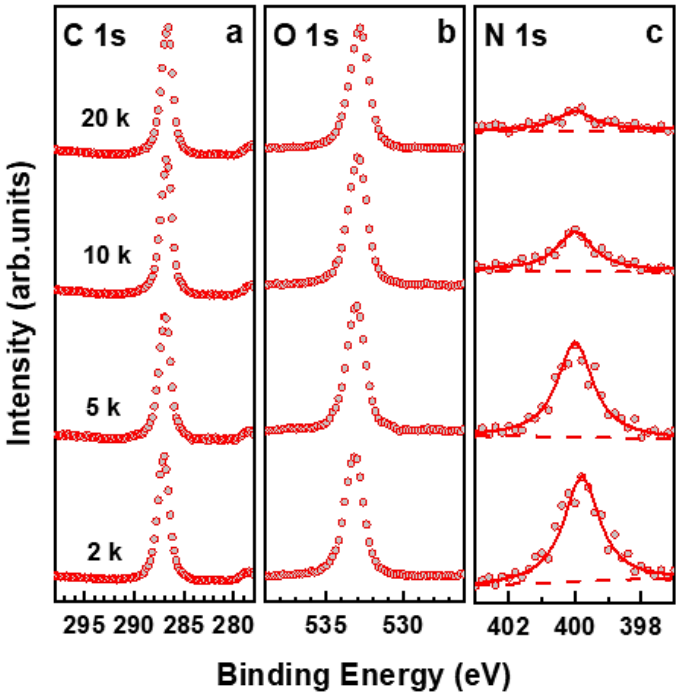

Figure 4.15. C 1s (a) and O 1s (b), and N 1s XPS spectra of the PEG films prepared from the precursors with the different MWs, as marked in panel a. The concentration of the precursors in the primary solutions was set to 30 mg/mL.

4.2.5. Swelling properties

The swelling properties of the PEG films were monitored by ellipsometry, at the temperature variation from room temperature to nearly 0 °C. Such a variation affects the relative humidity experienced by the PEG films and triggers the water uptake into the films.[27] The results of the experiments are presented in Figure 4.16, which shows the thickness variation for the films prepared at 4 different concentrations of the precursors in the primary solutions. All films exhibit progressive thickness increase at the low temperatures, representative of water-uptake-driven swelling, typical of hydrogels.

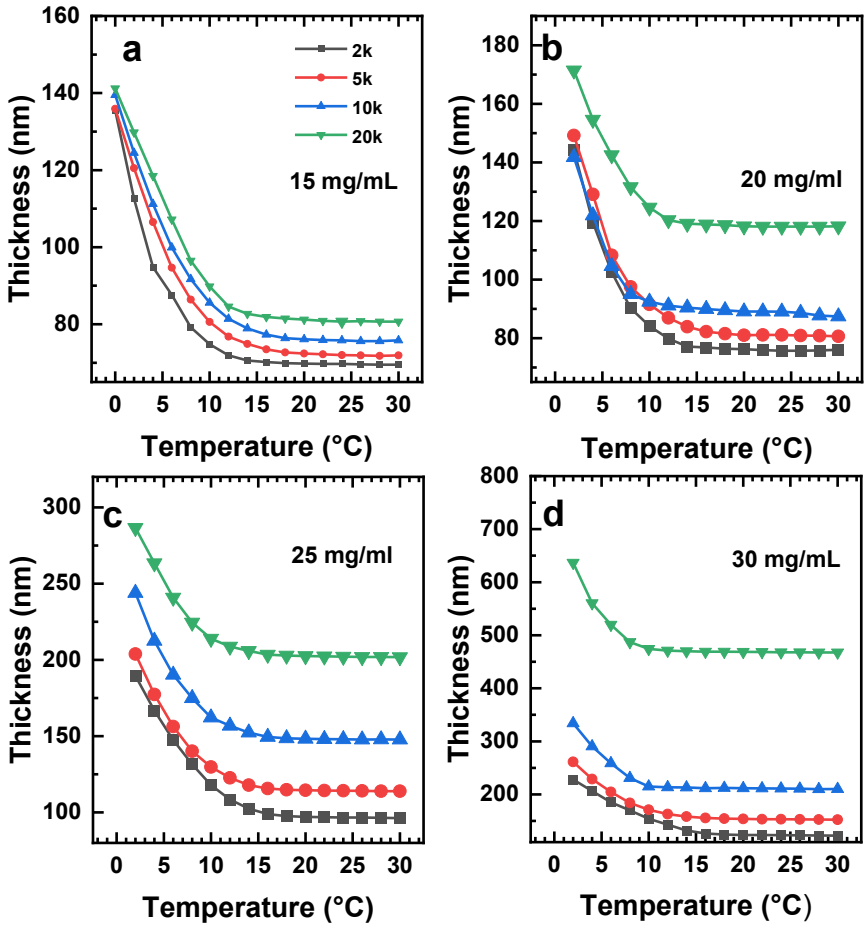

Figure 4.16. Thickness of the PEG films as a function of temperature. The concentration of the precursors in the primary solutions was set to 15 mg/mL (a), 20 mg/mL (b), 25 mg/mL (c), and 30 mg/mL (d), respectively.

The extent of the thickness increase was quantified by so-called swelling ratio, which is the ratio of the thicknesses at the lowest and room temperature. The resulting values of the swelling

ratio are presented in Figure 4.17. For all films studied, the swelling ratio decreases with the MW, with the higher extent of decrease at 20, 25, and 30 mg/mL as compared to 15 mg/mL. The dependence on the MW can be partly related to the higher film thickness, characteristic of the higher MW films (see Figure 4.12a). A decrease of the swelling ratio with increasing film thickness has been reported before and explained by progressively higher extent of crosslinking in the thicker films.[153]

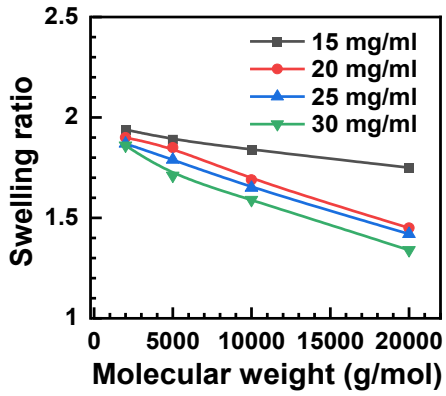

Figure 4.17. The swelling ratio as a function of the MW for the films prepared at the different concentrations of the precursors in the primary solutions.

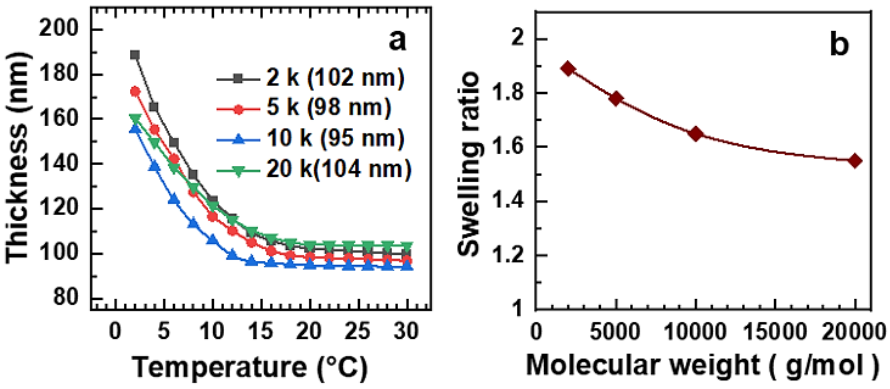

Figure 4.18. (a) Thickness of the PEG films prepared from the precursors with the different MWs as function of temperature; the thickness of the films was set to ~100 nm; the legend and exact thickness values are given in the panel. (b) The swelling ratio of these films as a function of the MW.

To exclude the above-mentioned effect of the film thickness, swelling properties of the films with different MWs but nearly the same thicknesses of ~100 nm were compared. The necessary

adjustment of the concentrations of the precursors in the primary solutions was performed in accordance with the data in Figure 4.12a. The results of the swelling experiments are shown in Figure 4.18. Whereas the thickness of all PEG films exhibits the typical increase with the decreasing temperature (Figure 4.18a), the exact evaluation of these data suggests a progressive lowering of the swelling ratio with the increasing MW (Figure 4.18b). Interestingly, this behavior is opposite to the expectations, since the films originating from the precursors with the higher MWs have, in view of their molecular structure (Figure 3.1), a lower extent of crosslinking than the films originating from the precursors with the lower MWs.

4.2.6. Biorepulsive properties

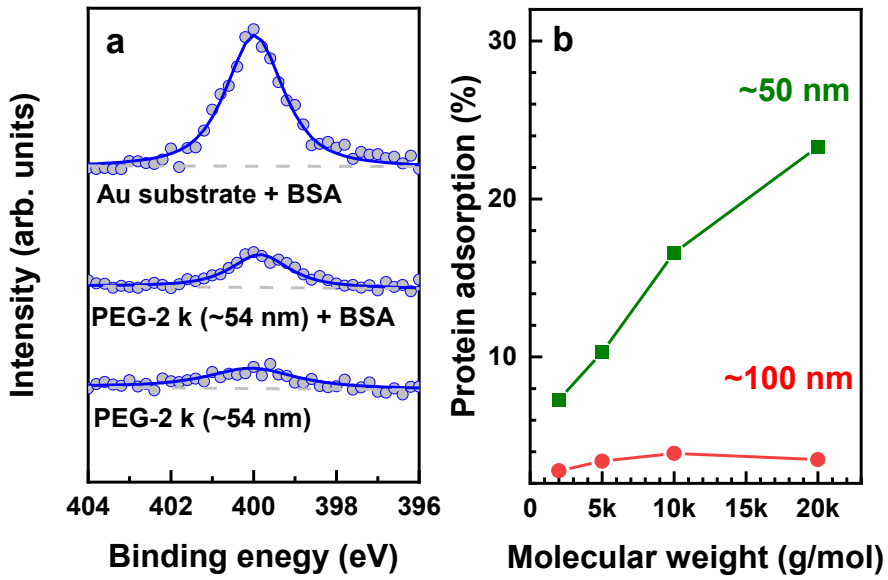

Figure 4.19. (a) N 1s XPS spectra of the PEG film (~54 nm; 2k) before and after the BSA exposure, along with the reference spectrum of a protein-adhesive substrate (Au) after the BSA exposure. (b) Relative protein absorption as a function of the MW for the films with the ~50 nm and ~100 nm thicknesses.

Biorepulsive properties of the PEG films were tested by the protein absorption experiments. The films with different MWs of the precursors but nearly the same thickness, set either to ~50 or ~100 nm, were exposed to BSA and the extent of absorption was monitored by XPS, relying on the characteristic N 1s signal and taken a protein-adhesive substrate as the reference. The results are presented in Figure 4.19. Figure 4.19a compiles the relevant N 1s spectra of a representative PEG film (~54 nm; 2k) before and after the BSA exposure as well as the reference spectrum of a protein-adhesive substrate (Au) after the BSA exposure; the full set of

the spectra can be found in Figures 4.20 and 4.21. The spectrum of the untreated film exhibits a small N 1s signal, stemming from the NH groups in the network (see Figure 3.1). This signal increases noticeably after the exposure of the film to BSA, suggesting a certain extent of the protein adsorption. Quantitative evaluation of the XPS data shows that this extent is quite small (~7.5%) but increases significantly with the increasing MW of the precursors, up to ~23% for a MW of 20000 g/mol (Figure 4.19b). This behavior is, however, only characteristic of the thin PEG films, such as those with a thickness of ~50 nm. In the case of the thicker films, such as those with a thickness of ~100 nm, protein adsorption at a level of 2.5–3.5% was recorded, with the extent being independent of the MW.

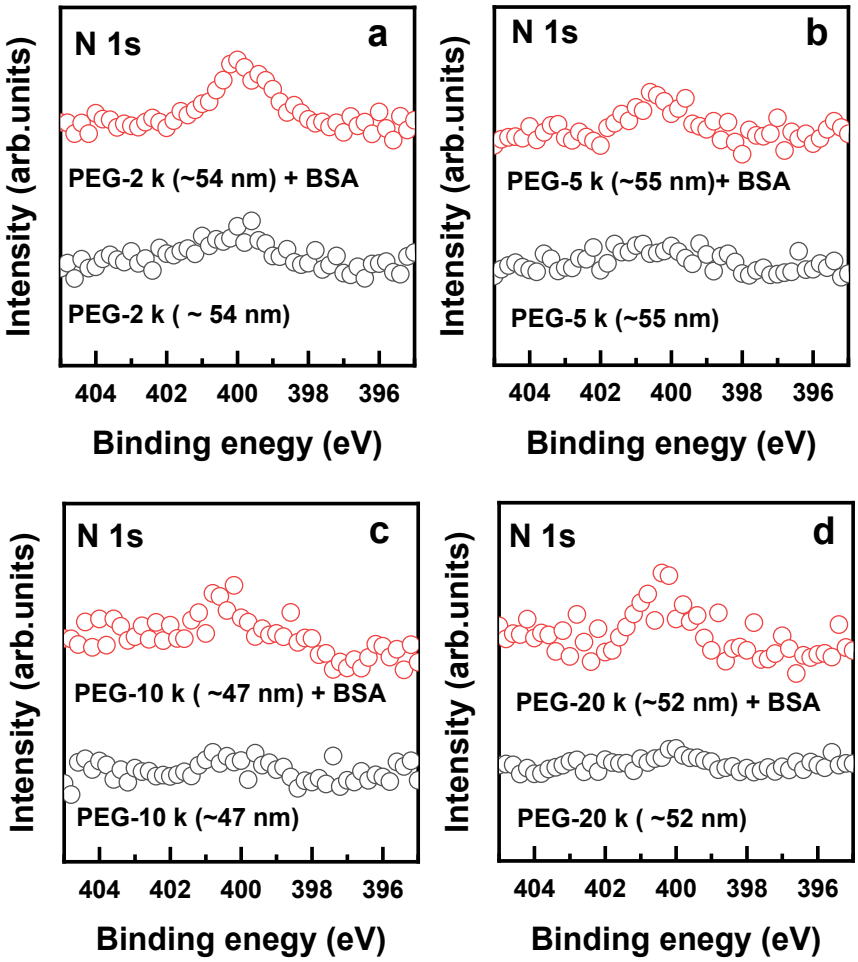

Figure 4.20. N 1s XPS spectra of the thinner PEG films with different MWs of the precursors but similar thickness (~50 nm) before and after the BSA exposure. The MWs and the exact values of the film thicknesses are marked at the respective spectra.

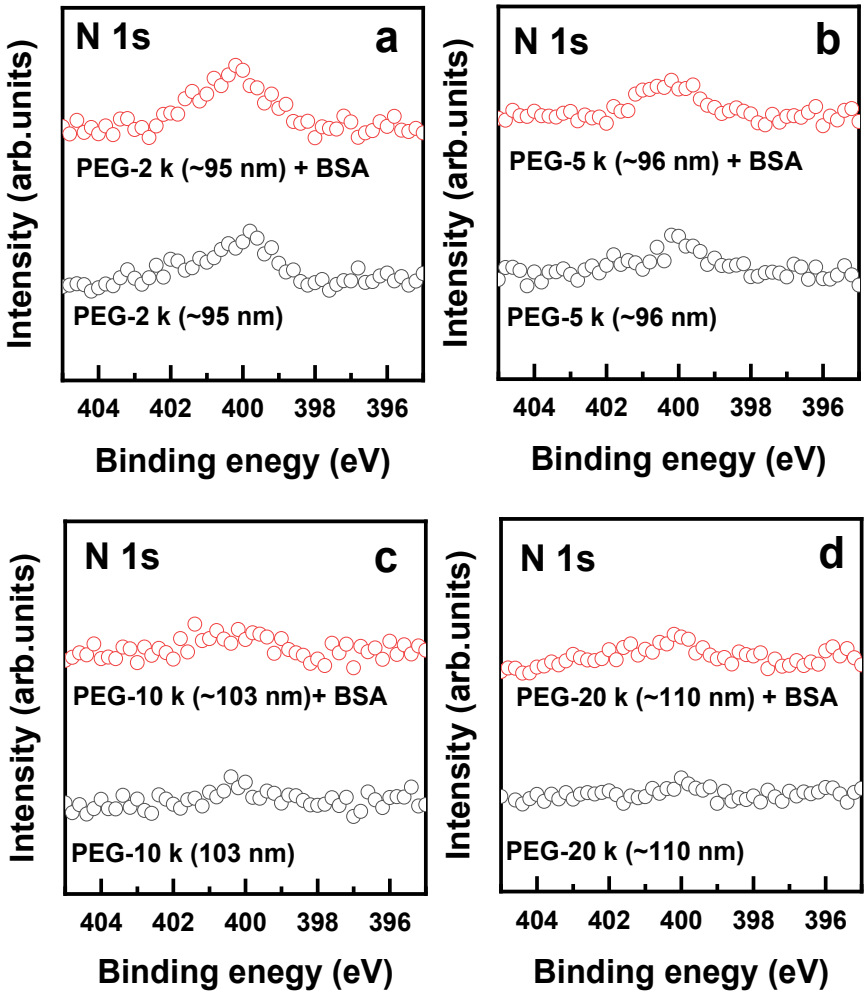

Figure 4.21. N 1s XPS spectra of the thicker PEG films with different MWs of the precursors but similar thickness (~100 nm) before and after the BSA exposure. The MWs and the exact values of the film thicknesses are marked at the respective spectra.

4.2.7. Nanoparticles loading

The ability of the PEG films to absorb nanoscale objects dissolved in water was tested by their exposure to AuNPs. Films with different MW but the same thickness (~100 nm) were used. SEM images of these films after the AuNP loading are presented in Figure 4.22; the size distribution of the NPs is shown in Figure 4.23. In all cases PEG/AuNP composites were formed but the density of the NP loading varied non-systematically with the MW of the precursors, which was verified by control experiments on several different samples. The highest AuNP density was observed for the 5k and 10k films (Figure 4.22b and 4.22c), with the former film exhibiting the most disperse NP distribution. The 2k film was characterized by a noticeably lower density of the AuNPs (Figure 4.22a), which were well dispersed in the PEG

matrix. The 20k films exhibited an even lower AuNPs density, accompanied by a noticeable extent of NP agglomeration.

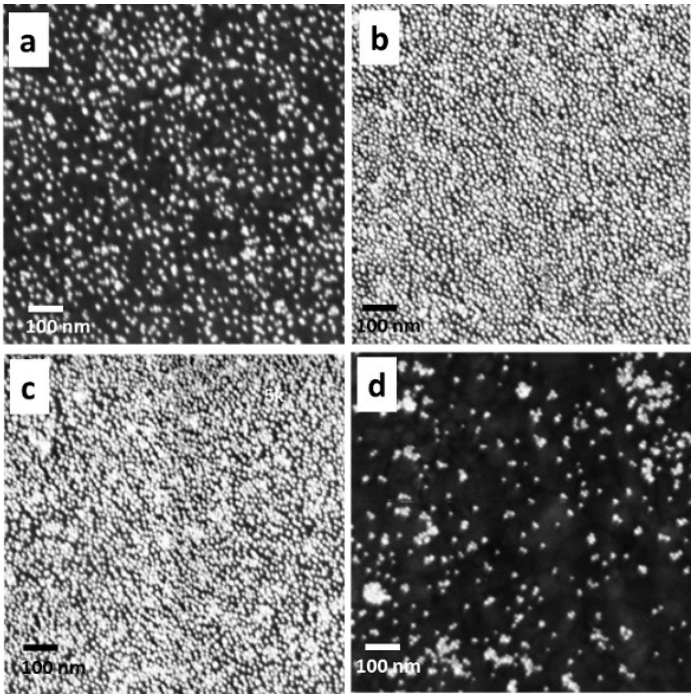

Figure 4.22. SEM images of the PEG/AuNP composite films (~100 nm) prepared from the precursors with MWs of 2000 g/mol (a), 5000 g/mol (b), 10000 g/mol (c) and 20000 g/mol (d).

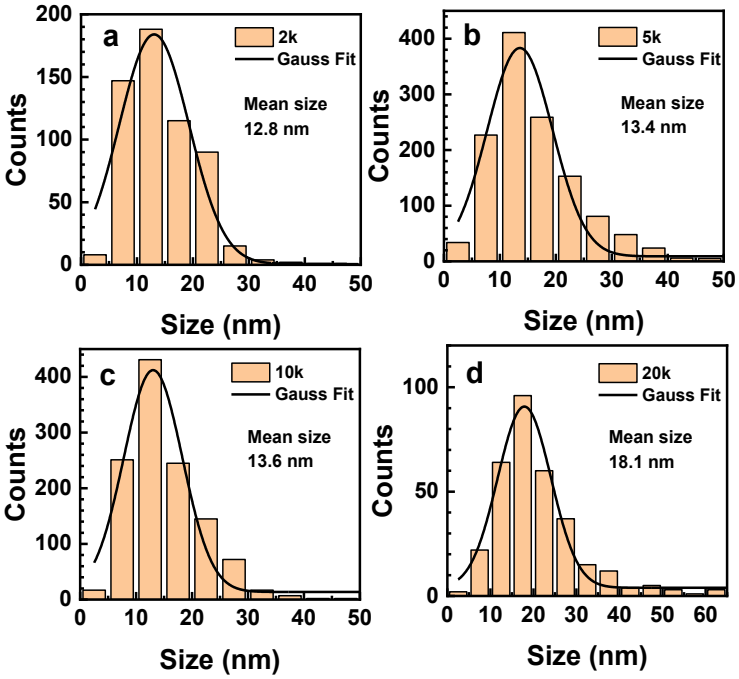

Figure 4.23. Size distributions of the AuNPs in the PEG-AuNP composites for the MWs of 2k (a), 5k (b), 10k (c), and 20k (d). The comparably larger average size for the 20k films stems

most likely from a partial coagulation of the NPs, resulting in an overestimate of the average size value.

In addition to the imaging of the PEG/AuNP composite films, their optical properties were monitored. The respective UV-vis spectra are shown in Figure 4.24. These spectra are dominated by characteristic local surface plasmon resonance (LSPR) in AuNPs.[31] The intensity of this band correlates well with the AuNP density in the composite films; it is the highest for the 5k and 10k films, somewhat lower for the 2k films, and the lowest for the 20k films. The position of this bands shows a progressive red shift with increasing MW of the precursors. This position depends on the size of NPs, their distance to the Au substrate, and their density, so that it is difficult to say which of these parameters is of primary importance in the given case. Considering the non-systematic variation of the packing density of the AuNPs, the most likely factor is the vertical distribution of the NPs in the films, defining their separation from the conductive substrate and, consequently, the coupling of the AuNP LSPR with that of the substrate.

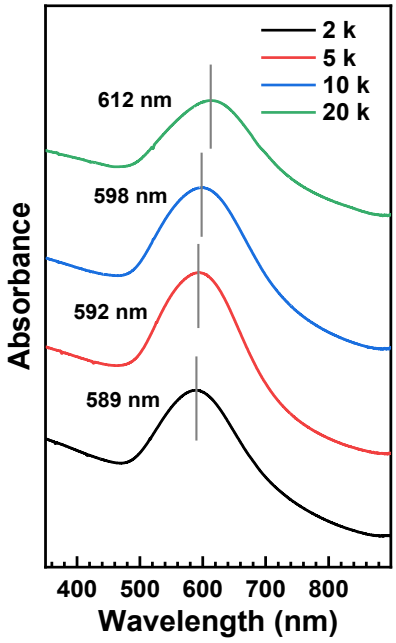

Figure 4.24. UV-vis spectra of the PEG/AuNP composite films (~100 nm) prepared from the precursors with different MWs. The maximum of the LSPR band is marked and its position is given.

4.2.8. Free-standing PEG nanosheets

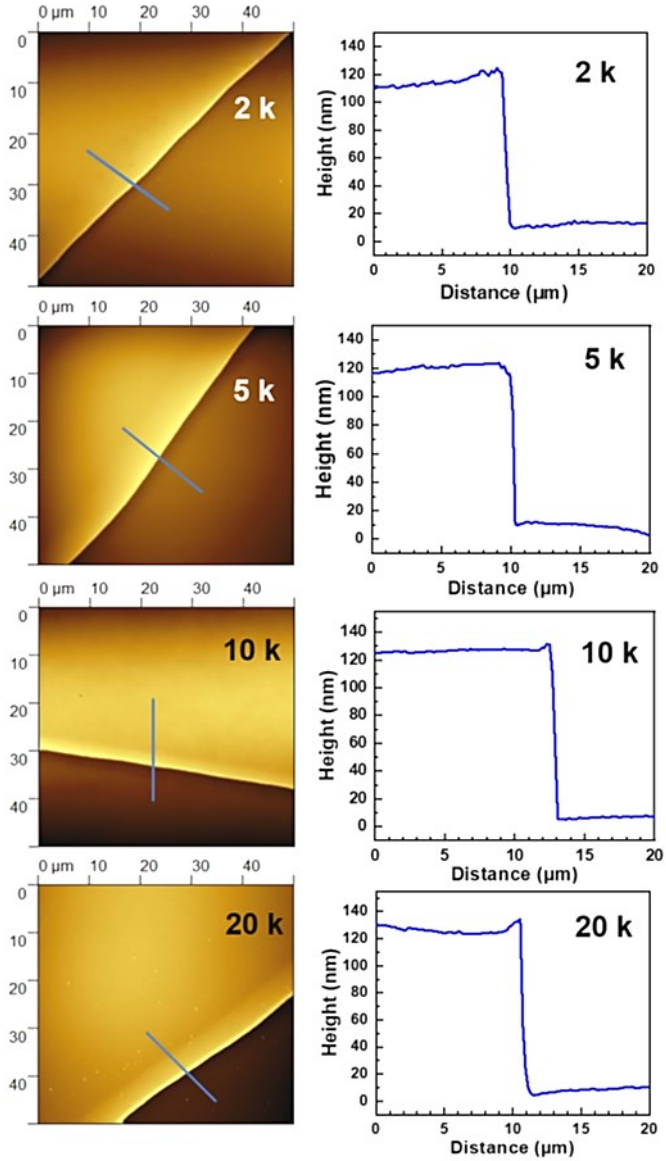

Figure 4.25. Left column: AFM images of the PEG nanosheets transferred onto Si substrate. Right column: the height profiles across the edges of the nanosheets, along the blue lines in the images.

The quality and thickness of the PEG nanosheets were controlled by the AFM measurements, performed after the transfer of the nanosheets onto a secondary Si substrate. The nanosheets originated from the PEG films which were prepared from the precursors with the different MWs but had nearly the same thicknesses, set to ~100 nm (by the adjustment of the precursor

concentration in the primary solutions; see Figure 4.12) according to the ellipsometry data. Representative AFM images of the PEG nanosheets with the different MWs of the precursors are shown in Figure 4.25, along with the height profiles across the edges of the nanosheets. The images demonstrate that the nanosheets are smooth and uniform, which are the features underlining their well-defined character and prerequisites for their good stability. The thicknesses of the 2k, 5k, 10k, and 20k nanosheets according to the height profiles are ~102 nm, ~104 nm, ~116 nm, and ~115 nm, respectively, which are quite close to the respective values measured by ellipsometry, viz. ~98 nm, ~103 nm, ~105 nm, and ~103 nm, respectively. Consequently, the evaluation of the ellipsometry data, relying on the same optical constants for the films prepared from the precursors with the different MWs is reliable and these constants, indeed, do not vary noticeably with the MW.

4.2.9. Mechanical properties of the nanosheets

The mechanical properties of the nanosheets with different MWs but similar thicknesses (100–116 nm) were studied by bulge test. Representative images of the deflected nanosheets captured during the test are presented in Figures 4.26. As seen in Figures 4.26a–d by the example of a 2k PEG nanosheet, the deflection of the nanosheets increases progressively with increasing loading pressure, achieving a value exceeding the radius of the opening (~0.57 mm) at Δp = 2.0 kPa for the 2k case, which indicates excellent elastic properties of the nanosheets. The extent of the deflection at the given Δp depends however on the MW of the precursors, as illustrated in Figures 26g–h for all MWs and Δp = 1.0 kPa. Accordingly, the deflection decreases with increasing MW, suggesting the respective trend in the elasticity of the nanosheets.

To quantify this qualitative statement, numerical evaluation of the bulge test data was performed. According to eq 2.6, a $\Delta p/h$ versus h^2 plot should represent a straight line with the slope defined by the parameters a, ν and E. This is indeed the case for the nanosheets of the present study, as evidenced by the data in Figure 4.27a, which can be well fitted by straight lines. The slopes of these lines reflect then the respective Young's moduli. Using the known value of a (~ 0.5 mm) and making a reasonable assumption for ν (0.25; on the basis of bulky gel-like material),[18] Young's moduli could be calculated. The respective values are presented in Figure 4.27b as a function of the MW, progressively increasing with the MW and varying from ~2.1 MPa for the 2k nanosheet to ~5.2 MPa for 20k nanosheet. Note that the E value for the 2k nanosheet correlates excellently with the results of the previous study on the 2 k PEG

nanosheets of the same thickness (~2 MPa),[18] verifying the correctness of the measurements and data evaluation procedure.

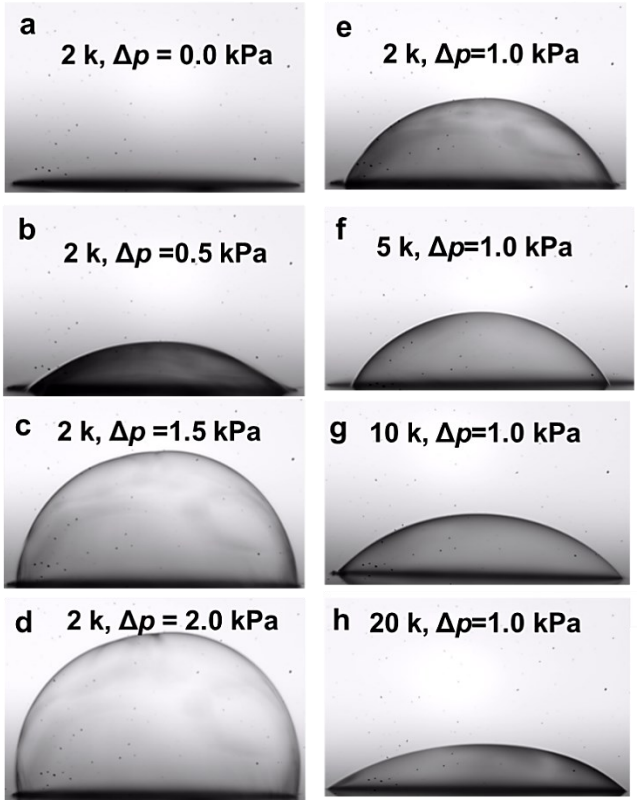

Figure 4.26. (a–h) Microscopy images of the deflected PEG nanosheets, including (a–d) a series of images for a 2k nanosheet taken at the progressively increasing Δp and (e–h) a series of images for 2k, 5k, 10k, and 20k nanosheets taken at the same Δp of 1.0 kPa. The MW and Δp values are given in the panels.

Note that the relations between h and Δp could be successfully reproduced during several successive load-unload cycles. The Δp range corresponding to the stable and reproducible deformation of the nanosheets varied to some extent depending on the MW. A tentative fingerprint of this deformation is the thickness of the deformed nanosheets, which could be calculated from the geometrical considerations. The respective data are shown in Figure 4.27c. As expected, the nanosheet thickness decreases progressively with increasing Δp. This increase is non-linear at the low pressures but becomes linear at the higher Δp. Independent of the MW, all nanosheets survive Δp up to ~1.9 kPa, but breaks at the higher pressures, with the 2k nanosheet being most stable. This nanosheet achieves a nearly one third of its original thickness before it breaks.

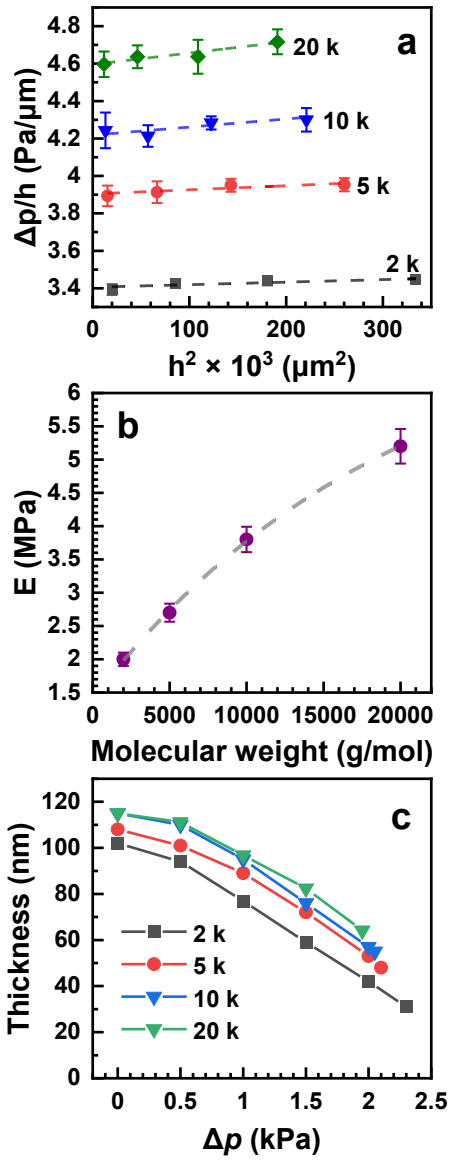

Figure 4.27. (a) Plots of $\Delta p/h$ as a function of h^2 for the PEG nanosheets with the different MWs but similar thicknesses of ~100 nm. (b) Calculated Young's moduli of the nanosheets vs. the MW. (c) A variation of the thickness of the PEG nanosheets during the bulge test. The original thicknesses of the nanosheets are based on the AFM-derived values. The last points of the curves correspond to the Δp values short before the nanosheet breakage.

4.2.10. Discussion

Whereas some of the experimental results presented above can be understood and interpreted in straightforward fashion, others need to be discussed.

First of such points is the relation between the film thickness and the MW (Figure 4.12a). Whereas the thickness increases with the MW at the given concentration of the precursors in

the primary solutions, this increase does not mimic the MW relation for the entire concentration range probed. On the one hand, this behavior can be related to a lower crosslinking ability of the precursors with higher MW, but, on the other hand, it can be associated with a larger confinement of the molecular chains in the higher MW films. Such a substrate-imposed confinement is most likely especially significant in the thin films, becoming progressively less pronounced with the increasing thickness.

The second point is the porosity of the films and nanosheets, which should increase noticeably with the increasing MW. Whereas this parameter could not be probed directly, indirect information is provided by the protein absorption experiments for the thin (~50 nm) PEG films (Figure 4.19b). The observed increase in the extent of the protein absorption with the increasing MW can be directly related to the size of the pores as far as we reasonably assume that the protein absorption is mediated by substrate, after the penetration of the proteins through the PEG network. Once again, the extent of the protein permeability through the nanosheet does not correlate exactly with the MW, varying by the factor of ~3 only at the MW variation by the factor of 10.

The third point is the suitability of the PEG films and nanosheets to form composites, e.g. by their loading with NPs. The 2k, 5k, and 10k films seem to be well suitable for this purpose, building composite with laterally homogeneous distributions of the AuNPs (see Figure 4.22a–c). In contrast, the 20k films exhibit an inhomogeneous distribution of the AuNPs, which also feature a noticeable extent of agglomeration (see Figure 4.22d), reflected also in a seeming larger average size (see Figure 4.23). This behavior is most likely related to the high porosity of the 20k matrix, diminishing its ability to “fix” NP and to prevent their agglomeration.

The fourth point is the swelling ability of the PEG films, which, surprisingly, does not increase but decreases with the MW at the nearly same film thicknesses (Figure 4.18b). This behavior correlates with the elasticity of the PEG-derived nanosheets, represented by their Young’s moduli.

For all the nanosheets studied, the Young’s modulus, varying from 2.1 to 5.2 MPa depending on the MW of the precursors, (Figure 4.27b), is extremely small not only compared to inorganic nanosheets, such as those from SiN (220 GPa for the 320 nm thickness),[154] but also to ultrathin carbon nanonanosheets (45 GPa)[155] and polyethylene nanosheets (10 GPa for the thickness of 55 nm).[156]

Being intrinsically small, the Young's modulus for the PEG nanosheets increases with the MW of the precursors, by a factor of ~2.5 at going from the 2k to 20k nanosheets. This increase is contra intuitive assuming that the most realistic model, explaining the extremely low values of *E*, is that of an elastomer. Accordingly, the crosslinked chains in the PEG network, fixed at the centers of the STAR-PEG moieties, are coiled and can be easily straightened at the applied load, resulting in a significant deformation of the PEG films even at a small load (see Figure 4.28), corresponding to a very small Young's modulus as observed in our experiments.

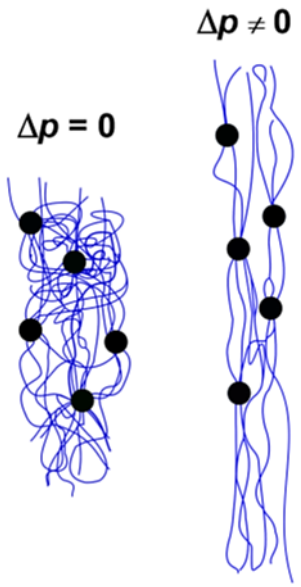

Figure 4.28. A model explaining the extremely high elasticity of the PEG nanosheets. Blue lines represent the crosslinked chains in the PEG network that can be stretched at an applied load; black circles are the centers of the STAR-PEG moieties; crosslinking points are not specifically marked.

An increase of the MW of the precursors should result in a decrease of the relative weight of the fixed points in the network, making it even more elastic, in contrast to the experimental data. The only way to solve this contradiction is to assume that the extent of coiling of the PEG chains in the network depends on the MW of the precursors. This is indeed possible because of a stronger interaction between longer molecular chains and preferable in-plain orientation of these chains imposed by the substrate. Such an in-plain orientation can be more pronounced for longer molecular chains because of their potentially stronger interaction with the substrate.

4.3. Elastic properties of free-standing PEG nanosheets and respective implications

4.3.1. Motivation

As discussed above, the free-standing PEG nanosheets are quite stable and possess an exceptional elasticity, emphasized by a very small Young's modulus of 2.1–5.2 MPa at a thickness of ~100 nm.[157] The value of the Young's modulus depends on the molecular weight of the STAR-NH_2 and STAR-EPX precursors, but is most likely a function of the nanosheet thickness and its composition at a deviation from the standard 1:1 ratio between STAR-NH_2 and STAR-EPX, useful for some applications.[30] It cannot also be excluded that the derived values of the Young's modulus are affected by the parameters of the experimental setup used for their measurement, which will strongly diminish their reliability.

These issues were specifically addressed in the respective subproject in which I also explored the possibility to tune the elastic properties of the PEG nanosheets by the modification of the parent films by electron irradiation and UV light. The latter experiments, in combination with additional measurements, shed also some light into the effect of UV light on PEG materials,[153] which was discussed above.

4.3.2. Specific experiments and procedures

Nanosheets fabrication. The fabrication of PEG nanosheets on bulge test substrate is described in chapter 3. Note that in this section, the ratio of STAR-NH_2 and STAR-EPX was varied to some extent in some specific cases (see section 4.3.3).

Optional modification. The PEG nanosheets were investigated in two conditions: as-prepared and after subjecting the primary PEG films (on SiO_2/Si) to additional treatments, viz. electron irradiation and UV light exposure (2 mW/cm^2), prior to their detachment from the original substrate. Detailed information on the technical aspects of UV treatment can be found in section 4.1.2. The electron irradiation was applied homogenously using a flood gun (FG20, Specs, Germany). The treatment was performed at room temperature and under UHV conditions with a base pressure lower than 8×10^{-8} mbar. The electron energy was set to 50 eV and the dose was calibrated with a Faraday cup. Several different doses were applied.

4.3.3. Parameters of the bulge test

In bulge test, the stress and strain in the film can be determined from measurements of pressure difference on both sides of the nanosheet (Δp) and the window's deflection (h). The further

relevant parameters are the geometrical shape and size of the window and film thickness (t). In our case, a circular window was used and its diameter ($2a$; a – radius) was varied as 0.3 mm, 0.5 mm, and 1 mm. The nanosheet thickness was set to 100 nm.

Representative microscopy images of the deflected PEG nanosheets for these windows are shown in Figures 4.29a, 4.29b and 4.29c, respectively. At a fixed Δp, the deflection depends strongly on the diameter of the window, being largest for 1 mm diameter and progressively smaller for the smaller windows. The maximal Δp corresponding to the rupture of the nanosheets showed an inverse behavior, being lowest for 1 mm diameter and progressively higher for the smaller windows.

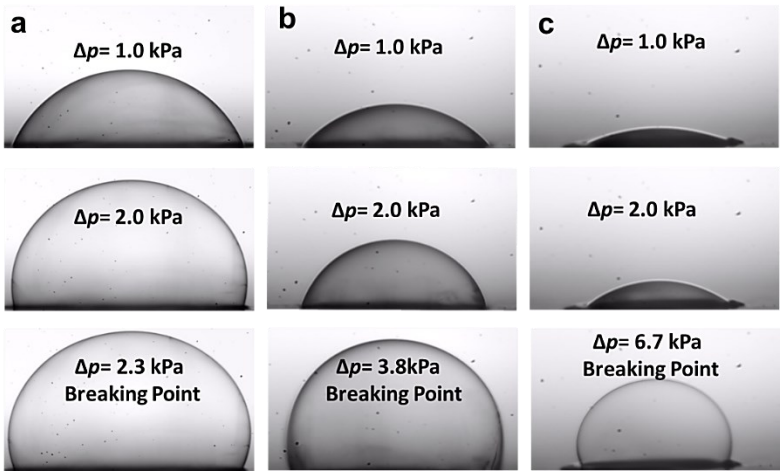

Figure 4.29. Selected optical images of the deflected PEG nanosheets, suspended over a circular window with a diameter of 1 mm (b), 0.5 mm (c), and 0.3 mm (d). The bottom image in each series corresponds to the pressure close to the breakdown point.

The entire bulk of the deflection data is presented in Figure 4.30a, in deflection versus Δp fashion. The relation between the pressure difference and the deflection of the suspended nanosheet over a circular window is shown in eq 2.6. The Δp vs h plots in Figure 4.30a exhibit a nearly linear behavior for all a values, corresponding to the first term on the right side of Eq 1 and framing the second term as contributing to a small extent only, which means that the E values for the PEG nanosheets are very small. Further, to avoid the influence of different geometrical parameters (a, t and h) on the apparent sensitivity of different nanosheets, a dimensionless aspect ratio of deflection (h) to window radius (a), denoted as δ, can be plotted

against Δp normalized by the aspect ratio of window diameter and nanosheet thickness according to the equation derived from eq 2.6 (ν was tentatively set to 0.25)

$$\Delta p\ a\ /\ t = 4\ \sigma_0 \cdot\ \delta + 3.6\ E\ \delta^3 \qquad (4.1)$$

The respective data are presented in Figure 4.30b, with the values for the different a perfectly matching each other and building together a nearly straight line, which once again manifests that the E values for the PEG nanosheets are very small. These values can be directly calculated on the basis of the strain and the stress, according to eq 2.7. The calculated values for 0.3 mm, 0.5 mm, and 1 mm diameters are 2.45 MPa, 2.47 MPa, and 2.41 MPa, respectively. These values are nearly identical, which suggests that the size of the window in a bulge test experiments does not influence the result. Note also that the Young's modulus values can also be calculated by an alternative approach, as described in the section 4.2, relying on the $\Delta p/h$ vs h^2 (Figure 4.31). plots according to eq 2.6. The respective values of 2.13–2.21 MPa are very close to those obtained by the strain/stress method, but depend, however, on the Poisson's ratio, the exact value of which for the PEG nanosheets is not known. Consequently, we consider evaluation of the Young's modulus on the basis of the strain and stress values as preferable.

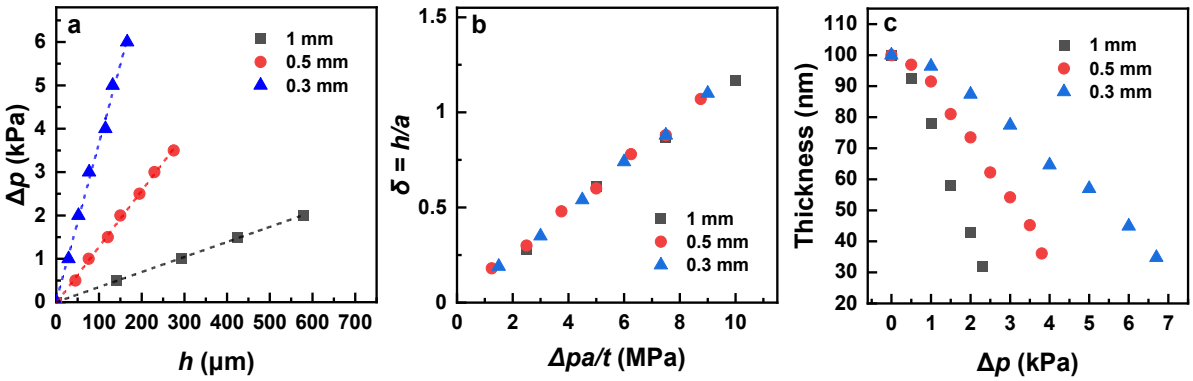

Figure 4.30. Δp vs h (a) and h/a vs $\Delta p \cdot a\ /\ t$ (b) plots for the PEG nanosheets suspended over the circular windows with the different diameters (see the legends); straight lines in (a) are tentatively drawn through the experimental points. (c) Thickness of the nanosheets as a function of Δp.

A further interesting point is the thickness of the PEG nanosheets upon their stretching, which was estimated from the geometrical considerations. The respective data are shown in Figure 4.30c. Accordingly, the thickness changes with different rates, depending on the size of the window. However, the ultimate thickness at the stretching close to the breakdown does not

vary much, estimated at ~32 nm, ~36 nm, and ~34.5 nm for a window diameter of 1 mm, 0.5 mm, and 0.3 mm, respectively. This correlation underlines, once again, a consistency of the bulge test data for different sizes of the window.

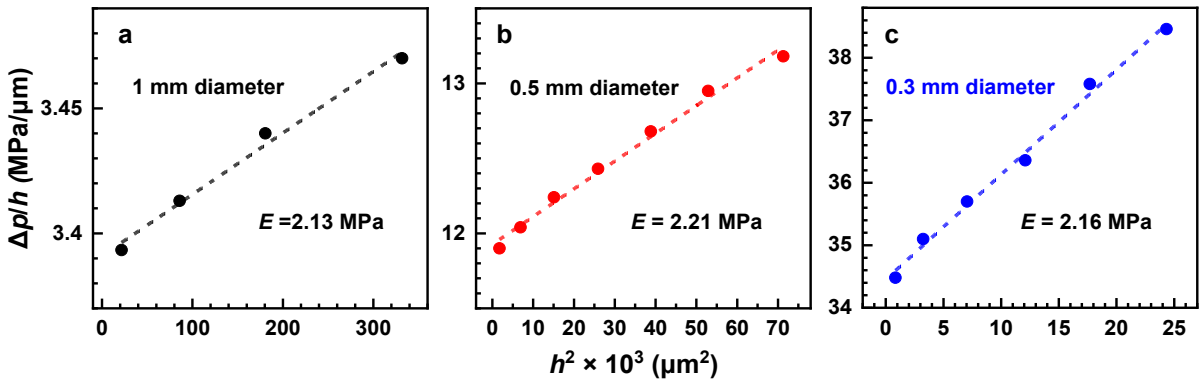

Figure 4.31. $\Delta p/h$ vs h^2 plots for the PEG nanosheets suspended over the circular window with a diameter of 1 mm (a), 0.5 mm (b), and 0.3 mm (c). The straight lines are linear fits to the experimental points. The E values were derived from the slopes of these lines, according to eq 2.6.

A final aspect is the value of the residual stress (σ_0) which a stress that remains in a material after the original cause of the stresses has been removed. The value of σ_0 can either be determined from the linear fit of the Δp vs h plots (Figure 4.30a) neglecting the second term on the right side of eq 2.6 or from the $\Delta p/h$ vs h^2 plots (Figure 4.31) as the intersection of the linear fit with the Y-axis. The first procedure gives 185 kPa, 194 kPa, and 190 kPa for the 0.3 mm, 0.5 mm, and 1 mm windows, respectively. The second procedure gives closer values of 204 kPa, 202 kPa, and 217 kPa, respectively. In both cases, the values do not vary noticeably with the window size.

4.3.4. Effect of nanosheet thickness

The dependence of the elastic properties on the thickness of the PEG nanosheets was studied in the 40–320 nm range. The results for two different windows were combined together since the thinnest nanosheets could not be suspended over the 1 mm window without a rupture. The derived values of the Young's modulus are shown in Figure 4.32a. The data for the different windows perfectly match and complement each other, which is one more evidence that the size of the window in a bulge test experiments does not influence the result. According to these data, the Young's modulus increases progressively with increasing film thickness, with a larger

rate at small thicknesses and a lower rate at large thicknesses. Such a behavior is understandable since a thin film is easier to deform and the effect should most likely be stronger at small thicknesses, at which the relative thickness changes more rapidly at a variation of the absolute thickness.

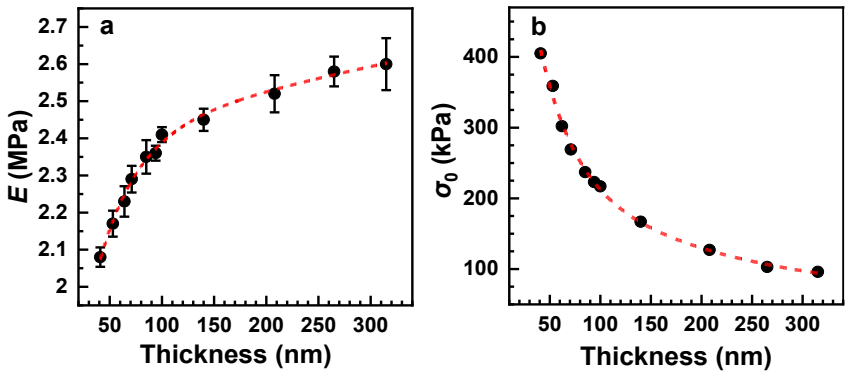

Figure 4.32. Young's modulus (a) and residual stress (b) as functions of the nanosheet thickness. The experimental points are tentatively traced by the red dashed curves. The data for the thicknesses below and above 60 nm were obtained with the 0.5 mm and 1 mm windows, respectively.

Note that the derived Young's modulus values of the PEG nanosheets in the entire thickness range studied are very small, which renders these nanosheets extremely elastic. For comparison, the Young's modulus of a 55 nm polyethylene nanosheet was estimated at 10 GPa,[156] that of a vapor-deposited, 30 nm tris(8-hydroxyquinoline) aluminum film – 2.81–3.88 GPa.[158] One of the lowest Young's modulus values (32 MPa) was reported for ~100 nm plasma-polymerized allylamine films,[159] but even this value is by more than an order of magnitude higher than that for the PEG nanosheets.

Along with Young's moduli, residual-stress values were calculated as well (Figure 4.32b). This parameter exhibits a progressive decrease with increasing film thickness. The behavioris nearly inverse to that of Young's modulus but the relative extent of the σ_0 variation is much larger.

4.3.5. Effect of nanosheet composition

Generally, STAR-NH_2 and STAR-EPX precursors should be mixed in relation 1:1 to have optimal mixing ratio for the efficient crosslinking. However, in this case, the vast majority of the amine and epoxy groups form ethanol-amine-like bridges (Figure 3.1) and the amount of the non-reacted groups is very small. This situation is of advantage for most applications but is

unfavorable in the case of post-functionalization of PEG films and nanosheets, relying on the reaction of a specific functional group or a receptor with the non-reacted amine or epoxy moieties. A possible solution is then a deviation from the standard mixing ratio, setting a certain amount of amine or epoxy groups free and capable of further reactions. At the same time, such a deviation can change the other parameters of the films and nanosheets, including their elasticity. In this context, I studied the respective effect varying the STAR-NH_2/STAR-EPX ratio to some extent, viz. as 1:2 and 2:1, and comparing the results with the reference nanosheet having the standard, most optimal composition (1:1). The respective Δp vs h plots are shown in Figure 4.33. For all three compositions, the experimental points exhibit nearly linear behavior, but the slope of the straight lines tracing this behavior for the both non-optimal compositions (1:2 and 2:1) is different from that for the optimal composition. This suggests different residual stress values in these films (see eq 2.6), which is most likely accompanied by the different Young's moduli. Indeed, the E values, calculated from the strain/stress relation (eq 2.7), are 4.11 MPa for the 2:1 ratio and 4.67 MPa for the 1:2 ratio, differing from the reference value of 2.41 MPa for the 1:1 ratio. Interestingly, nearly the same increase of E occurs both at the excess of STAR-NH_2 and at the excess of STAR-EPX. This makes sense since a distortion of the PEG network should be similar in both cases, with some of the PEG arms not participating in the crosslinking but staying loose. These arms cannot then participate in the stress-induced stretching of the matrix, which reduces its overall elasticity.

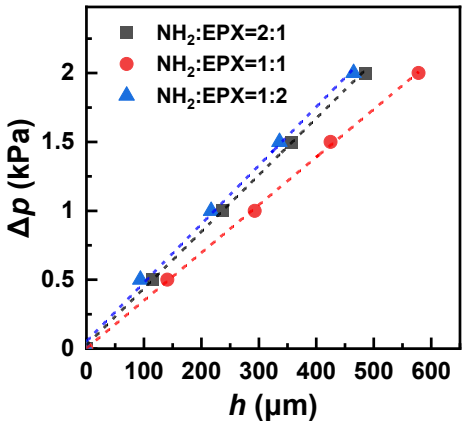

Figure 4.33. Δp vs h plots for the PEG nanosheets prepared at the different mixing ratios of the STAR-NH_2 and STAR-EPX precursors (see the legend); a nearly linear dependence is tentatively traced by the straight lines. The thicknesses of the nanosheets were close to 100 nm. The window diameter was 1 mm.

4.3.6. Effect of electron irradiation

Exposure of the PEG films to electrons results in partial desorption of the PEG material and transformation of at least a part of the residual film into carbon-enriched and oxygen-depleted matrix.[31] The respective changes, following first-order kinetics,[31] can be readily monitored by XPS. The XPS spectra of the pristine PEG nanosheet in Figure 4.34 show the characteristic C 1s and O 1s peaks of the intact PEG moieties at binding energies (BEs) of 286.6 eV and 532.8 eV, respectively. The intensity of both these peaks decreases progressively in the course of electron irradiation and a new peak at a BE of 284.9 eV, characteristic of carbon-enriched and oxygen-depleted residual matrix appears and increases in intensity. The depletion of oxygen is additionally emphasized by the intensity ratio of the overall C 1s and O 1s signals. If we set this ratio to 1.0 for the pristine film, the values for the irradiated film will be 1.46 (6 mC/cm^2) and 1.81 (40 mC/cm^2). The partial desorption of the PEG material is emphasized by the thickness reduction, which decreases from 86 nm to 81 nm (6 mC/cm^2) and further to 77 nm (40 mC/cm^2).

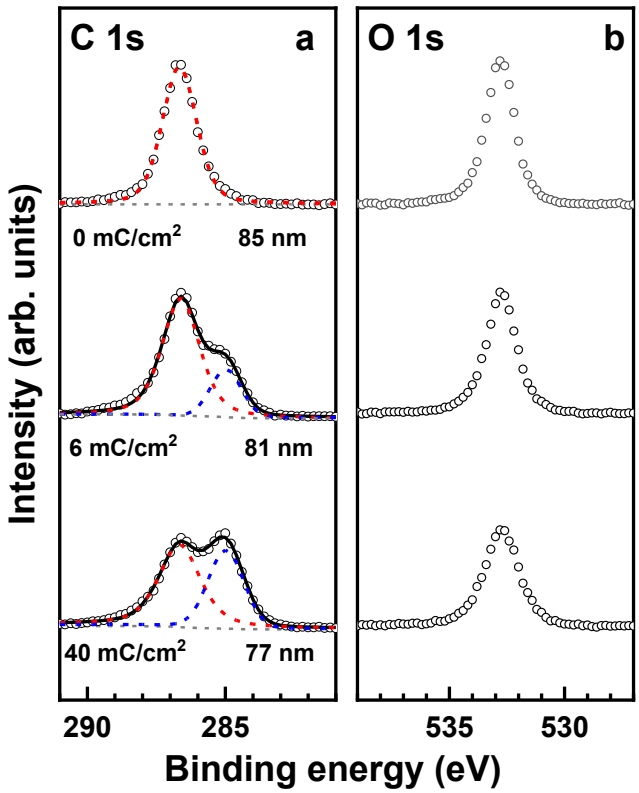

Figure 4.34. C 1s (a) and O 1s (b) XPS spectra of the pristine and irradiated PEG films (open circles). The dose and thickness are given at the respective spectra. The C 1s spectra are decomposed into the components related to the pristine (red dashed line) and modified (blue

dashed line) ether groups in the PEG film. The sum of these components for the irradiated films is drawn by the black solid line.

Note that XPS probes only the topmost part of the PEG films, within the effective sampling depth which is generally given by 3λ, where λ is the attenuation length of the photoelectrons depending on their kinetic energy.[84] For the PEG films and given excitation energy, the latter parameter was estimated at 3.9 nm (C 1s) and 3.3 nm (O 1s),[27] which gives the sampling depth of 10–12 nm. This is noticeably less than the thickness of the PEG films, so that it is not clear whether the electron-induced modification encloses the entire film or only a part of it. But, in any case, the extent of modification is significant, which can be reflected in elastic properties of the respective nanosheets.

These properties are illustrated in Figure 4.35. The Δp vs h plots for the pristine and irradiated nanosheets are presented in Figure 4.35a. For all three samples, the experimental points exhibit nearly linear behavior, but the slope of the straight lines tracing this behavior varies with the dose, suggesting different residual stress values. Another parameter, which varies significantly over the series, is the maximal applied pressure before the nanosheet breaking. As shown in Figure 4.35b, this pressure decreases noticeably with irradiation dose, manifesting progressive diminishing of the nanosheet stability. The Young's moduli, calculated from the strain/stress relation (eq 2.7), show a strong dependence on the dose as well (Figure 4.35c), with an increase by a factor of ~3.2 at 6 mC/cm^2 and by a factor of 7.4 at 40 mC/cm^2. This suggests a tremendous loss in elasticity upon electron irradiation.

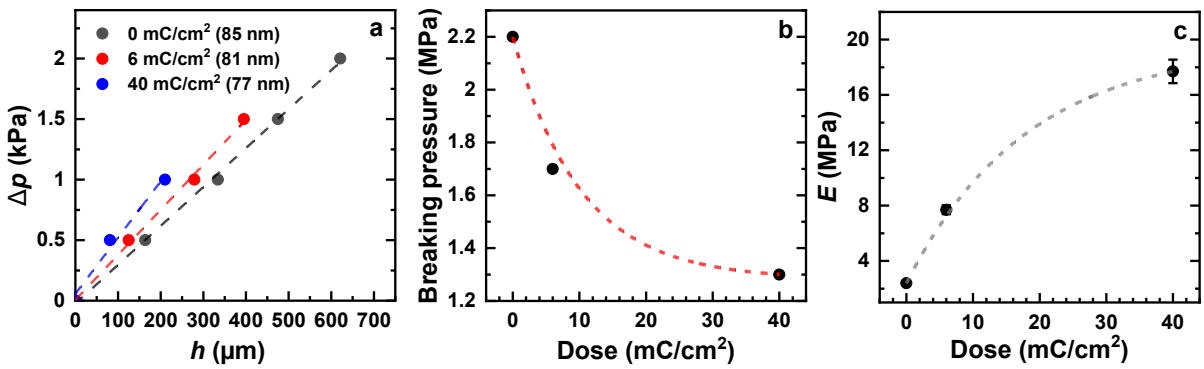

Figure 4.35. (a) Δp vs h plots for the pristine and irradiated (electrons) PEG nanosheets (see the legend giving also the thickness value); a nearly linear dependence is tentatively traced by the straight lines. (b) The pressure corresponding to the breaking of these nanosheets as a

function of irradiation dose. (c) Young's modulus of these nanosheets as a function of irradiation dose. The window diameter was 1 mm.

This loss is, however, understandable, assuming that the elastomer-like PEG network (Figure 3.1) transforms into an oxygen-depleted carbonaceous matrix with extensively cleaved PEG arms which cannot be overstretched any more. In addition, the residuals of these arms are capable to create additional crosslinks in the network, limiting further its elasticity. Such a tentative mechanism behind the decrease in elasticity agrees well with the earlier reported, progressive loss of hydrogel properties of the PEG films upon electron irradiation.[31] Note also that irradiation-induced crosslinking of aliphatic molecular assemblies is a well-known phenomenon, occurring complementary to the breaking of bonds.[52,160]

4.3.7. Effect of UV light

In contrast to electron irradiation, the exposure of the PEG films to UV light does not result in their modification but only in a partial loss of material, as discussed in section 4.1. The mechanism behind the respective decomposition of the PEG network, which follows zero-order kinetics, is however still unclear. Interestingly, the exposure of closely related, PEG-substituted SAMs to UV light results in the same effect as their exposure to electrons, viz. a decomposition of the PEG moieties and their chemical modification, accompanied by depletion of oxygen.[114,123,134] The most likely mechanism behind this behavior in the UV case is the effect of so-called "hot" electrons originating from the substrate. On the first sight, no photoelectrons and secondary electrons from the substrate can reach molecular adsorbates since their energy at the given wavelength of the UV light is lower than the work function of the substrate. However, these electrons, termed then as "hot", can tunnel into empty states at the substrate-adsorbate interface over the work function barrier.[145–148] Even though the penetration depth of these electrons into an organic film is limited, it is most likely sufficient to affect the entire SAM, which is just few nanometers thick.

Taking this model into account, one can reasonably assume that the modification of the PEG films by UV light is also mediated by "hot" electrons. This process will then exclusively involve the region close to the buried PEG/substrate interface, within the penetration depth of "hot" electrons, and be not traceable by any technique applied to the outer (ambient) side of the PEG film. The elastic properties of the respective PEG nanosheets should, however, be changed significantly, since the exposure of their "bottom" side to the "hot" electrons will most likely have a similar effect on the elastic properties as that described in the previous section.

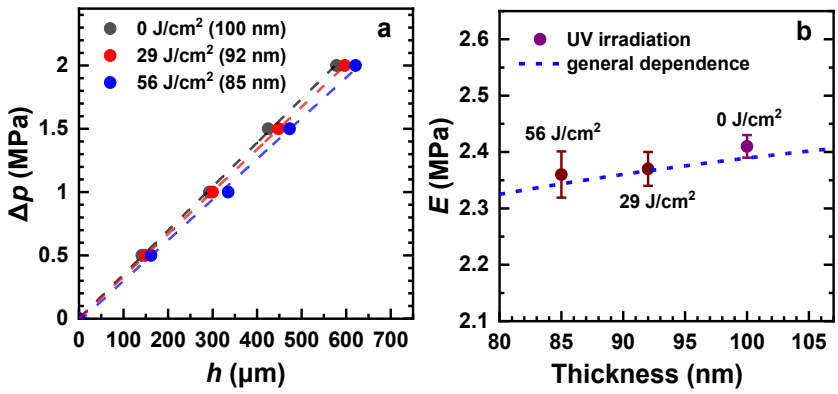

Figure 4.36. (a) Δp vs h plots for the pristine and irradiated (UV light) PEG nanosheets (see the legend); a nearly linear dependence is tentatively traced by the straight lines. (b) Young's modulus of these nanosheets as a function of the nanosheet thickness; the UV doses are marked; the blue dashed line represents the general E–t dependence for the pristine nanosheets (Figure 4.32). The window diameter was 1 mm.

Representative Δp vs h plots for the pristine and exposed-to-UV-light PEG nanosheets are shown in Figure 4.36a; the decrease in the nanosheet thickness, given in the legend, manifests the expected effect of UV light.[157] The experimental points for all the samples lie quite close to each other, which suggests a similarity of the elastic properties. Indeed, the Young's moduli of these nanosheets, calculated on the basis of the strain/stress relation (eq 2.7), do not show much variation (Figure 4.36b). Most importantly, in contrast to the electron irradiation series (Figure 4.35c), the E value does not increase but decreases in the course of the irradiation treatment. Moreover, this decrease correlates perfectly with the general dependence of the Young's modulus on the nanosheet thickness (Figure 4.32), as illustrated in Figure 4.36b. Thus, the elastic properties of the nanosheets exposed to UV light are identical to those of the pristine nanosheets with the same thickness, which exclude their partial modification by "hot" electrons. A further evidence for the lack of such a modification is provided by XPS, using the films and nanosheets on Au substrate for direct comparison with the data in section 4.1. According to these data and as shown in Figure 4.37, the characteristic XPS spectra of pristine and exposed-to-UV-light PEG films are nearly identical, suggesting a lack of UV-induced chemical modification. These spectra are however representative of the topmost 10–12 nm of the PEG films and do not contain any information about possible chemical processes at the buried PEG-substrate interface. This interface could, however, be directly accessed by the separation of the UV-treated film from the substrate and its placement onto the secondary substrate upside down, i.e. with the substrate side exposed to the XPS spectrometer. The respective spectra in Figure

37 are very similar to those of the opposite side and are distinctly different from the spectra of the films exposed to electrons (Figure 4.34). The low-intensity shoulders at the high BE and low BE sides of the C 1s peak in Figure 4.37 stem most likely from contamination on the surface of the substrate, sticking to the PEG film during its formation.

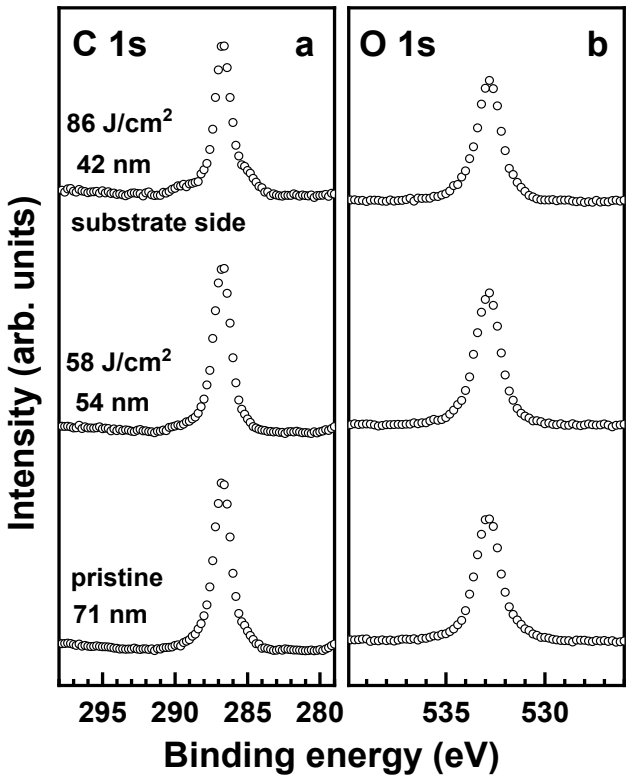

Figure 4.37. C 1s (a) and O 1s (b) XPS spectra of the pristine and irradiated (UV light) PEG films deposited on Au substrate. The dose and thickness are given at the respective spectra. The bottom and middle spectra, are identical to the spectra in Figure 4.5, correspond to the top side of the film facing the ambient, whereas the top spectra represent the side of the film facing the substrate. The irradiated film was turned around for the latter measurement.

The hypothesis of "hot" electrons can thus be fully excluded as the mechanism behind the decomposition of the PEG films and nanosheets by UV light. One can however ask why this effect is likely of importance for OEG-substituted SAMs and of no impact for the PEG films. A possible explanation can be the difference in the electronic coupling to the substrate for these two kinds of systems. The SAMs couple strongly to the substrate,[161] relying on the chemical bond between the anchoring group of the SAM-forming molecules and the substrate.[80] Consequently, tunneling of "hot" electrons between the respective, strongly coupled electronic systems is likely possible, as far as empty states at the molecular side of the interface are

available. In contrast, the coupling between the PEG film and the substrate can in the best case be described as physisorption, so that the electronic systems are weakly coupled (if at all) and the tunneling is hardly possible. Thus, one is only left with a direct effect of UV irradiation on the PEG films and nanosheets promoting the fragmentation of the PEG chains in contrast to their chemical modification, such as depletion of oxygen and chemical transformation.

4.4. Rational design of amine-rich PEG films as matrixes for ssDNA immobilization and hybridization

4.4.1. Motivation

The immobilization of ssDNA on solid supports is an important issue in physical chemistry of interfaces and biomedical research. To achieve a high hybridization efficiency and to form individual sensing spots, it is frequently necessary to immobilize ssDNA into a biocompatible matrix resisting non-specific ssDNA-surface interactions.[36–38] By this way one can control the density of the immobilized probe ssDNA and suppress non-specific adsorption of target ssDNA beyond the predefined sensing spots, improving thus the specificity and efficiency of a particular assembly or a device. In this context, PEG is frequently used and a good candidate.

The previous studies in our group demonstrated that the PEG films can serve as a bioinert matrix which can be decorated with proteins, subsequently used for specific biosensing, relying on the well-known biotin-avidin key-lock affinity.[30] With this achievement in mind, it was interesting and promising to explore whether such a strategy is also suitable for the immobilization and hybridization of ssDNA, which was the subject of this particular subproject. For this purpose, I used the STAR-NH_2 and STAR-EPX precursors with moderate molecular weights (2k), adjusting their mixing ratio to optimize the immobilization efficiency of ssDNA, and applied XPS and complementary electrochemical techniques to monitor the immobilization and hybridization processes.

4.4.2. Specific experiments and procedures

PEG film fabrication. Two specific kinds of PEG films were prepared in this specific study. They were prepared on SiO_2 passivated Si substrates (see chapter 3 for details). In the first case, the same concentration of the STAR-NH_2 and STAR-EPX precursors in the primary solutions was used (1:1 ratio), set to either 2 mg/mL or 25 mg/mL to get either thin (~15 nm) or thick (~100 nm) films. In the second case, the concentrations of 20 mg/mL for STAR-NH_2 and 10 mg/mL for STAR-EPX were used (2:1 ratio), to obtain PEG films (~80 nm thickness) with a noticeable amount of free NH_2 groups, suitable for the reaction with the NHS ester groups of the substituted homo-oligonucleotides. Note that the NHS esters are reactive groups formed by carbodiimide-activation of carboxylate molecules. NHS-ester-labeled compounds react with primary amines under physiologic to slightly alkaline conditions (pH 7.2 to 9) to yield stable amide bonds after the release of the NHS group.[162] For the sake of brevity, I will refer to these systems further in the manuscript as the 1:1 and 2:1 films, respectively. The 2:1 PEG films

were also fabricated on evaporated Au(111) substrates (30 nm Au on Si(100), 5nm Ti interlayer) – specifically for electrochemical measurements.

ssDNA immobilization and hybridization. The procedures are schematically illustrated in Figure 4.38. For ssDNA immobilization, PEG films were immersed into 1M $CaCl_2$-TE buffer (10 mM Tris-HCl and 1 mM EDTA, pH=7.4) containing 10 μM of ssDNA for 40 h at 37 °C. Note that the 1M $CaCl_2$-TE buffer was supplanted by PBS buffer (pH=7.4) in the NHS-T5 and NHS-T10 cases to avoid reaction between the NHS ester group of ssDNA and the NH_2 group of Tris-HCl. After the incubation, the samples were rinsed with Milli-Q water for 1 min and dried under N_2 flow. For hybridization tests, the samples were immersed in a 1 M NaCl buffer containing 10 μM of target sequences for 8 h at room temperature. After incubation, the samples were rinsed with 1 M NaCl buffer for 1 min, briefly dipped in a small amount of Milli-Q water (~0.5 mL) to remove excess salts, and finally dried with N_2.

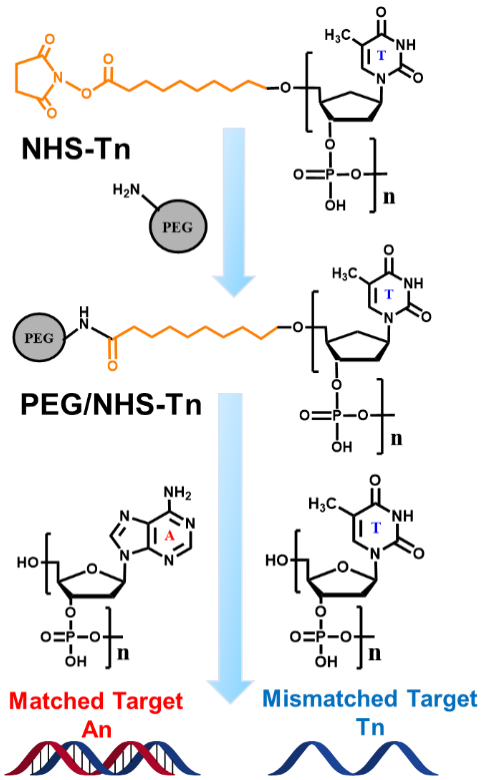

Figure 4.38. The structures of the NHS-Tn, An, and Tn compounds as well as a schematic illustration of the NHS-Tn immobilization in the PEG matrix (shown schematically as a gray circle) over the free (non-reacted) NH_2 groups and its subsequent reaction with the An and Tn targets.

4.4.3. XPS

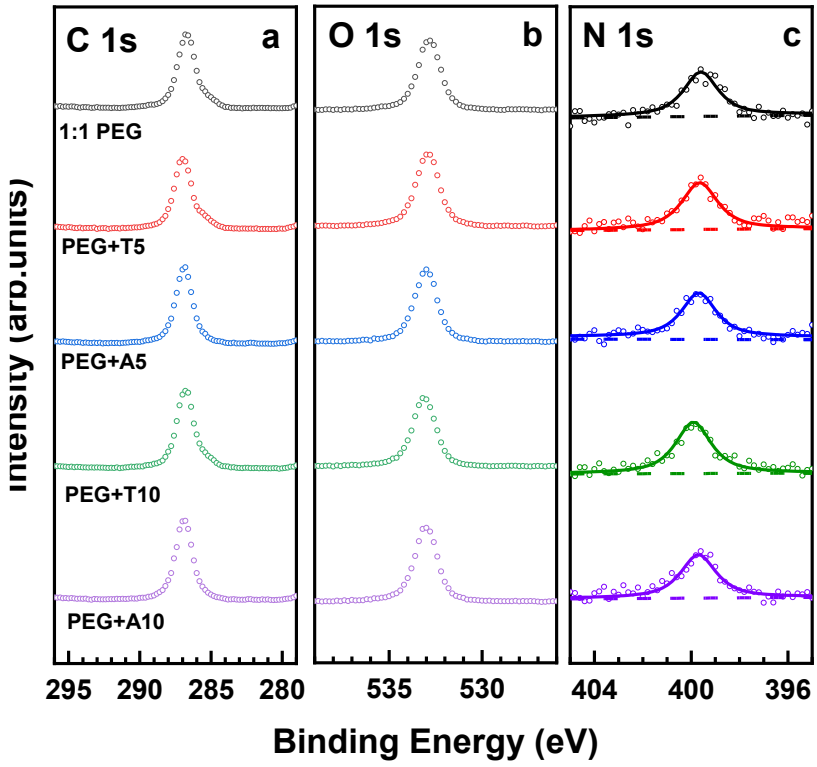

Figure 4.39. C 1s (a), O 1s (b) and N 1s (c) XPS spectra of 1:1 PEG films before (top curves) and after their incubation into the T5, A5, T10 and A10 solutions.

The monitoring of the relevant properties and processes within the given study relied on the well-known XPS spectra of pristine PEG films and thymine and adenine homo-oligonucleotides. In accordance with the chemical composition, the PEG films exhibit the characteristic singular peaks at BEs of 286.8 eV (C 1s), 532.8 eV (O 1s), and 399.6 eV (N 1s), as shown in Figures 4.39 and 4.40 for the standard 1:1 case. As discussed in previous subchapters, the first two peaks are related to the PEG arms of the network and the third peak is representative of the nitrogen atoms in the ethanol–amine bridges. The homo-oligonucleotides can be best traced by the N 1s and P 2p spectra, representative of the nucleobases and phosphate groups in the ssDNA backbone, respectively. The P 2p spectra, showing usually a merged P $2p_{3/2,1/2}$ doublet at a BE of 133.5–133.7 eV, are not nucleobase-specific, but are a suitable fingerprint for the presence of ssDNA in the PEG matrix, which originally contains no phosphorus. The N 1s spectra are nucleobase-specific, which not only allows to monitor the presence of ssDNA but also to distinguish between thymine and adenine homo-oligonucleotides. In the case of thymine, the spectrum exhibits a single peak at a BE of

~400.5 eV, sometimes accompanied by a weak shoulder at a BE of ~398.5 eV associated with thymine moieties which are in direct contact with the substrate.[64,163,167,168] In the case of adenine, the spectrum consists of two peaks at BEs of ~398.7 and ~400.5 eV with the characteristic intensity ratio of 2:1.[64,163,168] Significantly, the positions of these characteristic features do not change noticeably upon the T–A hybridization.[168–170]

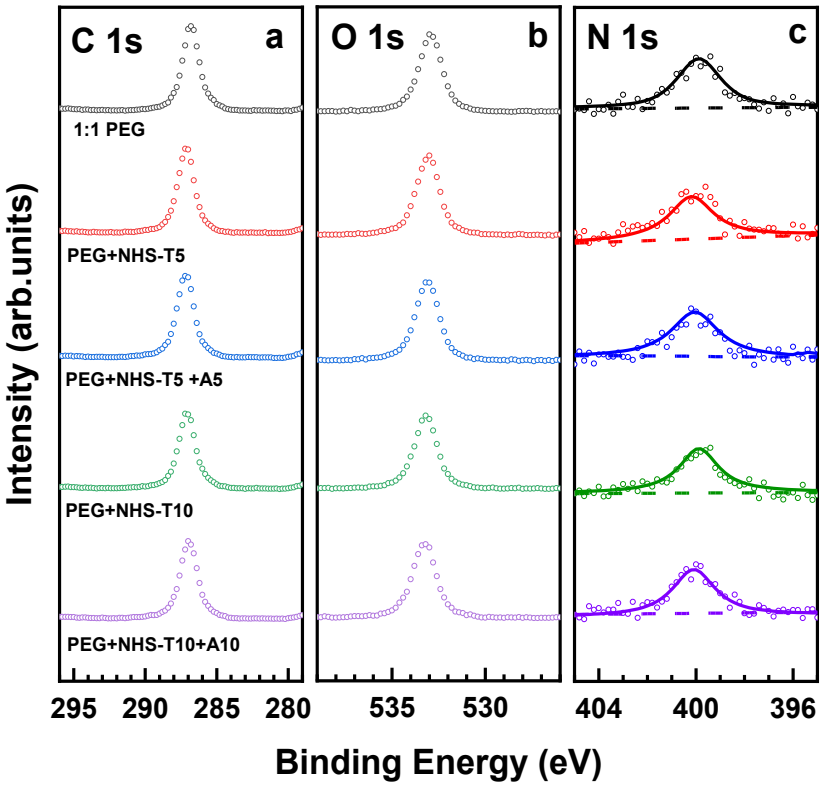

Figure 4.40. C 1s (a), O 1s (b), and N 1s XPS spectra of 1:1 PEG films before (top curves) and after their incubation into the T5 and T10 solutions, and the corresponding films after once more incubation into matching target ssDNA solutions (A5 and A10)

The PEG films are expected to be inert to ssDNA strands, similar to their behavior with respect to proteins, as demonstrated in chapters 4.1 and 4.2. To verify this assumption, 1:1 films were exposed to the unmodified ssDNA strands, viz. Tn and An (n = 5 and 10), and characterized by XPS. The respective C 1s, O 1s and N 1s XPS spectra were found to be identical (within the experimental accuracy) to those of the original films (Figure 4.40), which demonstrates that the PEG films with the optimal mixing ratio of the precursors are indeed bioinert.

These films contain, however, only a small amount of free amine groups (~3% according to our estimate, based on the infrared spectroscopy data from ref [27]), which can be insufficient for

an effective immobilization of the NHS-ssDNA. Consequently, decoration of ssDNA strands with NHS ester should be a reasonable strategy to immobilize these strands into the PEG matrix over the NH_2 groups which did not participate in the crosslinking reaction and retained their reactivity.

Indeed, after the exposure of the 1:1 PEG films to NHS-T5 and NHS-T10, no noticeable changes could be observed in the XPS spectra of the samples (Figure 4.40), indicating a very small (if at all) degree of immobilization. As an additional proof, these samples were subsequently exposed to the target ssDNA strands complementary to T5 and T10, viz. A5 and A10, and characterized by XPS. Again, the spectra remained unchanged (Figure 4.40), which fully exclude that the probe T5 and T10 strands, capable to hybridize with A5 and A10, were present in the PEG matrix.

The above results suggest that the 1:1 PEG films are not suitable for the immobilization of NHS-ester-modified ssDNA. A promising solution can then be a deviation from the 1:1 mixing ratio, resulting in a non-negligible amount of free amine groups, capable to react with the NHS ester moieties of the NHS-ssDNA. To verify this hypothesis, the STAR-NH_2/STAR-EPX mixing ratio was set to 2:1 and 2:1 PEG films were prepared. The XPS spectra of the 2:1 PEG films were found to be nearly identical to those of the 1:1 prototypes, with the characteristic C 1s, O 1s, and N 1s peaks at BEs of 286.8 eV, 532.8 eV, and 399.6 eV, respectively (Figure 4.41). The presence of only one N 1s peak in these spectra means that both crosslinked and free amine groups have the same XPS binding energy. This circumstance simplifies the analysis of the spectra but make it difficult to provide an estimate for the amount of free amine groups.

As the next step, bioinert properties of the 2:1 PEG films were tested. For this purpose, these films were exposed to A10 and T10 and characterized afterwards by XPS, relying on the characteristic C 1s, O 1s, and N 1s spectra. The respective data are presented in Figure 4.41. The spectra of the films exposed to A10 and T10 turned out to be identical (within the experimental accuracy) to those of the original films, which means that a moderate deviation from the optimal mixing ratio does not result in a deterioration of bioinert properties. Thus, the 2:1 films can readily serve as a bioinert matrix for immobilization of probe ssDNA strands and subsequent hybridization with the target ssDNA strands, as far as immobilization and hybridization can be performed.

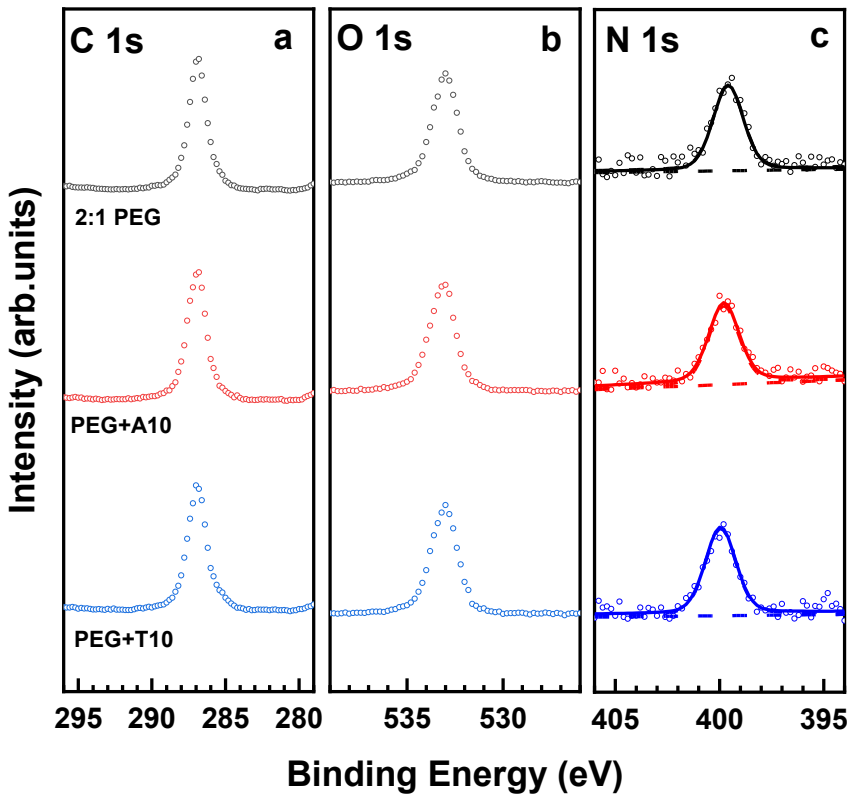

Figure 4.41. C 1s (a), O 1s (b), and N 1s (c) XPS spectra of the 2:1 PEG films before (top curves) and after their incubation into the A10 and T10 solutions. The N 1s spectra are tentatively fitted by a single peak (solid lines) and a background (dashed lines).

Both these processes turned out to be indeed possible. The immobilization of the probe ssDNA strands (T5 and T10) was carried out with the help of NHS-T5 and NHS-T10, relying on the reaction between the NHS ester group of the latter moieties and the free amine groups in the PEG films. The process was monitored by XPS, relying on the C 1s, N 1s and P 2p spectra. The respective data are shown in Figures 4.42 and 4.43 for the NHS-T5 and NHS-T10 case, respectively. Let us first discuss the data for NHS-T5 and later – for NHS-T10.

After the exposure of the 2:1 PEG films to NHS-T5, the C 1s spectrum of the resulting films (PEG/NHS-T5) looks similar to that of the original PEG film, whereas the N 1s and P 2p spectra change noticeably. In the N 1s spectrum, the peak at ~399.8 eV, associated with the PEG matrix, decreases in intensity and becomes accompanied by the characteristic peak of thymine at a BE of ~401.9 eV (see refs [64,163,167,168]). In the P 2p spectrum, a characteristic signature of the phosphate groups in the ssDNA skeleton at a BE of ~133.7 eV is observed.[91,163–166] This joint evidence indicates that the probe T5 strands were successively immobilized into the PEG matrix.

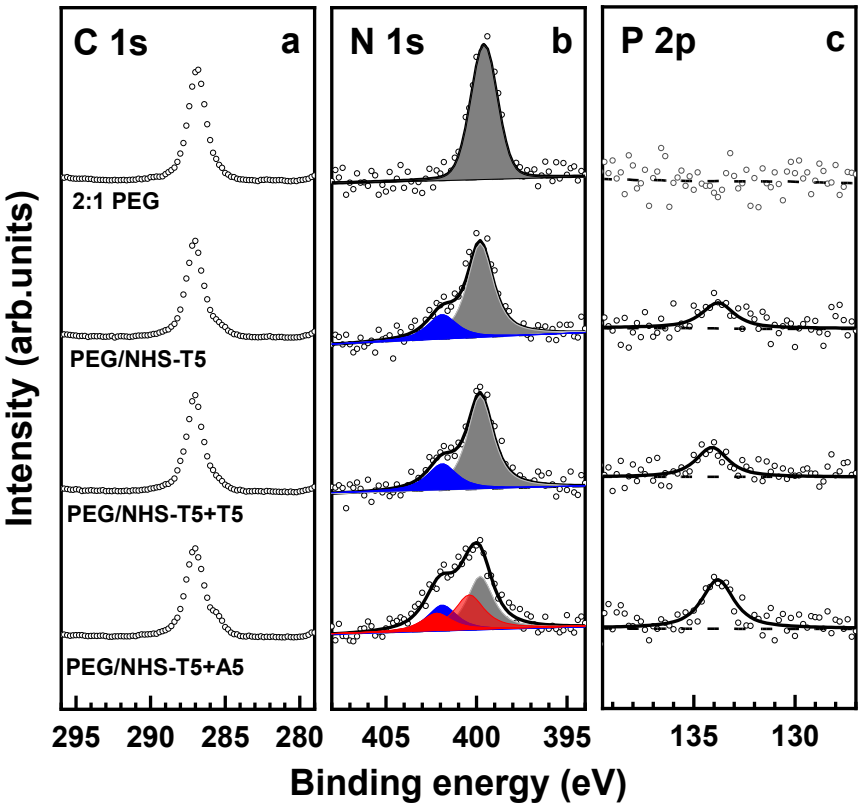

Figure 4.42. C 1s (a), N 1s (b), and P 2p (c) XPS spectra of the original 2:1 PEG film, PEG film exposed to NHS-T5 (PEG/NHS-T5), and PEG/NHS-T5 probe film exposed to mismatching (T5) and matching (A5) target ssDNA. The N 1s spectra are decomposed into individual contributions related to the amine groups in the PEG matrix (dark gray), thymine (blue), and adenine (red). The P 2p spectra are tentatively fitted by a single peak (solid lines) and a linear background (dashed lines).

Next, the ability of the T5-functionalized PEG films to probe a complimentary target ssDNA (A5) was tested by their incubation into A5 solution and subsequently characterized by XPS. Once again, the C 1s spectrum, representing predominantly the PEG matrix, did not change noticeably, whereas the N 1s and P 2p XPS spectra, representing the ssDNA species, showed pronounced changes. In the P 2p spectrum, an increase in the intensity of the characteristic phosphate feature by a factor of ~1.78 is observed, corresponding to a high extent of hybridization (~78%). In the N 1s spectrum, the shoulder at ~401.9 eV increases in intensity and becomes comparable to the main peak. Assuming that this increase stems from the T5–A5 hybridization, the spectrum was decomposed in three components associated with the NH_2 and NH groups in the PEG matrix, thymine, and adenine, with the PEG matrix represented by a

single peak at the BE of ~399.8 eV, thymine – by a single peak at 401.9 eV, and adenine – by two peaks at ~400.4 eV and ~402.2 eV with an intensity ratio of 2:1. As shown in Figure 4.42, the N 1s spectrum could be fully reproduced by such a combination. The relative weights of the thymine and adenine components corrected for the different contents of the nitrogen atoms in these bases (2 for thymine and 5 for adenine; see Figure 4.38) give then the extent of hybridization, which was estimated at ~80%, in excellent agreement with the P 2p data.

To verify selectivity of the T5-decorated PEG films to specific target, this film was exposed to a mismatching ssDNA sequence (T5) and examined by XPS. As shown in Figure 4.42, the C 1s, N 1s and P 2p XPS spectra of the film taken before and after such an exposure are identical (within the experimental error), which indicates that the hybridization is indeed highly selective.

The data for the immobilization of NHS-T10 into the 2:1 PEG films and the related hybridization tests with the matching (A10) and mismatching (T10) ssDNA sequence are presented in Figure 4.43. The same behavior as in the case of NHS-T5, A5, and T5 is observed (Figure 4.42) but the changes of the XPS spectra upon the immobilization of the probe strands and their hybridization with the matching target are even more pronounced, which is understandable in view of the longer ssDNA chain and, subsequently, a larger spectral weight of the respective fingerprint features. Based on the decomposition of the N 1s spectra, the extent of hybridization was estimated at ~89%, which is even somewhat higher than that for the shorter T5/A5 strands, driven, most likely by a larger energy gain. The ssDNA-backbone-representative P 2p spectra, which show an intensity increase by a factor of ~1.88 upon the specific hybridization (T10–A10), give nearly the same value of the hybridization efficiency, supporting the reliability of the derived value. In contrast, similar to the T5/A5 case, no changes in the XPS spectra were observed after the exposure of the T10-decorated PEG films to a mismatching sequence (T10).

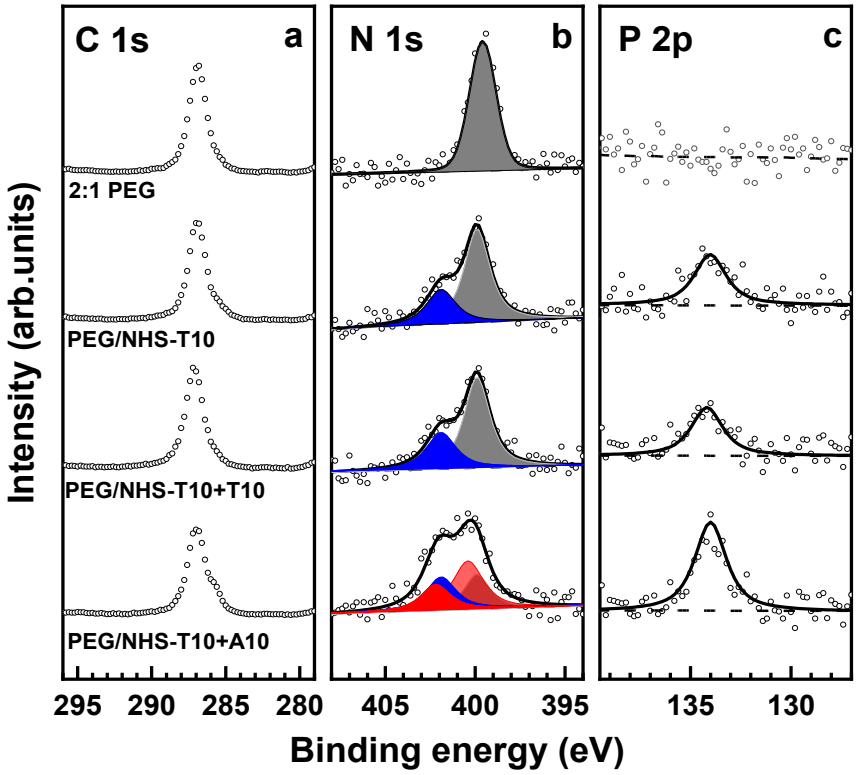

Figure 4.43. C 1s (a), N 1s (b), and P 2p (c) XPS spectra of the original 2:1 PEG film, PEG film exposed to NHS-T10 (PEG/NHS-T10), and PEG/NHS-T10 probe film exposed to mismatching (T10) and matching (A10) target ssDNA. The N 1s spectra are decomposed into individual contributions related to the amine groups in the PEG matrix (dark gray), thymine (blue), and adenine (red). The P 2p spectra are tentatively fitted by a single peak (solid lines) and a linear background (dashed lines).

The XPS data for the T5/A5 and T10/A10 series can also be compared to each other. In particular, both for the T10-decorated PEG films and the films subjected to the specific hybridization, the intensity of the P 2p signal is approximately double with respect to that in the T5/A5 case. This relation suggests a similar amount of the immobilized ssDNA species in the T10/A10 and T5/A5 cases, which indicates that the ssDNA immobilization ability of the 2:1 PEG film does not depend strongly on the length of ssDNA strands but is predominantly determined by the amount of free amine groups. A tentative evaluation of the areal densities of the immobilized T5 and T10 probe strands, performed on the basis of the N 1s XPS spectra and the nitrile-terminated SAM as a reference (see section 3.2.3 for the technical details), gives the areal densities of 3.6×10^{12} strands/cm^2 and 2.7×10^{12} strands/cm^2 for the PEG/NHS-T5 and PEG/NHS-T10 assemblies, respectively. Note, however, that both these values represent coarse estimates only and are most likely somewhat higher in reality since the N 1s

photoemission signal from the quasi-bulk PEG-ssDNA samples is diminished by self-attenuation, in contrast to the signal from the terminal nitrogen atoms of the reference SAM, which is not affected by the attenuation at all.

The somewhat higher areal density for the PEG/NHS-T5 assembly compared to the PEG/NHS-T10 case is most likely related to a better permeability of the shorted NHS-T5 moieties in the PEG matrix. Nevertheless, the permeability is obviously still good enough for the NHS-T10 species, but can probably become a problem for noticeably longer ssDNA strands. Based on the length of the precursor arms (3.5–4 nm), a 3D PEG mesh with a characteristic pore size of 7–8 nm can be expected, which is of course larger than the cross-sectional dimeter of ssDNA (~2 nm) but is, even for a short strand, much smaller than the ssDNA length, determined by the effective persistence length (~2 nm [171]) and the number of bases.

A related aspect is the behaviour of the C 1s XPS spectra. As was mentioned above and seen in Figures 4.42 and 4.43, these spectra do not exhibit noticeable changed upon the immobilization of the probe T5 and T10 strands into the PEG film, except probably a small decrease in intensity. This means that the signal of the PEG matrix, represented by a single peak at a BE of ~286.6 eV (see above), dominates over the signal of the ssDNA strands, overlapping partly with the PEG feature and represented by several peaks with specific intensity ratios and dominant spectral weight at a BE of 284.6–285.5 eV.[91,172] Consequently and most likely, the immobilization of ssDNA does not involve the entire PEG film but, predominantly, the topmost part of it, occurring in a gradient fashion. Only after the specific hybridization, a small ssDNA-stemming shoulder at the low BE side of the PEG-related C 1s peak is observed.

The permeability of ssDNA in the PEG matrix was additionally studied by exposure of comparably thin (15 nm) 1:1 PEG films to unmodified homo-oligonucleotides, T10 and A10. As demonstrated above, both 1:1 and 2:1 PEG films are generally inert to these biomolecules, so that any traces of T10 and A10 found in the spectra will most likely represent the strands penetrated through the film and adsorbed at the film-substrate interface, driven by their affinity to the non-bioinert Si/SiO_2 substrate. Indeed, such traces could be found in the XPS spectra of both PEG/T10 and PEG/A10 (Figure 4.44), suggesting that the permeability depth of these strand into the PEG film is at least 15 nm.

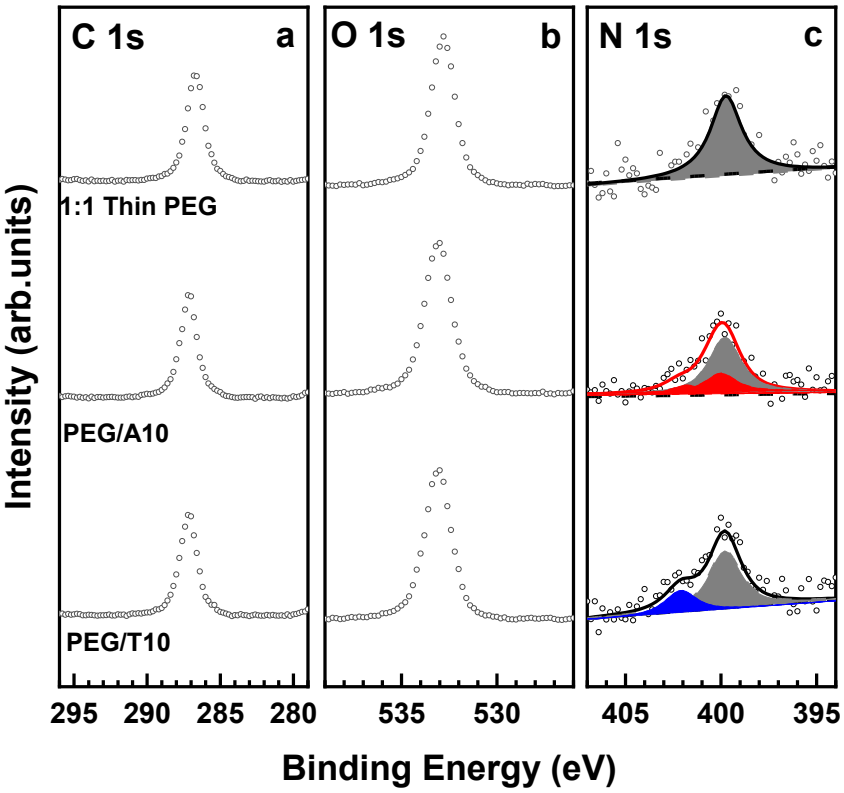

Figure 4.44. C 1s (a), O 1s (b), and N 1s XPS spectra of the ultrathin 1:1 PEG film (15 nm) before and after their incubation into the A10 and T10 solutions. The N 1s spectra are decomposed into individual contributions related to the amine groups in the PEG matrix (dark gray), thymine (blue), and adenine (red).

The affinity of the Si/SiO_2 substrates to the ssDNA was additionally verified by their exposure to T10 and A10. The resulting XPS spectra in Figure 4.45 show a noticeable increase in the intensity of the C 1s signal and appearance of the N 1s signal, which both indicate the adsorption of T10 and A10 onto the substrate. The C 1s spectra of both adsorbed ssDNA strands represent a single peak at a BE of 285.7–285.8 eV, accompanied by a weak high energy shoulder. Such spectra should indeed overlap significantly with the C 1s spectrum of the original PEG film, so that detection of ssDNA immobilization and hybridization on the basis of the C 1s XPS spectra is hardly possible.

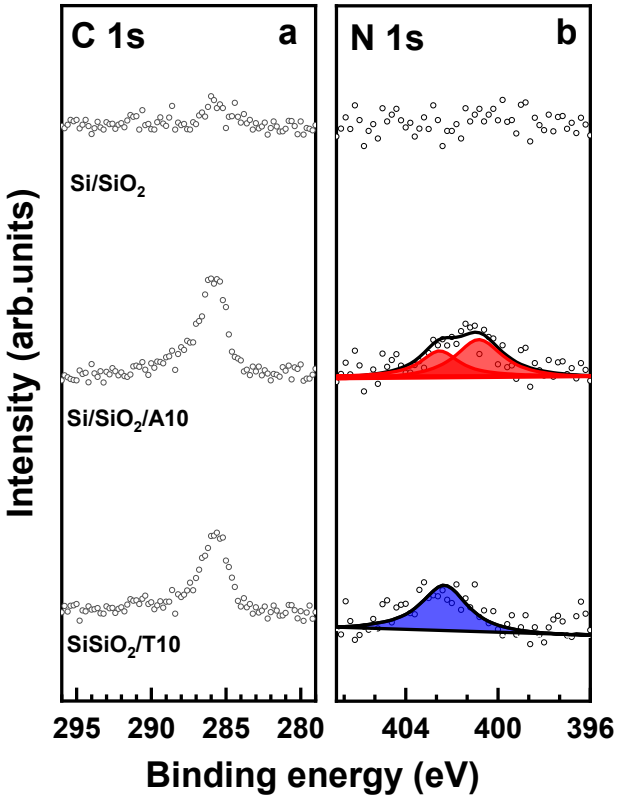

Figure 4.45. C 1s (a) and N1s (b) XPS spectra of the Si/SiO_2 substrate before and after their incubation into the A10 and T10 solutions. The N 1s spectra are decomposed into individual contributions related to thymine (blue), and adenine (red).

4.4.4. Electrochemical studies

The immobilization of the ssDNA into the PEG matrix and hybridization ability of the resulting assemblies were also monitored by electrochemical measurements, which were carried out for the 2:1 films only. These films were specifically fabricated on Au substrates serving as the working electrode in the electrochemical cell. The recorded cyclic voltammograms (CVs) provided then as a measure of the electrochemical passivating ability of the PEG films (Au/PEG) and PEG/ssDNA assemblies (Au/PEG/ssDNA) towards the $[Fe(CN)_6]^{3-/4-}$ redox couple in the electrolyte solution. In contrast, the EIS analysis provided an information on the R_{ct} of the electrochemical cell.

As the first step, electrochemical passivating ability and bioinertness of the PEG films were tested. The respective data are shown in Figure 4.46. According to the CVs (Figure 4.46a) and the data in Table 4.1, in which the numerical results of the electrochemical measurements are summarized, the presence of a ~80 nm PEG film on the Au electrode results in just a moderate suppression of the redox current and in just 33% decrease of the electrochemical capacitance,

which is proportional to the area encircled by the respective CV.[173] Such a moderate reduction is related to the porous structure of this film,[27,157] which is favorable for the efficient diffusion of the $[Fe(CN)_6]^{3-/4-}$ species towards the Au electrode. Also, the R_{ct} value did not changed much after the introduction of the PEG film, increasing from 25 Ω to 40 Ω (Table 4.1), as follows from the Nyquist plots for the Au and Au/PEG samples in Figure 4.46b. The diameters of the semicircles in the high frequency region of these plots correspond to the R_{ct} values of the samples.

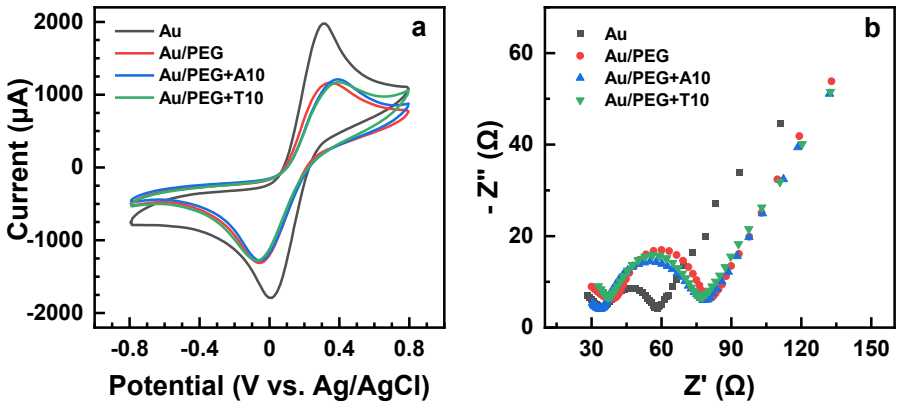

Figure 4.46. CVs (a) and Nyquist plots (b) for the blank Au electrode and Au/PEG electrode before and after its incubation into the non-substituted A10 and T10 solutions.

Table 4.1. Capacitance with respect to the cell with the blank Au working electrode and the charge transfer resistance sssociated with the specific samples.

Sample	Relative Capacitance	Charge Transfer Resistance
Au	100%	25 Ω
Au/PEG	67%	41 Ω
Au/PEG+A10	65%	40 Ω
Au/PEG+T10	65%	43 Ω
Au/PEG/NHS-T5	50%	95 Ω
Au/PEG/NHS-T5+T5	49%	97 Ω
Au/PEG/NHS-T5+A5	32%	195 Ω
Au/PEG/NHS-T10	34%	158 Ω
Au/PEG/NHS-T10+T10	33%	155 Ω
Au/PEG/NHS-T10+A10	19%	330 Ω

Exposure of the PEG films to the non-substituted ssDNA (A10 and T10) resulted in no obvious changes in their CVs (Figure 4.46a) and Nyquist plots (Figure 4.46b), with the nearly identical

values of the relative capacitance and R_{ct} before and after exposure (Table 4.1). This behavior indicates the bioinert character of the 2:1 PEG matrix, in full agreement with the XPS data (see section 4.4.3).

Subsequently, immobilization of NHS-T5 and NHS-T10 into the PEG matrix and the exposure of the resulting PEG-ssDNA films to the matching and non-matching target sequences were conducted, which were monitored by CV and EIS. The respective data are presented in Figures 4.47 and 4.48; the derived values of the relative capacitance and R_{ct} are compiled in Table 4.1. Let us first discuss the data for NHS-T5 and later – for NHS-T10. After the exposure of the Au/PEG to NHS-T5, the redox currents in the electrochemical cell decreased (Figure 4.47a), indicating a higher resistance of the working electrode. This effect is even more obvious in the Nyquist plots (Figure 4.47b), which shows a noticeable increase in the diameter of the semicircle corresponding to an increase in R_{ct} from 41 Ω to 95 Ω (Table 4.1). This increase manifests the immobilization of the probe T5 strands into PEG matrix and is explained by the effect of the negatively charged phosphate groups of the ssDNA, which hinder the $[Fe(CN)_6]^{3-/4-}$ from diffusing to the electrode surface.[174,175]

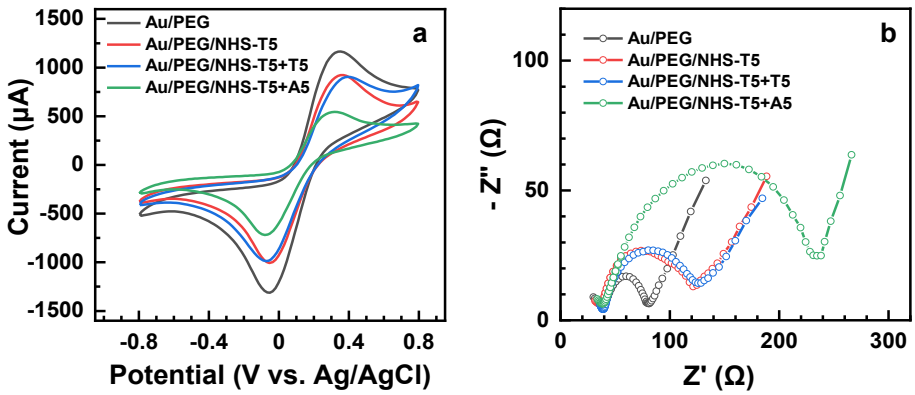

Figure 4.47. CVs (a) and Nyquist plots (b) for the Au/PEG working electrode and the Au/PEG/NHS-T5 electrode before and after its exposure to mismatching (T5) and matching (A5) target ssDNA.

The electrochemical data of the NHS-T10 immobilized Au/PEG electrode (Au/PEG/NHS-T10) and after its exposure to the mismatching (T10) and matching (A10) ssDNA sequences are shown in Figure 4.48. Both the CVs (Figure 4.48a) and the Nyquist plots (Figure 4.48b) exhibit the same behavior as the analogous data for the NHS-T5 case (Figure 4.47), which is also reflected by the relative capacitance and R_{ct} values in Table 4.1. In particular, the relative capacitance of Au/PEG decreased from 67% to 34% after the NHS-T10 exposure, while the

R_{ct} value increased from 41 Ω to 158 Ω, manifesting the NHS-T10 immobilization in the PEG matrix. The exposure of the PEG/NHS-T10 probe to the matching sequence (A10) resulted in a further decrease of the relative capacitance from 34% to 19% and an increase of R_{ct} from 158 Ω to 330 Ω, manifesting a high degree of the hybridization. In contrast, no noticeable changes both in the experimental curves (Figure 4.48) and the derived fingerprint values (Table 4.1) were observed after the exposure of the PEG/NHS-T10 probe to the mismatching sequence (T10), manifesting thus a high selectivity of this probe.

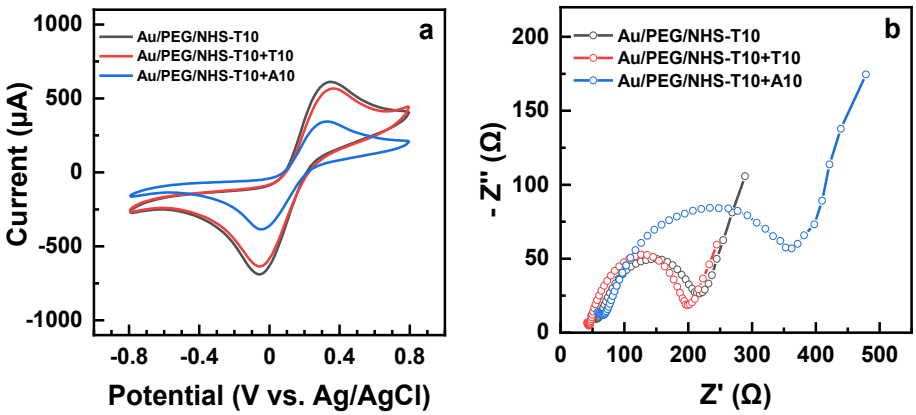

Figure 4.48. CVs (a) and Nyquist plots (b) for the Au/PEG/NHS-T10 working electrode before and after its exposure to mismatching (T10) and matching (A10) target ssDNA.

Comparing the values for the NHS-T5 case with those for the NHS-T10 case in Table 4.1, viz. PEG/NHS-T5 vs PEG/NHS-T10 and PEG/NHS-T5+A5 vs PEG/NHS-T10+A10, we find that both the relative capacitance and R_{ct} do not reproduce exactly the factor of 2 describing the base number difference between T5/A5 and T10/A10. The observed relations can, on the one hand, be affected by the contributions from the PEG matrix and, on the other hand, reflect the somewhat different areal densities of the immobilized T5 and T10 moieties in the matrix.

In contrast, both in the NHS-T5 and NHS-T10 case, the values of R_{ct} increase by a factor close to 2 after the hybridization with the matching A5 and A10 sequences, which means that R_{ct} can be used as a tentative measure for the extent of hybridization. Generally, looking at the data in Figures 4.46–4.48, one can say that the Nyquist plots represent a much clear and distinct way to monitor the immobilization and hybridization processes in the PEG matrix than the CVs. Thus, EIS can be efficiently used as a transduction technique for these processes.

Finally, the sensitivity of this technique in the case of PEG/NHS-T10+A10 was tested. The concentration of A10 was varied from 10 μM (the standard value in this study) to 0.1 μM. The

respective Nyquist plots are presented in Figure 4.49a and the derived values of R_{ct} are shown in Figure 4.49b. Accordingly and as expected, the R_{ct} value decreases progressively with the decreasing A10 concentration. This value is still noticeably higher than the reference value for PEG/NHS-T10 at 0.2 μM and nearly equal to the reference value at 0.1 μM. Consequently, the sensitivity of PEG/NHS-T10 to A10 is down to 0.1–0.2 μM, which can be probably improved even further by increasing the porosity of the PEG matrix and the areal density of the primary T10 probes.

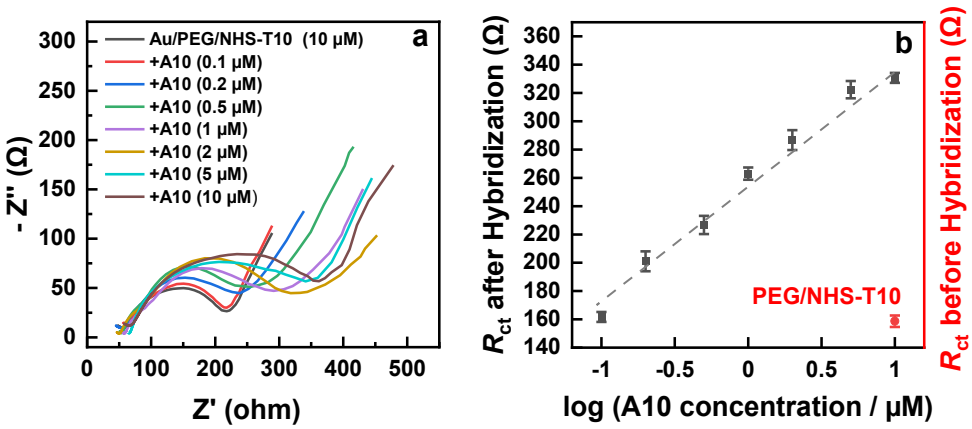

Figure 4.49. Nyquist plots (a) and the derived R_{ct} values (b) for the Au/PEG/NHS-T10 working electrode before (red symbol in b) and after (black symbols in b) its exposure to matching A10 target ssDNA. The concentration of A10 was varied. The R_{ct} behavior in (b) is tentatively traced by straight dashed line.

4.5. Exploiting epoxy-rich PEG films for highly selective ssDNA sensing via electrochemical impedance spectroscopy

4.5.1. Motivation

As demonstrated in chapter 4.4, the probe ssDNA receptor was immobilized into the amine-rich PEG matrix over the amine groups, using N-hydroxy succinimide ester groups as a docking moiety. Alternatively, not amine but epoxy docking sites can be used, providing coupling to thiolated probe ssDNA strands over the established thiol-epoxy click reaction that leads to the formation of a β-hydroxythio-ether linkage.[176,177] This approach, which I introduce in this specific subproject can then potentially provide an alternative to the ´direct´ assembly of thiolated ssDNA on gold substrates. Consequently, for a better comparison, I used the same gold substrate for the PEG films and compared their efficiency with that of the direct ssDNA assembly, both in terms of immobilization of the probe ssDNA and the hybridization ability and selectivity of the resulting DNA sensing platform. As the suitable transduction technique, electrochemical tools were applied, with an emphasis put on electrochemical impedance spectroscopy, which, as expected,[37,178–182] turned out to be particular efficient for the given purpose.

4.5.2. Specific experiments and procedures

PEG film fabrication. PEG films used in this subproject were prepared on Au substrates, the general preparation methods are described in chapter 3. Since the immobilization of the T10-SH probe strands into the PEG matrix relied on the reaction between the thiol and epoxy groups, epoxy-rich PEG films were primarily utilized. For these films, concentrations of 20 mg/mL for STAR-EPX and 10 mg/mL for STAR-NH_2 (2:1 ratio) were employed. Consequently, only a part of the terminal epoxy groups of STAR-EPX was involved into the formation of the crosslinking bridges, whereas the residual part was available for the T10-SH coupling. The thickness of the film was ~65 nm, as measured by ellipsometry (see chapter 3 for details). To test the validity of this approach and exclude the possibility of ssDNA penetration to the underlying Au substrate through the PEG film, equilibrium (EPX:NH_2 = 1:1) and epoxy-poor (EPX:NH_2 = 1:2) films with similar thicknesses were prepared. In the former case, the concentrations of both STAR-NH_2 and STAR-EPX precursors were set as 15 mg/mL, resulting in a film thickness of ~70 nm. In the latter case, the concentrations of 10 mg/mL for STAR-EPX and 20 mg/mL for STAR-NH_2 were utilized, resulting in a film thickness of ~63 nm.

ssDNA immobilization and hybridization. For the ssDNA immobilization, the epoxy-rich (primarily) and reference PEG films and the clean Au substrates were immersed into a 1M $CaCl_2$-TE buffer (10 mM Tris-HCl and 1 mM EDTA, pH=7.4) containing the probe ssDNA at different concentrations (2 μM−10 μM) for 30 h at 37 °C. Subsequently, the samples were rinsed with Milli-Q water for 1 min and dried under N_2 flow. The samples intended for the hybridization process were immersed in a 1M $CaCl_2$-TE buffer containing the target strands for 8 h at room temperature. Following the incubation, the samples were rinsed with a 1 M NaCl buffer for 1 min. They were then briefly dipped into a small amount of Milli-Q water (~0.5 mL) to remove excess salts, and finally dried with N_2.

4.5.3. General procedure and effect of concentration

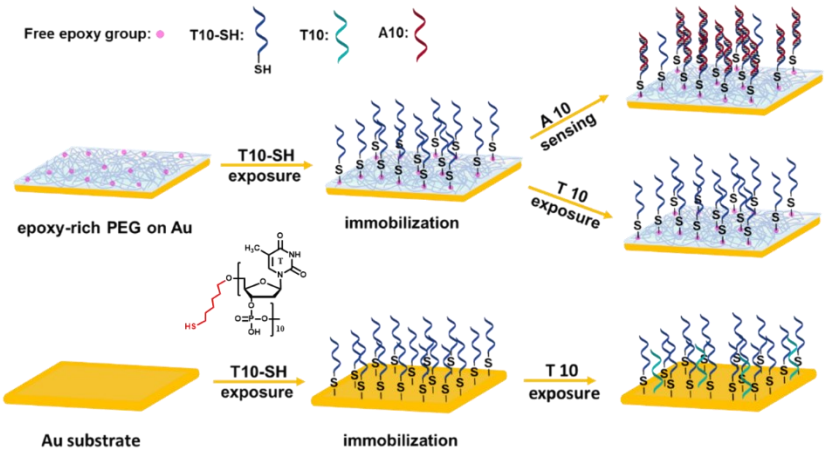

Figure 4.50. Schematic illustration of the immobilization of probe ssDNA (T10-SH) into an epoxy-rich PEG film, followed by the subsequent reaction with matched (A10) and (T10) targets; as well as the immobilization of T10-SH onto a pure Au substrate and its reaction with the mismatched T10.

The experiments are schematically illustrated in Figure 4.50. The PEG films were prepared on the gold substrates. Afterwards, the probe ssDNA (T10-SH) was immobilized into the PEG matrix relying on the thiol-epoxy link. Subsequently, the PEG-ssDNA films were exposed to either the matching A10 strands or reference, mismatching T10 homo-oligonucleotides. For the comparison, the probe T10-SH strands were directly immobilized on the gold substrate, relying on the thiolate–gold bond. Similar to the PEG-ssDNA case, these films were also exposed to A10 (not shown) and T10.

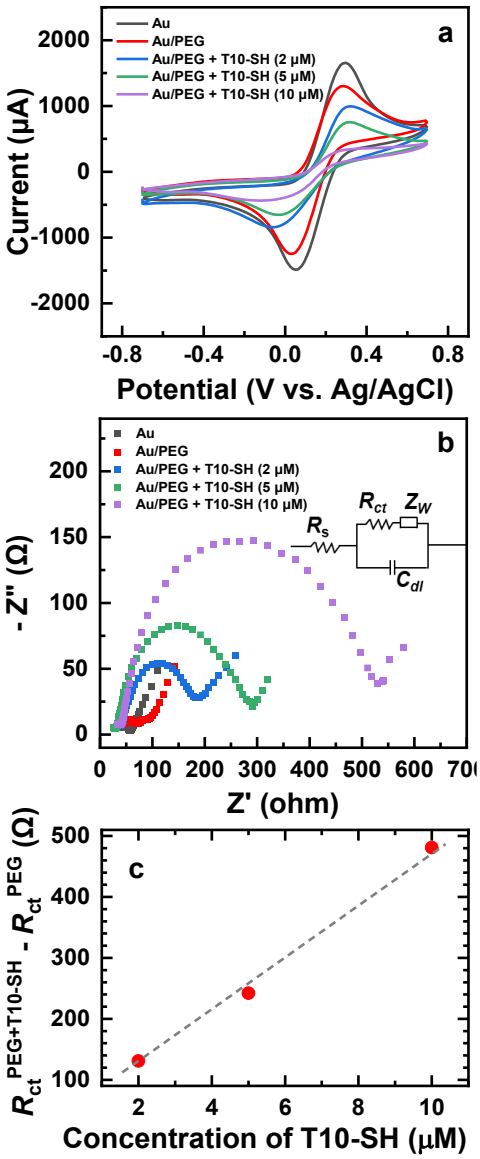

Figure 4.51. CV curves (a) and Nyquist plots (b) for the bare Au electrode and Au/PEG electrode (epoxy-rich film) before and after its incubation into the T10-SH solutions with different concentrations. (c) Dependence of the R_{ct} gain upon the exposure of Au/PEG to T10-SH on the concentration of T10-SH. Equivalent circuit is shown in panel (b).

All steps were monitored by the electrochemical tools. The data for the formation of the PEG film and the immobilization of T10-SH into the epoxy-rich PEG matrix are presented in Figure 4.51. The concentration of T10-SH in the buffer solution was varied. The CV curves displayed in Figure 4.51a reveal that the presence of a ~65 nm PEG film on the Au electrode leads to only a moderate reduction in the redox current. This behavior can be attributed to the porous nature of the film, which effectively mitigates the diffusion hindrance encountered by the $[Fe(CN)_6]^{3-/4-}$ species as they traverse the PEG matrix towards the Au surface. In contrast, the

redox current decreases noticeably upon incubating the Au/PEG electrode into T10-SH solution, with the larger effect at the increasing T10-SH concentration. This behavior suggests efficient immobilization of T10-SH into the PEG matrix, which results in a partial closure or narrowing of the pores, hindering the $[Fe(CN)_6]^{3-/4-}$ diffusion toward the gold electrode. An additional impact is provided by the negatively charged phosphate groups of the ssDNA, which further hinder the diffusion of $[Fe(CN)_6]^{3-/4-}$ to the electrode surface.[174]

The respective EIS data are in complete agreement with the CV results, as in particular can be directly seen from the Nyquist plots displayed in Figure 4.51b. The Nyquist plots can be described by an equivalent circuit, shown in Figure 4.51b, with four elements associated with four different parameters: the charge transfer resistance (R_{ct}), Warburg impedance (R_w), electric double layer capacitance (C_{dl}), and solution resistance (R_s). These plots change only slightly at going from the clean Au substrate to Au/PEG but rather significantly upon incubating the Au/PEG electrode into T10-SH solution, with progressively larger changes at the increasing T10-SH concentration. The respective changes can also be traced quantitatively, using R_{ct} as parameter (Table 4.2). This parameter can be derived from the diameter of the semicircle in the high-frequency region of the Nyquist plots. Accordingly, the R_{ct} value showed only a slight increase upon the introduction of the epoxy-rich PEG film, with an increase from 22 Ω to 31 Ω. When the epoxy-rich PEG film was exposed to T10-SH (2 μM), significant changes were observed in the diameter of its Nyquist plot, corresponding to a higher R_{ct} value of 162 Ω. Moreover, R_{ct} increased even further, in a nearly linear fashion at an increase in the T10-SH concentration (Figure 4.51c), indicating a progressively larger content of the immobilized T10-SH strands in the PEG matrix, without a tendency to the saturation. This behavior demonstrates that the epoxy-rich PEG matrix possesses a sufficient number of available epoxy groups for reacting with thiol-decorated ssDNA strands, so that an even larger amount of these strands than in the 10 μM case can be immobilized if necessary. In any case, by adjusting the concentration of the probe ssDNA in the buffer solution, it is possible to control their efficient packing density in the PEG film and, consequently, the impedance values of the respective DNA sensing platform, serving as a basis for the monitoring of the hybridization. However, to limit the parameter space and to make a better comparison with the reference Au/ssDNA system (see below), we decided to fix the concentration of T10-SH at 2 μM in all further experiments.

Table 4.2. R_{ct} values for Au, Au/PEG, and Au/PEG + T10-SH (variable concentration).

Sample	R_{ct}
Au	22 Ω (±2 Ω)
Au/PEG	31 Ω (±2 Ω)
Au/PEG + T10-SH (2 μM)	162 Ω (±4 Ω)
Au/PEG + T10-SH (5 μM)	273 Ω (±5 Ω)
Au/PEG + T10-SH (10 μM)	512 Ω (±8 Ω)

4.5.4. Validity of the thiol-epoxy linkage

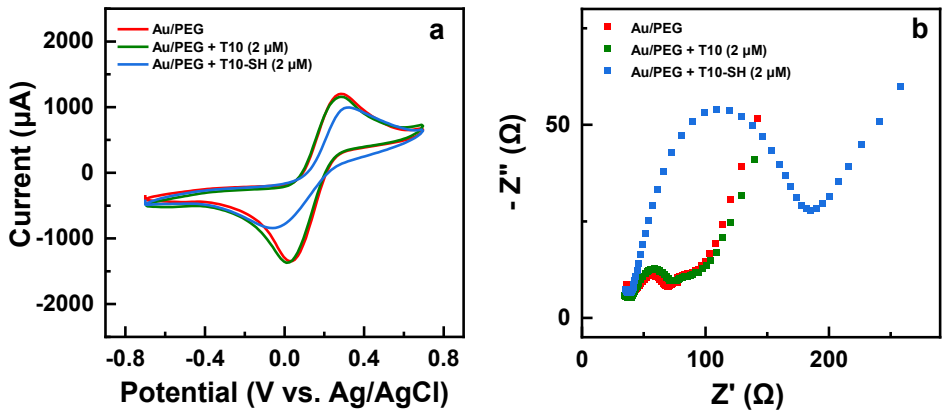

Figure 4.52. CV curves (a) and Nyquist plots (b) for the Au/PEG electrode before and after its exposure into T10 or T10-SH solutions (2 μM).

Assuming that the immobilization of T10-SH occurs exclusively over the thiol-epoxy linkage, we should exclude all other immobilization scenarios, including a coupling of the nucleobase part of T10-SH to the PEG network or its physical trapping in the PEG matrix. To this end, we conducted an experiment involving the exposure of the epoxy-rich PEG film to a solution of T10 (2 μM), lacking the thiol decoration. The resulting CV curve and Nyquist plot are presented in Figure 4.52, along with the corresponding data for the original epoxy-rich PEG film and its exposure to a T10-SH (2 μM) solution, shown once again for comparison. Remarkably, the exposure of the epoxy-rich PEG films to T10 showed no discernible changes in their CV curves

(Figure 4.52a) and Nyquist plots (Figure 4.52b). Also, the R_{ct} values of Au/PEG before and after the T10 exposure remained nearly identical, viz. 31 Ω and 33 Ω, respectively. This behavior is in stark contrast to the changes observed in the T10-SH case, highlighting the specific character of the thiol-epoxy coupling and bioinert nature of the epoxy-rich PEG matrix.

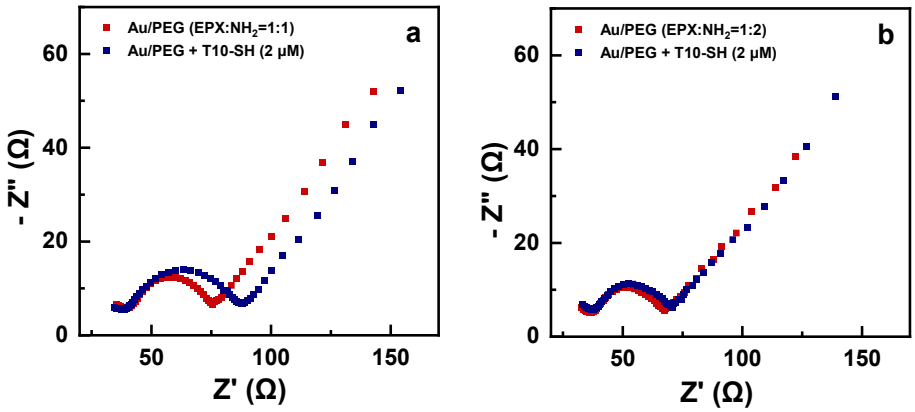

Figure 4.53. Nyquist plots for (a) the Au/equilibrium PEG electrode, and (b) the Au/epoxy-poor PEG electrode before and after their exposure into T10-SH solution (2 μM).

A further possibility which has to be excluded is the diffusion of the T10-SH moieties through the entire PEG film to the Au substrate and their subsequent immobilization at the Au/PEG interface relying on the strong affinity of the thiol groups to gold, including Au(111) in particular. Even though such an option is rather unlikely in view of the significant thickness of the PEG film in our specific case (~65 nm), a specific proof is necessary. To this end, we performed the T10-SH immobilization experiments for the equilibrium (EPX/NH_2 = 1:1) and the epoxy-poor PEG films (EPX:NH_2 = 1:2). The results are presented in Figures 4.53a and 4.53b, respectively. In contrast to the data for the epoxy-rich PEG film (Figure 4.52b), the exposure of the equilibrium (EPX/NH_2 = 1:1) PEG film to T10-SH results in only a small change in the Nyquist plot compared to that for Au/equilibrium PEG (Figure 4.53a), while nearly no change at all was recorded for the epoxy-poor film (Figure 4.53b). The respective R_{ct} values along with σ values are compiled in Table 4.3. Apart from the small differences for the pristine PEG films, associated with the slightly different film thicknesses, the R_{ct} values show a clear trend, with the large increase upon the exposure to T10-SH for the epoxy-rich film, only small increase for the equilibrium film, and nearly no increase for the epoxy-poor film. Since the gold substrate is the common element for all these films and the film thickness did not vary

much across the series, one is only left with the number of active epoxy groups as the reason behind the observed behavior. Consequently and as intended, these groups are responsible for the immobilization of T10-SH in the Au/PEG samples and the penetration of T10-SH to the substrate does not occur at the given film thicknesses.

Table 4.3. R_{ct} values before and after T10-SH exposure for the epoxy-rich, equilibrium, and epoxy-poor PEG films (the film thicknesses are given).

Sample	Thickness	R_{ct} before T10-SH exposure	R_{ct} after T10-SH exposure
Au/PEG (EPX:NH_2=2:1)	~65 nm	31 Ω (±2 Ω)	162 Ω (±4 Ω)
Au/PEG (EPX:NH_2=1:1)	~70 nm	37 Ω (±2 Ω)	51 Ω (±3 Ω)
Au/PEG (EPX:NH_2=1:2)	~63 nm	33 Ω (±2 Ω)	35 Ω (±2 Ω)

4.5.5. Hybridization ability of the ssDNA-loaded PEG film

After the above epoxy–thiol coupling validity tests, the hybridization ability of the PEG + T10-SH film was monitored by its exposure to the mismatching (T10) and matching (A10) target homo-oligonucleotides, which was monitored by CV and EIS. The corresponding data are presented in Figure 4.54 and the R_{ct} values derived from the EIS curves are compiled in Table 4.4. The exposure of the Au/PEG + T10-SH electrode to the mismatching sequence (T10) resulted in minimal changes in the CV profile and the Nyquist plot, leading to only a tiny increase in R_{ct} from 162 Ω to 165 Ω. These observations suggest that the hybridization did not occur for the mismatching sequence and that the T10-SH-loaded PEG matrix maintained its pristine bioinert properties, preventing adsorption or trapping of T10 in the matrix. In contrast, the exposure of the Au/PEG + T10-SH electrode to the matching sequence (A10) resulted in a significant reduction in the redox current (Figure 4.54a), indicating an enhanced resistance at the working electrode. This effect was even more pronounced in the Nyquist plots (Figure 4.54b), which exhibit a noticeably increased diameter of the semicircle, corresponding to an elevation in R_{ct} from 162 Ω to 339 Ω. This behavior demonstrates highly selective and efficient hybridization of the probe T10 and target A10.

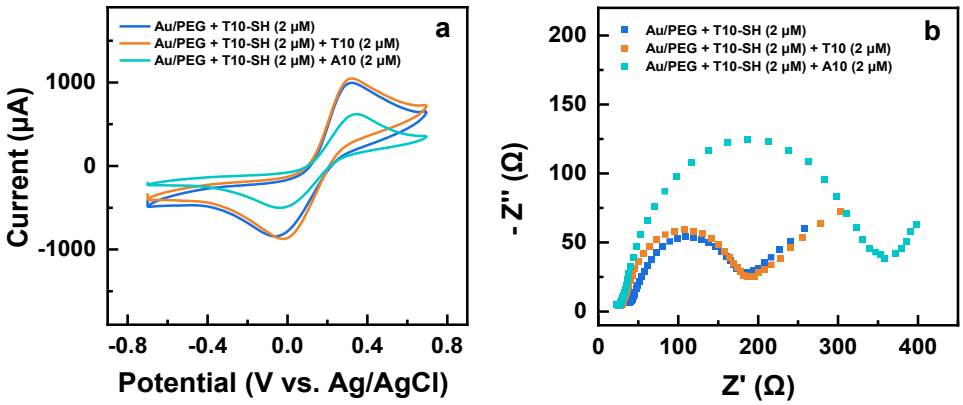

Figure 4.54. CV curves (a) and Nyquist plots (b) for the Au/PEG + T10-SH electrode before and after its exposure to mismatching (T10) and matching (A10) target ssDNA. The concentration of both probe and target ssDNA was set as 2 μM.

Table 4.4. R_{ct} values for the Au/PEG related samples.

Sample	R_{ct}
Au/PEG	31 Ω (±2 Ω)
Au/PEG + T10 (2 μM)	33 Ω (±2 Ω)
Au/PEG + T10-SH (2 μM)	162 Ω (±4 Ω)
Au/PEG + T10-SH (2 μM) + T10 (2 μM)	165 Ω (±4 Ω)
Au/PEG + T10-SH (2 μM) + A10 (2 μM)	339 Ω (±6 Ω)

4.5.6. Comparison to the reference Au/ssDNA system

The use of gold substrates has been extensively employed for the immobilization of thiol-decorated ssDNA and its subsequent hybridization. As we introduce epoxy-rich PEG films, serving as an alternative template for the same purpose, it is of interest to compare its ssDNA loading and hybridization ability to that of the standard Au/ssDNA assembly (see Figure 4.50). To this end, the immobilization of T10-SH directly onto the Au substrate was conducted, followed by exposure of the resulting Au + T10-SH film to the mismatching (T10) and matching target (A10) sequences. The respective steps were monitored by CV and EIS and the corresponding data are presented in Figure 4.55, complemented by the derived R_{ct} values, compiled in Table 4.5.

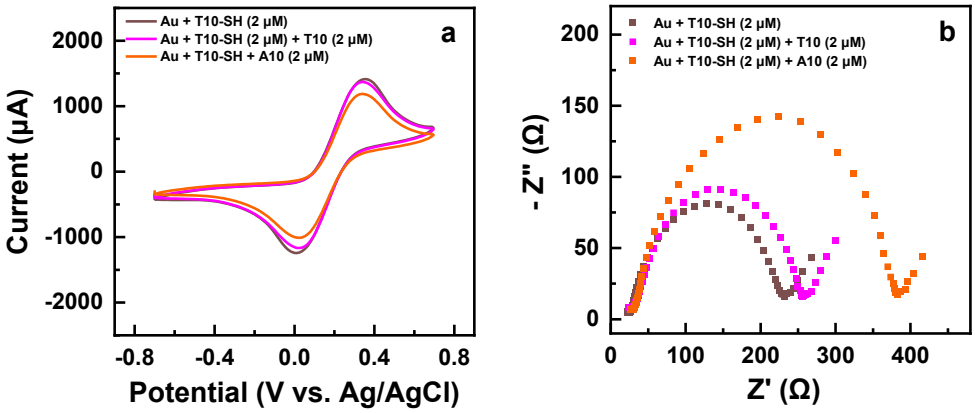

Figure 4.55. CV curves (a) and Nyquist plots (b) for the Au + T10-SH electrode before and after its exposure to mismatching (T10) and matching (A10) target ssDNA. The concentration of both probe and target ssDNA was set as 2 μM.

Let us begin the discussion with the CV curves (Figure 4.55a). The redox current observed for Au + T10-SH are still comparable to that of the original Au electrode (Figure 4.51a), and no significant change is observed after exposure to the T10 solution. Only when the Au + T10-SH film is exposed to the A10 solution, a visible decrease in the redox currents is observed. In the case of direct immobilization of ssDNA probes on a bare Au substrate, it's important to note that this process may not completely obstruct the entire active area of the conductive Au surface, thereby allowing electron transfer processes to persist on the electrode. Additionally, due to its inherently limited timescale, CV measurements may not fully capture the effects induced by the ssDNA immobilization. These findings indicate that the CV technique is not the preferred method for monitoring direct immobilization and hybridization of ssDNA on Au surface.

Table 4.5. R_{ct} values for the Au/ssDNA related samples.

Sample	R_{ct}
Au	22 Ω (±2 Ω)
Au + T10-SH (2 μM)	210 Ω (±5 Ω)
Au + T10-SH (2 μM) + T10 (2 μM)	241 Ω (±6 Ω)
Au + T10-SH (2 μM) + A10 (2 μM)	365 Ω (±6 Ω)

In contrast, the EIS data behave distinctly different (Figure 55b). The Nyquist plot of the clean gold electrode (Figure 51b) changes significantly upon the T10-SH assembly (Figure 55b), accompanied by the increase in R_{ct} from 22 Ω to 210 Ω (Table 4.5). This behavior clearly indicates the successful immobilization of T10-SH on the Au substrate. The substantial discrepancy between the CV and EIS data in the Au + T10-SH case can be rationalized by the higher sensitivity of the charge transfer in the high-frequency region, probed by EIS, to any hinderance imposed by deposited molecular films, such as T10-SH. Luckily, the value of 210 Ω for the Au + T10-SH assembly is not far away from the analogous value of 162 Ω for the T10-SH loaded PEG film, which simplifies comparison between these systems.

The exposure of the Au + T10-SH electrode to the matching sequence (A10) resulted in a significant increase in the semicircle diameter of the Nyquist plot, corresponding to an increase in R_{ct} from 210 Ω to 365 Ω. This behavior emphasizes the well-known high efficiency of the given system in context of ssDNA hybridization. Interestingly, the hybridization-triggered increase in R_{ct} for the Au + T10-SH assembly (155 Ω) is similar to that for the T10-SH loaded PEG film (177 Ω), which suggest similar hybridization efficiencies of both systems, with the value for the latter case being slightly higher.

Apart from the hybridization efficiency, high hybridization selectivity, successfully demonstrated for the PEG template (see Figure 54b and the related discussion), is also of importance. To this end, the Au + T10-SH sample was exposed to the mismatching sequence (T10) and the result was monitored by CV and EIS. Whereas the CV data (Figure 55a) did not allow any reliable conclusions (like in the A10 case), the EIS data turned out to be useful. In contrast to the ssDNA-loaded PEG template, which showed no change in the Nyquist plot and only a tiny increase in R_{ct} upon the exposure to T10, such an exposure resulted in visible changes in the analogous plot for the Au + T10-SH assembly, leading to an increase in R_{ct} from 210 Ω to 241 Ω. The respective changes and ~15% increase in R_{ct} suggest that the Au + T10-SH assembly is not entirely specific, which is most likely related to the presence of defects in the T10-SH monolayer, allowing a direct contact of mismatching ssDNA with the gold substrate.

4.5.7. XPS

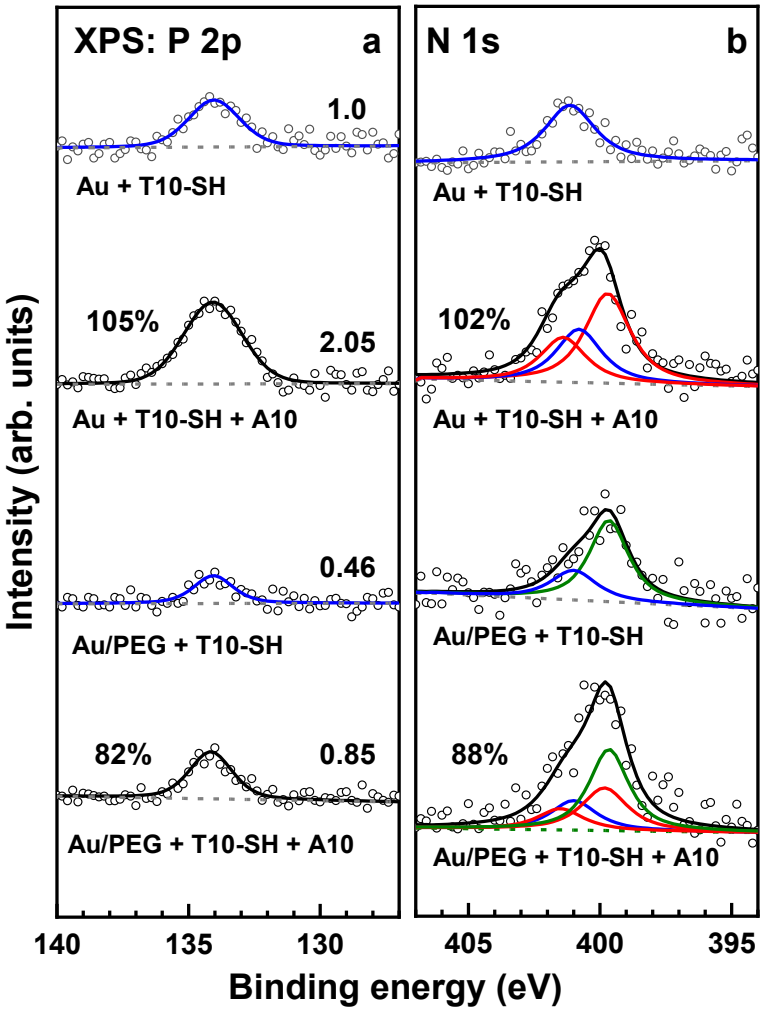

Figure 4.56. P 2p (a) and N 1s (b) XPS spectra of the Au + T10-SH (2μM) and Au/PEG + T10-SH (2μM) films before and after their exposure to the target A10 sequence (2μM). The N 1s spectra (open circles) are decomposed into individual contributions related to thymine (blue) adenine (red) and, in the case of the PEG film, amine groups in the PEG matrix (olive). The P 2p spectra (open circles) are fitted by a single peak (blue for T10-SH). The envelops of the multicomponent spectra are drawn in black; linear background is drawn by gray dashed lines. The intensities of the P 2p signal, normalized to the value for Au + T10-SH, are marked to the right of the peaks. The degrees of hybridization, derived from either P 2p or N 1s data, are marked to the left of the peaks (see text for details).

Complementary to the above electrochemical data, Au + T10-SH and Au/PEG + T10-SH films before and after their exposure to A10 were characterized by XPS. The respective data are

shown in Figure 4.56. These data include the P 2p (Figure 4.56a) and N 1s (Figure 4.56b) spectra, representative of the phosphate groups in the ssDNA backbone and nucleobases, respectively.

Whereas the P 2p spectra are not nucleobase-specific, the N 1s ones differ noticeably for thymine and adenine, allowing their recognition.[163,164,167,168] The P 2p spectra of all samples show a merged P $2p_{3/2,1/2}$ doublet at ~133.9 eV, in good agreement with the literature data.[91,163–166] The intensity of this doublet for the Au + T10-SH sample is by a factor of ~2 higher than that for Au/PEG + T10-SH, suggesting a similar relation for the packing density of the probe ssDNA. Assuming the literature value of 3–5 × 10^{13} molecules/cm^{-2} for Au/T10-SH,[163,165,183] one gets then ca. 1.5–2.5 × 10^{13} molecules/cm^{-2} for Au/PEG + T10-SH. Note, however, that in contrast to Au + T10-SH, the probe strands in the PEG matrix are not exclusively located at the PEG-ambient interface (2D) but are, most likely, distributed in a gradient-like fashion in the top part of the film (3D). It is remarkable that Au/PEG + T10-SH exhibits a similar electrochemical response to the matching target sequences as Au + T10-SH, at the twice lower density of the probe strands.

Upon the exposure of the above templates to A10, the intensity of the P 2p doublet increases by 83% for Au/PEG + T10-SH and by 105% for Au + T10-SH. In view of the lack of non-specific adsorption (see the previous section), the value for Au/PEG + T10-SH represents the respective degree of hybridization. In contrast, the value for Au + T10-SH, which exceeds 100%, do not entirely reflect the degree of hybridization but contains a contribution from a non-specific adsorption of A10. Note that because of the specific affinity of adenine to gold,[168] non-specific adsorption of A10 in the Au + T10-SH case should be even extensive than that for T10 (see the previous section).

The N 1s spectrum of Au + T10-SH exhibits the characteristic peak of thymine [163,164,167,168] at a BE of ~401 eV. For Au/PEG + T10-SH, this peak overlaps with that of the amine groups of the PEG film, at 399.7 eV. The exposure of these templates to A10, results in the appearance of the characteristic fingerprint of adenine, [163,164,168] viz. two peaks at BEs of ~399.7 and ~401.5 eV with an intensity ratio of 2:1, merging with the contributions of thymine and amine groups. Tentative decomposition of the N 1s spectra of Au/PEG + T10-SH + A10 and Au + T10-SH + A10 gave the relations between the contributions of thymine and adenine of 100:88 and 100:102, respectively, as far the different number of the nitrogen atoms in these nucleobases was considered. Similar to the P 2p case, the value for Au/PEG + T10-SH + A10 represents the degree of hybridization, with the average value, over both P 2p and N 1s data, of 85%. The

value for Au + T10-SH + A10, which once again exceeds 100%, contains a contribution of non-specific adsorption. We believe, however, that this contribution is limited, and the degree of hybridization for the direct ssDNA assembly is similar to that for the PEG case.

4.5.8. Sensitivity of the ssDNA-loaded PEG films

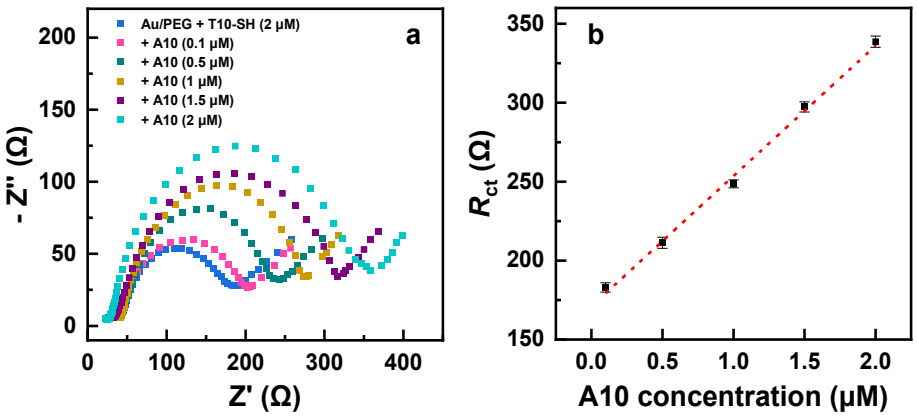

Figure 4.57. Nyquist plots (a) and the derived R_{ct} values (b) for the Au/PEG + T10-SH electrode after its exposure to matching A10 target ssDNA. The concentration of A10 was varied. The R_{ct} behavior in (b) is tentatively traced by straight dashed line.

Given the remarkable selectivity of the Au/PEG platform, its sensitivity to the specific hybridization was monitored as well. To this end, the Au/PEG + T10-SH sample was exposed to A10, while the concentration of A10 in the buffer solution was systematically varied from 0.1 μM to 2 μM. The corresponding Nyquist plots are presented in Figure 4.57a, while the resulting R_{ct} values as a function of A10 concentration are depicted in Figure 4.57b. As expected, the R_{ct} value exhibits a gradual decrease as the A10 concentration decreases. However, even at such a low concentration as 0.1 μM, the R_{ct} gain remains distinctly visible when compared to the reference value obtained for the Au/PEG + T10-SH probe. This outcome demonstrates the high sensitivity of the ssDNA-loaded PEG film to sequence-matching hybridization. The respective detection limit of 0.1 μM is quite reasonable and comparable with literature data for other types of ssDNA sensors.[180,181] One can reasonably assume that this detection limit can be improved even further, e.g. by a larger loading of the PEG film with the probe ssDNA. Whereas a moderate loading, comparable with that of the direct ssDNA assembly was selected for the most of the experiments in the present study, it can be easily

increased by at least a factor of 4–5 as shown in the data in section 3.1. An alternative option is to increase the density of the active epoxy groups by the changing the EPX:NH_2 ratio even further in the favor of STAR–EPX. Of course, there should be a limit in the stability of a non-equilibrium PEG network relying on the crosslinking between the epoxy and amino groups of the precursors, but the EPX:NH_2 ratios higher than 2:1, used in the present work and tested before for stability,[59] should be in principle possible.

An interesting feature of the plot in Figure 4.57 is a nearly linear correlation between the R_{ct} value and the target ssDNA concentration. This behavior is in contrast to some literature reports in which a logarithmic relationship with the concentration of target DNA was recorded.[14,15] This difference is probably related to the 3D character of our sensor in contrast to the 2D arrays designed in the above reports.

4.6. PEG-C60 composite films and free-standing nanosheets for flexible electronic devices and sensors

4.6.1. Motivation

Fullerene (C60) is a unique carbon allotrope consisting of 60 carbon atoms with sp^2 hybridization which form a spherical structure composed of 12 pentagons and 20 hexagons in icosahedral symmetry.[184] Due to its distinguished physicochemical properties, C60 and its derivatives attract significant interest of scientific and industrial communities.[39,40,185] Along with C60, C60-based composites are useful as well. As a representative example, C60-polymer composites can be mentioned,[186,187] serving in particular as active materials for such applications as electrochemical sensors,[188–192] and organic solar cells.[193–196] One of prospective materials in context of C60-polymer composites is PEG.

In this subproject, I explored a possibility to prepare PEG-C60 composite films on the basis of porous PEG matrix. It also gave an additional option to isolate such films as mechanically stable, free-standing nanosheets. The respective STAR-PEG-derived films represent, thus, a promising basis for the preparation of PEG-C60 composite films and nanosheets, which can be potentially useful for a variety of applications. For this purpose, I used three different preparation procedures, described in detail below. The properties of the composite films were monitored by SEM, AFM, XPS, UV-vis spectroscopy, and electrochemistry (voltammetry and impedance spectroscopy). The PEG-C60 nanosheets were assessed in context of their stability, elasticity, and persistence of the original properties of the parent films.

4.6.2. Specific experiments and procedures

Preparation of the C60 samples and PEG-C60 composite films. The preparation procedures for all the samples are illustrated in Figure 4.58. As a reference to the PEG-C60 composites**,** pure C60 samples were prepared by immersion of the substrates into a 2 mg/mL solution of C60 in toluene for 24 h at room temperature. The PEG-C60 composite films were prepared by three different methods, termed as immersion, one-pot, and reflux, respectively. The thickness of these films was in all cases in the range of 80−100 nm, as controlled by ellipsometry.

Within the immersion method, PEG-only films were first prepared and then exposed to a C60/toluene solution. In brief, STAR-NH_2 and STAR-EPX precursors were dissolved in toluene and mixed in a 1:1 fashion, resulting in a 10 mg/mL precursors solution, followed by a thermal crosslinking process. The resulting PEG were then immersed into a 2 mg/mL solution

of C60 in toluene for 24 h at room temperature. Within the one-pot method, a trinary solution of the precursors (10 mg/mL in toluene) and C60 (2 mg/mL in toluene) was spin-coated onto the substrates, and the PEG-C60 composite films were directly obtained after a thermal crosslinking process. Within the reflux method, the STAR-NH_2 compound and C60 were dissolved in toluene with a concentration of 10 mg/mL and 2 mg/mL, respectively. The binary solution was refluxed at 90 °C for 48 h under argon flow in order to link chemically C60 molecules to the NH_2 groups of the STAR-NH_2. After the reflux process, the STAR-EPX compound was added into the above solution with a concentration of 10 mg/mL. The final mixture was spin-coated onto the substrates and thermally-crosslinked to get the reflux composite film. All samples were rinsed with ethanol and deionized water before characterization. For the C60 stability test, performed as a separate experiment, the samples were rinsed with a large amount of toluene and the parameters before and after the rinsing were compared.

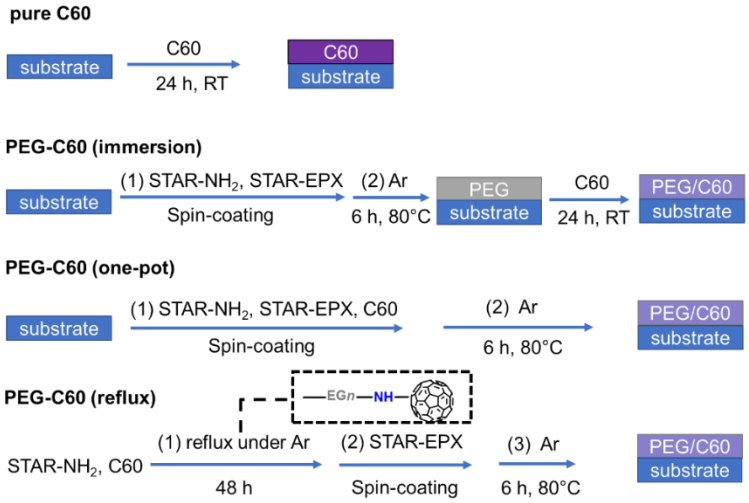

Figure 4.58. Schematic illustration of the fabrication procedures for pure C60 and different PEG-C60 composite films. Within these procedures, the concentration of C60 was always kept at 2 mg/mL, the concentration of STAR-NH_2 and STAR-EPX precursors was set to 10 mg/mL, and the solvent was toluene.

4.6.3. Morphology of the PEG-C60 films

The morphology of the PEG-C60 composite films was characterized by SEM. Representative images of the pure C60 sample (reference) and the composite films prepared on SiO_2/Si substrates are presented in Figures 4.59a–d. In all cases, we observe the formation of C60

aggregates (clusters), typical of this molecule,[197,198] with the size distribution displayed in the figure. For the substrate immersed into C60 solution (Figure 4.59a), the shape of the aggregates varies stochastically and their size varies from less than 100 nm to 1000 nm. The size distribution could be tentatively fitted by an exponential function, giving an average size of ~192 nm. In contrast, in the case of the PEG-C60 composite films (Figures 4.59b–d), we observe a close-to-spherical shape of the aggregates, a narrow size distribution, and a homogeneous lateral distribution for all preparation methods. In all cases, the size distribution can be coarsely described by a Gaussian-like function, with an average C60 cluster size of ~260 nm, ~226 nm, and ~310 nm for the immersion, one-pot, and reflux preparation methods, respectively (see also Table 4.6). The noticeably larger cluster size in the latter case is most likely related to the duration of the reflux procedure (48 h), favoring progressing aggregation of C60.

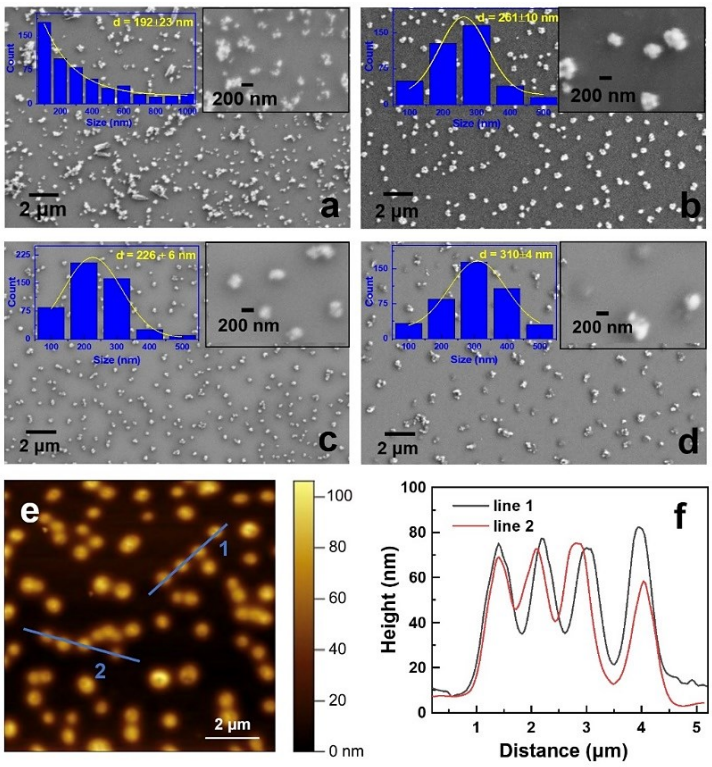

Figure 4.59. (a–d) SEM images of deposited C60 (a) and PEG-C60 composite films prepared by immersion (b), one-pot (c), and reflux (d) methods. Insets on the left: corresponding size distributions of the C60 clusters. Insets on the right: corresponding SEM images with a higher magnification. (e) Representative AFM image of the PEG-C60 film prepared by the reflux method and (f) height profiles along the (blue) lines shown in the AFM image.

The formation of the C60 aggregates in the composite films is expectable in view of the well-known ability of C60 towards supramolecular organization, with a broad variety of different aggregates and nanostructures reported.[199–202] This process is primarily driven by the van der Waals and π-stacking interactions between individual molecules,[199] while the shape, size, and dimensionality of the aggregates depend on the specific conditions of a particular experiment and the exact structure of C60-containing molecule.[199–202] In turn, the structural parameters of the aggregates, viz. their size, packing, and internal molecular order, jointly influence their optoelectronic properties.[200,201,203]

Even though the PEG-C60 blending stabilizes the shape and size of C60 clusters, the character of the respective composites is presumably different for the different preparation methods. Since the clusters most likely form in solution, they cannot penetrate into the PEG matrix in the case of immersion and are, therefore, most likely located on the surface of the PEG film. Indeed, the mesh size of the crosslinked PEG matrix is ~8 nm, as defined by the arm length of the STAR-PEG precursors. Consequently, this mesh is hardly accessible for the comparably large C60 clusters, so that the predominate process is their adsorption on the surface of the PEG film.

Table 4.6. The average C60 cluster size, portion of C60, absorbance, and absorbance maximum (λ_{max}) for the reference C60 sample and PEG-C60 films.

Sample	**Average size (SEM)**	**Portion of C60 (XPS)**	**Absorbance (UV-vis)**	**λ_{max} (UV-vis)**
C60 only	192 ± 23 nm		0.021	342 nm
PEG-C60 (immersion)	261 ± 10 nm	6.7%	0.017	314 nm
PEG-C60 (one-pot)	226 ± 6 nm	13.2%	0.034	326 nm
PEG-C60 (reflux)	310 ± 4 nm	29.4%	0.041	339 nm

In the case of the one-pot procedure, C60 clusters became integrated with the PEG matrix, getting embedded into the PEG network. There is, however, no chemical bonding between these clusters and the network; the clusters are just caught physically in the network, similar to a fly caught in the spider web. The situation changes, however, in the case of the reflux preparation. The peripheral fullerenes of the C60 clusters are then linked chemically to one of the precursors (STAR-NH_2; see Figure 4.58) and, consequently, to the entire matrix after the

PEG-C60 film formation. In contrast, individual molecules within the C60 cluster shell, most likely pack by local van der Waals forces.

The SEM results were verified by AFM, with the measurements performed for the PEG-C60 film prepared by the reflux method only. The respective data are shown in Figures 4.59e–f. A representative AFM image in Figure 4.59e shows C60 clusters distributed in the PEG matrix. The average diameter of the clusters is ~360 nm according to the water-shed algorithm analysis, which agrees well with the SEM value. Most interesting are the height profiles along the selected lines in the AFM image, shown in Figure 4.59f. Accordingly, the C60 clusters protrude from the surrounding PEG film, which is expectable since their average size (~310 nm according to SEM) exceeds the film thickness (80–100 nm), as far as one assumes a spherical form of these clusters. Interestingly, the height of the protrusions (60–70 nm) is somewhat smaller than the difference between the average size of the clusters and the film thickness (~210 nm), even if we assume that the protrusions occur at the both faces of the composite film. This means that the C60 clusters are not precisely spherical but compressed to some extent in the direction perpendicular to the substrate surface, representing, thus, ellipsoids or, using a simpler term, disks. The deformation of the clusters is probably enforced by their confinement in the thinner film on the solid substrate. Presumably, the clusters are not exposed directly to ambient and the substrate but covered by a thin PEG overlayer, representing a part of the PEG matrix.

4.6.4. Composition of the PEG-C60 films

The composition of the samples was monitored by XPS, from which the portion of C60 in the composite films was also obtained. Representative C 1s spectra of the PEG film, pure C60, and PEG-C60 composite films, all deposited on a Si substrate, are shown in Figure 4.60a. The spectrum of the PEG film exhibits a single C 1s peak at a BE of ~286.8 eV, which is characteristic of the carbon atoms in the PEG chains.[27] This spectrum verifies the formation of a high-quality PEG film without any contamination. The C 1s spectrum of pure C60 exhibits a peak at a BE of ~285.0 eV, corresponding to the carbon backbone of C60 with sp^2 hybridization.[204] The BE difference between the C60 and PEG features makes it possible to distinguish them in the C 1s spectra of the composite films. Indeed, the contribution of C60 is well distinguishable in these spectra, appearing as a shoulder at the low BE side of the PEG peak. This shoulder is quite weak for the immersion method, which suggests a low content of C60 in the respective composite film. In the case of the one-pot procedure, the shoulder is more pronounced than in the immersion case, indicating a higher content of C60. But the highest

intensity of the shoulder is observed for the reflux film, corresponding to the highest content of C60. Taking the relative spectral weights of the PEG and C60 features, C60 contents in the composite films prepared by the different methods were calculated and compiled in Table 4.6. Note that in view of the limited sampling depths of XPS,[84] which, for the given C 1s spectra, is about 12 nm,[27] the spectra in Figure 4.60a are only representative of the topmost part of the PEG-C60 films. Consequently, the entire C60 content in the ´immersion´ film, in which C60 cluster are predominantly located on the film surface, is noticeably lower than the derived value. In contrast, the values for the ´one-pot´ and ´reflux´ films, featuring the proposed homogeneous distribution of C60 clusters in the PEG matrix, are characteristic of the entire films.

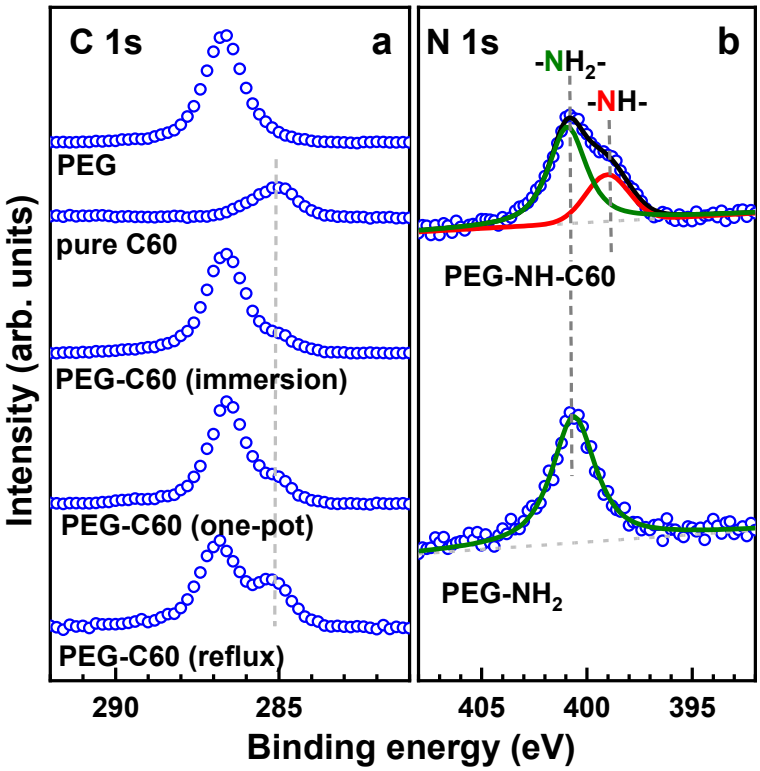

Figure 4.60. (a) C 1s XPS spectra of the PEG film (reference), pure C60 (reference), and PEG-C60 composite films prepared by different methods. The vertical dashed line traces the position of the characteristic C60 peak. (b) N 1s XPS spectra of the STAR-NH_2 precursor before and after its reaction with C60 under reflux for 24 h. The spectrum of the precursor before the reaction represents a single peak (a tentative fit is shown). The spectrum of the precursor after the reaction is decomposed into the contributions related to the original NH_2 groups (cyan peak) and the NH links (red peak). The vertical dashed lines are guides to the eye.

XPS was also used to verify the chemical bonding between the STAR-NH_2 precursors and C60 clusters, resulting in chemical incorporation of these clusters into the PEG matrix. The N 1s XPS spectra of the STAR-NH_2 before and after the reaction with C60 are presented in Figure 4.60b (the samples were prepared by drop-casting on Si substrate). The N 1s spectrum of the STAR-NH_2 exhibits a single peak at a BE of ~400.7 eV, characteristic of the NH_2 groups of the STAR-NH_2.[205] After the amination reaction with C60, the spectrum undergoes a significant change exhibiting a complex spectral envelope which can be decomposed into two peaks. The peak at a BE of ~400.8 eV represents the original NH_2 groups of STAR-NH_2. The new emerged peak at a BE of ~399.0 eV can be assigned to the NH–C60 moieties, proving the reaction between the NH_2 groups of STAR-NH_2 and C60 molecules.[206] Considering the spectral weights of both peaks, one can conclude that about ~30% of the NH_2 groups of the precursors became bonded to C60 and, consequently, were not available any more for the subsequent crosslinking reaction, resulting most likely in a certain distortion of the PEG network.

4.6.5. Optical properties

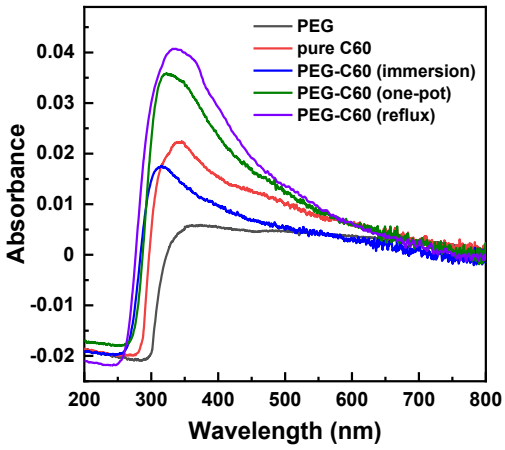

Figure 4.61. UV-vis spectra of the PEG film, pure C60, and PEG-C60 composite films prepared by the different methods. The negative absorption in the UV region comes from the subtracted glass absorption background.

The electronic absorption spectra monitored by UV-vis spectroscopy serve as a complementary measure of the C60 content in the PEG-C60 films. Additionally, the spectral features provide particular information about the nature of supramolecular organization of C60 in the hydrophilic PEG matrix. These representative UV-vis spectra of the pure PEG film, pure C60 and the PEG-C60 composite films on glass are shown in Figure 4.61. For the pure PEG film

no absorption peaks are observed, providing a reference for the other samples. The pure C60 and PEG-C60 composite films show a pronounced UV absorption around 315–345 nm and weak visible absorption which is known to contain several electronic transitions with low oscillator strengths.[207] The position and intensity of the absorbance peak vary strongly from sample to sample (see also Table 4.6). The position of the absorption peak, corresponding to the absorption wavelength λ_{max}, reflects the optical properties of fullerene aggregates, mainly influenced by their shape, size and environment.[200,201,203] The absorption spectrum of pure C60 shows a larger vis-contribution, and has its UV-absorption maximum (~342 nm) bathochromically shifted with respect to the other samples. This behavior is predominantly related to the non-symmetrical shape of the aggregates (see Figure 4.59a), differing strongly from centrosymmetry (I_h point group) of C60. This shape becomes more symmetrical for the composite films (Figures 4.59b–d), for which the absorption maxima increases progressively, going from the immersion (~314 nm) to one-pot (~326 nm) and further to reflux (~339 nm) case. This tendency does not correlate with the average size of the C60 clusters (see Table 4.6) but rather with the local intermolecular distances between fullerenes in those supramolecular aggregates, which is influenced by the hydrophilic PEG matrix and is presumably the largest in the immersion case (adsorption on the surface), somewhat smaller in the one-pot case (bulk physisorption), and the smallest in the reflux case (bulk chemisorption).

The absorbances at λ_{max} in the UV-vis spectra reflect the contents of C60 in the composite films. According to Figure 4.61 and Table 4.6, where the numerical values are compiled, the reflux film has the highest absorbance, followed by the one-pot film, and then by the immersion film, which correlates well with the XPS results (see Figure 4.60a and the respective data in Table 4.6). Notably, the absorbance of the immersion film is even lower than that of the reference C60 sample adsorbed on the glass substrate. This is an additional evidence that the immersion method mostly involves the deposition of C60 onto the PEG film, with a lower adhesion of C60 to the PEG surface compared to the glass surface.

4.6.6. Electrochemical properties

Electrochemical properties of the composite films were investigated by CV, SWV, and EIS; the technical details can be found in chapter 3. Figure 4.62a shows the CV curves of a GCE electrode before and after its immersion into a 2 mg/mL C60 solution. Whereas no redox features are observed for the bare electrode (as expected),[180] the CV curve of the C60 decorated electrode exhibits a variety of the characteristic redox peaks, with the first dominant reductive

peak of C60 observed at around –0.8 V (in agreement with the literature data).[208,209] Accordingly, we selected the scan range of 0 to –1 V for the complementary SWV measurements, which are more sensitive than CV. Representative SWV curves for the samples prepared on Au electrodes are displayed in Figure 4.62b. As expected, no reduction peaks are found for the pure PEG film. In contrast, the SWV curve of the reference, pure C60 sample reveals a single reductive peak at –0.8 V, in agreement with the CV result, proving the consistency of the different electrochemical methods. For the composite films, the peak current associated with the first fullerene reduction varies from sample to sample, with the reflux sample possessing the highest current, followed by the one-pot and immersion samples. The above tendency reflects the difference in the amount of C60 in the given composite films, in full agreement with the XPS and UV-vis data (see sections 4.5.4 and 4.5.5). It is also noteworthy that the position of the C60 reductive peak shifts to a more positive voltage with the increase of the C60 content in the composite films. The respective voltage values are listed in Table 4.7.

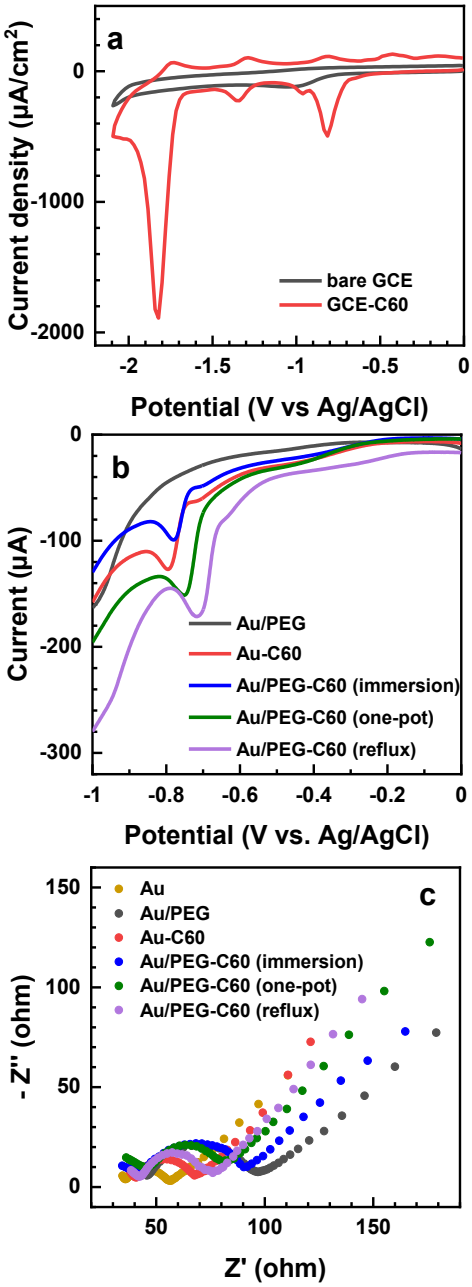

Figure 4.62. (a) CV curves of the bare and C60-decorated GCE working electrode in deoxygenated MeCN with 0.1 M $TBABF_4$ as supporting electrolyte, at a scan rate of 100 mV/s. (b) SWV curves of the Au/PEG, Au-C60, and Au/PEG-C60 electrodes in deoxygenated MeCN with 0.1 M $TBABF_4$ as supporting electrolyte. (c) Nyquist plots for these electrodes. The measurements were conducted in a 10 mM $[Fe(CN)_6]^{3-/4-}$electrolyte containing 0.1 M KCl.

Table 4.7. Position of the first reduction peak, LUMO energy, and charge ransfer resistance of the specific electrodes.

Electrode	Reduction peak	E_{LUMO}	R_{ct}
Au/PEG	none	none	52 Ω
Au/PEG-C60 (immersion)	–0.78 V	–3.99 eV	46 Ω
Au/PEG-C60 (one-pot)	–0.75 V	–4.02 eV	41 Ω
Au/PEG-C60 (reflux)	–0.71 V	–4.06 eV	34 Ω
Au-C60	–0.8 V	–3.97 eV	29 Ω
Au	none	none	21 Ω

The SWV technique can also be used to evaluate the energies of the frontier molecular orbital of C60 and its derivatives which are important parameters with regards to their electron-accepting properties.[200,210] Accordingly, the energy of the LUMO of C60 in the different composite films were obtained based on the SWV results, with the assistance of ferrocene/ferrocenium redox couple as reference sample. To this end, the LUMO energy, E_{LUMO}, was calculated on the basis of the onset potential of the first reduction peak, E_{red}^{onset}, by the following equation[210]

$$E_{LUMO} = -\left(E^{onset}_{[\text{red vs.Fc+/ Fc}]} + 5.1\right) \text{ eV}$$

and the results are summarized in Table 4.7. The pure C60 sample has the largest LUMO energy of −3.97 eV. The E_{LUMO} value of the composite films varies with the preparation method, with the value being successively lower at going from the immersion to one-pot and further to the reflux case. The ´reflux´ film features the lowest LUMO energy of −4.06 eV, which is shifted by ~90 meV compared with the pure C60 and by ~70 meV compared with the immersion case. Such a shift is related to the ratio of the number of surface states versus bulk states in a cluster, with a maximal possible value of 120 meV according to literature.[200] In the present case, this ratio changes between the samples because of differences in the supramolecular organization of the hydrophobic fullerenes, governed by the hydrophilicity of the PEG counterpart.

The electrochemical conductivity of the composite films, essential in context of some of their potential applications,[190,192,211] was characterized by EIS, in the presence of $[Fe(CN)_6]^{3-/4-}$. The respective Nyquist plots for the bare Au electrode and PEG, C60, and PEG-C60 modified electrodes with the corresponding impedance data are presented in Figure 4.62c and Table 4.7.

The diameters of the semicircles in the high frequency region of these plots correspond to the charge transfer resistance between the SAM and the electrolyte solution (R_{ct}), while the linear part of the plots at low frequencies indicates the diffusion processes. The blank Au electrode has a lowest R_{ct} value of 21 Ω. After the deposition of C60 onto the electrode, the R_{ct} value shows a slight increase, reaching 29 Ω, indicating a good conductivity of C60 and the presence of uncovered electrode areas. The deposition of a PEG film onto the Au electrode also changes the R_{ct} value, which increases to 52 Ω. Such an increase is quite moderate compared to other non-conducting polymers,[212] which can be tentatively explained by the porous structure of the PEG films (see Figure 3.1) and its related swelling and permeability properties, favorable for the diffusion of the $[Fe(CN)_6]^{3-/4-}$ moieties toward the Au electrode. Note that the porosity and permeability of these films can be increased even further, if necessary, by the use of the precursors with larger molecular weights, which also slightly affects the swelling and elastic properties of these films, as demonstrated in chapter 4.2. But, in any case, the obtained results indicate that the PEG film serves as a suitable matrix for the fabrication of PEG-C60 composite films in context of electrochemical applications. As expected, the moderate R_{ct} value of the PEG film decreases even further at the introduction of C60, being 46 Ω, 41 Ω, and 34 Ω, for the immersion, one-pot, and reflux PEG-C60 films, respectively (see also Table 4.7). Notably, the value of 34 Ω is quite close to the ultimate limit of the deposited C60 (29 Ω), showing the particular high potential of the ´reflux´ film for electrochemical applications.

4.6.7. Stability of the composite films

In order to investigate the stability of C60 in the composite films, we rinsed the samples with a large amount of toluene, which is a good solvent for C60, and monitored the outcome by SWV and SEM. Figures 4.63a–d present the SWV curves for the different samples before and after the toluene rinse. Note that the former curves are the same as those in Figure 4.62b, shown here again for comparison. In the case of deposited C60 and ´immersion´ PEG-C60 film, the reductive peak disappeared completely after the toluene rinse (Figures 4.63a and 4.63b), which is a good evidence that the immersed C60 can be efficiently washed off both from the Au surface (pure C60) and the surface of the PEG film (immersion). This behavior is reasonable considering that the C60 clusters are most likely physically adsorbed on the Au and PEG surface in the case of immersion, being prone to the effect of solvent. The removal of C60 was further proved by the SEM. The SEM images of the PEG-C60 film (immersion) before and after toluene rinse are shown in Figures 4.63e and 4.63f, respectively. The well-visible C60 clusters indeed disappear completely after the film rinsing with toluene. In contrast, the SWV

reductive peak for the one-pot sample does survive the toluene rinse, even though the respective current decreases to some extent (Figure 4.63c). This behavior means that a part of the C60 fraction was removed from the PEG-C60 film, most likely the clusters with small size and those "loosely" incorporated in the PEG matrix. The remained clusters are those that are incorporated better into this matrix.

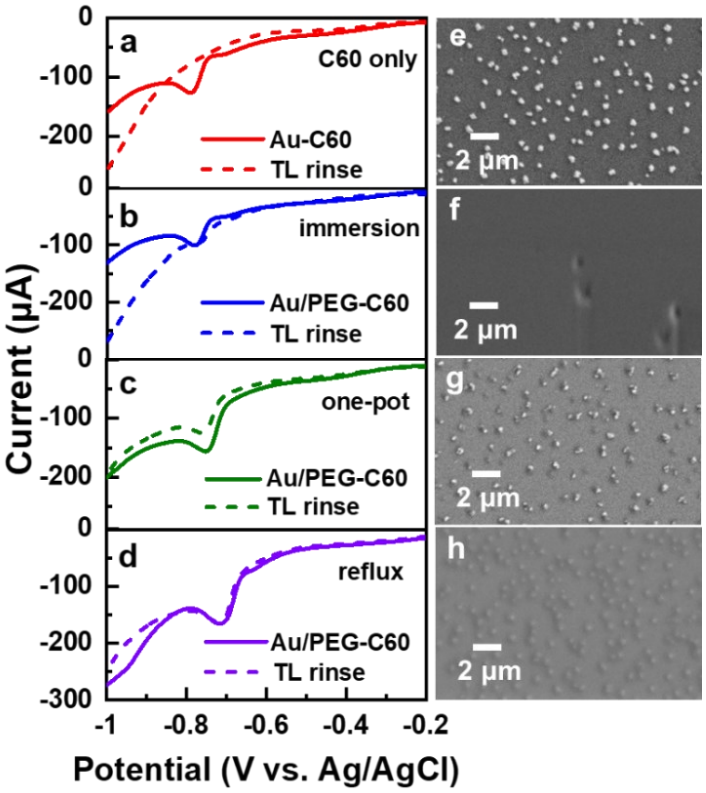

Figure 4.63. (a–d) SWV curves for the Au/C60 electrode and Au/PEG-C60 electrodes prepared by the different methods before (solid lines) and after (dashed lines) extensive rinse with toluene. The measurements were conducted in deoxygenated MeCN containing 0.1 M $TBABF_4$ as supporting electrolyte. (e-h) SEM images of the electrodes, including those of Au/PEG-C60 (immersion) electrode before (e) and after (f) extensive rinse with toluene as well as those of the Au/PEG-C60 (reflux) electrode before (g) and after (h) rinse with toluene.

In contrast to the one-pot case, the SWV curves of the reflux sample before and after the toluene rinse are nearly identical, indicating a high stability of the fullerenes in the given composite film. The corresponding SEM images shown in Figures 4.63g (before the rinse) and 4.63h (after the rinse) provide more insights. As can be seen in these images, the C60 clusters on the surface of the PEG film (bright spots in the SEM image) were rinsed away, resulting in a new

morphology with a pattern of voids (or vesicles) inside the PEG film. It looks, however (according to the electrochemistry data), that only a small part of all clusters was affected by the rinsing, hardly changing the overall electrochemical performance of the entire composite film (Figure 4.63d).

4.6.8. Free-standing and transferred nanosheets

One of the favorable properties of PEG films formed from the STAR-PEG precursors is the possibility of their separation from the original substrate, followed by either relocation onto a secondary substrate or placement over a window or a supporting mesh as a free-standing nanosheet.[28,213] It turned out that this option is also available for the PEG-C60 composite films. To this end, we successfully separated the PEG (reference) and PEG-C60 nanosheets from the primary SiO_2/Si substrates and placed them onto the secondary substrate with a circular window for the bulge test. The applied pressure and the corresponding deflection of the nanosheet are recorded during the measurements, reflecting the elastic properties and mechanical stability of the nanosheet.

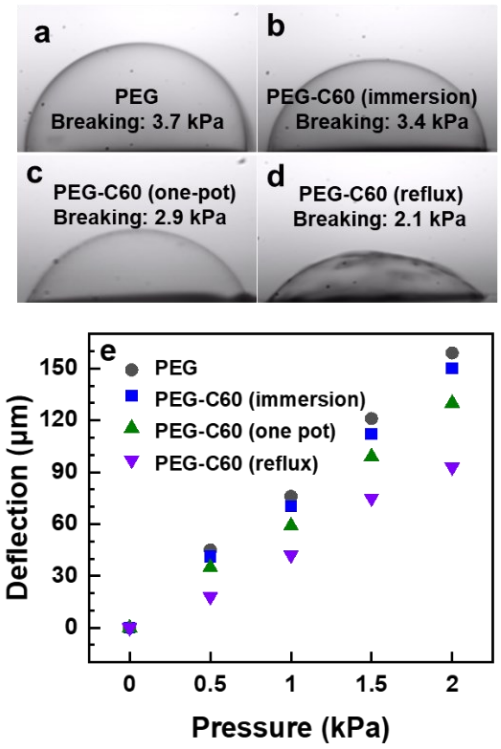

Figure 4.64. (a–d) Optical images of the deflected PEG and PEG-C60 nanosheets close to their breaking points, marked in the panels. The nanosheets were suspended over a circular window with a diameter of 0.5 mm. (e) Deflection vs. pressure plots for these nanosheets.

Representative microscopy images of the deflected nanosheets close to their breaking points are shown in Figures 4.64a–d and the respective deflection vs. pressure plots for these nanosheets are presented in Figure 4.64e. Compared with the PEG-only nanosheet, the PEG-C60 nanosheets reveal worse elastic properties and mechanical stability, deteriorating to some extent progressively as the content and involvement of C60 increase. This is reflected by both the differences in the breaking pressure and by different deflections at a specific pressure, reflected quantitatively by the Young's moduli of the nanosheets. For instance, deflections of the PEG and reflux nanosheets at a pressure of 2 kPa are 155 μm and 90 μm, respectively, and the respective breaking points are 3.7 kPa and 2.1 kPa. Nevertheless, the reflux nanosheet is still highly elastic and stretchable, which is also characteristic of the immersion and one-pot nanosheets and, consequently, for the respective parent films as well. The Young's moduli of the nanosheets were calculated by fitting the experimental data to the theoretical equation describing the relation between the pressure difference and the deflection of a nanosheet suspended over a circular window; the details of the procedure can be found in Chapter 4.3. The resulting Young's moduli for the ´immersion´, ´one-pot´, and ´reflux´ nanosheets were estimated as 2.9 MPa, 4.7 MPa, and 11.5 MPa, as calculated by eq 2.7. which all are higher than that for the reference PEG nanosheet (2.1 MPa) but still exceptionally small compared to other inorganic and organic nanosheets with similar thicknesses.

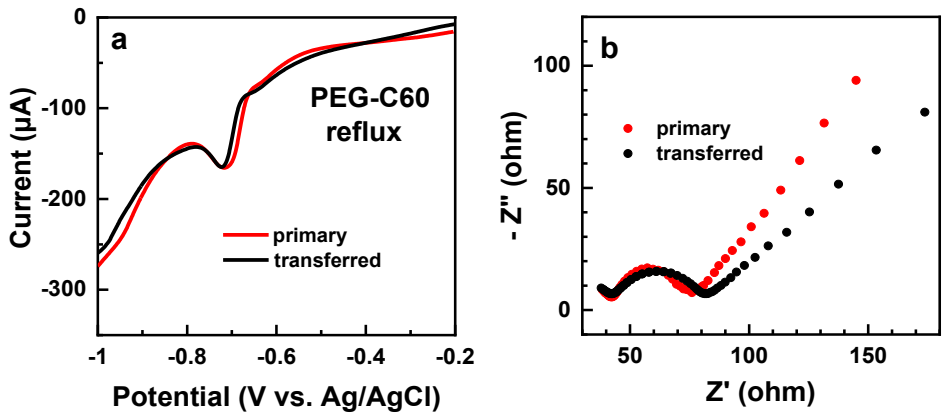

Figure 4.65. (a) SWV curves of the reflux PEG-C60 film on the primary Au electrode and the same film transferred as a free-standing nanosheet onto the Au electrode (secondary substrate) from the primary SiO_2/Si substrate. (b) Nyquist plots for these samples.

Finally, electrochemical measurements on the transferred PEG-C60 (reflux) nanosheets were conducted to investigate their electrochemical properties. For this purpose, a reflux film prepared on the primary SiO_2/Si substrate was separated from this substrate and transferred as

a free-standing nanosheet onto a Au electrode (secondary substrate), which was then subjected to SWV and EIS measurements. The SWV curve and the Nyquist plot of the transferred nanosheet are shown in Figure 4.65a,b respectively, along with the reference data for the analogous film prepared on the primary Au electrode. According to the SWV curves, the transferred nanosheet reproduces the electrochemical behavior of the film on the primary electrode completely. Only a slight negative shift and a small (if at all) intensity diminishment are found for the reductive peak of the transferred nanosheet. The Nyquist plots of the spin-coated film and the transferred nanosheet have slightly different diameters in the high-frequency region, corresponding to the R_{ct} values of 34 and 38 Ω, respectively, and different diffusion contributions in the low-frequency regime. The increase in R_{ct} after the transfer is quite small and most likely related to the coupling of the nanosheet to the substrate and fine details of the respective interface (contamination, etc.). Generally, one can conclude that the electrochemical properties of the PEG-C60 nanosheets correspond to those of the original films and are only minorly deteriorated at their transfer to the secondary substrate.

4.7. Electron-induced modification of Triptycene SAM in context of lithography and nanofabrication

4.7.1. Motivation

As discussed in the introduction part, CNMs, as another important type of ultra-thin nanosheets, have gained significant research interest.[45,46,48,50] Our group and our partners recently reported the fabrication of a well-ordered and densely packed tripodal SAM on the basis of triptycene.[61,214–216] The respective scaffold consists of three phenyl rings, which are disposed at a dihedral angle of 120° with respect to each other and connected by the aliphatic bridge. This scaffold can be flexibly decorated by different numbers of the anchoring and tail groups, with the most basic structure represented by 1,8,13-trimercaptomethyl-triptycene (Trip-T1, Figure 4.66).[61] These unique (for a tripodal monolayer) properties make the Trip-T1 SAM a potentially promising system for nanofabrication.

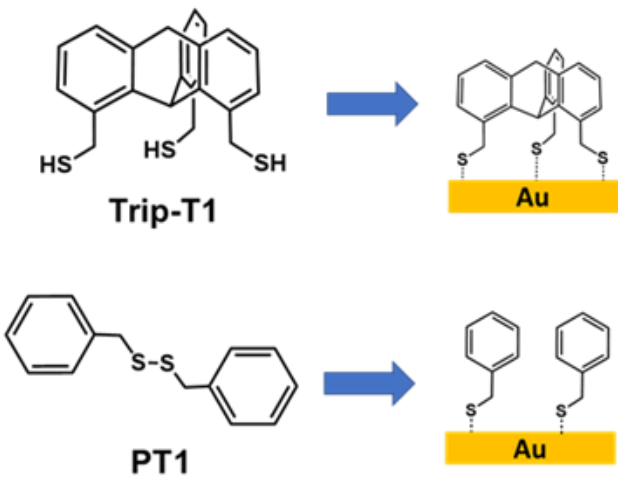

Figure 4.66. Structures of the precursors for the SAM studied, along with their abbreviations (related to the assembled state) and schematics of monomolecular assembly on Au(111).

To this end, within this particular subproject in the framework of my PhD thesis, I intended to explore the potential of using Trip-T1 SAM on Au(111) in the context of lithography and CNM fabrication. The respective study included also complementary spectroscopic experiments aiming to understand the effects of electron irradiation on the Trip-T1 SAM. These findings revealed that this monolayer behaves similar to conventional, monopodal aromatic SAMs, with crosslinking dominating over electron irradiation, which is then most likely characteristic of a variety of other aromatic multipodal SAMs, extending, thus, significantly, the "pool" of

potential precursors for the CNM fabrication. Additionally, we demonstrated that the Trip-T1 SAM can be utilized as a negative resist in EBL and for CNM fabrication, showing a similar performance as the reference monopodal system (PT1; see Figure 4.66), corresponding to a single "blade" of Trip-T1. Note that this system is of interest in its own, since it represents the shortest aromatic SAM suitable for EBL and CNM fabrication. The closest analogue of this system, phenylthiolate (PT) SAM on Au(111), showed a poor performance in context of nanofabrication, which was explained by its limited ability to form an extensive, 2D crosslinked network.

4.7.2. Specific experiments and procedures

Homogenous electron irradiation. The homogenous (over a large, macroscopic area) electron irradiation of the samples was conducted with an FG20 flood gun. See section 4.3.2 for technical details.

Spectroscopy experiments. The NEXAFS spectroscopy experiments were conducted for the pristine and irradiated Trip-T1 SAMs only, which were performed at the bending-magnet HE-SGM beamline of the synchrotron storage ring BESSY II in Berlin, using a custom-designed endstation.[90] The spectra were measured at the carbon K-edge in the partial electron yield mode with a retarding voltage of −150 V. The primary X-ray beam was linearly polarized with a polarization degree of ~90%. The molecular orientation was determined by varying the incidence angle of the beam from normal (90°) to grazing (20°) incidence geometry.[220] The former and latter geometries refer to the electric field vector (**E**) of the primary X-rays, being respectively parallel and nearly perpendicular to the sample surface. The photon energy (PE) scale was referenced to the most pronounced π* resonance of highly oriented pyrolytic graphite at 285.38 eV.[221]

EBL experiments. Test lithographic patterns consisting of 6 pair of squares (3 × 3 μm) corresponding to the progressively increasing doses (5, 10, 20, 40, 80, and 100 mC/cm^2) were written with a LEO 1530 scanning electron microscope (Zeiss) equipped with a Raith Lithography System. The primary electron beam energy was set as 5 keV and the irradiation dose was calibrated by a Faraday cup. The patterning was conducted at a base pressure of ~8 × 10^{-6} mbar. To transfer the fabricated patterns to the gold underlayer, the samples were immersed into an etching solution consisting of 1 KOH, 0.1 M $K_2S_2O_3$, 10 Mm $K_3[Fe(CN)_6]$, and 1 mM $K_4[Fe(CN)_6]$ for 30 min at room temperature. Afterwards, the samples were rinsed with H_2O and dried with argon.

CNM fabrication. The preparation of the CNMs followed the literature procedures.[51] As the first step, the SAMs were homogeneously irradiated by electrons (50 eV) with a dose of either 40 or 80 mC/cm^2. Subsequently, the crosslinked SAM (CL-SAM) were spin-coated with two layers of PMMA at 4000 rpm, including a low molecular weight PMMA layer (50 K, dissolved in ethyl acetate) and a high molecular weight PMMA layer (950 K, dissolved in chlorobenzene). The PMMA/CL-SAM/gold/silicon samples were then slowly immersed into water under a grazing angle to separate the PMMA/CL-CAM/gold sandwiches from the underlying Si wafers. Further, these sandwiches were transferred from the water surface to a Lugol's solution (aqueous KI/I_2, 2%), in which the gold layers were dissolved within 20 min. The resulting PMMA/CL-SAM bilayers were then transferred to a KI solution (1:10) for 2 min and then to H_2O for subsequent cleaning. Afterwards, the bilayers were transferred onto supporting metal grids (1500 mesh, Plano) and baked on hot plate at 50 °C for 2 min. Then, the PMMA/CL-SAM/metal grid samples were mounted on a custom-designed sample holder and introduced into the chamber of a critical point dryer (Automated Critical Point Dryer, Leica EM CPD300), filled with acetone. After immersion in acetone for ~1 hour to remove the PMMA layer, a critical point drying program was performed.

4.7.3. XPS

The effect of electron irradiation was monitored by XPS. Representative XPS spectra of the pristine and irradiated Trip-T1 SAMs are shown in Figure 4.67. The irradiation was performed homogeneously over the entire sample area; the electron energy was set to 50 eV; the dose was varied from 3 to 40 mC/cm^2.

The Au 4f spectrum of the pristine SAM in Figure 4.67a exhibits the characteristic Au $4f_{7/2,5/2}$ doublet from the gold substrate. The intensity of this doublet does not change noticeably upon irradiation. For better visualization, this parameter as a function of dose is presented in Figure 4.68a. It is indeed nearly constant over the entire dose range, within the error of the experiments. This suggests that the material loss resulting from the irradiation is very small (if any at all), which is also supported by the behavior of the effective thickness calculated using the standard procedure, [84,88,89] on the basis of the attenuation of the Au 4f signal by the SAM overlayer and using a sample with a known thickness (C16/Au) as a reference (see section 3.2.3 for details), to determine the spectrometer-specific constant for the giving photoemission signal. The effective thickness of the pristine Trip-T1 SAM was estimated as 10.2 Å, in good agreement with the previous report.[61] Interestingly, it did not decrease after the irradiation but even slightly increased instead, viz. to 10.6 Å at 40 mC/cm^2. Such an increase stems presumably from the

adsorption of airborn molecules onto the chemically reactive surface of the irradiated SAMs, which is a well-known phenomenon.[223] Alternatively, deposition of the residual gas molecules during the irradiation was possible as well,[224,225] even though its extent was most likely very small (if any at all) at the given pressure in the chamber.

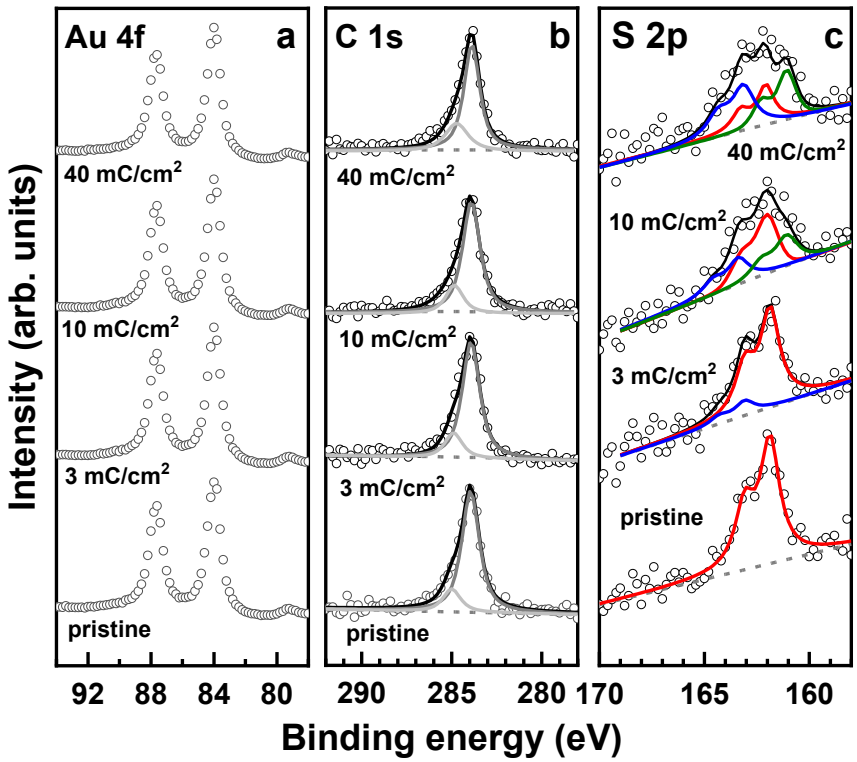

Figure 4.67. Au 4f (a), C 1s (b), and S 2p (c) XPS spectra of the pristine and irradiated Trip-T1 SAMs. The doses are given at the respective spectra. The C 1s spectra are tentatively decomposed into two peaks, associated with aromatic (gray) and aliphatic (light gray) carbon; The S 2p spectra are decomposed into the doublets corresponding to the pristine thiolate species (red), irradiation-induced sulfur species (blue), and atomically bound sulfur (olive). The background is shown by dashed grey lines.

The C 1s spectrum of the pristine Trip-T1 SAM in Figure 4.67b shows a single, slightly asymmetric peak at a BE of 284.0 eV. No contributions related to oxidative species or contamination are observed. The form and intensity of this peak hardly changes upon the irradiation, except a slight increase in the spectral weight at its high BE sign, well visible in particular at 40 mC/cm^2 and traced by the tentative spectra decomposition in two individual contributions. Considering that the high BE contribution is predominantly characteristic of aliphatic carbon (in contrast to the low BE contribution, characteristic of aromatic carbon),[25]

the observed behavior suggests an increase in the portion of single bonds in the irradiated SAMs. The total intensity of the C 1s signal and the intensities of the individual contributions are additionally presented in Figure 4.68b as functions of the irradiation dose. Whereas the total C 1s intensity shows no noticeable change, similar to the Au 4f signal, the intensities of the individual contributions exhibit a certain evolution, corresponding to a progressive decrease in the portion of double bonds and an increase in the portion of single bonds in the course of irradiation.

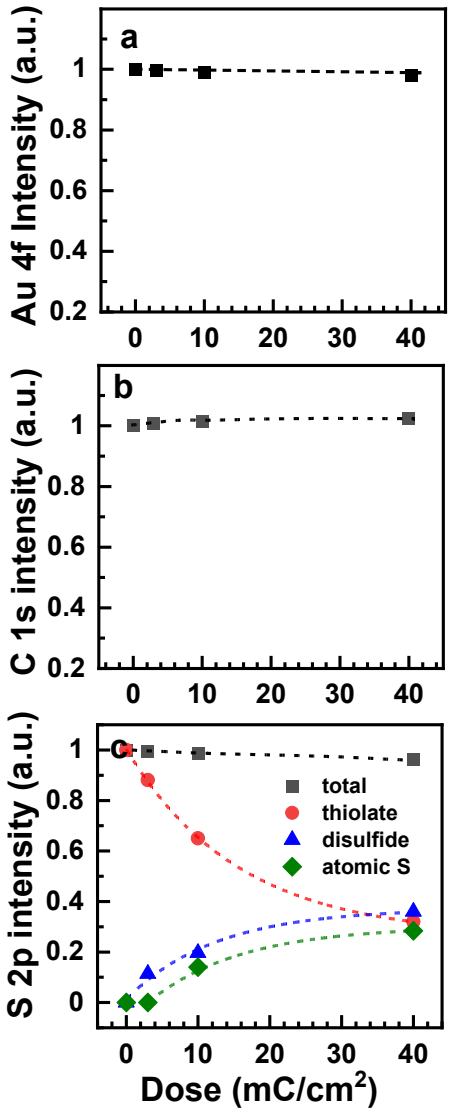

Figure 4.68. Dependence of the intensities of the characteristic XPS peaks and doublets in the spectra of the Trip-T1 SAM (Figure 4.67) on irradiation dose: (a) Au 4f signal; (b) total, aromatic, and aliphatic C 1s signal; (c) total, thiolate, "disulfide", and atomic sulfur S 2p signals. The legends are given in the panels. The dependences are tentatively traced by the color-coded dashed lines; for the thiolate and "disulfide" curves in panel (c) these are exponential functions.

The SAM-substrate interface was also affected by electron irradiation, as evidenced by the S 2p XPS spectra of the Trip-T1 SAMs shown in Figure 4.67c. For the pristine monolayer, only a single S $2p_{3/2,1/2}$ doublet at a BE of ~162.0 eV (S $2p_{3/2}$) is observed, indicative of the thiolate species bound to gold substrate.[226,227] No contributions associated with unbound sulfur, atomically adsorbed sulfur, disulfide, or oxidized sulfur species are observed, suggesting, in accordance with the previous report,[61] that all molecules in the Trip-T1 SAM are anchored to the substrate in the tripodal fashion. A packing density of 3.9×10^{14} thiolate/cm^2 was calculated using the standard procedure,[222] on the basis of the S 2p / Au 4f intensity ratio and a sample with a known packing density (C16/Au) as the reference. This value is somewhat lower than that which was reported before (4.6×10^{14} thiolate/cm^2)[61] but is still in the reasonable range, corresponding to a dense molecular packing. The difference between the current and reported packing density values is most likely related to the limited accuracy of the applied experimental techniques and evaluation procedures and lies within the precision of such estimations. At the same time, a certain variation in the quality and exact parameters of the Trip-T1 SAMs cannot be excluded.

The character of the spectra changes noticeably in the course of the irradiation treatment, which is well visible in Figure 4.67c and additionally traced in Figure 4.68c where the intensities of the relevant signals are shown. The intensity of the thiolate-related doublet decreases progressively with irradiation dose, accompanied by the appearance and progressive intensity increase of two new doublets at ~163.3 eV (S $2p_{3/2}$) and 161.1 eV (S $2p_{3/2}$). The first of these features is characteristic of thiol, weakly bound S, and disulfide species[227] appearing after the cleavage of the original thiolate-substrate bonds, which occurs typically in aromatic thiolate SAMs, with the extent depending on the molecular packing.[53,228] The second doublet is generally related to atomically adsorbed sulfur[222,229] appearing most likely after the cleavage of the C–S bonds, which does not happen typically at the electron irradiation of monopodal aromatic thiolate SAMs[53,228] but is rather characteristic of their modification at elevated temperatures.[222,229,230] Significantly, the total S 2p intensity decreases only slightly during irradiation, indicating a small extent of irradiation-induced material loss in the Trip-T1 SAM, which is consistent with the Au 4f and C 1s XPS data. The behavior of the thiolate and "disulfide" signal can be described by exponential function, as typical of most of irradiation-induced processes.[52] Only about 30% of the original thiolate bonds survive the extensive irradiation (40 mC/cm^2), which means that the coupling of the SAM to the substrate is

weakened. Otherwise, in view of the tripodal character of the monolayer, this means that, at the average, each SAM-forming molecule, is still anchored to the substrate by at least one thiolate bond. In contrast to the "disulfide" species, atomically bound S ones appear not immediately upon the irradiation but are recorded first at a certain dose, evolving then with a similar rate as the "disulfide" moieties.

4.7.4. NEXAFS Spectroscopy

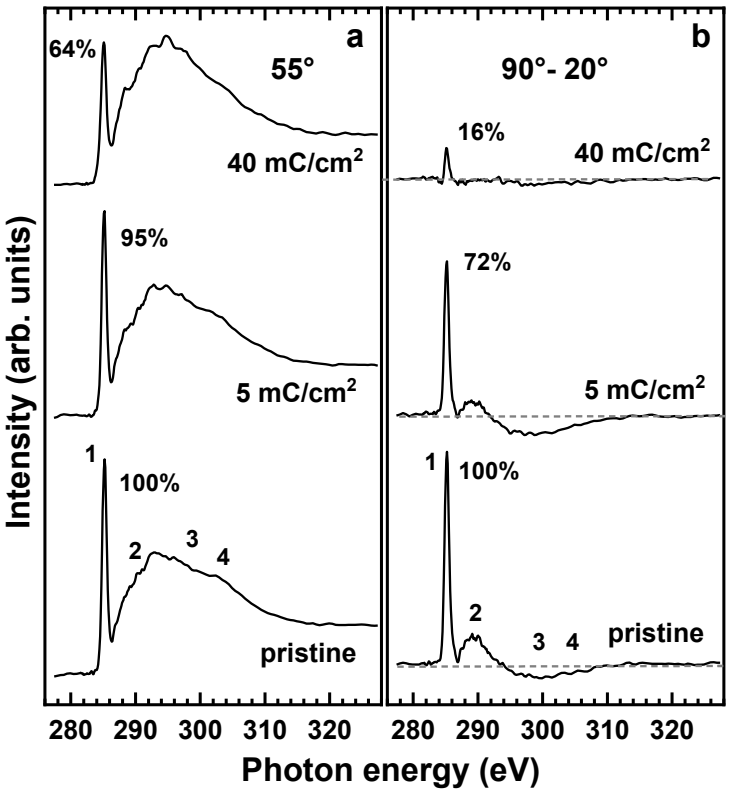

Figure 4.69. C K-edge NEXAFS data for the pristine and irradiated Trip-T1 SAMs: (a) the spectra acquired at an X-ray incidence angle of 55° and (b) the difference between the spectra acquired at X-ray incidence angles of 90° and 20°. The characteristic absorption resonances are marked by numbers, as detailed in the text. The doses are given at the respective spectra. Normalized intensities of the π_1* resonance and respective difference peak are marked at these features. The horizontal dashed lines in the difference spectra correspond to zero. Both panels have the same vertical scale, so that the intensities of the absorption resonances and respective difference peaks can be directly compared. The measurements were performed by Prof. M. Zharnikov.

Insight into the structural quality and molecular orientation of the Trip-T1 SAM before and after electron irradiation was obtained through the NEXAFS spectroscopy experiments. The representative data in Figure 4.69 include the spectra acquired at the magic angle of X-ray incidence (55°; Figure 4.69a) and the differences between the spectra obtained under normal (90°) and grazing (20°) incidence (Figure 4.69b). The former spectra exclusively display the electronic structure of the SAMs (unoccupied molecular orbitals) and are independent of the molecular orientation.[220,231] In contrast, the difference curves represent a useful fingerprint of the orientational order and molecular orientation.[220,231]

The 55° spectrum of the pristine Trip-T1 SAM in Figure 4.69a is dominated by the characteristic[61] π_1* resonance of the phenyl rings comprising the triptycene framework, located at a photon energy of ~285.25 eV (1). This feature is accompanied by several strongly overlapping π* (2) and σ* (3 and 4) resonances at the higher excitation energies. The spectra of the pristine Trip-T1 SAM exhibit strong linear dichroism (i.e., dependence of the resonance intensity on the X-ray incidence angle), as emphasized by the respective difference curve in Figure 4.69b. This curve shows the strong positive peak at the position of the π_1* resonance, which, in view of the orientation of the respective orbital (perpendicular to the phenyl blades), suggests a nearly upright orientation of the individual molecules in the SAM, in good agreement with the tripodal adsorption mode and the literature data.[61]

Both the 55° spectra and the difference curves change significantly at the irradiation, with the changes reflecting relative changes of the composition since the spectra are always normalized to the entire number of the carbon atoms. The major effects of the irradiation are (i) noticeable decrease in the intensity of the π_1* resonance (1), (ii) its slight broadening with irradiation dose (by ~10% at 40 mC/cm^2), (iii) its slight shift to the lower excitation energy (~285.1 eV at 40 mC/cm^2), (iv) changes in the fine structure of the 55° spectra, and (v) drastic decrease of the linear dichroism, best emphasized by the behavior of the π_1* peak (1) in the difference spectra.. The former three processes emphasize extensive transformation of the initial molecular assembly, involving a partial "damage" of the pristine triptycene frameworks and appearance of crosslinking bonds between the individual molecules. These new bonds have most likely a single-bond character, as follows from the intensity decrease of the π_1* resonance, which is generally not only representative of the intact phenyl rings but also of C=C bonds, even though with a slightly lower PE (285.0–285.05 eV).[220] The drastic decrease of the linear dichroism suggests a progressive and extensive loss of the orientational order in the SAMs, occurring parallel to their chemical modification and the changes in their coupling to the substrate.

4.7.5. EBL Studies

As follows from the above spectroscopic data, irradiation-induced crosslinking of the Trip-T1 SAM is accompanied by significant damage of the SAM-substrate interface, resulting in diminishing of the coupling to the substrate. Apart from the hybrid, aromatic-aliphatic structure of Trip-T1, this behavior raises a question of whether this SAM is capable of functioning as a negative resistor for electron lithography, similar to conventional, monopodal aromatic monolayers.[53,55,219] To this end, EBL experiments for Trip-T1 and PT1 SAMs were conducted, with the latter film serving as a reference monopodal system due to its similarity to an individual "blade" of Trip-T1. Representative patterns, written by EBL, transferred to the underlying gold film by the chemical etching, and visualized by AFM are shown in Figures 4.70 and 4.71 for the Trip-T1 and PT1 SAMs, respectively. Both patterns look very similar, exhibiting a good lithographic contrast with the well-defined, square-shaped gold features. These features mimic the areas irradiated by electrons, which means that both Trip-T1 and PT1 SAMs represent negative resists in context of electron lithography – the finding that is particular important for the tripodal Trip-T1 system. Note that the basic concept of utilizing aromatic SAMs as negative resists for EBL is based on the ability of crosslinked SAMs within the irradiated areas to safeguard the underlying substrate from etching, while the unirradiated areas covered by pristine SAM, consisting of individual molecules, can be etched away much more easily.

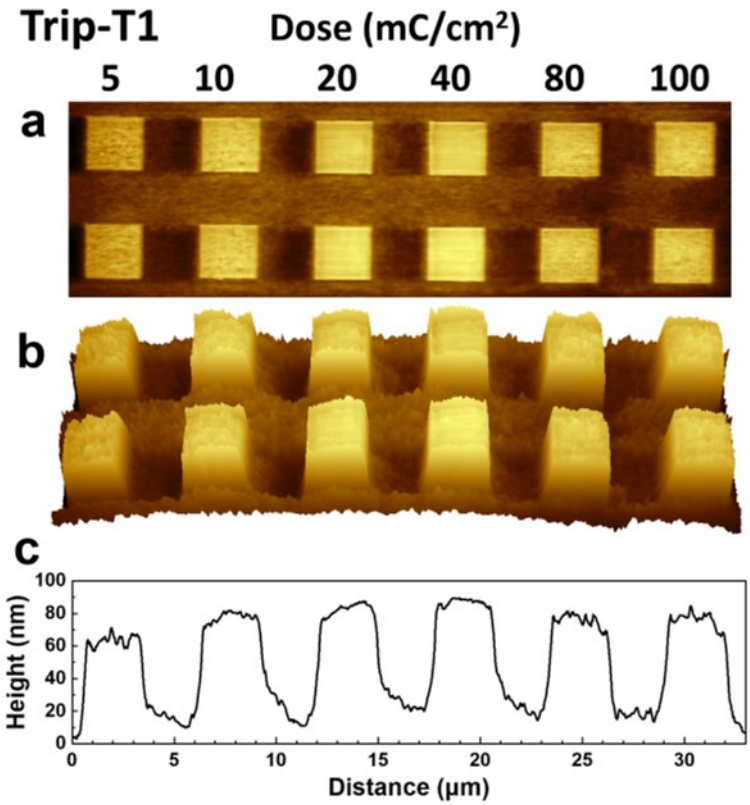

Figure 4.70. (a) 2D and (b) 3D view of the AFM images of Au/Si(100) patterns created using EBL (5 keV) with the Trip-T1 SAM resist, along with the respective height profile across the written, square-shaped Au features (c). The doses corresponding to the individual features were varied (from left to the right); they are marked at the top of the images.

The height and profile of the square-shaped features in the lithographic patterns in Figures 4.70 and 4.71 serve as indicators of the resist ability of the SAMs, which is proportional to the extent and "quality" of the crosslinking. For most of the irradiation doses, this height (~80 nm) is close to the thickness of the original gold film (~100 nm) which underlines a good performance of both SAM resists. Apart from the features for the lowest dose (5 mC/cm^2), which have a smaller height and less defined profile for the both SAMs, both patterns show a slight variation in the height and exact profile, which, on the one hand, can be an effect of the dose and, on the other hand, reflect a slight inhomogeneity of the etching. The lowest dose is obviously insufficient for complete crosslinking while the highest dose (100 mC/cm^2), corresponding to the somewhat lower features, induces probably too much damage, diminishing the efficiency of the resists. As to the range of the intermediate doses, the PT1-based pattern (Figure 4.71) looks slightly more homogeneous and square-shaped than the Trip-T1-stemming one (Figure 4.70), even though both patterns are quite similar, as mentioned above. This difference is probably related to the higher carbon atom density in the PT1 SAM compared to the Trip-T1

monolayer, which likely promotes better crosslinking in the case if the same dose is applied (see discussion in the next section).

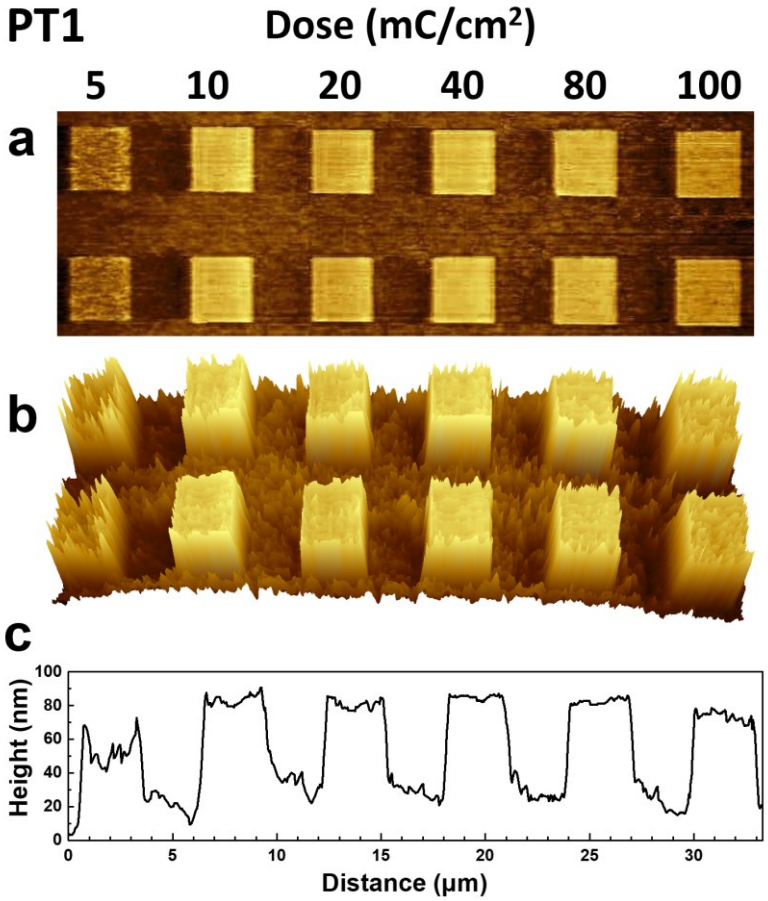

Figure 4.71. (a) 2D and (b) 3D view of the AFM images of Au/Si(100) patterns created using EBL (5 keV) with the PT1 SAM resist, along with the respective height profile across the written, square-shaped Au features (c). The doses corresponding to the individual features were varied (from left to the right); they are marked at the top of the images.

4.7.6. CNM Fabrication

The ability of Trip-T1 and PT1 SAMs to serve as precursors for CNMs was tested. The primary step of the preparation procedure was the irradiation of the pristine SAMs with a sufficiently high dose for extensive crosslinking. Afterwards, the films were separated from the substrate and transferred as CNMs onto the supporting metal mesh. SEM images of the resulting CNMs are presented in Figure 4.72. On the basis of the previous experience and the literature data,[219] a dose of 40 mC/cm^2, generally sufficient for a variety of aromatic SAMs, was initially applied. As displayed in Figures 4.72a and 4.72d, CNMs could be formed from both Trip-T1 and PT1

SAMs, even though with the different quality. Whereas the PT1-stemming CNM is nearly defect-free, that in the Trip-T1 case features numerous defects, such as holes, raptures, and folds. This means that the degree of crosslinking, associated with the dose of 40 mC/cm^2, is not entirely sufficient in the latter case, so that the respective Trip-T1-stemming film was obviously not robust enough to survive all the fabrication steps, necessary for its separation from the substrate and transfer onto the supporting grid. Considering this situation, a higher dose of 80 mC/cm^2 was then applied, resulting in the nearly defect-free CNMs for both Trip-T1 and PT-1 case, as shown in Figures 4.72b and 4.72c (larger area) for Trip-T1 and Figures 4.72e and 4.72f (larger area) for PT-1. Obviously, the corresponding extent of crosslinking is better suitable for the Trip-T1 SAM, whereas the PT1-stemming CNMs show the similar quality as in the 80 mC/cm^2 case. Note, also, that a dose of 80 mC/cm^2 should not be considered as an extremely high since, e.g., it is well comparable with a dose of 60 mC/cm^2 (50 and 100 eV electrons) reported for a variety of CNMs prepared from different precursors.[51]

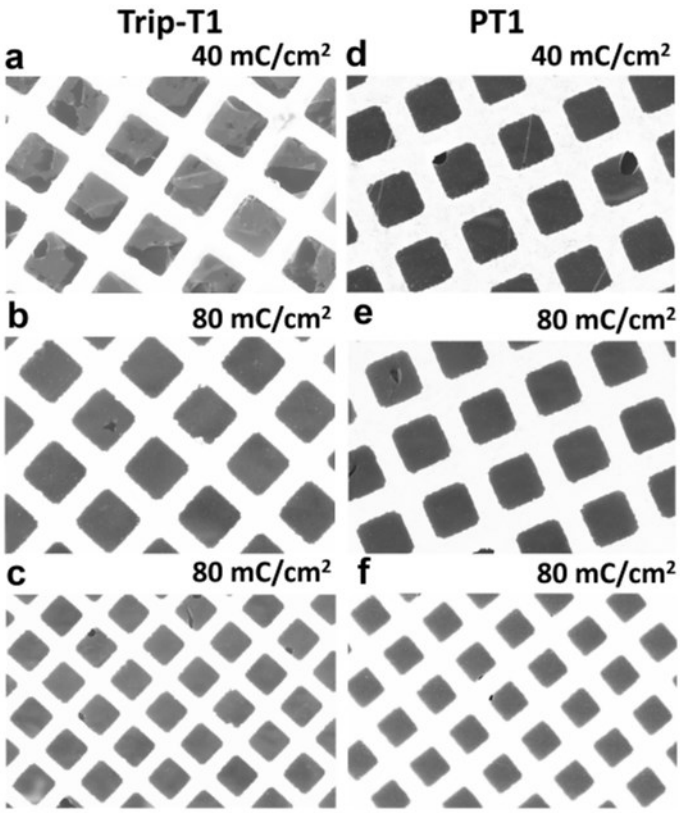

Figure 4.72. SEM images of the CNMs fabricated from the Trip-T1 (a–b) and PT1 (d–e) SAMs at two different doses, viz. 40 mC/cm^2 (a, d) and 80 mC/cm^2 (b, e). The images corresponding to a dose of 80 mC/cm^2 are additionally presented for a larger area, at a lower magnification (c, f). The length of the edge of the square openings of the supporting mesh is 10 μm.

4.7.7. Discussion

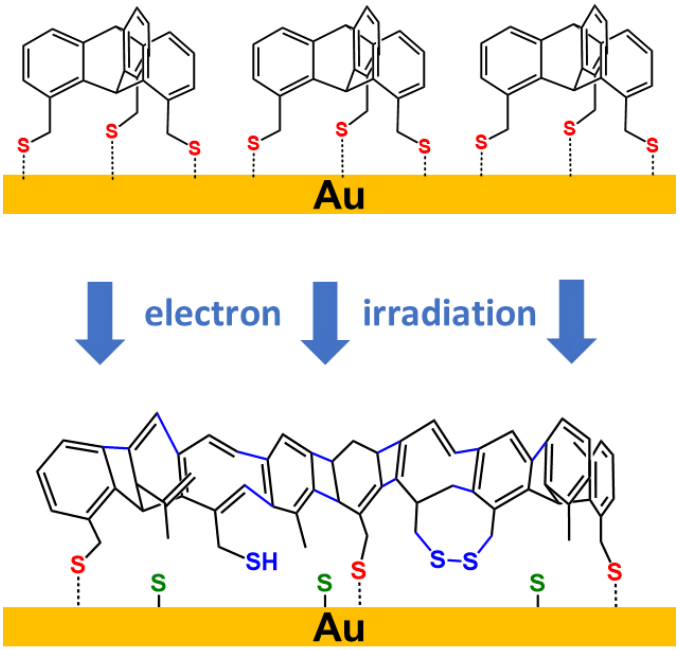

Figure 4.73. Schematic illustration of the irradiation-induced modification of the Trip-T1 SAM (a high dose).

Based on the entire bulk of the spectroscopy data, I propose a possible scheme illustrating the effect of electron irradiation on the Trip-T1 SAM, which is shown in Figure 4.73. Similar to the monopodal aromatic and aromatic-aliphatic monolayers, the crosslinking of the Trip-T1 SAM prevails over the film decomposition, apart from extensive chemical modification of the irradiated film. The intramolecular crosslinking is driven by the breakage of the original bonds within the triptycene frameworks, with the cleavage of less stable, peripherical C–H bonds playing probably the leading role. The interesting features of the Trip-T1 SAM are extensive modification of the SAM-substrate interface and the strong disordering at high irradiation doses. Note that, according to the literature data for monopodal monolayers,[228] the extent of these processes, occurring in correlated fashion,[228,232] depends strongly on the packing density and exact molecular arrangement in the film, being lower for the densely packed and highly oriented films and noticeably higher for the films featuring loose molecular packing and large molecular inclination. The latter features are not characteristic of the Trip-T1 SAM but, obviously, the specific character of the SAM-constituents and specific molecular arrangement[61] make this film particular prone to the cleavage of the original thiolate bonds and structural

disordering. Among other parameters, a pronounced feature of the triptycene molecule is the presence of the two bridging C atoms connecting the aromatic rings. The bridging C–C bonds are aliphatic in character and, consequently, similar to aliphatic SAMs, should be particular prone to cleavage. Breakage of these bridging bonds (also in combination with the cleavage of C–S bonds; see below) would open up new conformational degrees of freedom for the aromatic rings with the possibility to rotate out of their original plane. This, in turn, should allow for a more efficient crosslinking. As for the S–C bonds, they become cleaved at the SAM-substrate interface, in addition to the rapture of the thiolate-gold bonds. This process, manifested by the appearance of the characteristic fingerprint of atomically adsorbed S, viz. a doublet at 161.1 eV.[222,229] is untypical for monopodal aromatic and aromatic-aliphatic monolayers but seems to be significant for the Trip-T1 SAM and, probably, for other tripodal monolayers as well. Note that this doublet is frequently observed in such monolayers in the pristine state (see, e.g., refs [217,218]), and seems to gain even more weight upon electron irradiation.

The efficient crosslinking occurring in the Trip-T1 SAM upon electron irradiation ensures their ability to serve as a negative resist for EBL, which was verified by the dedicated experiments. Well-defined lithographic patterns, transferred to the underlaying gold substrate by chemical etching, could be formed over a broad range of irradiation doses (Figure 4.70). The quality of these patterns was comparable with that obtained with the reference monopodal resist – the PT1 monolayer, the constituents of which mimic individual "blades" of Trip-T1. According to the fabricated patterns, even a dose of 10 mC/cm^2 at an electron energy of 5 keV is sufficient for high lithographic contrast. Considering that the efficiency of 5 keV electrons in the context of the crosslinking is even somewhat lower than that of the 50 eV electrons, used in the spectroscopic experiments,[219] this behavior means that even a moderate crosslinking of the Trip-T1 SAM is sufficient for high lithographic contrast.

The situation is, however, distinctly different as soon as it comes to the CNM fabrication. Whereas CNMs could be successfully fabricated on the basis of the Trip-T1 SAM (Figure 4.72), it required quite a high dose (80 mC/cm^2) to get them sufficiently robust to survive the separation from the substrate, getting rid of the underlying Au and protective PMMA layers, and transfer to the supporting mesh as defect-free, free-standing films. In contrast, in the case of the reference PT1 SAM, a nearly defect-free CNM could already be obtained at a dose of 40 mC/cm^2, even though the quality of the analogous CNM obtained at a dose of 80 mC/cm^2 was somewhat higher (Figure 4.72).

An interesting aspect of the use of the Trip-T1 and PT1 SAM as resists for EBL and precursors for CNMs is their areal density, which was estimated at ~29.1 and ~32.2 C atoms/nm^2, respectively, on the basis of the molecular structure and the XPS data. These values are noticeably smaller than that for the biphenylthiolate SAM on Au(111) (55.6 C atoms/nm^2), representing the most frequently used platform in the given context,[44,45,53] and even smaller than that for graphene (38.2 C atoms/nm^2), serving as an ultimate reference for ultrathin carbonous films. Nevertheless, both Trip-T1 and PT1 SAMs could be successfully used in the EBL and CNM context. Significantly, the phenylthiolate (PT) monolayer, differing from PT1 by the methylene linker only (a single C atom), exhibited a poor performance for EBL and did not result in robust CNMs,[219] which could first be obtained from napthalenethiolate SAM (46.3 C atoms/nm^2).[51,219] Consequently, PT1 represents the smallest SAM-forming compound used so far for the CNM fabrication. The reason for the superior performance of PT1 compared to PT is not just the presence of one more carbon atom but the significant impact of the methylene linker on the SAM quality. Whereas the PT monolayer is poorly defined,[233,234] the introduction of the methylene linker improves the quality of the SAM considerably,[25,44] relying on the optimal adjustment of the adsorption geometry to the bending potential at the Au–S–C joint (odd-even effects in monomolecular assembly).[235–238] The design of Trip-T1 takes advantage of the same concept, which, along with the structure of the triptycene framework, ensures the tripodal adsorption mode and superior structural quality of the respective SAM.

5. Conclusions and Outlook

In conclusion, within my PhD project, I studied the properties of the PEG films and nanosheets, formed by crosslinking of the epoxide- and amino-terminated four-arm STAR-PEG precursors, while also delving into respective applications of these systems. In addition to the freestanding nanosheets on the PEG basis, I also demonstrated the potential of using multipodal aromatic SAMs in the context of EBL and CNM fabrication, with the latter being another representative example of freestanding nanosheets. The details are as follows:

In the first subproject, I studied the modification of the PEG films by UV light (254nm). The thickness of the pristine PEG films was varied from ~32 to ~124 nm; the flux was mostly kept at 2 mW/cm^2, and the dose was varied up to 85 J/cm^2. The exposure of the films to UV light leads to progressive decomposition of the PEG material with desorption of the vast majority of the released fragments directly during the irradiation. This process, however, does not affect the chemical composition of the residual film, which preserves all the properties of the original PEG material, including the hydrogel behavior and bioinertness, as was specifically demonstrated by the dedicated experiments. This behavior was in the striking contrast to the effect of electron irradiation on the PEG films and the effect of UV irradiation on OEG-substituted SAMs, for which the removal of the PEG/OEG material was accompanied by substantial chemical modification of the residual part, losing its bioinert properties.

Further, I studied the effect of MW on the properties of the PEG films. It was demonstrated that these films can be prepared from the precursors with different MWs, varying from 2000 to 20000 g/mol. The separation of these films as free-standing nanosheets was also possible. The thickness of the films and nanosheets could be varied in the range from 10 to 330 nm by setting the concentration of the precursors in the primary solution, with a noticeable dependence on the MW at the sufficiently high concentrations. The films and nanosheets prepared from the different precursors exhibited pronounced bioinert, hydrogel and elastic properties, with the exact parameters depending on the MW of the precursors. The most important differences were the efficient mesh size of the crosslinked network, probed by the protein absorption experiments on the comparably thin films, and the elastic properties studied by the bulge test on the nanosheets. The efficient mesh size expectedly increased with the MW, most likely not that much as the MW itself but still sufficient to improve noticeably the permeability of the PEG films for biomolecules. The PEG nanosheets have very small Young's module (E) values, ranging from of 2.1 to 5.2 MPa for 100 nm thickness. Interestingly, the E

value does not decrease with the MW, as can be assumed from general considerations of the PEG network architecture, but progressively increases, which was tentatively explained by the enhanced alignment of the PEG chains in the network at the high MWs.

Considering the exceptional elastic properties of the PEG nanosheets, I studied them in depth, taking the nanosheets prepared from the precursors with a moderate MW (2k) as a representative example. A variety of parameters was varied and the effect of electron and UV-light treatment on the elastic properties of PEG nanosheets was studied as well. As the main experimental technique, bulge test was used. It was demonstrated that the major parameter of the bulge test approach – size of the window – does not influence the results, which was in particular useful to monitor the dependence of the Young's modulus on the nanosheet thickness. The *E* value was found to increase from 2.08 MPa to 2.6 MPa at the thickness variation from 40 to 320 nm, with a stronger variation at small thicknesses. These values are very small, rendering the PEG nanosheets extremely elastic, presumably – due to elastomer-like behavior of the crosslinked network. This behavior does not change dramatically but deteriorates only slightly at a deviation from the standard, 1:1 composition of the films, characterized by a lesser extent of crosslinking. A significant deterioration of the elastic properties occurs, however, at the electron irradiation of the films, which is associated with their extensive chemical modification, apart from a reduction of their thickness. In contrast, UV light (254 nm) only causes a reduction of their thickness and does not result in any change of their elastic properties. This is one more evidence that the only effect of UV light on all-PEG films is decomposition of the PEG material, followed by desorption of the released fragments. The exact mechanism behind this behavior is not fully understood yet and should be clarified. However, one of the possible scenarios, viz. the effect of UV-induced, "hot" electrons from the substrate could be excluded by the comparison of the electron- and UV-light-treated membranes and by the additional spectroscopic data. A most likely reason for the failure of this mechanism for the PEG membranes is their weak electronic coupling to the substrate, making the tunneling of "hot" electrons into the film material hardly possible.

Within the further subprojects, I explored the possibility of using the PEG films as a platform for ssDNA sensing, relying on the immobilization of probe ssDNA strands, capable of hybridization with complementary target sequences, in the PEG matrix. Two approaches were employed for ssDNA immobilization in the PEG films. The first method involved the reaction of free NH_2 groups in the PEG films and NHS groups in NHS-ester-substituted homo-oligonucleotide ssDNA. XPS and electrochemical techniques were utilized to monitor the

immobilization and hybridization. While XPS monitoring is generally complex and costly, EIS was found to be efficient, cost-effective, and label-free transduction technique. Within the second method, the introduction of the probe ssDNA relied on thiol-epoxy linkage, leveraging the epoxy-rich PEG film and thiol-modified ssDNA. Control over probe ssDNA immobilization was achieved by adjusting its concentration in the buffer solution. Electrochemical tools, especially EIS, effectively monitored these processes, offering qualitative and quantitative insights. The latter approach was compared to thiolated ssDNA directly attached to the same Au substrate. Both systems showed similar hybridization efficiencies to target strands, but the direct ssDNA assembly on Au did not fully prevent non-specific adsorption of mismatching sequences, likely accessing the Au substrate at defect sites of the probe ssDNA film. Within both approaches, reasonable density of the immobilized probe ssDNA was realized. The resulting ssDNA-decorated PEG film displayed high hybridization activity and selectivity toward matching target ssDNA strands while preventing non-specific adsorption of non-matching strands. The above findings underscore the potential of employing EIS as an effective method for ssDNA sensing, useful in particular in the combination with the ssDNA-decorated, bioinert PEG platform. This platform holds promise for diverse applications in biosensing, ssDNA detection, and nanotechnology.

Along with the pure PEG films and related, free-standing nanosheets, I fabricated a series of PEG-C60 composite films on the basis of 2k STAR-PEG precursors. Three different methods, termed as immersion, one-pot, and reflux, were used. In all cases, C60 formed disc-like shaped clusters with a narrow size distribution (an average diameter of 226–310 nm) which were either located on the surface of the PEG films (immersion) or embedded in their bulk, wrapped physically in the PEG network (one-pot) or coupled to it chemically (reflux). The portion of C60 in the composite films varied depending on the preparation method, achieving ~30% in the case of reflux. The composite films exhibited distinct optical and electrochemical properties associated with variations in the supramolecular organization of C60 clusters governed by the physical interplay between the hydrophobicity of fullerenes and the hydrophilicity of PEG. Specifically, the characteristic absorption peak of C60 at 314–329 nm, with the intensity defined by the C60 content in the films, was observed in the UV-vis spectra. The position of this peak was affected by the coupling between individual C60 molecules in the clusters, governed by their interaction with the PEG matrix. The CV and SWV curves of the composite films exhibited the characteristic reduction feature of C60 at –(0.71–0.84) V. The variation of the respective voltage suggested a variation of the LUMO energy for the C60 clusters, with up

to 70 meV difference for the different preparation methods. The R_{ct} value of the PEG films, which was comparably low due to their porosity, was found to decrease even further by the admixture of C60, favoring electrochemical applications of the composite films. Moreover, these films adopted the superior elastic properties of the parent PEG layers, which was demonstrated by the fabrication and testing of free-standing composite nanosheets. Significantly, the transfer of these nanosheets to a secondary substrate involved only a minor deterioration of the electrochemical properties.

The PEG-related subprojects hold great potential for future research, in view of the exceptional properties of the PEG films and free-standing nanosheets as proved above, including the unique bioinert, hydrogel and elastic properties in particular. For example, such PEG films can be potentially interesting for applications, such as biomolecule-friendly supports for biological samples in high-resolution TEM,[28,239,240] a sensitive element of pressure sensors[156] or microelectromechanical systems,[241,242] and a matrix for biosensors, and so on. Moreover, the effect of UV light on the PEG films can be applied to 3D patterning of an all-PEG material, which can be potentially useful for applications involving, e.g., morphology control of bioinert surfaces or fabrication of specific microchannel structure on such a surface. In addition, the MW of the STAR-PEG precursors is a useful tool, allowing fine-tuning of the parameters to meet specific requirements of a particular application. Moreover, the studies of the probe-ssDNA loaded, bioinert PEG films underscore the potential of employing EIS as an effective method for ssDNA sensing. This platform holds promise for diverse applications in biosensing, ssDNA detection, and nanotechnology. The PEG film is also a suitable playground for the fabrication of hybrid materials, as demonstrated by the PEG-C60 composite films and free-standing nanosheets, which can be potentially useful for flexible thin-film transistors, optical sensors, and electrochemical applications, which can be the subjects of studies in the future. The bioinert character of the PEG network makes applications in the field of biosensors especially promising and it would be great to extend the laboratory proof-of-principle experiments to prototype devices.

Finally, I studied the potential of multipodal aromatic SAMs in context of EBL and CNM fabrication. As a test system, tripodal-anchored, aromatic-aliphatic Trip-T1 monolayer on Au(111) was used. The detailed spectroscopy characterization of this SAM confirmed its high quality, including the homogeneous anchoring chemistry, dense molecular packing, and high orientational order. Exposure of the SAM to electron irradiation resulted in its extensive chemical transformation, damage of the SAM-substrate interface, and the loss of orientational

order. All these modifications were, however, not accompanied by noticeable loss of material, which suggested extensive irradiation-induced crosslinking within the molecular matrix, similar to the traditional, monopodal aromatic SAMs. The above behavior suggested that the Trip-T1 SAM might be a suitable candidate for EBL, serving as a negative resist, which was indeed verified by the dedicated lithographic experiments. The quality of the lithographic patterns fabricated with the Trip-T1 resist over a broad range of irradiation doses was found to be similar to that of the reference monopodal system – PT1 monolayer, whose constituents represented individual "blades" of Trip-T1. Moreover, similar to the monopodal aromatic SAMs, including PT1 monolayer in particular, the Trip-T1 SAM turned out to be suitable to serve as a precursor for CNM fabrication. The only difference with respect to the monopodal PT1 system was the comparably high irradiation dose (80 mC/cm^2) necessary for the fabrication of sufficiently robust and defect-free Trip-T1-stemming CNMs. Interestingly, the lateral material density of both Trip-T1 and PT1 SAMs is lower than that of all other precursors used for the CNM fabrication so far, which makes them unique in this regard and probably useful for specific applications.

This latter part of my work opens thus new possibilities for SAM-based EBL and CNM fabrication, showing that multipodal molecular systems can serve as useful alternative to traditional monopodal films and nanosheets, extending thus the pool of the primary materials and providing new possibilities for applications.

Lists

List of Figures

2.1. Structures of STAR-PEGs with various functional end groups

2.2. Illustration of an ideally ordered SAM

2.3 Energy level diagram in XPS measurements, including the *hv*, BE, KE, as well as the work function of the spectrometer and the sample

2.4. Schematic representation of an XPS system

2.5. XPS overview spectrum of a PEG (50 nm) film on Au substrate

2.6. A NEXAFS spectrum

2.7. Schematic potential for an isolated atom and a diatomic molecule

2.8. Schematic illustration of an ellipsometry experiment

2.9. Schematic illustration of a bulge test setup along with relevant parameters

2.10. Schematic illustration of SEM

2.11. Illustration of an electrochemistry system

2.12. CV technique along with its input and output response

2.13. General input nature of the linear sweep square-wave voltammogram and output of a linear sweep square-wave voltammogram

2.14. A basic equivalent circuit model along with its corresponding Nyquist plot

3.1. The chemical structures of STAR-NH_2 and STAR-EPX and a schematic drawing of the reaction between the terminal epoxy and amine groups of the precursors resulting in the appearance of ethanol-amine-like crosslinking bonds

4.1. Thicknesses of different PEG films as a function of the UV dose

4.2. Thickness of a PEG film as a function of the UV dose under different fluxes

4.3. Au 4f XPS spectra of the pristine (~32 nm) and irradiated PEG films on Au substrate

4.4. Thickness of a PEG film measured by ellipsometry and XPS as a function of the UV dose

4.5. C 1s and O 1s XPS spectra of the pristine (~71 nm) and UV-irradiated PEG films

4.6. Thickness of the pristine and UV-irradiated PEG films as a function of temperature

4.7. Swelling ratio for the PEG films as a function of the UV dose

4.8 N 1s XPS spectra of the pristine and irradiated PEG films exposed to BSA along with the spectrum of the pristine PEG film before the BSA exposure and spectrum of a protein-adhesive substrate (Au) after the BSA exposure

4.9. Relative extent of the protein adsorption as a function of the thickness of PEG films

4.10 Schematic of the modification of the PEG films in the case of electron and UV irradiation
4.11. Schematic of the patterning of the PEG films in proximity printing geometry, along with an AFM image of a PEG pattern fabricated with a dose of 28.8 J/cm^2 and its height profile
4.12. Thickness of the PEG films with the different MWs determined by ellipsometry as a function of the concentration of the precursors (in mg/mL or mM)
4.13. C 1s, O 1s, and N 1s XPS spectra of the PEG films prepared from the precursors (10 mg/mL) with the different MWs
4.14. C 1s, O 1s, and N 1s XPS spectra of the PEG films prepared from the precursors (20 mg/mL) with the different MWs
4.15. C 1s, O 1s, and N 1s XPS spectra of the PEG films prepared from the precursors (30 mg/mL) with the different MWs
4.16. Thickness of the PEG films (different MWs) as a function of temperature
4.17. The swelling ratio as a function of the MW for the films prepared at the different concentrations of the precursors
4.18. Thickness of the PEG films prepared from the precursors with the different MWs as function of temperature and the swelling ratio of these films as a function of the MW.
4.19. N 1s XPS spectra of the PEG film before and after the BSA exposure, along with the reference spectrum of a protein-adhesive substrate (Au) after the BSA exposure; Relative protein absorption of PEG films as a function of the MW.
4.20. N 1s XPS spectra of the thinner PEG films with different MWs of the precursors but similar thickness (~50 nm) before and after the BSA exposure.
4.21. N 1s XPS spectra of the thicker PEG films with different MWs of the precursors but similar thickness (~100 nm) before and after the BSA exposure.
4.22. SEM images of the PEG/AuNP composite films (~100 nm) prepared from the precursors with different MWs.
4.23. Size distributions of the AuNPs in the PEG-AuNP composites prepared from the precursors with different MWs.
4.24. UV-vis spectra of the PEG/AuNP composite films (~100 nm) prepared from the precursors with different MWs
4.25. AFM images of the PEG nanosheets transferred onto Si substrate, along with the height profiles across the edges of the nanosheets
4.26. Microscopy images of deflected PEG nanosheets with different MWs.

4.27. Plots of $\Delta p/h$ as a function of h^2 for the PEG nanosheets (~100 nm) with different MWs, and calculated Young's moduli of the nanosheets vs. the MW, as well as a variation of the thickness of the PEG nanosheets during the bulge test
4.28. A model explaining the extremely high elasticity of the PEG nanosheets
4.29. Selected optical images of the deflected PEG nanosheets, suspended over a circular window with different diameters
4.30. Δp vs h, and h/a vs $\Delta p\ a\ /\ t$ plots for the PEG nanosheets suspended over the circular windows with the different diameters, as well as the thickness of the nanosheets as a function of Δp
4.31. $\Delta p/h$ vs h^2 plots for the PEG nanosheets suspended over the circular window with different diameters
4.32. Young's modulus and residual stress as a function of the nanosheet thickness
4.33. Δp vs h plots for the PEG nanosheets prepared at the different mixing ratios of the STAR-NH_2 and STAR-EPX precursors
4.34. C 1s and O 1s XPS spectra of the pristine and electron-irradiated PEG films.
4.35. Δp vs h plots for the pristine and electron-irradiated PEG nanosheets, and the pressure corresponding to the breaking of these nanosheets as a function of irradiation dose, as well as Young's modulus of these nanosheets as a function of irradiation dose
4.36. Δp vs h plots for the pristine and UV-irradiated PEG nanosheets, and Young's modulus of these nanosheets as a function of the nanosheet thickness
4.37. C 1s and O 1s XPS spectra of the pristine and UV-irradiated PEG films deposited on Au substrate
4.38. The structures of the NHS-Tn, An, and Tn compounds, as well as a schematic illustration of the NHS-Tn immobilization in the PEG matrix over the free NH_2 groups and its subsequent reaction with the An and Tn targets
4.39. C 1s, O 1s, and N 1s XPS spectra of 1:1 PEG films before and after their incubation into the T5, A5, T10 and A10 solutions
4.40. C 1s, O 1s, and N 1s XPS spectra of 1:1 PEG films before and after their incubation into the T5 and T10 solutions, and the corresponding films after once more incubation into A5 and A10 target ssDNA solutions
4.41. C 1s, O 1s, and N 1s XPS spectra of the 2:1 PEG films before and after their incubation into the A10 and T10 solutions

4.42. C 1s, N 1s, and P 2p XPS spectra of the original 2:1 PEG film, PEG/NHS-T5, and PEG/NHS-T5 probe film exposed to T5 and A5 target ssDNA
4.43. C 1s, N 1s, and P 2p XPS spectra of the original 2:1 PEG film, PEG/NHS-T10, and PEG/NHS-T10 probe film exposed to T10 and A10 target ssDNA
4.44. C 1s, O 1s, and N 1s XPS spectra of the ultrathin 1:1 PEG film (15 nm) before and after their incubation into the A10 and T10 solutions
4.45. C 1s and N1s XPS spectra of the Si/SiO_2 substrate before and after their incubation into the A10 and T10 solutions
4.46. CVs and Nyquist plots for the blank Au electrode and Au/PEG electrode before and after its incubation into the non-substituted A10 and T10 solutions
4.47. CVs and Nyquist plots for the Au/PEG working electrode and the Au/PEG/NHS-T5 electrode before and after its exposure to T5 and A5 target ssDNA.
4.48. CVs and Nyquist plots for the Au/PEG/NHS-T10 working electrode before and after its exposure to T10 and A10 target ssDNA
4.49. Nyquist plots and the derived R_{ct} values for the Au/PEG/NHS-T10 working electrode before and after exposure to A10 target ssDNA
4.50. Schematic illustration of the immobilization of probe ssDNA (T10-SH) into an epoxy-rich PEG film, followed by the subsequent reaction with matched (A10) and (T10) targets; as well as the immobilization of T10-SH onto a pure Au substrate and its reaction with the mismatched T10.
4.51. CV curves and Nyquist plots for the bare Au electrode and Au/PEG electrode (epoxy-rich film) before and after its incubation into the T10-SH solutions with different concentrations. Dependence of the R_{ct} gain upon the exposure of Au/PEG to T10-SH on the concentration of T10-SH.
4.52. CV curves and Nyquist plots for the Au/PEG electrode before and after its exposure into T10 or T10-SH solutions (2 μM).
4.53. Nyquist plots for the Au/equilibrium PEG electrode, and the Au/epoxy-poor PEG electrode before and after their exposure into T10-SH solution (2 μM).
4.54. CV curves and Nyquist plots for the Au/PEG + T10-SH electrode before and after its exposure to mismatching (T10) and matching (A10) target ssDNA. The concentration of both probe and target ssDNA was set as 2 μM.
4.55. CV curves and Nyquist plots for the Au + T10-SH electrode before and after its exposure to mismatching (T10) and matching (A10) target ssDNA. The concentration of both probe and target ssDNA was set as 2 μM.

4.56. P 2p (a) and N 1s (b) XPS spectra of the Au + T10-SH (2μM) and Au/PEG + T10-SH (2μM) films before and after their exposure to the target A10 sequence (2μM).
4.57. Nyquist plots and the derived R_{ct} values for the Au/PEG + T10-SH electrode after its exposure to matching A10 target ssDNA.
4.58. Schematic illustration of the fabrication procedures for pure C60 and different PEG-C60 composite films
4.59. SEM images of deposited C60 and PEG-C60 composite films prepared by different methods, as well as AFM image of the reflux PEG-C60 film and height profiles along the blue lines in the AFM image
4.60. C 1s XPS spectra of the PEG film, pure C60, and PEG-C60 composite films prepared by different methods, as well as N 1s XPS spectra of the STAR-NH_2 precursor before and after its reaction with C60 under reflux
4.61. UV-vis spectra of the of the PEG film, pure C60, and PEG-C60 composite films prepared by different methods
4.62. CV curves of the bare and C60-decorated GCE working electrode; SWV curves of the Au/PEG, Au-C60, and Au/PEG-C60 electrodes and Nyquist plots for these electrodes
4.63. SWV curves for the Au/C60 electrode and Au/PEG-C60 electrodes prepared by the different methods before and after extensive rinse with toluene, as well as SEM images of the Au/PEG-C60 (immersion) and Au/PEG-C60 (reflux) electrodes before and after extensive rinse with toluene
4.64. Optical images of the deflected PEG and PEG-C60 nanosheets close to their breaking points and Deflection vs. pressure plots for these nanosheets
4.65. SWV curves of the reflux PEG-C60 film prepared on Au electrode and the same film transferred as a free-standing nanosheet onto the Au electrode from the primary SiO_2/Si substrate, as well as Nyquist plots for these samples
4.66. Structures of the precursors for the SAM studied, along with their abbreviations and schematics of monomolecular assembly on Au(111)
4.67. Au 4f, C 1s, and S 2p XPS spectra of the pristine and electron-irradiated Trip-T1 SAMs
4.68. Dependence of the intensities of the characteristic XPS peaks and doublets in the spectra of the Trip-T1 SAM on irradiation dose
4.69. C K-edge NEXAFS data for the pristine and irradiated Trip-T1 SAMs, including the spectra acquired at an X-ray incidence angle of 55° and the difference between the spectra acquired at X-ray incidence angles of 90° and 20°

4.70. 2D and 3D view of the AFM images of Au/Si(100) patterns created using EBL (5 keV) with the Trip-T1 SAM resist, along with the respective height profile across the written, square-shaped Au features
4.71. 2D and 3D view of the AFM images of Au/Si(100) patterns created using EBL (5 keV) with the PT1 SAM resist, along with the respective height profile across the written, square-shaped Au features
4.72. SEM images of the CNMs fabricated from the Trip-T1 and PT1 SAMs at 40 mC/cm^2 and 80 mC/cm^2
4.73. Schematic illustration of the irradiation-induced modification of the Trip-T1 SAM (a high dose).

List of Tables

4.1. Capacitance with respect to the cell with the blank Au working electrode and the charge transfer resistance associated with the specific samples

4.2. R_{ct} values for Au, Au/PEG, and Au/PEG + T10-SH (variable concentration)

4.3. R_{ct} values before and after T10-SH exposure for the epoxy-rich, equilibrium, and epoxy-poor PEG films

4.4. R_{ct} values for the Au/PEG related samples

4.5. R_{ct} values for the Au/ssDNA related samples

4.6. The average C60 cluster size, portion of C60, absorbance, and absorbance maximum (λ_{max}) for the reference C60 sample and PEG-C60 films

4.7. Position of the first reduction peak, LUMO energy, and charge transfer resistance of the specific electrodes.

List of Abbreviations

A	Adenine
A5	5'−AAAAA−3'
A10	5'−AAAAAAAAAA−3'
AFM	Atomic force microscopy
BE	Binding energy
BSA	Bovine serum albumin
C16	1-Hexadecanethiol
CL-CAM	Crosslinked self-assembled monolayers
CNM	Carbon nanomembrane
CV	Cyclic voltammetry
EBL	Electron beam lithography
EIS	Impedance spectroscopy
IP	Ionization potential
KE	Kinetic energy
LSPR	Local surface plasmon resonance
LUMO	Lowest unoccupied molecular orbital
MW	Molecular weight
NEXAFS	Near edge X-ray adsorption fine structure spectroscopy
NHS-T5	N-hydroxy succinimide ester−$(CH_2)_{10}$−5'−TTTTT−3'
NHS-T10	N-hydroxy succinimide ester−$(CH_2)_{10}$−5'−TTTTTTTTTT−3'
PBS	Phosphate-buffered saline
PEG	Poly(ethylene glycol)
PMMA	Polymethylmethacrylate
PT	Phenylthiolate
PT1	Dibenzyl disulfide
SAM	Self-assembled monolayer
SEM	Scanning electron microscopy
STAR-PEG	Star poly(ethylene glycol)
STAR-NH_2	4-arm star PEG precursor terminated with amine
STAR-EPX	4-arm star PEG precursor terminated with epoxy
ssDNA	Single-stranded deoxyribonucleic acid
SWV	Square-wave voltammetry

T	Thymine
T5	5'−TTTTT−3'
T10	5'−TTTTTTTTTT−3'
T10-SH	Thiol−$(CH_2)_6$−5'−TTTTTTTTTT−3'
Trip-T1	1,8,13-trimercaptomethyl-triptycene
UHV	Ultra-high vacuum
UV-vis	Ultraviolet and visible
XPS	X-ray photoelectron spectroscopy

List of Publications

Included in this thesis

1. Zhao, Z.; Yan, R.; Zharnikov, M. The Effect of Ultraviolet Light on Biorepulsive Hydrogel Poly(ethylene glycol) Films. *ACS Appl. Polym. Mater*. **2021**, *3*, 3446–3454.

2. Zhao, Z.; Das, S.; Zharnikov, M. Tuning the Properties of Poly(ethylene glycol) Films and Membranes by the Molecular Weight of the Precursors. *ACS Appl. Polym. Mater*. **2022**, *4*, 645–653.

3. Zhao, Z.; Zharnikov, M. Elastic Properties of Poly(ethylene glycol) Nanomembranes and Respective Implications. *Membranes* **2022**, *12*, 509.

4. Zhao, Z.; Das, S.; Zharnikov, M. Rational Design of Porous Poly(ethylene glycol) Films as a Matrix for ssDNA Immobilization and Hybridization. *Bioengineering* **2022**, *9*, 414.

5. Zhao, Z.; Das, S.; Zharnikov, M. Poly (ethylene glycol)-Fullerene Composite Films and Free-Standing Nanosheets for Flexible Electronic Devices and Sensors. *ACS Appl. Nano Mater.* **2023***, 6,* 2151−2161.

6. Zhao, Z.; Fukushima, T.; Zharnikov, M. Electron-Induced Modification of Triptycene Self-Assembled Monolayer in Context of Lithography and Nanofabrication. *J. Phys. Chem. C* **2023**, *127*, 15582−15590.

7. Zhao, Z.; Zharnikov, M. Exploiting Epoxy-Rich Poly(ethylene glycol) Film for Highly Selective ssDNA Sensing via Electrochemical Impedance Spectroscopy. *Phys. Chem. Chem. Phys*. **2023**, *25*, 26538–26548.

Besides this thesis

1. Das, S.; Zhao, Z.; Terfort, A.; Zharnikov, M. Probing Matrix Effects in the Course of Electron Transfer across a Self-Assembled Monolayer. *J. Phys. Chem. C* **2022**, *126*, 17415–17423.

2. Balser, S.; Zhao, Z.; Zharnikov, M.; Terfort, A. Effect of the Crosslinking Agent on the Biorepulsive and Mechanical Properties of Polyglycerol Membranes. *Colloids Surf. B* **2023**, *225*, 113271.

3. Guo, P.; Singer, L.; Zhao, Z.; Kukułka, W.; Sebastian, F.; Mijowska, E.; Zharnikov, M.; Comba, P.; Klingeler, R. a Facile Preparation Method and Proof of Cycle-Stability of Carbon-Coated Metal Oxide and Disulfide Battery Materials. *Electrochim. Acta* **2023**, *459*, 142540.

4. Zhao, Z.; Zharnikov, M. Gold Nanoparticle Loaded Porous Poly(ethylene glycol) Nanosheets for Electrochemical Detection of H_2O_2. *Nanomaterials*, In press.

References

(1) Shi, D. *Functional Thin Films and Functional Materials: New Concepts and Technologies*; Springer: Berlin, 2003.

(2) Barber, Z. H.; Blamire, M. G. High Throughput Thin Film Materials Science. *Mater. Sci. Technol*. **2008**, *24*, 757–770.

(3) McGinn, P. J. Thin-Film Processing Routes for Combinatorial Materials Investigations–A Review. *ACS Comb. Sci.* **2019**, *21*, 501–515.

(4) Kawaguchi, D. Aggregation States, Thermal Molecular Motion and Carrier Properties in Functional Polymer Thin Films. *Polym. J.* **2023**, *55*, 1237–1245.

(5) Fujie, T. Development of Free-Standing Polymer Nanosheets for Advanced Medical and Health-Care Applications. *Polym. J*. **2016**, *48*, 773–780.

(6) Mounasamy, V.; Mani, G. K.; Tsuchiya, K.; Madanagurusamy, S. Preparation of Free-Standing V_2O_5 Nanosheets for Ammonia Sensing Application: A potential Candidate for Flexible Sensors. *J. Sci. Adv. Mater. Devices*. **2022**, *7*, 100415.

(7) Tri Murti, B.; Huang, Y.J.; Darumas Putri, A.; Lee, C.P.; Hsieh, C.M.; Wei, S.M.; Tsai, M.L.; Peng, C.W.; Yang, P.K. Free-Standing Vertically Aligned Tin Disulfide Nanosheets for Ultrasensitive Aptasensor Design toward Alzheimer's Diagnosis Applications. *Chem. Eng. J.* **2023**, *452*, 139394.

(8) Zhao, J.; Chi, Z.; Yang, Z.; Chen, X.; Arnold, M. S.; Zhang, Y.; Xu, J.; Chi, Z.; Aldred, M. P. Recent Developments of Truly Stretchable Thin Film Electronic and Optoelectronic Devices. *Nanoscale* **2018**, *10*, 5764–5792.

(9) Elanjeitsenni, V.P.; Vadivu, K.S.; Prasanth, B.M. A Review on Thin Films, Conducting Polymers as Sensor Devices. *Mater. Res. Express* **2022**, *9*, 022001.

(10) Chen, Z.; Zhao, X.; Tang, Y. Thin Films for Energy Harvesting, Conversion, and Storage. *Coatings* **2019**, *9*, 608.

(11) Lotnyk, A.; Behrens, M.; Rauschenbach, B. Phase Change Thin Films for Non-Volatile Memory Applications. *Nanoscale Adv.* **2019**, *1*, 3836–3857.

(12) Nambi Krishnan, J.; Venkatachalam, K.R.; Ghosh, O.; Jhaveri, K.; Palakodeti, A.; Nair, N. Review of Thin Film Nanocomposite Membranes and Their Applications in Desalination. *Front. Chem.* **2022**, *10*, 781372.

(13) Rodríguez-San-Miguel, D.; Montoro, C.; Zamora, F. Covalent Organic Framework Nanosheets: Preparation, Properties and Applications. *Chem. Soc. Rev.* **2020**, *49*, 2291.

(14) Harris, J. M. *Polyethylene Glycol Chemistry: Biotechnical and Biomedical Applications,* ed.; Plenum Press, New York, 1992.
(15) Greenwald, R. B. PEG drugs: An Overview. *J. Controlled Release* **2001**, *74*, 159–171.
(16) Jeon, S. I.; Lee, J. H.; Andrade, J. D.; De Gennes, P. G. Protein-Surface Interactions in the Presence of Polyethylene Oxide: I. Simplified Theory, *J. Colloid Interface Sci*. **1991**, *142*, 149–158.
(17) Rosenhahn, A.; Schilp, S.; Kreuzer, H. J.; Grunze, M. The role of ''Inert'' Surface Chemistry in Marine Biofouling Prevention. *Phys. Chem. Chem. Phys*. **2010**, *12*, 4275–4286.
(18) Jia, F.; Lu, X.; Tan, X.; Wang, D.; Cao, X.; Zhang, K. Effect of PEG Architecture on the Hybridization Thermodynamics and Protein Accessibility of PEGylated Oligonucleotides. *Angew. Chem., Int. Ed.* **2017**, *56*, 1239–1243.
(19) Holmberg, K.; Bergström, K.; Brink, C.; Österberg, E.; Tiberg, F.; Harris, J. M. Effects on Protein Adsorption, Bacterial Adhesion and Contact Angle of Grafting PEG Chains to Polystyrene. *J. Adhes. Sci. Technol*. **1993**, *7*, 503–517.
(20) Lowe, S.; O'Brien-Simpson, N. M.; Connal, L. A. Antibiofouling Polymer Interfaces: Poly(ethylene glycol) and Other Promising Candidates. *Polym. Chem*. **2015**, *6*, 198–212.
(21) Christophis, C.; Grunze, M.; Rosenhahn, A. Quantification of the Adhesion Strength of Fibroblastcells on Ethylene Glycol Terminated Self-Assembled Monolayers by a Microfluidic Shear Force Assay. *Phys. Chem. Chem. Phys.* **2010,** *12*, 4498–4504.
(22) Gölander, C. G.; Herron, J. N.; Lim, K.; Claesson, P.; Stenius, P.; Andrade, J. D. *Poly(Ethylene Glycol) Chemistry: Biotechnical and Biomedical Applications*, 2 ed.; Harris, J. M., Ed.; Plenum Press: New York, 1992; pp 221–245.
(23) Sharma, S.; Popat, K. C.; Desai, T. A. Controlling Nonspecific Protein Interactions in Silicon Biomicrosystems with Nanostructured Poly(ethylene glycol) Films. *Langmuir* **2002**, *18*, 8728−8731.
(24) Prime, K. L.; Whitesides, G. M. Adsorption of Proteins onto Surfaces Containing End-Attached Oligo(ethylene oxide): a Model System Using Self-Assembled Monolayers. *J. Am. Chem. Soc.* **1993,** *115*, 10714−10721.
(25) Herrwerth, S.; Eck, W.; Reinhardt, S.; Grunze, M. Factors that Determine the Protein Resistance of Oligoether Self-Assembled Monolayers – Internal Hydrophilicity, Terminal Hydrophilicity, and Lateral Packing Density, *J. Am. Chem. Soc.* **2003**, *125*, 9359−9366.
(26) Kim, S.; Gim, T.; Jeong, Y.; Ryu, J. H.; Kang, S. M. Facile Construction of Robust Multilayered PEG Films on Polydopamine-Coated Solid Substrates for Marine Antifouling

Applications. *ACS Appl. Mater. Interfaces* **2018**, *10*, 7626–7631.
(27) Meyerbröker, N.; Kriesche, T.; Zharnikov, M. Novel Ultrathin Poly(ethylene glycol) Films as Flexible Platform for Biological Applications and Plasmonics. *ACS Appl. Mater. Interfaces* **2013**, *5*, 2641−2649.
(28) Meyerbröker, N.; Zharnikov, M. Ultraflexible, Freestanding Nanomembranes Based on Poly(ethylene glycol). *Adv. Mater*. 2**014**, *26*, 3328−3332.
(29) Khan, M.; Schuster, S.; Zharnikov, M. Giant Electrical Response of Pristine and Nanoparticle-Loaded Hydrogel Nanomembranes to Humidity Variation. *J. Phys. Chem. C* **2015**, *119*, 14427−14433.
(30) Khan, M.; Schuster, S.; Zharnikov, M. Chemical Derivatization and Biofunctionalization of Hydrogel Nanomembranes for Potential Biomedical and Biosensor Applications. *Phys. Chem. Chem. Phys.* **2016**, *18*, 12035−12042.
(31) Meyerbröker, N.; Zharnikov, M. Modification and Patterning of Nanometer-Thin Poly(ethylene glycol) Films by Electron Irradiation. *ACS Appl. Mater. Interfaces* **2013**, *5*, 5129−5138.
(32) Meyerbröker, N.; Zharnikov, M. Hydrogel Nanomembranes as Templates for Patterned Deposition of Nanoparticles on Arbitrary Substrates. *ACS Appl. Mater. Interfaces* **2014**, *6*, 14729–14735.
(33) Rao, A. N.; Grainger, D. W. Biophysical Properties of Nucleic Acids at Surfaces Relevant to Microarray Performance. *Biomater. Sci.* **2014**, *2*, 436–471.
(34) Zhang, X.; Hu, H. DNA Molecules Site-Specific Immobilization and Their Applications. *Cent. Eur. J. Chem*. **2014**, *12*, 977–993.
(35) Du, Y.; D, S. Nucleic Acid Biosensors: Recent Advances and Perspectives. *Anal. Chem.* **2017**, *89*, 189–215.
(36) Cattani-Scholz, A.; Pedone, D.; Blobner, F.; Abstreiter, G.; Schwartz, J.; Tornow, M.; Andruzzi, L. PNA-PEG Modified Silicon Platforms as Functional Bio-Interfaces for Applications in DNA Microarrays and Biosensors. *Biomacromolecules*, **2009**, *10*, 489–496.
(37) Singh, A.; Sinsinbar, G.; Choudhary, M.; Kumar, V.; Pasricha, R.; Verma, H. N.; Arora, K. Graphene Oxide-Chitosan Nanocomposite Based Electrochemical DNA Biosensor for Detection of Typhoid. *Sens. Actuators B* **2013**, *185*, 675–684.
(38) Park, S. R.; Hauver, J.; Zhang, Y.; Revyakin, A.; Coleman, R. A.; Tjian, R, Chu, S.; Pertsinidis, A. A Single-Molecule Surface-Based Platform to Detect the Assembly and Function of the Human RNA Polymerase II Transcription Machinery. *Structure*. **2020**, *28*, 1337–1343.

(39) Dos Santos, L. J.; Rocha, G. P.; Alves, R. B.; de Freitas, R. P. Fullerene C_{60}: Chemistry and Applications. *Quim. Nova* **2010**, *33*, 680–693.
(40) Shrestha, L. K.; Ji, Q.M.; Mori, T.; Miyazawa, K.; Yamauchi, Y.; Hill, J. P.; Ariga, K. Fullerene Nanoarchitectonics: From Zero to Higher Dimensions. *Chem. Asian J.* **2013**, *8*, 1662–1679.
(41) Chen, F. C.; Tsai, T. H.; Chien, S. C. Simple Source/Drain Contact Structure for Solution-Processed n-Channel Fullerene Thin-Film Transistors. *Org. Electron.* **2012**, *13*, 599–603.
(42) Mohammed, M. I.; Yahia, I. S. Towards Multifunctional Applications of Fullerene-filled (PVA-PEG) Polymeric Nanocomposite Films: Structural, Optical, and Electrical Properties. *Phys. Scr.* **2022**, *97*, 065813.
(43) Isoda, T.; Sato, H.; Urushibara, I.; Uchida, S.; Kusuyama, K.; Kojima, T.; Asaka, T.; Nitta, I. Evaluation of Immunoglobulin Sensing Function Using a Fullerene-Composite-Polymer-Coated Sensor Electrode. *Sens. Mater.* **2011**, *23*, 237–249.
(44) Eck, W.; Küller, A.; Grunze, M.; Volkel, B.; Gölzhäuser, A. Freestanding Nanosheets from Crosslinked Biphenyl Self-Assembled Monolayers. *Adv. Mater.* **2005**, *17*, 2583−2586.
(45) Turchanin, A.; Gölzhäuser, A. Carbon Nanomembranes. *Adv. Mater*. **2016**, *28*, 6075−6103.
(46) Naberezhnyi, D.; Gölzhäuser, A.; Dementyev, P. Water-Assisted Permeation of Gases in Carbon Nanomembranes. *J. Phys. Chem. Lett*. **2019**, *10*, 5598–5601.
(47) Stroganov, V.; Hüger, D.; Neumann, C.; Noethel, T.; Steinert, M.; Hübner, U.; Turchanin, A. Gas Transport Mechanisms through Molecular Thin Carbon Nanomembranes. *Small* **2023**, 2300282.
(48) Yang, Y.; Dementyev, P.; Biere, N.; Emmrich, D.; Stohmann, P.; Korzetz, R.; Zhang, X.; Beyer, A.; Koch, S.; Anselmetti, D.; Gölzhäuser, A. Rapid Water Permeation through Carbon Nanomembranes with Sub-Nanometer Channels. *ACS Nano* **2018**, *12*, 4695–4701.
(49) Meyerbröker, N.; Li, Zi-An; Eck, W.; Zharnikov, M. Biocompatible Nanomembranes Based on PEGylation of Cross-Linked Self-Assembled Monolayers. *Chem. Mater.* **2012**, *24*, 2965−2972.
(50) Kaiser, D.; Tang, Z.; Küllmer, M.; Neumann, C.; Winter, A.; Kahle, R.; Georgi, L.; Weimann, T.; Siegmann, M.; Gräfe, S.; Centeno, A.; Zurutuza, A.; Turchanin, A. pH Sensors Based on Amino-Terminated Carbon Nanomembrane and Single-Layer Graphene van Der Waals Heterostructures. *Appl. Phys. Rev*. **2021**, *8*, 031410.
(51) Angelova, P.; Vieker, H.; Weber, N.-E.; Matei, D.; Reimer, O.; Meier, I.; Kurasch, S.; Biskupek, J.; Lorbach, D.; Wunderlich, K.; Chen, L.; Terfort, A.; Klapper, M.; Müllen, K.;

Kaiser, U.; Gölzhäuser, A.; Turchanin, A. A Universal Scheme to Convert Aromatic Molecular Monolayers into Functional Carbon Nanomembranes. *ACS Nano* **2013**, *7*, 6489–6497.
(52) Zharnikov, M.; Grunze, M. Modification of Thiol-Derived Self-Assembling Monolayers by Electron and X-ray Irradiation: Scientific and Lithographic Aspects. *J. Vac. Sci. Technol., B: Microelectron. Process. Phenom*. **2002**, *20*, 1793−1807.
(53) Geyer, W.; Stadler, V.; Eck, W.; Zharnikov, M.; Gölzhauser, A.; Grunze, M. Electron Induced Cross-Linking of Aromatic Self-Assembled Monolayers: Negative Resists for Nanolithography. *Appl. Phys. Lett.* **1999**, *75*, 2401−2403.
(54) Cyganik, P.; Vandeweert, E.; Postawa, Z.; Bastiaansen, J.; Vervaecke, F.; Lievens, P.; Silverans, R. E.; Winograd, N. Modification and Stability of Aromatic Self-Assembled Monolayers upon Irradiation with Energetic Particles. *J. Phys. Chem. B* **2005**, *109*, 5085−5094.
(55) Turchanin, A.; Kafer, D.; El-Desawy, M.; Wöll, C.; Witte, G.; Gölzhauser, A. Molecular Mechanisms of Electron-Induced Cross-Linking in Aromatic SAMs. *Langmuir* **2009**, *25*, 7342−7352.
(56) Amiaud, L.; Houplin, J.; Bourdier, M.; Humblot, V.; Azria, R.; Pradier, C.-M.; Lafosse, A. Low-Energy Electron Induced Resonant Loss of Aromaticity: Consequences on Cross-Linking in Terphenylthiol SAMs. *Phys. Chem. Chem. Phys*. **2014**, *16*, 1050−1059.
(57) Gölzhauser, A.; Geyer, W.; Stadler, V.; Eck, W.; Grunze, M.; Edinger, K.; Weimann, Th.; Hinze, P. Nanoscale Patterning of Self-Assembled Monolayers with Electrons. *J. Vac. Sci. Technol. B: Microelectron. Process. Phenom*. **2000**, *18*, 3414−3418.
(58) Chinwangso, P.; Jamison, A. C.; Lee, T. R. Multidentate Adsorbates for Self-Assembled Monolayer Films. *Acc. Chem. Res*. **2011**, *44*, 511–519.
(59) Lindner, M.; Valášek, M.; Homberg, J.; Edelmann, K.; Gerhard, L.; Wulfhekel, W.; Fuhr, O.; Wächter, T.; Zharnikov, M.; Kolivoška, V.; et al. Importance of the Anchor Group Position (Para *versus* Meta) in Tetraphenylmethane Tripods: Synthesis and Self-Assembly Features. *Chem. Eur. J.* **2016**, *22*, 13218–13235.
(60) Li, Z.-Q.; Tang, J.-H.; Zhong, Y.-W. Multidentate Anchors for Surface Functionalization. Chem. − Asian J. **2019**, *14*, 3119−3126.
(61) Ishiwari, F.; Nascimbeni, G.; Sauter, E.; Tago, H.; Shoji, Y.; Fujii, S.; Kiguchi, M.; Tada, T.; Zharnikov, M.; Zojer, E.; Fukushima, T. Triptycene Tripods for the Formation of Highly Uniform and Densely Packed Self-Assembled Monolayers with Controlled Molecular Orientation. *J. Am. Chem. Soc*. **2019**, *141*, 5995–6005.
(62) Shen, M. C.; Martinson, L.; Wagner, M. S.; Castner, D. G.; Ratner, B. D.; Horbett, T. A. PEO-like Plasma Polymerized Tetraglyme Surface Interactions with Leukocytes and

Proteins: in vitro and in vivo Studies. *J. Biomater. Sci., Polym. Ed.* **2002,** *13*, 367−390.
(63) D'souza, A. A.; Shegokar, R. Polyethylene Glycol (PEG): A Versatile Polymer for Pharmaceutical Applications. Expert Opin. *Drug Delivery* **2016**, *13*, 1257–1275.
(64) Zhang, Y.; Chan, H. F.; Leong, K. W. Advanced Materials and Processing for Drug Delivery: the Past and the Future. *Adv. Drug Delivery Rev*. **2013**, *65*, 104–120.
(65) Sellaturay, P.; Nasser, S.; Ewan, P. Polyethylene Glycol-Induced Systemic Allergic Reactions (Anaphylaxis). *J. Allergy Clin. Immunol. Pract.* **2021**, *9*, 670−675.
(66) Zhao, X.; Si, J.; Huang, D.; Li, K.; Xin, Y.; Sui, M. Application of Star Poly(ethylene glycol) Derivatives in Drug Delivery and Controlled Release. *J Contr Rel.* **2020**, *323*, 565−577.
(67) Kizil, S.; Sonmez, H.B. Star PEG Based Amphiphilic Polymers: Synthesis, Characterization and Swelling Behaviors. *Polym. Bull.* **2019**, *76*, 2081−2096.
(68) Tan, H.; DeFail, A.; Rubin, J. P.; Chu, C. R.; Marra, K. G. Novel Multi-Arm PEG-Based Hydrogels for Tissue Engineering. *J. Biomed. Mater. Res. Part A* **2011**, *92*, 979–987.
(69) Akintayo, C.O.; Creusen, G.; Straub, P.; Walther, A. Tunable and Large-Scale Model Network StarPEG-DNA Hydrogels. *Macromolecules* **2021**, *54*, 7125–7133.
(70) Schwartz, D. K. Mechanisms and Kinetics of Self-Assembled Monolayer Formation. *Annu. Rev. Phys. Chem*. **2001**, *52*, 107–137.
(71) Yan, R.; Terfort, A.; Zharnikov, M. Modification of Alkanethiolate Self-Assembled Monolayers by Ultraviolet Light: The Effect of the Wavelength. *J. Phys. Chem. C* **2021**, *125*, 3, 1855–1864.
(72) Sayin, M.; Nefedov, A.; Zharnikov, M. Spectroscopic Study of Water Adsorption and Desorption on/from Oligo(ethylene glycol)-Substituted Alkanethiolate Self-Assembled Monolayers. *J. Phys. Chem. C* **2018**, *122*, 10918–10928.
(73) Salci, A.; Solmaz, R. Fabrication of Rhodamine Self-Assembled Monolayer Thin Films on Copper: Solvent Optimization and Corrosion Inhibition Studies. *Prog. Org. Coatings,* **2018***,* 125, 516−524.
(74) Schoenfisch, M. H.; Pemberton, J. E. Air Stability of Alkanethiol Self-Assembled Monolayers on Silver and Gold Surfaces. *J. Am. Chem. Soc*. **1998**, 120, 4502−5413.
(75) Lim, M. S.; Feng, K.; Chen, X. Q.; Wu, N. Q.; Raman, A.; Nightingale, J.; Gawalt, E. S.; Korakakis, D.; Hornak, L. A.; Timperman, A. T. Adsorption and Desorption of Stearic Acid Self-Assembled Monolayers on Aluminum Oxide. *Langmuir* **2007**, *23*, 2444–2452.
(76) Yan, C.; Zharnikov, M.; Gölzhäuser, A.; Grunze, M. Preparation and Characterization of Self-Assembled Monolayers on Indium Tin Oxide. *Langmuir* **2000**, *16*, 6208–6215.

(77) Ulman, A. Formation and Structure of Self-Assembled Monolayers. *Chem. Rev*. **1996**, *96*, 1533–1554.

(78) Casalini, S.; Bortolotti, C. A.; Leonardi, F.; Biscarini, F. Self-Assembled Monolayers in Organic Electronics. *Chem. Soc. Rev*. **2017**, *46*, 40–71.

(79) Ruckenstein, E.; Li, Z. F. Surface Modification and Functionalization through the Self-Assembled Monolayer and Graft Polymerization. *Adv. Colloid Interface Sci*. **2005**, *113*, 43–63.

(80) Love, J. C.; Estroff, L. A.; Kriebel, J. K.; Nuzzo, R. G.; Whitesides, G. M. Self-Assembled Monolayers of Thiolates on Metals as a Form of Nanotechnology. *Chem. Rev*. **2005**, *105*, 1103–1169.

(81) Mandler, D.; Kraus-Ophir, S. Self-Assembled Monolayers (SAMs) for Electrochemical Sensing. *J. Solid State Electrochem*. **2011**, *15*, 1535–1558.

(82) Ali, F.; Roldan-Carmona, C.; Sohail, M.; Nazeeruddin, M. K. Applications of Self-Assembled Monolayers for Perovskite Solar Cells Interface Engineering to Address Efficiency and Stability. *Adv. Energy Mater*. **2020**, *10*, 2002989.

(83) Choi, Y.; Tran, H.-V.; Lee, T. R. Self-Assembled Monolayer Coatings on Gold and Silica Surfaces for Antifouling Applications: A Review. *Coatings* **2022**, *12*, 1462.

(84) Ratner, M.; Castner, D. in *Surface Analysis – The Principal Techniques*; Vickerman, J., Ed.; John Wiley & Sons: Chichester, 1997; pp 43–98.

(85) Stevie, F. A.; Donley, C. L. Introduction to X-ray Photoelectron Spectroscopy. *J. Vac. Sci. Technol.* ***2020***, *A 38*, 063204.

(86) Cushman, C.; Chatterjee, S.; Major, G.H.; Smith, N.; Roberts, A.; Linford, M. Trends in Advanced XPS Instrumentation. *Vac. Technol. Coat*. **2017**, 9, 1–9.

(87) Jablonski, A.; Powell, C. J. The Electron Attenuation Length Revisited. *Surf. Sci. Rep*. **2002**, *47*, 35–91.

(88) Thome, J.; Himmelhaus, M.; Zharnikov, M.; Grunze, M. Increased Lateral Density in Alkanethiolate Films on Gold by Mercury Adsorption. *Langmuir* **1998**, *14*, 7435−7449.

(89) Heister, K.; Johansson, L. S. O.; Grunze, M.; Zharnikov, M. A Detailed Analysis of the C 1s Photoemission of n-Alkanethiolate Films on Noble Metal Substrates. *Surf. Sci*. **2003**, *529*, 36−46.

(90) Nefedov, A.; Wöll, C. *Advanced Applications of NEXAFS Spectroscopy for Functionalized Surfaces.; In Surface Science Techniques*; Bracco, G., Holst, B., Eds.; Springer Series in Surface Science; Springer-Verlag: Berlin, 2013; Vol. 51, pp 277–306.

(91) Lee, C.-Y.; Gong, P.; Harbers, G. M.; Grainger, D. W.; Castner, D. G.; Gamble, L. Surface Coverage and Structure of Xixed DNA/Alkylthiol Monolayers on Gold: Characterization by XPS, NEXAFS, and Fluorescence Intensity Measurements. *J. Anal. Chem.* **2006**, *78*, 3316–3325.

(92) Smith, A. P., Urquhart, S. G., Winesett, D. A., Mitchell, G. & Ade, H. Use of Near Edge X-ray Absorption Fine Structure Spectromicroscopy to Characterize Multicomponent Polymeric Systems. *Appl. Spectrosc*., **2001**, *55*, 1676–1681.

(93) Tompkins, H. G. I., and Eugene, A. *A Handbook of Ellipsometry*; William Andrew Publishing: New York, 2005.

(94) Fujiwara, H. *Spectroscopic Ellipsometry: Principles and Applications*; John Wiley & Sons Ltd.: New York, 2007; pp 249–303.

(95) Small, M. K.; Vlassak, J. J., Powell, S. F., Daniels, B. J.; Nix, W. D. Accuracy and Reliability of Bulge Test Experiments, *Mat. Res. Soc. Symp. Proc.* **1993,** *308*, 159–164.

(96) Paul, O.; Gaspar, J. *Thin-Film Characterization using the Bulge Test.* In *Advanced Micro and Nanosystems Vol. 6. Reliability of MEMS*; Tabata O.; Tsuchiya T., Eds.; WILEY-VCH Verlag GmbH & Co. KGaA, Weinheim, Germany, 2008; pp 67–121.

(97) Chen, K.-S.; Ou, K.-S. in *Handbook of Silicon Based MEMS Materials and Technologies*; Tilli, M., Paulasto-Krockel, M., Petzold, M., Theuss, H., Motooka, T., Lindroos, V. Eds.; Elsevier: Amsterdam, 2015; pp. 398–412.

(98) Ali, A.S. Application of Nanomaterials in Environmental Improvement. In Nanotechnology and the Environment; IntechOpen, 2020.

(99) Vernon-Parry, K. D. Scanning Electron Microscopy: An Introduction. *III–Vs Rev*. **2000**, *13*, 40–44.

(100) Magonov, S. N.; Whangbo, M.-H. *Surface Analysis with STM and AFM*; VCH: New York, 1996.

(101) Tissue, B.M. *Ultraviolet and Visible Absorption Spectroscopy, in Characterization of Materials*; John Wiley & Sons, Ltd, 2012; pp. 1–13.

(102) Creighton, J. A.; Eadon, D. G. Ultraviolet-Visible Absorption Spectra of the Colloidal Metallic Elements. *J. Chem. Soc. Faraday Trans*. **1991**, *87*, 3881–3891.

(103) Haiss, W.; Thanh, N. T. K.; Aveyard, J.; Fernig, D. G. Determination of Size and Concentration of Gold Nanoparticles from UV-Vis Spectra. *Anal. Chem*. **2007**, *79*, 4215–4221.

(104) Brandt, I.S.; de Araujo, C.I.L.; Stenger, V.; Delatorre, R.G.; Pasa, A.A. Electrical Characterization of Cu/Cu_2O Electrodeposited Contacts. *ECS Transactions*, **2008**, *14*, 413.

(105) Choudhary, Y. S.; Jothi, L.; Nageswaran, G. *Electrochemical Characterization. In Spectroscopic Methods for Nanomaterials Characterization*; Thomas, S.; Thomas, R.; Zachariah, A. K.; Mishra, R. K., Eds.; Elsevier, 2017; Chapter 2, pp 19–54.
(106) Ramaley, L.; Dalziel, J.A.; Tan, W.T. Adsorption Enhancement in Square Wave Polarography, *Can. J. Chem*. **1981**, *59*, 3334−3340.
(107) Mei, B.A.; Munteshari, O.; Lau, J.; Dunn, B.; Pilon, L. Physical Interpretations of Nyquist Plots for EDLC Electrodes and Devices. *J. Phys. Chem. C* **2017**, *122*, 194–206.
(108) Chang, T.H.P. Combined Micro-Miniature Processing and Microscopy using a Scanning Electron Probe System. PhD Dissertation, University of Cambridge. 1967.
(109) Hatzakis, M. Electron Resists for Microcircuit and Mask Production. *J. Electrochem. Soc*. **1969**, *116*, 1033–1037.
(110) Altissimo, M. E-Beam Lithography for Micro-/Nanofabrication. *Biomicrofluidics* **2010**, *4*, 026503.
(111) Kolodziej, C. M.; Maynard, H. D. Electron-beam Lithography for Patterning Biomolecules at the Micron and Nanometer Scale. *Chem. Mater*. **2012**, *24*, 774–780.
(112) Barcelo, S.; Li, Z. Nanoimprint Lithography for Nanodevice Fabrication. *Nano Converg.* **2016**, *3*, 21.
(113) Moulder, J. F.; Stickle, W. E.; Sobol, P. E.; Bomben, K. D. *Handbook of X-ray Photoelectron Spectroscopy*; Chastian, J., Ed.; Perkin-Elmer Corp.: Eden Prairie, MN, 1992.
(114) Jeyachandran, Y. L.; Terfort, A.; Zharnikov, M. Controlled Modification of Protein-Repelling Self-Assembled Monolayers by Ultraviolet Light: The Effect of the Wavelength. *J. Phys. Chem. C* **2012**, *116*, 9019–9028.
(115) Jeyachandran, Y. L.; Weber, T.; Terfort, A.; Zharnikov, M. Application of Long Wavelength Ultraviolet Radiation for Modification and Patterning of Protein-Repelling Monolayers. *J. Phys. Chem. C* **2013**, *117*, 5824−5830.
(116) Huang, J.; Dahlgren, D. A.; Hemminger, J. C. Photopatterning of Self-Assembled Alkanethiolate Monolayers on Gold: A Simple Monolayer Photoresist Utilizing Aqueous Chemistry. *Langmuir* **1994**, *10*, 626−628.
(117) Brewer, N. J.; Rawsterne, R. E.; Kothari, S.; Leggett, G. J. J. Oxidation of Self-Assembled Monolayers by UV Light with a Wavelength of 254 nm. *J. Am. Chem. Soc.* **2001**, *123*, 4089−4090.
(118) Weber, T.; Meyerbröker, N.; Khan Hira, N.; Zharnikov, M.; Terfort, A. UV-Mediated Tuning of Surface Biorepulsivity in Aqueous Environment. *Chem. Commun.* **2014**, *50*, 4325−4327.

(119) Ducker, R. E.; Janusz, S.; Sun, S.; Leggett, G. J. One-Step Photochemical Introduction of Nanopatterned Protein-Binding Functionalities to Oligo(ethylene glycol)-Terminated Self-Assembled Monolayers. *J. Am. Chem. Soc.* **2007**, *129*, 14842–14843.
(120) Reynolds, N. P.; Tucker, J. D.; Davison, P.A.; Timney, J. A.; Hunter, C. N.; Leggett, G. J. Site-Specific Immobilization and Micrometer and Nanometer Scale Photopatterning of Yellow Fluorescent Protein on Glass Surfaces. *J. Am. Chem. Soc.* **2009**, *131*, 896–897.
(121) Ahmad, S. A.; Hucknall, A.; Chilcoti, A.; Leggett, G. J. Protein Patterning by UV-Induced Photodegradation of Poly(oligo(ethylene glycol) methacrylate) Brushes. *Langmuir* **2010**, *26*, 9937–9942.
(122) Adams, J.; Tizazu, G.; Janusz, S.; Brueck, S. R. J.; Lopez, G. P.; Leggett, G. J. Large-Area Nanopatterning of Self-Assembled Monolayers of Alkanethiolates by Interferometric Lithography. *Langmuir* **2010**, *26*, 13600–13606.
(123) Montague, M.; Ducker, R. E.; Chong, K. S. L.; Manning, R. J.; Rutten, F. J. M.; Davies, M. C.; Leggett, G. J. Fabrication of Biomolecular Nanostructures by Scanning Near-Field Photolithography of Oligo(ethylene glycol)-Terminated Self-Assembled Monolayers. *Langmuir* **2007**, *23*, 7328–7337.
(124) Sun, S.; Leggett, G. J. Matching the Resolution of Electron Beam Lithography by Scanning Near-Field Photolithography. *Nano Lett.* **2004**, *4*, 1381–1384.
(125) ul Haq, E.; Liu, Z.; Zhang, Y.; Alang Ahmad, S. A.; Wong, Lu-S.; Armes, S. P.; Hobbs, J. K.; Leggett, G. J.; Micklefield, J.; Roberts, C. J.; Weaver, J. M. R. Parallel Scanning Near-Field Photolithography: The Snomipede. *Nano Lett.* **2010,** *10*, 4375–4380.
(126) Chen, S.; Smith, L. M. Photopatterned Thiol Surfaces for Biomolecular Immobilization. *Langmuir* **2009**, *25*, 12275–12282.
(127) Waldbaur, A.; Waterkotte, B.; Schmitz, K.; Rapp, B. E. Maskless Projection Lithography for the Fast and Flexible Generation of Grayscale Protein Patterns. *Small* **2012**, *8*, 1570–1578.
(128) Jeyachandran, Y. L.; Meyerbröker, N.; Terfort, A.; Zharnikov, M. Maskless Ultraviolet Projection Lithography with a Biorepelling Monomolecular Resist. *J. Phys. Chem. C* **2015**, *119*, 494−501.
(129) Brandl, F. P.; Seitz, A. K.; Tessmar, J. K.; Blunk, T.; Gopferich, A. M. Enzymatically Degradable Poly(Ethylene Glycol) based Gydrogels for Adipose Tissue Engineering. *Biomaterials* **2010**, *31*, 3957−3966.
(130) Kang, H.; Liu, H.; Zhang, X.; Yan, J.; Zhu, Z.; Peng, L.; Yang, H.; Kim, Y.; Tan, W. Photoresponsive DNA-Cross-Linked Hydrogels for Controllable Release and Cancer Therapy. *Langmuir* **2011**, *27*, 399−408.

(131) Buwalda, S. J. Boere, K. W.M. Dijkstra, P. J. Feijenc, J. Vermonden, T. Hennink, W. E. Hydrogels in a Historical Perspective: From Simple Networks to Smart Materials. *J. Control. Release* **2014**, *190*, 254–273.

(132) Koetting, M. C.; Peters, J. T.; Steichen, S. D.; Peppas, N. A. Stimulus-Responsive Hydrogels: Theory, Modern Advances, and Applications. *Mater. Sci. Eng., R* **2015**, *93*, 1−49.

(133) Rastogi, S. K.; Anderson, H. E.; Lamas, J.; Barret, S.; Cantu, T.; Zauscher, S.; Brittain, W. J.; Betancourt, T. Enhanced Release of Molecules upon Ultraviolet (UV) Light Irradiation from Photoresponsive Hydrogels Prepared from Bifunctional Azobenzene and Four-Arm Poly(ethylene glycol). *ACS Appl. Mater. Interfaces* **2018**, *10*, 30071−30080.

(134) Ballav, N.; Thomas, H.; Winkler, T.; Terfort, A.; Zharnikov, M. Making Protein Patterns by Writing in a Protein-Repelling Matrix. *Angew. Chem. Int. Ed.* **2009**, *48*, 5833–5836.

(135) Yan, R.; Le Pleux, L.; Mayor, M.; Zharnikov, M. Promoted Exchange Reaction between Alkanethiolate Self-Assembled Monolayers and an Azide-Bearing Substituent. *J. Phys. Chem. C* **2016**, *120***,** 25967–25976.

(136) Valiokas, R.; Malysheva, L.; Onipko, A.; Lee, H.-H.; Ruzele, Z.; Svedhem, S.; Svensson, S. C. T.; Gelius, U.; Liedberg, B. On the Quality and Structural Characteristics of Oligo(Ethylene Glycol) Assemblies on Gold: An Experimental and Theoretical Study. *J. Electron Spectrosc. Relat. Phenom.* **2009**, *172*, 9−20.

(137) Turchanin, A.; Tinazli, A.; El-Desawy, M.; Großmann, H.; Schnietz, M.; Solak, H. H.; Tampé, R.; Gölzhäuser, A. Molecular Self-Assembly, Chemical Lithography, and Biochemical Tweezers: A Path for the Fabrication of Functional Nanometer-Scale Protein Arrays. *Adv. Mater.* **2008**, *20*, 471–477.

(138) Olsen, C.; Rowntree, P. A. Bond-Selective Dissociation of Alkanethiol Based Self-Assembled Monolayers Adsorbed on Gold Substrates, Using Low-Energy Electron Beams. *J. Chem. Phys.* **1998**, *108*, 3750–3764.

(139) Huels, M. A.; Dugal, P. C.; Sanche, L. Degradation of Functionalized Alkanethiolate Monolayers by 0–18 eV Electrons. *J. Chem. Phys.* **2003**, *118*, 11168–11178.

(140) Houplin, J.; Dablemont, C.; Sala, L.; Lafosse, A.; Amiaud, L. Electron Processing at 50 eV of Terphenylthiol Self-Assembled Monolayers: Contributions of Primary and Secondary Electrons. *Langmuir* **2015**, *31*, 13528−13534

(141) Schmid, M.; Wan, X.; Asyuda, A.; Zharnikov, M. Modification of Self-Assembled Monolayers by Electron Irradiation: The Effect of Primary Energy (10−500 eV). *J. Phys. Chem. C* **2019**, *123*, 28301−28309.

(142) Neumann, C.; Wilhelm, R. A.; Küllmer, M.; Turchanin, A. Low-Energy Electron Irradiation Induced Synthesis of Molecular Nanosheets: An Influence of the Electron Beam Energy. *Faraday Discuss.* **2021**, *227*, 61−79.
(143) Jeyachandran, Y. L.; Zharnikov, M. A Comprehensive Analysis of the Effect of Electron Irradiation on Oligo(ethylene glycol) Terminated Self-Assembled Monolayers Applicable for Specific and Non-specific Patterning of Proteins. *J. Phys. Chem. C* **2012**, *116*, 14950–14959.
(144) Derry, G. N.; Kern, M. E.; Worth, E. H. Recommended Values of Clean Metal Surface Work Functions. *J. Vac. Sci. Technol. A* **2015**, *33*, 060801.
(145) Zhou, X.-L.; Zhu, X.-Y.; White, J. M. Photochemistry at Adsorbate / Metal Interfaces. *Surf. Sci. Rep.* **1991**, *13*, 73–220.
(146) Hasselbrink, E. Mechanisms in Photochemistry on Metal Surfaces. *Appl. Surf. Sci.* **1994**, *79/80*, 34–40.
(147) Brewer, N. J.; Janisz, S.; Critchley, K.; Evans, S. D.; Leggett, G. J. Photooxidation of Self-Assembled Monolayers by Exposure to Light of Wavelength of 254 nm: A Static SIMS Study. *J. Phys. Chem. B* **2005**, *109*, 11247–11256.
(148) Correa-Puerta, J.; del Campo, V.; Henríquez, R.; Esaulov, V. A.; Hamoudi, H.; Flores, M.; Häberle, P. Unoccupied Interface and Molecular States in Thiol and Dithiol Monolayers. *Langmuir* **2017**, *33*, 12056–12064.
(149) Goldberg, S. M.; Fadley, C. S.; Kono, S. Photoionization Cross-Sections for Atomic Orbitals with Random and Fixed Spatial Orientation. *J. Electron. Spectr. Relat. Phenom.* **1981**, *21*, 285–363.
(150) Yeh, J. J.; Lindau, I. Atomic Subshell Photoionization Cross Sections and Asymmetry Parameters: $1 \leqslant Z \leqslant 103$. *At. Data Nuc. Data Tables* **1985**, *32*, 1–155.
(151) Seinfeld, J. H. *Athmospreric Chemistry and Physics of Air Pollution;* John Wiley & Sons: New York, 1996.
(152) Jeong, H.-C.; Won, J.; Lee, Ju H.; Kim, D. H.; Lee, D. W.; Oh, B.-Y.; Han, J.-M.; Seo, D.-S. Ion-Beam Irradiation Modified Chemical and Physical Surface Characteristics of Polyethylene Glycol Film for Liquid Crystal Aligning. *Soft Mater.* **2019**, *17*, 368–374.
(153) Zhao, Z.; Yan, R.; Zharnikov, M. The Effect of Ultraviolet Light on Biorepulsive Hydrogel Poly(ethylene glycol) Films. *ACS Appl. Polymer Mater.* **2021**, *3*, 3446−3454.
(154) Vlassak, J. J.; Nix, W. D. A New Bulge Test Technique for the Determination of Young's modulus and Poisson's Ratio of Thin Films. *J. Mater. Res.* **1992**, *7*, 3242–3249.
(155) Zhang, X. H.; Beyer, A.; Gölzhauser, A. Mechanical Characterization of Carbon

Nanomembranes from Self-Assembled Monolayers. *Beilstein J. Nanotechnol.* **2011**, *2*, 826–833.
(156) Jiang, C. Y.; Markutsya, S.; Pikus, Y.; Tsukruk, V. V. Freely Suspended Nanocomposite membraness as Highly Sensitive Sensors. *Nat. Mater.* **2004**, *3*, 721–728.
(157) Zhao, Z.; Das, S.; Zharnikov, M. Tuning the Properties of Poly(ethylene glycol) Films and Membranes by Molecular Weight of the Precursors. *ACS Appl. Polymer Mater.* **2021**, *4*, 645−653.
(158) Datta, K.; Deotare, P. B. Optical Determination of Young's Modulus of Nanoscale Organic Semiconductor Thin Films for Flexible Devices. *ACS Appl. Nano Mater.* **2020**, *3*, 992−1001.
(159). Toda, M.; Miyake, K.; Chu, Li-Q.; Zakerin, M.; Förch, R.; Berger, R.; Itakura, A. N. Young's Modulus of Plasma-Polymerized Allylamine Films using Micromechanical Cantilever Sensor and Laser-Based Surface Acoustic Wave Techniques. *Plasma Process. Polym.* **2018**, *15*, e1800083.
(160) Ballav, N.; Shaporenko, A.; Terfort, A.; Zharnikov, M. A Flexible Approach to the Fabrication of Chemical Gradients. *Adv. Mater.* **2007**, *19*, 998–1000.
(161). Zharnikov, M. Femtosecond Charge Transfer Dynamics in Monomolecular Films in the Context of Molecular Electronics. *Acc. Chem. Res.* **2020**, *53*, 2975−2984.
(162) Mädler, S.; Bich, C.; Touboul, D.; Zenobi, R. Chemical Cross-Linking with NHS Esters: A Systematic Study on Amino Acid Reactivities. *J. Mass Spectrom*. **2009**, *44*, 694–706.
(163) Ballav, N.; Koelsch, P.; Zharnikov, M. Orientation and Ordering in Monomolecular Films of Sulfur-Modified Homo-Oligonucleotides on Gold. *J. Phys. Chem. C* **2009**, *113*, 18312–18320.
(164) Saprigin, A.; Thomas, C.; Dulcey, C.; Patterson, C.; Spector, M. Spectroscopic Quantification of Covalently Immobilized Oligonucleotides. *Surf. Interface Anal.* **2004**, *36*, 24–32.
(165) Petrovykh, D. Y.; Kimura-Suda, H.; Tarlov, M. J.; Whitman, L. J. Quantitative Characterization of DNA Films by X-ray Photoelectron Spectroscopy. *Langmuir* **2004**, *20*, 429–440.
(166) Rei Vilar, M.; Botelho do Rego, A. M.; Ferraria, A. M.; Jugnet, Y.; Nogues, C.; Peled, D.; Naaman, R. J. Interaction of Self-Assembled Monolayers of DNA with Electrons: HREELS and XPS Studies. *J. Phys. Chem. B* **2008**, *112*, 6957–6964.
(167) Petrovykh, D. Y.; Perez-Dieste, V.; Opdahl, A.; Kimura-Suda, H.; Sullivan, J. M.; Tarlov, M. J.; Himpsel, F. J.; Whitman, L. Nucleobase Orientation and Ordering in Films of

Single-Stranded DNA on Aold. *J. Am. Chem. Soc.* **2006**, *128*, 2–3.
(168) Opdahl, A.; Petrovykh, D. Y.; Kimura-Suda, H.; Tarlov, M. J.; Whitman, L. J. Independent Control of Grafting Density and Conformation of Single-Stranded DNA Brushes. *Proc. Natl. Acad. Sci. U. S. A*. **2007**, *104*, 9–14.
(169) Howell, C.; Jeyachandran, Y. L.; Koelsch, P.; Zharnikov, M. Orientation and Ordering in Sequence- and Length-Mismatched Surface-Bound DNA Hybrids. *J. Phys. Chem. C* **2012**, *116*, 11133−11140.
(170) Howell, C.; Hamoudi, H.; Zharnikov, M. Thymine/Adenine Diblock-Oligonucleotide Monolayers and Hybrid Brushes on Gold: A Spectroscopic Study. *Biointerphases* **2013**, *8*, 6.
(171) Roth, E.; Glick Azaria, A.; Girshevitz, O.; Bitler, A.; Garini, Y. Measuring the Conformation and Persistence Length of Single-Stranded DNA using a DNA Origami Structure. *Nano Lett.* **2018**, *18*, 6703−6709.
(172) Petrovykh, D. Y.; Kimura-Suda, H.; Whitman, L. J.; Tarlov, M. J. Quantitative Analysis and Characterization of DNA Immobilized on Gold. *J. Am. Chem. Soc.* **2003**, 125, 5219−5226.
(173) Zhang, S.; Pan, N. Supercapacitors Performance Evaluation. *Adv. En. Mater.* **2015**, *5*, 1401401.
(174) Mohammadian, N.; Farnoush F. ALS Genosensing using DNA-Hybridization Electrochemical Biosensor based on Label-Free Immobilization of ssDNA on Sm_2O_3 NPs-rGO/PANI Composite. *Sensor. Actuat. B - Chem.* **2018**, *275*, 432−438.
(175) Liu, R.; Pan, S.; Liu, M.; Huang, W.; Lv, Z.; He, A. A Label-Free Electrochemical Biosensor with Magnetically Induced Self-Assembly for the Detection of CYP2C9* 3 Gene. *Appl. Surf. Sci.* **2021**, *537*, 147868.
(176)Yang, B.; Gordiyenko, K.; Schäfer, A.; Dadfar, S. M. M.; Yang, W.; Riehemann, K.; Kumar, R.; Niemeyer, C. M.; Hirtz, M. Fluorescence Imaging Study of Film Coating Structure and Composition Effects on DNA Hybridization. *Adv. NanoBiomed Res*. **2023**, *2*, 2200133.
(177) Stuparu, M. C.; Khan, A. Thiol-Epoxy "Click" Chemistry: Application in Preparation and Postpolymerization Modification of Polymers. *J. Polym. Sci., Part A: Polym. Chem.* **2016**, *54*, 3057–3070.
(178) Ngavouka, M. D. N.; Capaldo, P.; Ambrosetti, E.; Scoles, G.; Casalis, L.; Parisse, P. Mismatch Detection in DNA Monolayers by Atomic Force Microscopy and Electrochemical Impedance Spectroscopy. *Beilstein J. Nanotechnol.* **2016**, *7,* 220–227.
(179) Carr, O.; Raymundo-Pereira, P. A.; Shimizu, F. M.; Sorroche, B. P.; Melendez, M. E.; de Oliveira Pedro, R.; Miranda, P. B.; Carvalho, A. L.; Reis, R. M.; Arantes, L. M. R. B.;

Oliveira, O. N. Genosensor Made with a Self-Assembled Monolayer Matrix to Detect MGMT Gene Methylation in Head and Neck Cancer Cell Lines. *Talanta* **2020**, *210*, 120609.

(180) Zhao, Z.; Das, S.; Zharnikov, M. Rational Design of Porous Poly(ethylene glycol) Films as a Matrix for ssDNA Immobilization and Hybridization. *Bioengineering* **2022**, *9*, 414.

(181) Han, H.; Sabani, N. B.; Nobusawa, K.; Takei, F.; Nakatani, K.; Yamashita, I. On-Demand Ligand-Base DNA Sensor with Electrochemical Impedance Spectroscopy. *Anal. Chem.* **2023**, *95*, 9729−9733.

(182) Raymundo-Pereira, P. A.; de Oliveira Pedro, R.; Carr, O.; Melendez, M. E.; Gobbi, A. L.; Helena de Oliveira Piazzetta, M.; Carvalho, A. L.; Reis, R. M.; Miranda, P. B.; Oliveira, O. N. Influence of the Molecular Orientation and Ionization of Self-Assembled Monolayers in Biosensors: Application to Genosensors of Prostate Cancer Antigen 3. *J. Phys. Chem. C* **2021**, *125*, 498–506.

(183) Gong, P.; Lee, C. Y.; Gamble, L. J.; Castner, D. G.; Grainger, D. W. Hybridization Behavior of Mixed DNA/Alkylthiol Monolayers on Gold: Characterization by Surface Plasmon Resonance and ^{32}P Radiometric Assay. *Anal. Chem.* **2006**, *78*, 3326−3334.

(184) Kratschmer, W.; Lamb, L.D.; Fostiropoulos, K.; Huffman, D. R. Solid C60 - A New Form of Carbon. *Nature* **1990**, *347*, 354−358.

(185) Jariwala, D.; Sangwan, V. K.; Lauhon, L. J.; Marks, T. J.; Hersam, M. C. Carbon Nanomaterials for Electronics, Optoelectronics, Photovoltaics, and Sensing. *Chem. Soc. Rev.* **2013**, *42*, 2824−2860.

(186) Penkova, A. V.; Acquah, S. F. A.; Piotrovskiy, L. B.; Markelov, D. A.; Semisalova, A. S.; Kroto, H. W. Fullerene Derivatives as Nano-Additives in Polymer Composites. *Russ. Chem. Rev.* **2017**, *86*, 530−566.

(187) Gradzka, E.; Wysocka-Zolopa, M.; Winkler, K. Fullerene-Based Conducting Polymers: n-Dopable Materials for Charge Storage Application. *Adv. Energy Mater.* **2020**, *10*, 2001443.

(188) Prasad, S. B.; Kumar, A.; Singh, R. Molecularly Imprinted Polymer-Based Electrochemical Sensor using Functionalized Fullerene as a Nanomediator for Ultratrace Analysis of Primaquine. *Carbon* **2016**, *109*, 196−207.

(189) Shahhoseini, L.; Mohammadi, R.; Ghanbari, B.; Shahrokhian, S. Ni(II) 1D-Coordination Polymer/C_{60}-Modified Glassy Carbon Electrode as a Highly Sensitive Non-Enzymatic Glucose Electrochemical Sensor. *Appl. Surf. Sci.* **2019**, *478*, 361–372.

(190) Suresh, L.; Bondili, J. S.; Brahman, P. Fabrication of Immunosensor Based on Polyaniline, Fullerene-C_{60} and Palladium Nanoparticles Nanocomposite: An Electrochemical Detection Tool for Prostate Cancer. *Electroanalysis* **2020**, *32*, 1439–1448.
(191) Apetrei, R. M.; Guven, N.; Camurlu, P. Biosensing Efficiency of Nanocarbon-Reinforced Polyacrylonitrile Nanofibrous Matrices. *J. Electrochem. Soc.* **2022**, *169*, 020548.
(192) Kurbanoglu, S.; Cevher, S. C.; Toppare, L.; Cirpan, A.; Soylemez, S. Electrochemical Biosensor Based on Three Components Random Conjugated Polymer with Fullerene (C_{60}). *Bioelectrochemistry* **2022**, *147*, 108219.
(193) Thompson, B. C.; Fréchet, J. M. J. Polymer–Fullerene Composite Solar Cells. *Angew. Chem. Int. Ed.* **2008**, *47*, 58–77.
(194) Zhang, F.; Inganäs, O.; Zhou, Y.; Vandewal, K. Development of Polymer-Fullerene Solar Cells. *Natl. Sci. Rev.* **2016**, *3*, 222–239.
(195) Xie, C.; Tang, X.; Berlinghof, M.; Langner, S.; Chen, S.; Späth, A.; Li, N.; Fink, R. H.; Unruh, T.; Brabec, C. J. Robot-Based High-Throughput Engineering of Alcoholic Polymer: Fullerene Nanoparticle Inks for an Eco-Friendly Processing of Organic Solar Cells. *ACS Appl. Mater. Interfaces* **2018**, *10*, 23225–23234.
(196) Meresa, A. A.; Parida, B.; Long D. X.; Kim, D.; Kim, T.; Earmme, T.; Hong, J.; Kang, D. W.; Kim, F. S. Enhanced Dissociation of Excitons and Charge Transfer in Organic Solar Cells of Polymer: Fullerene Blends with Molecular BPFZn Doping. *Int. J. Energy Res.* **2022**, *46*, 8716–8725.
(197) Geng, Y. F.; Zeng, Q. D.; Wang, C. Dependence of the Surface-Assisted Fullerene-Based Complex Structure on the Template Molecule Design. *Nano Res.* **2019**, *12*, 1509−1537.
(198) Yin, H. L.; Lin, H. T.; Zong, Y.; Wang, X. D. The Recent Advances in C_{60} Micro/Nanostructures and Their Optoelectronic Applications. Org. Electron. **2021**, *93*, 106142.
(199) Babu, S. S.; Möhwald, H.; Nakanishi, T. Recent Progress in Morphology Control of Supramolecular Fullerene Assemblies and its Applications. *Chem. Soc. Rev.* **2010**, *39*, 4021–4035.
(200) Das, S.; Preiß, J.; Plentz, J.; Brückner, U.; von der Lühe, M.; Eckardt, O.; Dathe, A.; Schacher, F. H.; Täuscher, E.; Ritter, U.; Csáki, A.; Andrä, G.; Dietzek, B.; Presselt, M. Controlling Intermolecular Interactions at Interfaces: Case of Supramolecular Tuning of Fullerene's Electronic Structure. *Adv. Energy Mater.* **2018**, *8*, 1801737.
(201) Das, S.; Presselt, M. Progress and Development in Structural and Optoelectronic Tunability of Supramolecular Nonbonded Fullerene Assemblies. *J. Mater. Chem. C* **2019**, *7*, 6194–6216.

(202) Guldi, D. M.; Zerbetto, F.; Georgakilas, V.; Prato, M. Ordering Fullerene Materials at Nanometer Dimensions, *Acc. Chem. Res.* **2005**, *38*, 38–43.
(203) Das, S.; Herrmann-Westendorf, F.; Schacher, F. H.; Täuscher, E.; Ritter, U.; Dietzek, B.; Presselt, M. Controlling Electronic Transitions in Fullerene van der Waals Aggregates via Supramolecular Assembly. *ACS Appl. Mater. Interfaces* **2016**, *8*, 21512−21521.
(204) Friedrich, D.; Henkel, K.; Richter, M.; Schmeißer, D. Fullerenol as Probed by Synchrotron X-ray Photoemission and Absorption Spectroscopy. *BioNanoSci.* **2011**, *1*, 218–223.
(205) Meyerbroeker, N.; Waske, P.; Zharnikov, M. Amino-Terminated Biphenylthiol Self-Assembled Monolayers as Highly Reactive Molecular Templates. *J. Chem. Phys.* **2015**, *142*, 101919.
(206) Zhang, X.; Teplyakov, A. V. Adsorption of C_{60} Buckminster Fullerenes on an 11-Amino-1-Undecene-Covered Si(111) Substrate. *Langmuir* **2008**, *24*, 810–820.
(207) Das, S.; Fiedler, J.; Stauffert, O.; Walter, M.; Buhmann, S. Y.; Presselt, M. Macroscopic Quantum Electrodynamics and Density Functional Theory Approaches to Dispersion Interactions between Fullerenes. *Phys. Chem. Chem. Phys.* **2020**, *22*, 23295–23306.
(208) Jehoulet, C.; Obeng, Y. S.; Kim, Y.; Zhou, F.; Bard, A. J. Electrochemistry and Langmuir Trough Studies of C_{60} and C_{70} Films. *J. Am. Chem. Soc.* **1992**, *114*, 4237–4247.
(209) Bond, A. M.; Miao, W.; Raston, C. L. Identification of Processes that Occur after Reduction and Dissolution of C_{60} Adhered to Gold, Glassy Carbon, and Platinum Electrodes Placed in Acetonitrile (Electrolyte) Solution. *J. Phys. Chem. B* **2000**, *104*, 2320–2329.
(210) Cardona, C. M.; Li, W.; Kaifer, A. E.; Stockdale, D.; Bazan, G. C. Electrochemical Considerations for Determining Absolute Frontier Orbital Energy Levels of Conjugated Polymers for Solar Cell Applications. *Adv. Mat.* **2011**, *23*, 2367–2371.
(211) Wang, X.; Tang, F.; Cao, Q.; Qi, X.; Pearson, M.; Li, M.; Pan, H.; Zhang, Z.; Lin, Z. Comparative Study of Three Carbon Additives: Carbon nanotubes, Graphene, and Fullerene-C60, for Synthesizing Enhanced Polymer Nanocomposites. *Nanomaterials* **2020**, *10*, 838.
(212) Anthi, J.; Kolivoška, V.; Holubová, B.; Vaisocherová-Lísalová, H. Probing Polymer Brushes with Electrochemical Impedance Spectroscopy: A Mini Review. *Biomater. Sci.* **2021**, *9*, 7379–7391.
(213) Zhao, Z.; Zharnikov, M. Elastic Properties of Poly(ethylene glycol) Nanomembranes and Respective Implications. *Membranes* **2022**, *12*, 509.
(214) Das, S.; Nascimbeni, G.; de la Morena, R. O.; Ishiwari, F.; Shoji, Y.; Fukushima, T.; Buck, M.; Zojer, E.; Zharnikov, M. Porous Honeycomb Self-Assembled Monolayers: Tripodal

Adsorption and Hidden Chirality of Carboxylate Anchored Triptycenes on Ag. *ACS Nano* **2021**, *15*, 11168–11179.

(215) Das, S.; Asyuda, A.; Shoji, Y.; Kosaka, A.; Fukushima, T.; Zharnikov, M. Cyano-Substituted Triptycene-Based Monolayers on Au(111): Tripodal Adsorption, Dipole Engineering, and Charge Transfer. *J. Phys. Chem. C* **2021**, *125*, 18968−18978.

(216) Das, S.; Ishiwari, F.; Shoji, Y.; Fukushima, T.; Zharnikov, M. Triptycene-Based Self-Assembled Monolayer as a Template for Successive Click Reactions. *J. Phys. Chem. C* **2023**, *127*, 5178−5185.

(217) Weidner, T.; Krämer, A.; Bruhn, C.; Zharnikov, M.; Shaporenko, A.; Siemeling, U.; Träger, F. Novel Tripod Ligands for Prickly Self-Assembled Monolayers. *Dalton Trans.* **2006**, 2767–2777.

(218) Weidner, T.; Ballav, N.; Siemeling, U.; Troegel, D.; Walter, T.; Tacke, R.; Castner, D. G.; Zharnikov, M. Tripodal Binding Units for Self-Assembled Monolayers on Gold: A Comparison of Thiol and Thioether Headgroups. *J. Phys. Chem. C* **2009**, *113*, 19609−19617.

(219) Yildirim, C.; Füser, M.; Terfort, A.; Zharnikov, M. Modification of Aromatic Self-Assembled Monolayers by Electron Irradiation: Basic Processes and Related Applications. *J. Phys. Chem. C* **2017**, *121*, 567– 576.

(220) Stöhr, J. NEXAFS Spectroscopy; Springer-Verlag: Berlin, 1992.

(221) Batson, P. E. Carbon 1s Near-Edge-Absorption Fine Structure in Graphite. *Phys. Rev. B* **1993**, *48*, 2608–2610.

(222) Asyuda, A.; Das, S.; Zharnikov, M. Thermal Stability of Alkanethiolate and Aromatic Thiolate Self-Assembled Monolayers on Au(111): An X-ray Photoelectron Spectroscopy Study. *J. Phys. Chem. C* **2021**, *125*, 21754−21763.

(223) Chen, C.-H.; Huang, M.-L.; Wang, S.-C.; Klauser, R.; Shaporenko, A.; Zharnikov, M. Exposure of Monomolecular Lithographic Patterns to Ambient: An X-ray Photoemission Spectromicroscopy Study. *J. Phys. Chem. B* **2006**, *110,* 17878−17883.

(224) Lukasczyk, T.; Schirmer, M.; Steinrück, H.-P.; Marbach, H. Electron-Beam Induced Deposition in Ultrahigh Vacuum: Lithographic Fabrication of Clean Iron Nanostructures. *Small* **2008**, *4*, 841−846.

(225) Walz, M.-M.; Schirmer, M.; Vollnhals, F.; Lukasczyk, T.;Steinrück, H.-P.; Marbach, H. Electrons as ″Invisible Ink″: Fabrication of Nanostructures by Local Electron Beam Induced Activation of SiOx. *Angew. Chem., Int. Ed*. **2010**, *49*, 4669−4673.

(226) Zharnikov, M.; Grunze, M. Spectroscopic Characterization of Thiol-Derived Self-Assembled Monolayers. *J. Phys.: Condens. Matter* **2001**, *13*, 11333−11365.

(227) Zharnikov, M. High-Resolution X-Ray Photoelectron Spectroscopy in Studies of Self-Assembled Organic Monolayers. *J. Electron Spectrosc. Relat. Phenom*. **2010**, *178−179*, 380−393.

(228) Frey, S.; Rong, H.-T.; Heister, K.; Yang, Y.-J.; Buck, M.; Zharnikov, M. Response of Biphenyl-Substituted Alkanethiol Self-Assembled Monolayers to Electron Irradiation: Damage Suppression and Odd-Even Effects. *Langmuir* **2002**, *18,* 3142−3150.

(229) Yang, Y. W.; Fan, L. J. High-Resolution XPS Study of Decanethiol on Au(111): Single Sulfur-Gold Bonding Interaction. *Langmuir* **2002**, *18*, 1157−1164.

(230) Ossowski, J.; Wächter, T.; Silies, L.; Kind, M.; Noworolska, A.; Blobner, F.; Gnatek, D.; Rysz, J.; Bolte, M.; Feulner, P.; Terfort, A.; Cyganik, P.; Zharnikov, M. Thiolate versus Selenolate: Structure, Stability and Charge Transfer Properties. *ACS Nano* **2015**, *9*, 4508−4526.

(231) Zharnikov, M. Near-Edge X-ray Absorption Fine Structure Spectroscopy in Studies of Self-Assembled Monomolecular Films. *J. Electron Spectrosc. Relat. Phenom.* **2023**, *264*, 147322.

(232) Weidner, T.; Ballav, N.; Grunze, M.; Terfort, A.; Zharnikov, M. Modification of Biphenylselenolate Monolayers by Low-Energy Electrons. *Phys. Status Solidi B* **2009**, *246*, 1519–1528.

(233) Tao, Yu-T.; Wu, C.-C.; Eu, Ji-Y.; Lin, W.-L.; Wu, K.-C.; Chen, C.-h. Structure Evolution of Aromatic-Derivatized Thiol Monolayers on Evaporated Gold. *Langmuir* **1997,** *13,* 4018–4023.

(234) Frey, S.; Stadler, V.; Heister, K.; Eck, W.; Zharnikov, M.; Grunze, M.; Zeysing, B.; Terfort, A. Structure of Thioaromatic Self-Assembled Monolayers on Gold and Silver, *Langmuir* **2001,** *17,* 2408–2415.

(235) Zharnikov, M.; Frey, S.; Rong, H.; Yang, Y.-J.; Heister, K.; Buck, M.; Grunze, M. The Effect of Sulfur–metal Bonding on the Structure of Self-Assembled Monolayers. *Phys. Chem. Chem. Phys.* **2000**, *2*, 3359–3362.

(236) Rong, H.-T.; Frey, S.; Yang, Y.-J.; Zharnikov, M.; Buck, M.; Wühn, M.; Wöll, C.; Helmchen, G. On the Importance of the Headgroup Substrate Bond in Thiol Monolayers: A Study of Biphenyl-Based Thiols on Gold and Silver. *Langmuir* **2001**, *17*, 1582–1593.

(237) Cyganik, P.; Buck, M.; Azzam, W.; Wöll, C. Self-Assembled Monolayers of ω-Biphenylalkanethiols on Au(111): Influence of Spacer Chain on Molecular Packing. *J. Phys. Chem. B* **2004**, *108*, 4989–4996.

(238) Tao, F.; Bernasek, S. L. Understanding Odd-Even Effects in Organic Self-Assembled Monolayers. *Chem. Rev.* **2007**, *107*, 1408–1453.

(239) Scherr, J.; Parey, K.; Klusch, N.; Murphy, B. J.; Balser, S.; Neuhaus, A.; Zickermann, V.; Kühlbrandt, W.; Terfort, A.; Rhinow, D. Self-Perforated Hydrogel Nanomembranes Facilitate Structural Analysis of Proteins by Electron Cryo-Microscopy. *ACS Nano* **2017**, *11*, 6467−6473.

(240) Scherr, J.; Tang, Z.; Küllmer, M.; Balser, S.; Scholz, A. S.; Winter, A.; Parey, K.; Rittner, A.; Grininger, M.; Zickermann, V.; Rhinow, D.; Terfort, A.; Turchanin, A. Smart Molecular Nanosheets for Advanced Preparation of Biological Samples in Electron Cryo-Microscopy. *ACS Nano* **2020**, *14*, 9972−9978.

(241) Liu. C. Recent Developments in Polymer MEMS. *Adv. Mater*. **2007**, *19*, 3783−3790.

(242) Fan, S. C.; Meng, L. J.; Dan, L.; Zheng, W.; Wang, X. H. Polymer Microelectromechanical System-Integrated Flexible Sensors for Wearable Technologies. *IEEE Sensors J.* **2019**, *19*, 443−450.

Acknowledgements

First and foremost, I would like to express my sincere gratitude to my supervisor, Prof. (apl.) Dr. Michael Zharnikov, for his invaluable guidance, insightful criticism, unwavering support, and thoughtful suggestions throughout my PhD study. His mentorship and expertise have been instrumental in shaping the directions of my projects and fostering my growth as a researcher.

I am indebted to the China Scholarship Council for offering me the scholarship that made my PhD study possible.

My thanks also go to Prof. Dr. Christine Selhuber-Unkel for serving as the second referee of my thesis.

I want to extend my appreciation to the people who provided me with various forms of help in my projects. I am grateful to Dr. Rui Yan and Dr. Nicolaus Meyerbröker for their valuable advice during the early stages of my PhD study. I thank Dr. Andika Asyuda for teaching me the use of several machines, and Dr. Saunak Das for providing thoughtful ideas and useful instructions in some projects. I would also like to acknowledge the collaboration with Dr. Sebastian Balser, Prof. Dr. Andreas Terfort, and Prof. Dr. Takanori Fukushima in some projects. I am thankful to Dr. Can Yildirim for guiding me in using the EBL equipment, Sonja Wieland for performing some experiments in the context of the PEG-C60 subproject, and Prof. Dr. Christine Selhuber-Unkel for providing access to the critical point dryer.

I must express my gratitude to my colleagues at APC. Working, discussing, and spending time with all of you has been a pleasure. They include, again Dr. Andika Asyuda, again Dr. Saunak Das, Yangbiao Liu, Christian Busch, Dr. Andreas Stöcklin, Dr. Huang Yan, Elisabeth Wolcke, Lucca Neupert, and Chaoran Zhang. I would also like to acknowledge the technical staff at and beyond APC, including Günter Meinusch, Klaus Schmitt, Sebastian Weber, and Peter Jeschka, for their assistance with experimental setups and computers.

My gratitude also extends to my friends, such as Shaojie Zheng, Xuzhe Liu, and my sister, Hui Zhao. Although they have been in China during my PhD study, their strong encouragement and constant concern for me have warmed my heart and kept me moving forward.

Finally, I would like to express my wholehearted thanks to Yuqi Wang, for her help, understanding, encouragement, and support throughout this long and challenging journey.